UNIVERSITY OF SOUTHAMPTON
FACULTY OF ENGINEERING AND PHYSICAL SCIENCES
School of Engineering

Development of new virtual fields for the non-linear virtual fields method

DOI: 10.5258/SOTON/D0725

by
Aleksander Marek
ORCID ID: 0000-0002-2254-3773

Thesis for the degree of Doctor of Philosophy

Supervisors: Prof. Fabrice Pierron, Dr. Frances M. Davis

January, 2019

Acknowledgements

First and foremost I would like to thank my supervisors: Prof. Fabrice Pierron and Dr. Frances Davis. Without your insight, advice and help this thesis would never materialize. I am grateful for all the time you have dedicated to my training and development as a researcher. I would also like to thank for all the opportunities you have given me to travel and network with other researchers through conferences, training courses and seminars.

The PhD programme was definitely very challenging and demanding psychologically and I could never complete it without the support from my partner K., who helped me to get through rough times with her loving, attention and patience for me. My dear - thank you for being there for me.

I would also like to thank my family, especially my parents. Without the encouragement, support and education you have given me I would have never been able to move to the UK to continue my education and study in Southampton. To my grandfather: thank you for always believing in me and pushing me to work hard and strive for the best.

My sincere thanks also goes to my examiners: Prof. Martin Browne, Dr. Georges Limbert and Prof. Sandrine Thuillier who dedicated their time to critically review my work during internal and final examinations. Their insight helped to shape this thesis as well as the research publications that are an outcome of this project.

A special thanks goes to Dr. Tomasz Garbowski who was my mentor at Poznan University of Technology where I did my engineering degree. It was your encouragement and supervision that made me interested in the wonderful world of solid mechanics.

Finally, I would like to thank colleagues at University of Southampton: Dr. Lloyd Fletcher, Dr. Xavier Régal and Dr. Rian Seghir for all the discussions we had on full-field measurements, material behaviour and inverse analysis. I would like to thank Dr. Andrew Robinson who trained me in experimental mechanics and helped to solve any issues while I worked in Testing and Structures Research Laboratory at University of Southampton. Last but not least, I would like to thank fellow PhD students who made this degree one of the best experiences I ever had.

Development of new virtual fields for the non-linear virtual fields method

Aleksander Marek

January 10, 2019

Abstract

Extraction of material parameters from full-field measurements is an increasingly important part of experimental mechanics. Due to development of full-field techniques, such as digital image correlation, new types of mechanical tests are being developed that lead to a more efficient investigation of materials behaviour. One of the popular techniques for the extraction of material parameters from full-field measurements is the virtual fields method.

The virtual fields method is centred around a concept of virtual fields, which are spatial functions that act as a filter for experimental measurements during the identification procedure. The choice of appropriate virtual fields is crucial for tackling the problems of experimental noise and complex structure of the data obtained in an experiment.

This project explores a new type of virtual fields, designed to improve the identification of material parameters for non-linear material models with the virtual fields method. The proposed virtual fields are based on the sensitivity of the reconstructed stress field to the values of material parameters allowing them to be automatically generated during the identification. They can be used with any test geometry and material model, which constitutes a very general method that is easily applicable to many static and dynamic tests.

In this thesis, the development and testing of the sensitivity-based fields are presented. The method was applied to the identification of material parameters in the context of metal plasticity, in particular, small deformation isotropic plasticity and large deformation anisotropic plasticity. The validation was performed using a series of numerical and experimental tests; a significant improvement was found in terms of the accuracy of identification compared to the standard user-defined virtual used in previous studies.

Contents

List of Figures

List of Tables

List of Symbols

Symbol	Description
$\mathbf{B}$	Strain-displacement matrix.
$\bar{\mathbf{B}}$	Modified strain-displacement matrix (accounting for boundary conditions).
$\mathbf{b}$	Body forces vector.
$\mathbf{C}^{el}$	Plane stress compliance matrix.
$\boldsymbol{\sigma}$	Cauchy stress tensor.
$\hat{\boldsymbol{\sigma}}, \hat{\mathbf{D}}$	Tensors in corotational frame.
$\hat{\sigma}_{Ap}$	Apparent yield stress.
σ_{eq}	Equivalent (scalar) measure of stress.
σ_y	Hardening function.
$\delta\widetilde{\boldsymbol{\sigma}}$	Cauchy incremental stress sensitivity tensor.
$\delta\boldsymbol{\sigma}$	Cauchy stress sensitivity tensor.
$\mathbf{D}^{ep}$	Tangential elasto-plastic stiffness matrix.
E	Young's modulus.
$\boldsymbol{\varepsilon}_L$	Logarithmic (Hencky) strain tensor.
$\bar{\varepsilon}^p$	Equivalent plastic strain.
$\boldsymbol{\varepsilon}$	Small deformation strain tensor.
$\boldsymbol{\varepsilon}^*$	Virtual strain tensor.
$\mathbf{F}$	Deformation gradient.
$\mathbf{F}^{load}$	Force load vector.
h	Thickness of a specimen.
$\mathbf{J}$	Jacobian matrix for coordinate transformation.
$\mathbf{K}$	Stiffness matrix of an finite element.
$\mathbf{K}^*$	Modified stiffness matrix of an finite element.
$\Delta\lambda$	Plastic multiplier.

Symbol	Description
$\mathbf{N}$	Shape function.
ν	Poisson's ratio.
$\mathbf{P}_{vM}$	Projection matrix for von Mises criterion.
$\mathbf{P}$	1^{st} Piola-Kirchhoff stress tensor.
$\delta\widetilde{\mathbf{P}}$	1^{st} Piola-Kirchhoff incremental stress sensitivity tensor.
$\mathbf{R}$	Rotation tensor.
ρ	Density of a body.
$\mathbf{R}_{mat}$	Rotation tensor for material coordinate system.
S	Surface of a body.
∂S	Boundary of a body (2D).
$\mathbf{S}$	2^{nd} Piola-Kirchhoff stress tensor.
$\mathbf{t}$	Traction vector.
t	Time (time step, time index).
$\mathbf{u}$	Displacement of a point (small deformation/current configuration).
$\mathbf{U}, \mathbf{V}$	Right, left stretch tensors.
$\mathbf{U}^*$	Virtual displacements vector in the reference configuration.
$\mathbf{u}^*$	Virtual displacement vector.
V	Volume of a body.
∂V	Boundary of a body (3D).
W^*_{ext}	External virtual work.
W^*_{int}	Internal virtual work.
$\mathbf{x}$	Position of a point in the reference configuration.
$\mathbf{X}$	Position of a point in the deformed configuration.
$\boldsymbol{\xi}$	Vector of material parameters.

Nomenclature

Term	Description	Abbreviation
Constitutive equation gap method	An inverse method for identification of material parameters.	CEGM
Charged-coupled device	A type of camera sensor	CCD
Constitutive law	Relationship between stress and strain.	
Digital image correlation	A full-field measurement technique.	DIC
Dynamics	Mechanical problem where inertial forces are considerable.	
Equilibrium gap method	An inverse method for identification of material parameters.	EGM
Finite element	a part of FEM, adjective referring to a part of finite element model	FE
Finite element method	A numerical method for solving systems of partial derivative equations.	FEM
Finite element model updating	An inverse method for identification of material parameters.	FEMU
Full-field measurements	Experimental techniques to measure deformation of a body over certain region, e.g. DIC, GM	
Grid method	A full-field measurement technique.	GM
Integrated digital image correlation	An inverse method for identification of material parameters.	I-DIC
Kinematic admissibility	Condition imposed on virtual displacements about their value at boundaries of a solid ($\mathbf{u}^* = 0$ on ∂V)	KA
Large deformation theory	Assumption about deformation of the body; the deformed configuration is different than the reference configuration	
Material coordinate system	Material system aligned with planes of symmetry of a material	
Plane stress	Assumption about distribution of stress within a planar body. The out-of-plane stress components are null and the stress is constant across the thickness.	
Principle of virtual work	Weak form of the equilibrium equation	PVW
Reciprocity gap method	An inverse method for identification of material parameters.	

Term	Description	Abbreviation
Region of interest	Region of available full-field measurements	ROI
Shape functions	Interpolation functions used in FEM	
Small deformation theory	Assumption about deformation of the body; the deformed configuration is the same as the reference configuration	
Statics	Mechanical problem where inertial forces negligible.	
Uni-axial test	Test in which stress field is uniform and 1D	
Virtual fields	Virtual strains (spatial derivatives of virtual displacements)	VFs
Virtual fields method	An inverse method for identification of material parameters.	VFM
Virtual work, external	Virtual work done by external forces (traction) over virtual displacements	W^*_{ext}
Virtual work, internal	Virtual work done by internal forces (stresses) over virtual fields	W^*_{int}

Chapter 1

Introduction

Over the last few decades the design process transitioned from using analytical models and more extensive use of prototypes to advanced numerical modelling of whole engineering systems. Given the improvements in computational performance and accessibility to modelling software it is now possible to predict behaviour of structures involving complicated mechanical phenomena such as yielding, fracture, fatigue and many more. One of the challenges in numerical modelling is choosing an appropriate material model, called a constitutive law, that accurately describes the response of real materials.

Material models can range from simple, such as linear elasticity, to very complex multi-scale models that include anisotropy of properties, damage, fatigue or plastic deformation. In reality, no model describes the behaviour of a material perfectly, and so the goal is to approximate it as closely as possible. Hundreds of constitutive models have been already proposed, and it is likely further refinements will be necessary to make modelling more accurate. Often, complex models involve as many as tens of parameters which need to be provided by the investigator. With so many different models and materials, availability of correct parameters is often limited due to lack of data in literature.

The inevitable step in modelling is calibration of material models to experimental data to validate the simulations and increase their accuracy. Calibration usually consists of conducting multiple simple experiments, such as uni-axial tensile tests. In these tests, closed-form solutions are known and can be used to calculate material parameters explicitly. The availability of closed-form solutions is a very strict assumption and only simple loading conditions can be used. To improve the understanding of material behaviour multiple experimental techniques have been proposed to introduce multi-axial loading within the specimen, yet maintaining closed-form solutions. Among the most prominent are plane bi-axial, the Brazilian disc or bulge tests. They can be used to explore more complex states of stress, but are still limited to only a few measurement points from strain gauges and extensometers.

A major breakthrough in experimental mechanics came with development of full-field techniques. These methods are based on optical measurements of the kinematics of the test specimen, allowing much richer data to be collected from large portions of the test pieces. The major advantage of full-field measurements is that they enable removal of some assumptions regarding strain and stress distributions within the specimen, as the deformation field is directly measured during the experiment. Moreover, the material no longer needs to be homogeneous allowing

investigation of a range of complex materials, such as welds, more freely.

Most of the methods for measuring deformation full-field are based on a concept of tracking deformation of a pattern during the experiment. The images of the pattern are taken with charge-coupled device (CCD) cameras in the reference (usually unloaded) and deformed configurations. The pictures are then used to obtain displacement and strain fields at the surface of the specimen. The number of data points obtained depends on the spatial resolution of the images. However, in most of applications a few thousands data points are collected from a single image.

The most prominent technique for measuring deformation at the surface is digital image correlation (DIC) [1, 2]. It is based on tracking a random pattern of white and black speckles between pictures taken in the reference and deformed states. The accuracy of the measurements is sub-pixel allowing to measure displacements of the order of 0.01 pixel size.

Another interesting white-light technique is the grid method (GM) [3]. The principle of the method is similar to that used in DIC, however the random pattern is replaced with a regular pattern of black lines on a white contrast, forming a grid used to measure displacements and strains. Although the regular pattern is more difficult to obtain in practice, the method provides higher spatial resolution than DIC and can offer a significant improvement when the measured displacements are small and/or gradients high.

Introduction of full-field measurements into experimental mechanics has enabled the design of new advanced tests. By discarding assumptions on the stress and strain distributions, innovative geometries can be used to investigate material behaviour under complex loading. Potentially, these new tests can be designed to be capable of identifying many material parameters at once, compared to the standard approach (one parameter at a time). A classical example would be characterisation of strain-rate dependent materials; it is possible to design a test geometry such that it induces a range of strain rates, *e.g.* from quasi-static to dynamic values: 10^{-5}–10^{0} s^{-1} [4]. Thus, a strain-rate dependent model can be identified from a single test, as opposed to the standard approach of conducting multiple simple tests at different loading rates. Additionally, full-field measurements provide thousands of independent data points representing hundreds of different stress/strain states, which can be used to understand the response of materials more completely.

Full-field measurements provide rich, but complex, data. Designing advanced tests gives an opportunity to capture whole range of material responses, however since the test geometry is unrestricted, the analysis of experimental results is much more complex. Since the stress cannot be measured directly with the full-field techniques, there are no analytical tools to link stresses in the test to the measured strains. As a result, identification of material properties becomes a complex problem. The procedure in almost all cases relies on building an error function (cost function) which depends on the material parameters and the measurements. The identification of material properties becomes an inverse problem, where the input (experimental set-up) and the output (kinematic fields) are known, however the model (material parameters) is not. Solving this problem is a challenging task.

Since the early 1990s many novel techniques have been proposed for extracting material parameters from full-field measurements. Some of them, such as finite element model updating (FEMU), the equilibrium gap method (EGM), the constitutive equation gap method (CEGM) or the virtual fields method (VFM) are briefly

summarized in [5]. The methods have been applied to characterize a wide range of materials including: metals [6], composites [7], concrete [8], rubber [9] and biological tissues [10].

The two most popular methods used to identify material models from full-field measurements are FEMU and the VFM [11]. The former is based on finding material parameters such that the corresponding finite element model of the experimental set-up matches the full-field data. The latter is based on the principle of virtual work, *i.e.* the parameters are chosen so that the stresses corresponding to the measured strains are in balance with the external loading measured in the experiment. Each method has its own merits and limitations, but the major advantage of the VFM over FEMU is its computational efficiency, in addition to the mechanism by which the experimental boundary conditions are included in the process.

The central element of the VFM are the so-called virtual fields (VFs). These are functions that act as a spatial filter on the data, *i.e.* assign weights to data points. The VFs are capable of filtering out redundant points that do not carry any information but noise, and to focus on areas rich in information to obtain the signal more effectively. This property of VFs is crucial when non-linear material models are considered. Often, the information about a particular parameter is available only in a part of the test piece. To identify this parameter VFs should focus on the areas where the signal is present, otherwise the information can be masked by noise. For the non-linear VFM choosing appropriate VFs is still an open problem.

Typically, VFs are selected from a set of well-defined mathematical formulas such as polynomials or sine functions. This approach was one of the first to be used with the VFM and was demonstrated to be successful in the case of linear elasticity as well as with non-linear models. Since there is an infinite number of valid fields, the investigator must be proficient in defining VFs to ensure accurate identification of material parameters. Moreover, VFs usually have to satisfy some virtual boundary conditions which differ from test to test and need to be included in the process.

As both the experiments and models become more complex, choosing VFs manually becomes a very challenging task. There is a strong need for an automated method for constructing dynamic virtual fields (*i.e.* time-dependent) that can adjust to the geometry of a test, suit all material models and trace the evolution of the signal with time. This is especially important for reducing the number of experiments needed for complete characterisation of material models. Improving VFs could have a significant impact on the scientific community, as more complex tests could be considered (due to better processing of the experimental data), resulting in a more accurate identification of parameters.

This thesis explores a new method for generating high quality virtual fields. The new type of VFs, called the sensitivity-based virtual fields (SBVFs), are based on the idea that the information about each parameter can be identified by analysing sensitivity of the reconstructed stress field to the value of the parameter. As a result, separate VFs are constructed - one for each parameter - facilitating identification of material models from experimental measurements.

The proposed SBVFs have many advantages, but their main strength is the ability to identify where the signal corresponding to each parameter is. They are not built upon any assumption about the geometry of the test, loading or material, thus constitute a generic technique applicable to many different experimental test

configurations.

This thesis documents this work, and is organised in the following manner. Chapter 2 presents the virtual fields theory and applications, with a particular focus on the choice of virtual fields. It is followed by a brief discussion of digital image correlation. Chapter 3 presents the first step in developing new virtual fields published in *Computational Mechanics* [12]. In this work the concept of the sensitivity-based virtual fields was presented and they were tested in the case of numerically simulated tensile test used to identify an elastoplastic material. Chapter 4 is the extension of this work and it was published in *International Journal of Material Forming* [13]. There, the sensitivity-based virtual fields were extended to the large deformation framework and applied to a numerical test in order to identify properties of an anisotropic-plastic material. Chapter 5 contains the third and final step in developing the new VFs and is intended to be submitted to *Experimental Mechanics (Springer)*. In the report the proposed method is validated experimentally by identifying anisotropic properties of a cold-rolled sheet of DC04 steel alloy. Finally, Section 6.1 summarizes the work presented in this thesis, and Section 6.2 outlines prospects for future work.

Chapter 2

Theory review and literature survey

2.1 The virtual fields method

2.1.1 Overview

In this section the virtual fields method is reviewed. First, the theoretical background is presented, followed by a more detailed discussion about the linear and the non-linear variants of the VFM. Different types of virtual fields are discussed in order to set this project in the context of current state of the field. The state-of-the-art applications of the non-linear VFM are presented, to show how general the VFM is, but also to illustrate current limitations when choosing VFs for the non-linear VFM. The chapter is concluded with a short review of different inverse techniques used to extract material properties from full-field measurements in order to set the method in a wider context.

2.1.2 Theoretical background

Inverse problems in general deal with identifying unknown causes, which might be either an input or the system itself, from a known output [14]. A common problem in mechanical testing corresponds to identifying the system (mechanical model) from know input (applied loads) and output (kinematic fields). Usually, a mathematical form of the system is known as it consists of principles such as equilibrium equations, kinematic equations relating displacements to strains and constitutive equations relating strains to stresses. In that case inverse problems focus on identifying unknown constitutive parameters that define the material using known effects of the imposed load.

The VFM is an inverse method for extracting material properties from full-field measurements. The method is based on the principle of virtual work (PVW), which expresses the equilibrium of forces within a body.

Any point within a solid body obeys a local equilibrium equation:

$$\mathrm{div}\boldsymbol{\sigma} + \mathbf{b} = \rho\boldsymbol{a}, \tag{2.1}$$

where div is the divergence operator with respect to the current configuration, $\boldsymbol{\sigma}$ the Cauchy stress tensor, $\mathbf{b}$ the body forces vector, ρ the density and $\boldsymbol{a}$ the acceleration

vector. The equation applies to a fully 3D state of stress and deformation, however the VFM is usually applied to thin, planar geometries. In the remainder of the work, following convention will be used with respect to tensor components: in-plane components will be denoted with numbers 1 and 2, the out-of-plane component will be denoted with number 3.

The same principle can be expressed in a weak form, *i.e.* as an integral evaluated over the whole body. The weak form of the local equilibrium equation is called the principle of virtual work, and can be mathematically expressed as:

$$-\int_{\mathrm{V}} \boldsymbol{\sigma} : \boldsymbol{\varepsilon}^* \mathrm{dV} + \int_{\partial \mathrm{V}} \mathbf{t} \cdot \mathbf{u}^* \mathrm{d}\partial \mathrm{V} + \int_{\mathrm{V}} \mathbf{b} \cdot \mathbf{u}^* \mathrm{dV} = \int_{\mathrm{V}} \rho \boldsymbol{a} \cdot \mathbf{u}^* \mathrm{dV} \tag{2.2}$$

In this equation V is the volume of the body, ∂V is the surface of the body where traction is applied, $\mathbf{t}$ is the traction vector and $\mathbf{u}^*$ is a test function called virtual displacement. This function is assumed to be continuous and differentiable over the whole body. Note that $\boldsymbol{\varepsilon}^*$ present in Eq. (2.2) is called virtual strain (or virtual field) and is simply a spatial derivative of the virtual displacement function:

$$\boldsymbol{\varepsilon}^* = \frac{1}{2}\left[\bigtriangledown \mathbf{u}^* + \bigtriangledown \mathbf{u}^{*T}\right] \tag{2.3}$$

This definition holds, when small deformation is assumed. It should be stressed that virtual displacements are not related to real displacements in any sense. Both virtual displacements and strains do not have any physical interpretation, they are simply test functions used to weight the stress field and formulate the weak form of the equilibrium equation.

Often, in engineering applications it is reasonable to neglect body forces and so the general form of the PVW for dynamics can be expressed as:

$$-\int_{\mathrm{V}} \boldsymbol{\sigma} : \boldsymbol{\varepsilon}^* \mathrm{dV} + \int_{\partial \mathrm{V}} \mathbf{t} \cdot \mathbf{u}^* \mathrm{d}\partial \mathrm{V} = \int_{\mathrm{V}} \rho \boldsymbol{a} \cdot \mathbf{u}^* \mathrm{dV} \tag{2.4}$$

Further simplification can be obtained when the inertia forces experienced by a body are negligible. In that case, the static equilibrium can be expressed as:

$$-\int_{\mathrm{V}} \boldsymbol{\sigma} : \boldsymbol{\varepsilon}^* \mathrm{dV} + \int_{\partial \mathrm{V}} \mathbf{t} \cdot \mathbf{u}^* \mathrm{d}\partial \mathrm{V} = 0 \tag{2.5}$$

The principle of virtual work is useful for checking whether a stress distribution is valid over the body. Assuming that the loading is known (traction term), a predicted distribution of stress can be validated just by means of the principle of virtual work. Practically, strains are measured over a region of the body, and are used to reconstruct stress field by means of an assumed constitutive law. If the material parameters used in the model are correct, the stress field satisfies the stress equilibrium. Conversely, if incorrect parameters were are fed to the material model, the calculated stress field does not satisfy the equilibrium, thus violates the PVW. This principle is used in the VFM to identify material parameters.

The PVW and VFM are formulated in 3D, but often kinematic data can only be measured at the surface of a material. To overcome this problem, usually flat specimens are used. If a flat sample is sufficiently thin (thickness much smaller compared to the other dimensions of the specimen), the plane stress condition can be assumed, under which the out-of-plane stress components are negligible

($\sigma_{13} = \sigma_{23} = \sigma_{32} = \sigma_{31} = \sigma_{33} = 0$). What follows is that the stress state across the thickness remains constant, and surface measurements are sufficient to identify material parameters. Since the stress state is constant across the thickness, Eq. (2.5) can be simplified to:

$$-h \int_{\mathrm{S}} \boldsymbol{\sigma} : \boldsymbol{\varepsilon}^* \mathrm{dS} + h \int_{\partial \mathrm{S}} \mathbf{t} \cdot \mathbf{u}^* \mathrm{d}\partial \mathrm{S} = 0, \tag{2.6}$$

where h is the thickness of the specimen, S the surface and ∂S is the traction boundary. Moreover, both the stress tensor

$$\boldsymbol{\sigma} = \begin{bmatrix} \sigma_{11} & \sigma_{12} \\ \sigma_{12} & \sigma_{22} \end{bmatrix},$$

and the virtual strain

$$\boldsymbol{\varepsilon}^* = \begin{bmatrix} \varepsilon^*_{11} & \varepsilon^*_{12} \\ \varepsilon^*_{12} & \varepsilon^*_{22} \end{bmatrix},$$

can be represented with the in-plane components only.

Full-field measurements are characterised by a large density of data points. As a result, the variation of stress within a data point is negligible. It is therefore justifiable to transform the integral of the stress field (often called the internal virtual work) from Eq. (2.6) into a discrete sum:

$$W^*_{int} = \int_{\mathrm{S}} \boldsymbol{\sigma} : \boldsymbol{\varepsilon}^* \mathrm{dS} = \sum_{i=1}^{\mathrm{nPoints}} \boldsymbol{\sigma}^i : \boldsymbol{\varepsilon}^{*i} \mathrm{S}^i, \tag{2.7}$$

where nPoints is the number of data points, index i refers to the individual data point and S^i is an area corresponding to the data point.

The strain field can be obtained using kinematic data measured with techniques such as DIC or GM by means of a constitutive law and initially unknown set of material parameters. The idea behind the VFM is to find a set of parameters that produces a stress field satisfying Eq. (2.6). Although in this work the VFM is applied under plane stress conditions, it has been applied under different set of kinematic assumptions, such as for bending and using 3D kinematic data [7, 15–17]. Recently, Rossi *et al.* proposed a method for reconstructing 3D displacement fields from stereo-DIC measurements at two opposite faces of the specimen using Bézier curves. This approach can be used to apply the VFM when plane stress assumption is no longer valid, such as during and after necking in ductile materials [18].

Virtual fields serve an important role in the VFM. As they act as a spatial weighting function on the stress field, their objective is to filter the data, reducing the impact of experimental noise as much as possible and enhancing the signal from relevant parts of the specimen to increase the accuracy of identification. Since the only assumptions imposed on the virtual displacements is that they are continuous and differentiable, it follows that there is an infinite number of valid fields to choose from. As a result there is a strong need for techniques that help selecting appropriate virtual fields effectively, improving the identification procedure in the process.

Initially, the VFM was applied to quasi-static linear elasticity problems, to identify parameters such as Young's modulus or Poisson's ratio. Later, the method was extended to any non-linear model both in statics and dynamics. Since the procedures for identifying material parameters differ considerably for the two cases, the VFM can be characterised either as the linear VFM (linear constitutive models), or the non-linear VFM (all others).

2.1.3 Linear virtual fields method

Linear elasticity is one of the simplest model that a material can be described with. It is characterised with stiffness parameters, such as Young's modulus or shear modulus, but also with cross-directional interaction effects expressed in terms of Poisson's ratio. Depending on the complexity of the material, the model can be isotropic (behave the same in all directions), orthotropic (material properties aligned with an orthogonal set of axes) or anisotropic (different in all directions).

The constitutive relationship is called Hooke's law and relates strains to stresses. In the case of plane stress isotropic elasticity, the equation is usually expressed as:

$$\begin{bmatrix} \sigma_{11} \\ \sigma_{22} \\ \sigma_{12} \end{bmatrix} = \begin{bmatrix} Q_{11} & Q_{12} & 0 \\ Q_{21} & Q_{22} & 0 \\ 0 & 0 & Q_{33} \end{bmatrix} \begin{bmatrix} \varepsilon_{11} \\ \varepsilon_{22} \\ 2\varepsilon_{12}, \end{bmatrix} \tag{2.8}$$

where:

$$Q_{11} = Q_{22} = \frac{E}{1-\nu^2}$$

$$Q_{12} = Q_{21} = \nu Q_{11} = \frac{E\nu}{1-\nu^2}$$

$$Q_{33} = \frac{Q_{11} - Q_{12}}{2}.$$

The elastic constants - Young's modulus, E, and Poisson's ratio, ν, are to be identified. The parameters can be obtained either with standard techniques, or inverse techniques such as the linear VFM.

Traditionally, Young's modulus is measured in a uni-axial test and computed as the slope of the resulting stress-strain curve. Strain is measured with a strain gauge and stress is obtained from the resultant force measured with a load cell divided by the cross-section area. The Poisson's ratio is derived from the ratio of longitudinal and transverse strains, also measured with the strain gauge. Although only one experiment is needed to measure the stiffness of an isotropic material, in the case of anisotropic materials several tests need to be performed along different loading directions with respect to the material.

Provided that the test is well designed, the linear VFM is capable of identifying all elastic properties with just a single experiment. This remark is true not only for isotropic materials, but for anisotropic as well. This is a clear advantage of the VFM over standard testing procedures as it reduces the experimental effort involved in calibrating material models. The principles of the method are outlined here, with a focus on the isotropic elasticity. The method however is valid for elasticity in general and the only difference is in the number of parameters to identify.

When isotropic Hooke's Law (Eq. (2.8)) is applied to Eq. (2.6), the resulting equation reads:

$$\begin{aligned} \int_S Q_{11}\varepsilon_{11}\varepsilon^*_{11}\mathrm{dS} + \int_S Q_{11}\varepsilon_{22}\varepsilon^*_{22}\mathrm{dS} + \int_S Q_{12}\left(\varepsilon_{11}\varepsilon^*_{22} + \varepsilon_{22}\varepsilon^*_{11}\right)\mathrm{dS} + \\ + \int_S \frac{(Q_{11} - Q_{12})}{2}\varepsilon_{12}\varepsilon^*_{12}\mathrm{dS} = \int_{\partial S} \mathbf{t}\cdot\mathbf{u}^*\mathrm{d}\partial\mathrm{S} \end{aligned} \tag{2.9}$$

As both the real strains, $\boldsymbol{\varepsilon}$, the resultant force, $\mathbf{F}^{load} = \int \mathbf{t} \mathrm{d}\partial\mathrm{S}$[1], are measured in the experiment and the virtual fields, $\boldsymbol{\varepsilon}^*$, are chosen, the only unknown quantities in this equation are the two stiffness coefficients, namely: Q_{11}, Q_{12}.

The PVW is valid for any continuous and differentiable virtual displacement field, thus applying any two different, linearly independent, virtual fields to Eq. (2.9) yields two a system of independent linear equations. Solving the system results in the identified coefficients Q_{11} and Q_{12} which can be then used to obtain E and ν. The system of equations can be written in a general form using matrix notation:

$$\mathbf{A}\boldsymbol{Q} = \mathbf{T}, \tag{2.10}$$

where:

$$\mathbf{A} = \begin{bmatrix} \int_S \left(\varepsilon_{11}\varepsilon_{11}^{*(1)} + \varepsilon_{22}\varepsilon_{22}^{*(1)} + \frac{1}{2}\varepsilon_{12}\varepsilon_{12}^{*(1)} \right) \mathrm{dS} & \int_S \left(\varepsilon_{11}\varepsilon_{22}^{*(1)} + \varepsilon_{22}\varepsilon_{11}^{*(1)} - \frac{1}{2}\varepsilon_{12}\varepsilon_{12}^{*(1)} \right) \mathrm{dS} \\ \int_S \left(\varepsilon_{11}\varepsilon_{11}^{*(2)} + \varepsilon_{22}\varepsilon_{22}^{*(2)} + \frac{1}{2}\varepsilon_{12}\varepsilon_{12}^{*(2)} \right) \mathrm{dS} & \int_S \left(\varepsilon_{11}\varepsilon_{22}^{*(2)} + \varepsilon_{22}\varepsilon_{11}^{*(2)} - \frac{1}{2}\varepsilon_{12}\varepsilon_{12}^{*(2)} \right) \mathrm{dS} \end{bmatrix}$$

$$\boldsymbol{Q} = \begin{bmatrix} Q_{11} \\ Q_{12} \end{bmatrix}$$

$$\mathbf{T} = \begin{bmatrix} \int_{\partial\mathrm{S}} \boldsymbol{t}\boldsymbol{u}^{*(1)} \mathrm{d}\partial\mathrm{S} \\ \int_{\partial\mathrm{S}} \boldsymbol{t}\boldsymbol{u}^{*(2)} \mathrm{d}\partial\mathrm{S} \end{bmatrix}$$

The same general reasoning can be extended to orthotropy, where four independent VFs are needed to calculate four stiffness parameters, or anisotropy with six VFs needed to determine the stiffness of a material.

Since the integrals are replaced with discrete sums as shown in Eq. (2.7), the method is straightforward and suitable for a computer implementation. By solving a simple system of equation, two stiffness coefficients are found which can be later used to calculate Young's modulus and Poisson's ratio.

Here, no particular form of virtual fields was assumed in order to present the most general approach to the linear VFM. The selection of robust VFs is significant, as it drives the error embedded in the identified coefficients. Many techniques have been developed to provide noise-optimising virtual fields for the linear VFM, they are discussed in Section 2.1.5.

The main advantage of the linear VFM over its main competitor - FEMU - is its computational performance with respect to the time needed to obtain the solution. As shown above, only a small system of linear equations has to be solved in order to obtain the stiffness coefficients, as opposed to building and updating a large FE model.

2.1.4 Non-linear virtual fields method

The procedure presented in Section 2.1.3 is valid only for constitutive models in which stress depends linearly on measured strains. This assumption allowed to replace the stress field from Eq. (2.6) with the measured strains and formulate a linear equation with respect to the unknown parameters. In many cases, constitutive models are much more complex and the relation between stress and strain is non-linear. In models such as plasticity, visco-elasticity, hyperelasticity *etc.* the stress

[1] This follows from the definition of the total force, and can be used in practice if $\mathbf{u}^*$ is constant across $\partial\mathrm{S}$

cannot be replaced explicitly with the measured total strains and so the procedure outlined for the linear VFM is not valid.

As the VFM simply expresses the equilibrium of forces it can be applied to any non-linear model. The main difference in comparison to the linear VFM is that parameters can no longer be obtained from a system of linear equations. An alternative approach has to be adopted, where the stress field is calculated from the measured strains with an unknown set of material parameters, using an assumed constitutive law. The unknown set of parameters can be assumed *a priori*, but in general it will not produce a stress field that satisfies the stress equilibrium. The main idea behind the non-linear VFM is to find a set of parameters such that the corresponding stress field satisfies the PVW in the best possible way.

Often, stress distribution changes with time and loading. This can be either because of time dependence of the material (such as with viscous or strain-rate sensitive materials), anisotropy induced by load and micro-structural rearrangement, or because some permanent deformation is accumulated during the loading history as in the case of plastic materials. As a result, kinematic data measured at different times, or load levels, must be included in the identification procedure. This can be achieved by investigating how much the PVW is violated at each time step. As a result, the identification procedure becomes an iterative process, in which the error in the PVW is minimised across all the time steps with respect to sought material parameters.

For any time step, a residual (error) in the PVW can be written as:

$$r(t) = \int_{\mathrm{S}} \boldsymbol{\sigma}(t) : \boldsymbol{\varepsilon}^* \mathrm{dS} - \int_{\partial \mathrm{S}} \mathbf{t}(t) \cdot \mathbf{u}^* \tag{2.11}$$

The residual depends on the sought parameters and the chosen virtual fields. If the virtual displacements obey all the necessary assumptions, any choice is valid and the residual will be mostly driven by the quality of material parameters guess. A cost function can be defined, based on the residuals calculated at all load levels:

$$\Phi(\boldsymbol{\xi}, \boldsymbol{\varepsilon}) = \sum_{i=1}^{\mathrm{nVF}} \left[\sum_{t=1}^{\mathrm{nTime}} \left(\sum_{j=1}^{\mathrm{nPoints}} \left(\boldsymbol{\varepsilon}^{*j(i)}(t) : \boldsymbol{\sigma}^j(\boldsymbol{\varepsilon}, \boldsymbol{\xi}, t) \mathrm{S}^j \right) - \int_{\partial \mathrm{S}} \mathbf{t}(t) \cdot \mathbf{u}^{*(i)}(t) \mathrm{d}\partial \mathrm{S} \right)^2 \right], \tag{2.12}$$

Where, $\boldsymbol{\xi}$, is a vector of unknown parameters, nVF, nTime, nPoints are the numbers of independent virtual fields, time steps (load levels) and data points respectively. $\boldsymbol{\varepsilon}^{*j(i)}$ is the i-th virtual field at the point j. The material parameters are identified as those that minimize the cost function.

The non-linear VFM requires, but is not limited to, only one virtual field. This field can vary from time step to time step in order to adapt to changes in the stress field. Moreover, multiple virtual fields can be applied to condition the optimisation problem and improve the stability of solution. The optimal choice of virtual fields for the non-linear problems is still an open problem. Possible choices found in the literature are presented in Section 2.1.5. The optimization is performed with numerical algorithms such as those based on Newton method for unconstrained optimization (no limitations on the search space). Constraints can be introduced into the optimization problem reducing the search space for example by restricting the parameters to be physically admissible, *e.g.* positive values for yield stress. In that case more sophisticated algorithms such as sequential quadratic programming

(SQP) can be used. The choice of the algorithm heavily depends on the problem and available software. A review of the most commonly used algorithms and their applications can be found in [19].

Clearly, from a computational perspective the non-linear VFM is much more demanding than the linear counterpart. However, when compared to the FEMU it still provides a significant computational improvement as no FEM computations need to be performed to identify the parameters.

2.1.5 Selection of virtual fields

In the VFM, the selection of appropriate virtual fields is crucial. Since VFs spatially filter stress data, they have a strong influence on the magnitude of both the random and systematic errors. This is particularly important when high noise is present. In that case, virtual fields should be chosen to minimise the corruption of parameters due to noise.

An additional challenge for virtual fields is posed when a parameter is only 'active'[2] within a small part of the specimen, or only during certain load steps. In that case, the information about it can only be captured if the fields focus on that particular regions in time and space. In fact, this is a significant challenge for most of non-linear models for which parameters activity have a strong spatial and temporal sensitivity. To identify models efficiently, the virtual fields should evolve with the data and follow the information in the test. Practically, virtual fields can be generated by a number of methods based on criteria such as minimisation of noise influence in the case of elasticity, or location of information for the non-linear models. In this section different types of virtual fields are reviewed, but firstly basic assumptions are presented.

There are number of assumptions that virtual displacement fields have to obey. The most important ones are that they are C^0 continuous and differentiable. Often, an additional assumption is made of kinematic admissibility (KA). It means that the virtual displacements satisfy certain virtual boundary conditions[3] over ∂S. By assuming null virtual displacements over ∂S it is possible to discard the traction term in Eq. (2.6), which is practical as the distribution of traction is generally unknown. This assumption allows to apply the VFM to parts of the body, without knowing the deformation over the entire domain. By removing the traction term it is possible to discard the effects of the far-field enabling to use of the VFM even when data is available only within an enclosed part of the body. Often, the assumption of kinematic admissibility is relaxed. When a total load over ∂S is known, (*e.g.* the loading force measured in a uni-axial tensile test) it is possible to include the traction term, provided that the virtual displacements are constant along that boundary. In that case, the traction term (often referred to as external virtual work) can be simplified:

$$W^*_{ext} = h \int_{\partial \mathrm{S}} \mathbf{t} \cdot \mathbf{u}^* \mathrm{d}\partial \mathrm{S} = h\mathbf{u}^* \cdot \int_{\partial \mathrm{S}} \mathbf{t} \mathrm{d}\partial \mathrm{S} = \mathbf{u}^* \cdot \mathbf{F}^{load} \tag{2.13}$$

The loading force can be measured during the experiment using a load cell. By in-

[2]Here, by 'active' it is meant that the parameter actively drives the response of the material under present loading conditions

[3]virtual boundary conditions refer to the conditions that virtual displacements satisfy over traction boundaries

cluding the traction term in the identification procedure, the mathematical problem of the VFM becomes much more stable with respect to noise, thus it is generally desirable.

The final remark regarding virtual fields concerns the number of independent virtual fields needed to characterize the material. The number of fields generally depends on the type of the problem. As discussed earlier, in case of the linear VFM, one independent virtual field is needed for each elastic parameter to produce the necessary number of independent linear equations. This is not the case for the non-linear VFM in which one virtual field is sufficient. However, more virtual fields can be considered to improve the cost function leading to a more accurate solution.

2.1.5.1 User-defined virtual fields

The simplest method for selecting VFs is choosing an analytical function that obeys virtual boundary conditions. The choice depends on the investigator and can heavily affect the quality of identification. Among the popular choices are functions such as [11]: shrinking/swelling in one of the directions:

$$\begin{cases} \mathrm{u}_1^* = kx_1 \\ \mathrm{u}_2^* = 0 \end{cases} \qquad \begin{cases} \varepsilon_{11}^* = k \\ \varepsilon_{22}^* = 0 \\ \varepsilon_{12}^* = 0 \end{cases}, \tag{2.14}$$

a barrel-shaped function:

$$\begin{cases} \mathrm{u}_1^* = 0 \\ \mathrm{u}_2^* = x_1(L - x_1)x_2 \end{cases} \qquad \begin{cases} \varepsilon_{11}^* = 0 \\ \varepsilon_{22}^* = x_1(L - x_1) \\ \varepsilon_{12}^* = (L - 2x_1)x_2 \end{cases}, \tag{2.15}$$

or sine-based functions, *e.g.*:

$$\begin{cases} \mathrm{u}_1^* = \frac{L}{2\pi} \sin \frac{2\pi x_1}{L} \\ \mathrm{u}_2^* = 0 \end{cases} \qquad \begin{cases} \varepsilon_{11}^* = \cos \frac{2\pi x_1}{L} \\ \varepsilon_{22}^* = 0 \\ \varepsilon_{12}^* = 0 \end{cases}, \tag{2.16}$$

where k is a constant, and L is usually a dimension of the region of interest (ROI) in the x_1 direction. The first virtual field is especially popular in the non-linear VFM, due to its simplicity and physical interpretation. Given the uniform virtual strain field, the integral of stresses is proportional to the internal reaction force, thus the VFM equation is simplified to the difference between the external loading and the internal reaction in terms of the forces.

The second virtual field includes an additional stress component, which is important for heterogeneous strain fields. Practically it is not always beneficial to include all of the stress components in the identification as some of them might carry mostly noise and thus have an adverse effect on the accuracy. It can be caused either by a very stiff response of the material due to a significant anisotropy of properties, or due to a loading that does not activate these components. In that case it is reasonable to deliberately ignore the noise-carrying components and focus only on the ones with information. Note that if the measured strain field is symmetric,

one should not use anti-symmetric virtual fields as they would lead to trivialisation of the PVW equation resulting in a large error due to numerical inaccuracy.

This method was the first type of virtual fields ever applied to the VFM and so was extensively used in early publications. User-defined virtual fields (UDVFs) require a significant input from the investigator, as a particular form of function must be chosen. Considerable experience is required to formulate UDVFs that tackle the experimental noise in an efficient way. As a result, new techniques have been developed allowing to generate high quality VFs. This was mostly done for the linear VFM and the UDVFs still remain the most commonly used VFs in the non-linear VFM.

2.1.5.2 Virtual fields expanded over whole body

Often it is desirable to have virtual fields that obey some assumptions, but are not explicitly expressed in terms of analytical functions. In that case they might be expanded over the ROI using interpolants such as polynomials, harmonic or piece-wise functions. One of the first reports on how virtual fields can be expanded over the whole body using polynomial interpolants was due to Grédiac *et al.* [20]. They assumed the following form of polynomials:

$$\begin{cases} \mathrm{u}_1^* = \sum_{i=0}^{m} \sum_{j=0}^{n} A_{ij} \left(\frac{x_1}{L}\right)^i \left(\frac{x_2}{B}\right)^j \\ \mathrm{u}_2^* = \sum_{i=0}^{p} \sum_{j=0}^{q} B_{ij} \left(\frac{x_1}{L}\right)^i \left(\frac{x_2}{B}\right)^j, \end{cases} \tag{2.17}$$

where m, n, p, q are the desired orders of polynomials, $A_{ij},\ B_{ij}$ are the unknown coefficients, $L,\ B$, are the dimensions of the body in $x_1,\ x_2$ directions respectively. The unknown coefficients were determined based on virtual boundary conditions. In the work, they proposed that the stability of identification could be improved if the virtual fields obeyed a speciality condition. They defined special virtual fields, such that the matrix $\mathbf{A}$ in Eq. (2.10) becomes the identity matrix $\mathbf{I}$:

$$\mathbf{A} = \mathbf{I}. \tag{2.18}$$

This condition ensures that the conditioning of the system of equations is the best and it reduces the effect of the noisy measurements of the loading. This assumption introduces additional constraints on the coefficients $A_{ij},\ B_{ij}$ reducing the number of possible combinations.

Often, the speciality condition and virtual boundary conditions are not sufficient to generate a unique set of virtual fields and some freedom in choosing unknown coefficients remain. Generally, extra conditions might be imposed on Eq. (2.17), such as ratios between the coefficients, which eventually leads to a unique set of virtual fields.

Although the concept is relatively simple this method has few downsides. First, it is effective only on regular geometries due to the way polynomials are defined. Moreover, application of boundary conditions poses a significant challenge. Initially the method was derived for a finite number of hinge supports [20], but later it was extended to linear supports as well [21]. Still complex geometries are very difficult, if not impossible, to tackle.

2.1.5.3 Piecewise virtual fields

A common approach to ensure the continuity of virtual displacements within a domain is to use linear piece-wise functions [22]. The main advantage of this approach is that the virtual fields are independent of the specimen geometry, allowing them to span over complex shapes. The approach is very similar to what is done in the finite element method (FEM) and is based on interpolation of nodal values of virtual displacements over the entire domain using shape functions.

Usually, a virtual mesh is built consisting of isoparametric linear quadrilateral elements defined with four nodes. Each node corresponds to two degrees of freedom *i.e.* two virtual displacements in two perpendicular directions $\{x,\ y\}$. Within an element, virtual displacements are interpolated as:

$$\mathbf{u}^*(\xi,\eta) = \sum_{i=1}^{4} \mathbf{N}^{(i)}(\xi,\eta)\mathbf{u}^{(i)*}, \tag{2.19}$$

where, ξ, η are the local coordinates of each element, $\mathbf{N}^{(i)}$ are the shape functions corresponding to the node i at the point (ξ,η), $\mathbf{u}^{(i)*}$ are the nodal values of displacements at the node i. Virtual strains are calculated by interpolation of virtual displacements using derivatives of shape functions with respect to the global coordinate system:

$$\boldsymbol{\varepsilon}^*(x,y) = \sum_{i=1}^{4} \mathbf{B}^{(i)}(x,y)\mathbf{u}^{(i)*} = \sum_{i=1}^{4} \mathbf{J}^{-1}\mathbf{B}^{(i)}(\xi,\eta)\mathbf{u}^{(i)*}, \tag{2.20}$$

where $x,\ y$ are the global coordinates, $J_{ij} = \frac{\partial x_i}{\partial \xi_j}$ is the Jacobian matrix of the local-to-global coordinate transformation, and $\mathbf{B}^{(i)}$ is the strain-displacement matrix corresponding to the node i. For details reader can refer to any book on the FEM and isoparametric elements, *e.g.* [23]. This approach is not only computationally very efficient, but also allows to handle boundary conditions easily just by enforcing them directly at the constrained nodes.

The important property of the piece-wise linear functions is that the virtual mesh does not need to be compatible with the geometry of the specimen, it is sufficient that it encloses the region of interest (ROI). However, the boundaries of the virtual mesh must be aligned with the traction edges of the specimen in order to ensure the kinematic admissibility of the produced VFs.

Although the procedure is very similar to the FEM, there is a major difference in the density of the mesh. Whereas in FEM usually a fine mesh is desired, that is not the case for the VFM. The ROI is usually meshed with grids ranging from 5×5–12×12 virtual elements in order to introduce some spatial smoothing. The method is valid for the small deformation framework when the virtual mesh does not need to follow the deformed ROI, but can also be adjusted to the large deformation framework with some effort, as shown in Chapter 4.

2.1.5.4 Optimised virtual fields

Both polynomial and piecewise VFs are just techniques to ensure the continuity and kinematic admissibility of virtual displacements over the whole ROI; they do not uniquely define VFs for a given set of data. Virtually, applying correct virtual

boundary conditions and the speciality condition does not produce a unique set of virtual fields and some additional input based solely on the investigator's experience is required.

The work of Avril *et al.* [24] was an attempt to add additional constraints and optimise special virtual fields so that the variance of the identified stiffnesses is minimised with respect to the noise. By assuming Gaussian distribution of the noise, uncorrelated between strain components, they were able to derive an explicit expression for the variance of elastic parameters. They showed that there exists a unique virtual field that minimizes the variance of the stiffness and presented a method for finding it.

The method depends on the stiffness of the material and the measured strains so no closed form of these fields is available. In fact, they are obtained in an iterative manner during the identification procedure.

The special optimised virtual fields highlight areas of high strain, which contain more signal-to-noise ratio effectively increasing their contribution to the identified parameters. As a result, the identified stiffness coefficients are less affected by the noise yielding higher accuracy. An additional benefit of the special optimised VFs is that their formulation is explicitly defined, thus no user input is required.

Finally, it must be noted that the special optimised virtual fields are applicable to data corrupted with relatively low noise as they were developed with this assumption. Although, some of the assumptions do not hold in practice, the optimised VFs provide a very good choice for most applications in linear elasticity, are now routinely used by the VFM community and were implemented on the commercial DIC/VFM platform MatchID [25].

2.1.5.5 Eigenfunction virtual fields method

Another method for constructing virtual fields was presented by Nigamaa and Subramanian [26] and it differs significantly from the previously discussed methods. The virtual fields presented in that work are based on the measured strains and directly related to the eigenfunctions of strain components, producing a method that based on physical quantities.

The method was developed with the assumption of the data grid being formed in a regular, rectangular format which limits the applications to regular geometries. The strain field is analysed over ROI with the principal component analysis and singular value decomposition is used to compute the eigenfunctions. These eigenfunctions, are later used to develop virtual fields and the corresponding virtual displacements.

In contrast to other types of virtual fields, here virtual strains are computed in the first place and then they are integrated in order to obtain the corresponding virtual displacements. Initially, that was a very limiting assumption, as the produced virtual fields could only represent uniform stretching and simple shear in order to produce constant virtual displacements over the surfaces where traction was applied. In fact, the authors showed that this assumption introduces very high variance in two out of four stiffness components they measured [26].

The method was improved further by Subramanian and Nigamaa [27] by relieving the assumption of a constant virtual displacement over traction boundaries. By assuming linear elasticity they expressed the integral of traction over the boundary in terms of unknown elastic coefficients and measured strains. As a result a set

of uniform linear equations could be generated from which the stiffness coefficients could be calculated. The authors showed that only in one of these equations the virtual displacements must be constant along the edges, and as a result they significantly improved the identification, obtaining the variation of the parameters on the level competitive with the special optimised virtual fields.

The method yields good accuracy and low sensitivity to noise, but the assumptions it is based on are very strict. A regular grid of data points is required so it is inadequate to specimens of complex geometry such as double-notched tensile specimens. Until this assumption is relieved it might be difficult to apply the method to non-linear models, which are often calibrated with specimens of complex geometries introducing strain heterogeneity.

2.1.5.6 Stiffness-based virtual fields

As discussed before, there are many different types of virtual fields applicable to the linear VFM which offer different levels of accuracy and stability with respect to the noise level. The methods were specifically developed with the assumption of linear elasticity. A little effort has been done to develop optimal virtual fields for non-linear problems and as a result the most common type of virtual fields in that case are still UDVFs.

The first attempt to improve virtual fields for non-linear applications is due to Pierron *et al.* [28]. Similarly to the case of special optimised virtual fields, they considered the effect of white noise on the error introduced to the PVW, this time expressed in the incremental form. A new type of VFs was developed, suitable for plasticity, which was expanded over a base of piecewise linear functions. The fields were formulated such that they were dependent on the stiffness of the virtual mesh, explicitly related to the instantaneous stiffness of the non-linear material.

In order to reduce the bias associated with low strain data points (low signal-to-noise ratio) they scaled the stiffness matrix with the von Mises stress (Eq. (2.23)), effectively putting more weight to the areas where plastic deformation localizes. Virtual displacements were obtained by solving a Lagrangian problem minimising the variance of the PVW under constraints associated with virtual boundary conditions:

$$\begin{bmatrix} \mathbf{H} & \mathbf{\Gamma}^T \\ \mathbf{\Gamma} & \mathbf{0} \end{bmatrix} \begin{bmatrix} \mathbf{u}^* \\ \boldsymbol{\lambda} \end{bmatrix} = \begin{bmatrix} \mathbf{0} \\ \mathbf{u}_{BC} \end{bmatrix} \tag{2.21}$$

where $\mathbf{H}$ is the matrix derived from the tangent stiffness matrix, $\boldsymbol{\lambda}$ is the vector containing Lagrangian multipliers, $\mathbf{u}_{BC}$ is the vector containing values of the prescribed displacements and $\mathbf{\Gamma}$ is the matrix containing the prescribed virtual boundary conditions. In particular, when a tensile test is considered, one way to set boundary conditions is to assume null displacements for all nodes at the bottom edge of ROI and a constant value *e.g.* 1 across the loading edge to simplify the external virtual work.

The matrix $\mathbf{H}$ is obtained with:

$$\mathbf{H} = \mathbf{K}^* \mathbf{K}^* \tag{2.22}$$

where $\mathbf{K}^*$ is the modified global stiffness matrix, as defined in Eq. (2.23). The matrix depends on n, the number of virtual elements, h, the thickness of specimen,

σ^{eq}, the von Mises stress, $\mathbf{B}$, the strain-displacement matrix, and $\mathbf{D}^{ep}$, the tangential elastoplastic stiffness matrix.

$$\mathbf{K}^* = \sum_{\text{elem}=1}^{n} \int_S h\,\sigma^{eq}\,\left(\mathbf{B}^T\mathbf{D}^{ep}\mathbf{B}\right)\,\mathrm{dS} \tag{2.23}$$

Once the virtual displacements are identified, the corresponding virtual fields can be calculated using Eq. (2.20). The method was implemented with constant strain triangular elements and was shown to be an improvement over UDVFs.

There are however few limitations to the method. It was developed with the aim of reducing the influence of white noise on the PVW. While this is important for elastic materials, for which signal-to-noise ratio is relatively small, it is not as relevant for the ductile materials for which much higher strains are generally measured. A more important issue is the variation of information during the test, and these VFs do not address that. Additionally, the method requires a significant amount of computations in order to identify the virtual fields. The virtual mesh needs to be constructed, the tangential material stiffness matrix must be computed, for which not always an explicit form is available. Finally, the global stiffness matrix must be assembled.

The method was specifically designed to be used together with the interpolation of raw data onto a triangular mesh. This approach is quite limiting and so implementing the method with a standard data format poses a challenge, as in that case the virtual mesh would no longer be consistent with the data grid.

Overall, the method provides a significant improvement over the UDVFs. The major advantage is that it targets areas where the signal-to-noise ratio is the highest and adapts with time, allowing for a more optimal extraction of parameters from an experiment.

2.1.5.7 Strain virtual fields

Full-field measurements help to discard limiting assumptions in material testing *e.g.* of stress uniformity, enabling investigation of complex phenomena such as post-necking behaviour of a tensile specimen. This was done by Coppieters *et al.* [29] who used a DIC set-up to investigate post-necking hardening of a steel sheet. In their work they used the VFM with the measured strain acting as virtual fields. As a result, their criterion for minimisation of the cost function was based on the difference between the real internal and external work.

They made a strong assumption about the distribution of displacements over the boundaries of their ROI and to obey it, a large ROI had been used, reducing the spatial resolution of the measurement. Additionally, they assumed plane stress condition (strain and stress field constant across the thickness) to allow the analysis. They reported that fitting a hardening models to data including post-necking behaviour leads to a more accurate calibration overall.

The spatial resolution of the test could be improved by interpolating the measured strains onto a virtual mesh. Then, the assumption of constant virtual displacements along the boundaries could be enforced directly at virtual nodes, regardless of the measured displacements and the virtual strains could be matched to the real strains in a least-square sense.

2.1.6 Applications of the non-linear VFM

The virtual fields method is a versatile tool applicable to many different materials and experimental set-ups. It has been applied to various materials including metals, biological tissues, elastomers, foams, concrete and composites. The method has been found to be successful under both static and dynamic loadings, as well as with homogeneous and heterogeneous materials.

2.1.6.1 Metal plasticity

Metal plasticity has attracted much attention from the VFM community and the non-linear VFM has been applied to study a wide range of ductile materials. Many models have been investigated, with complexity ranging from isotropic plasticity with linear hardening to: anisotropic plasticity, viscoplasticity, kinematic hardening and heterogeneous materials such as welds.

A survey of publications is conveniently summarized in Table 2.1. Clearly, most of the experimental set-ups are based on a modified tensile test. Usually, the standard geometry is modified by means of notches or holes to induce a heterogeneous strain field. Models can then be identified using a broad range of stress states (important for anisotropy) or strain rates (important for viscoplastic models).

The most addressed problem has been isotropic plasticity, with various isotropic hardening models such as linear, Voce, Swift or power laws. Some attempts have been also made on viscoplasticity by combining multiple tests in a single cost function with Johnson-Cook being the most popular model considered. Some effort has been done on kinematic hardening, as well as anisotropic yield criteria (Hill48, Yld2000-2D). Overall, a wide range of material models for metals has already been tested using the VFM.

2.1.6.2 Elastomers

The VFM has been also applied to a range of hyperelastic materials.

The first approach was from Promma *et al.* [30], where they extended the VFM to the large deformation theory. They investigated a rubber and considered Mooney model, in which stresses can be written as a linear function of deformation, thus the linear VFM was used.

Palmieri *et al.* [9] investigated rubbers using different planar geometries. They used both linear (Mooney-Rivlin) and non-linear (Ogden) models. They reported that the VFM gave a better estimation of the parameters compared to FEMU, while not relying on strong assumptions about the boundary conditions which is a considerable advantage over FEMU.

Sasso *et al.* [31] investigated fluoro-silicon rubbers by means of a bi-axial test on a cruciform specimen. They were able to obtain reliable parameters for a third order Ogden model, as well as to characterise visco-elastic properties using Prony series.

Rubbers were studied under medium strain rates by Yoon *et al.* [32] using a drop-weight test and under high strain rates by Yoon *et al.* [33]. In both cases, visco-hyperelastic behaviour was described using one-term Ogden model as well as Prony series. In these set-ups, the dynamic formulation of the VFM was used, to

discard the contribution of external forces (which are difficult to measure). Instead, acceleration fields causing inertial forces were used as a load cell.

2.1.6.3 Biological tissues

Avril *et al.* [10] were the first to apply the VFM to a tissue (human arteries) to which they fitted an anisotropic hyperelastic model.

Kim *et al.* [34] studied human aneurismal aortic tissues by means of an inflation test and identified parameters of Holzapfel model describing anisotropic hyperelasticity.

Recently, Zhang *et al.* [35] reported a study on the mechanical properties of human optic nerve head tissues using the VFM. In their study they found that the VFM was well-suited for their problem, in particular in terms of computational speed (125 times faster than FEMU). Additionally they reported that the VFM dealt with the unknown boundary conditions in a convenient way, by including only a known load over a portion of geometry and setting virtual displacements to zero elsewhere.

2.1.6.4 Prospects

The VFM has been applied to a large number of different materials, constitutive models and experimental set-ups, which proves how useful the method is. Novel tests are being developed, which potentially will be able of reducing the experimental effort of characterising a material.

What is remarkable is that over ten years of applying the VFM to non-linear models, there was only one attempt at developing virtual fields suited for non-linear models [28]. Although the stiffness-based optimised virtual fields showed an improvement in quality of identified parameters, still the majority of identification is done using UDVFs. In fact, many authors acknowledged that the identification of parameters is hindered by a lack of a systematic procedure for generating robust virtual fields. Often, this was identified as a major challenge to be addressed before tackling more complex constitutive models is possible.

Therefore, developing a complete method for generating well-performing virtual fields for non-linear models will definitely have a significant impact on the community. Those virtual fields should be suitable for any constitutive model, and ideally generated with a minimal input from the investigator.

Table. 2.1. Literature survey of the application of the non-linear VFM to elastoplastic materials. The table continues on next page.

Reference	Material	Test	Material model	Main outcomes	Virtual fields
Grédiac and Pierron (2006) [36]	Numerical	Tensile (notched)	IH[4] (linear)	Extended the VFM to non-linear models	UD[5]
Pannier *et al.* (2006) [37]	Mild steel	Tensile (waisted)	IH (Voce)	Experimental confirmation of [36]	UD
Avril *et al.* (2008) [38]	Mild steel	Tensile (deep notches)	IH (linear)	Experimental confirmation of [36]	UD
Avril *et al.* (2008) [39]	Mild steel	Tensile (deep notches)	Viscoplasticity (Perzyna)	Applied the VFM to strain-rate dependent material	UD
Pierron *et al.* (2010) [28]	Austenitic stainless steel	Tensile (deep notches)	NLKH[6]	Presented stiffness-based VFs, cyclic loading	UD, Stiffness-based
Coppieters *et al.* (2010) [29]	Steel (DC05)	Tensile (dog-bone)	IH (Swift, Voce)	Better description of hardening compared to standard methods	Strain fields
Kim *et al.* (2013) [40]	Steel (DP780, TRIP780, EDDQ)	Tensile (coupon)	IH (Voce, Swift)	Better description of hardening compared to standard methods; Voce law does not represent post-necking hardening correctly	UD
Rossi and Pierron (2011) [41]	Numerical	Tensile (deep notched)	Anisotropic (Hill48)	Presented complete methodology for applying the VFM to 3D large deformation data.	UD
Kim *et al.* [42]	Advanced high strength steel	Tensile (Σ-shaped)	Anisotropic (Hill48)	Applied the VFM to experimental data of an anisotropic material	UD
Rossi *et al.* [43]	stainless steel	Tensile (deep notches)	Anisotropic (Hill48, Yld2000-2D)	Applied the VFM to large deformation anisotropic plasticity	UD

[4]Isotropic hardening (IH)
[5]User-defined VFs (UD)
[6]Non-linear kinematic hardening (NLKH)

Table. 2.1. Literature survey of the application of the non-linear VFM to elastoplastic materials. The table continues on next page.

Reference	Material	Test	Material model	Main outcomes	Virtual fields
Notta-Cuvier *et al.* (2013) [44]	Titanium alloy (Ti6Al4V)	Tensile (deep notches) × 2	Viscoplasticity (Johnson-Cook)	All Johnson-Cook parameters from only 2 tests	UD
Grama *et al.* (2015) [45]	Numerical	Shear test	Viscoplasticity (Anand)	Studied plausibility of their test to identification of the Anand model	UD
Notta-Cuvier *et al.* (2015) [46]	Simulated	Tensile (deep notches, perforated)	Coupled elastoplastic-damage	The VFM was able to characterise the model on simulated data	UD
Valeri *et al.* (2017) [47]	Stainless steel	Tensile test (dog-bone)	Viscoplasticity (Johnson-Cook)	Fitted parameters of the model over a range of temperatures up to 900°C	UD
Le Louëdec *et al.* (2013) [48]	Friction stir weld	Tensile (coupon)	IH (linear)	Characterised heterogeneous material under static loading	UD
Le Louëdec *et al.* (2015) [49]	Friction stir weld	SHPB[7] (Compressive)	Viscoplasticity	Applied the VFM to the dynamic loading; characterised heterogeneous material	UD
Jones *et al.* (2018) [4]	304L stainless steel	Tensile (D-shaped)	Viscoplasticity (BCJ)	Identified BCJ model using numerical data. Discussed uniqueness issues of the model.	
Saranath and Ramji (2015) [50]	Titanium alloy electron beam welded	Tensile (dog-bone)	IH (power-law)	Extracted local properties of a weld on Ti6Al4V and compared to the standard method	UD
Fu *et al.* (2016) [51]	High strength steel	Shear	NLKH	Obtained parameters for multi-component NLKH model using 2 cycles of forward-reverse simple shear.	UD

[7] Split Hopkinson Pressure Bar (SHPB)

2.1.7 Alternative inverse methods

The virtual fields method is one of many available techniques developed to identify material parameters from full-field measurements. Naturally, other methods have been developed that might be applied to the same problem. In this section, other inverse techniques are reviewed and compared in order to present the whole spectrum of possibilities for material identification. A more complete comparison in terms of the performance and accuracy can be found in [5, 52].

2.1.7.1 Finite element model updating

The finite element model updating (FEMU) is the most popular approach for identification of material parameters using full-field measurements. The idea behind it is very natural and thus easy to understand. An experiment is simulated using a finite element (FE) model of the test. The model is then matched to the experimental measurements as close as possible. It is essential that the geometry and boundary conditions are reproduced as accurately as possible. Then, the response of the model depends only on the material parameters fed to it, and thus they are adjusted iteratively in order to obtain the best possible match, by minimising an error (cost) function.

There are multiple ways to formulate the cost function for FEMU. The simplest method is based on comparing the forces measured in the experiment to those generated by the FE model (FEMU-F). The forces are computed using the displacements measured in the experiment. In practice it is virtually impossible to measure forces corresponding to FE nodes, but only a collective force corresponding for example to an entire loading edge. The force variant of FEMU can be constructed under such constraint and solved iteratively to provide a set of material parameters [53]. However, the force is a very global and integrative quantity and retrieving several parameters from this single quantity quickly leads to severe uniqueness issues. To alleviate this, adding full-field data to the cost function is an attractive option.

An alternative is to build up a cost function based on the computed and measured displacements (FEMU-U) see *e.g.* [54]. In this case, the displacements computed by the FE model are interpolated to the geometrical positions of the data points. The model can be loaded with a set of prescribed displacements, which can be either theoretical or measured, at the loaded boundaries. A force loading can also be incorporated, usually by means of the total force measured with a load cell, as the exact distribution of the loading over the boundaries is not known.

More options for setting up the cost function exist, *e.g.* the two methods can be combined so that the cost function includes both the forces and displacements (FEMU-UF) [55] . The cost function can also depend on such quantities as measured strains [56–58], and the measured bi-axial yield stress [59].

FEMU is a universal tool that can be utilised in many diverse set-ups. The main advantage of the method is that it does not require full-field data over the entire domain. If fact, any overdetermined data can be used which is suitable when complex 3D geometries are used or plane stress condition cannot be guaranteed, as in the case of necking of ductile materials. Moreover, it is based on the finite element method (FEM) which is familiar to the most of the engineering community facilitating its spread, use and understanding.

Although universal and easily approachable, the method also has its own short-

Table. 2.2. Comparison of major characteristics of FEMU and the VFM

Characteristic	**FEMU**	**VFM**
Geometry of a specimen	Any	2D (Unless full 3D displacement fields are measured)
Measurements	Any overdetermined data	Required full-field over domain (ROI)
Cost function	Displacement, Force, Strain, Stress (Numerical vs Experimental)	Stress (Global equilibrium)
Material models	Any	Any
Noise control	Through adding weights to points in the cost function	Through virtual fields (crucial to the method)
Computational performance	Requires running FE model multiple times (slow)	Very high performance with linear model. For non-linear models does not require solving forward problem. (fast)
Boundary conditions	Modelled	Can be accounted for exactly
Pre-requisites	FEM Package + Optimization routine (e.g. Matlab)	Simple script (e.g. Matlab)
Integration with DIC software	Not commercially available	Commercially available (MatchID[8])

comings. One of the major challenges with FEMU is reproducing the correct boundary conditions imposed on the model. Although kinematic constraints can be set based on optical measurements, setting up force loadings can be challenging.

Since the process of minimising the cost function involves solving the direct problem multiple times, this method suffers from very poor computational performance. This can be an important down-side if for some reason the results are expected in real time, *e.g.* for biomedical scanning purposes, when costly computations are needed to evaluate FE model, *e.g.* non-linear explicit dynamics, or when many identifications are required *e.g.* when uncertainty propagation is to be studied. In that case, the VFM performs much better, with authors reporting VFM being as much as 468 times faster than FEMU for metal plasticity [52], or 125 times faster in the case of anisotropic hyperelasticity [35].

A comparison between FEMU and the VFM is conveniently summed up in Table 2.2. Clearly, both methods have their own strong sides and limitations and both can find niches in which they perform very well. Overall, the VFM is an interesting alternative to the FEMU when full-field measurements are available over the entire ROI.

2.1.7.2 The equilibrium gap method

The equilibrium gap method [60, 61] has been developed for characterisation of damage distribution in a material. Assuming that the damage is isotropic, the stiffness of the material can be expressed as a function of damage scalar D. If a finite element mesh is established over the data grid, the gap in equilibrium can be investigated by summing the internal forces over each element. It is worth noting, that the internal forces corresponding to the element depend on the stiffness of

[8] http://www.matchid.eu/

the element, hence are affected by the damage parameter assigned to the element (damage is assumed to be uniform across the element). This principle serves as a basis for the identification. For all data points, the gap in equilibrium is minimized with respect to the damage parameters. Since the system is usually overdetermined, this is solved in a least square sense.

This method does not require any updating of the finite element model, however the FE mesh has to be built-up before the identification. The method is equivalent to the VFM with a particular type of piecewise functions [5] hence requires full-field data.

2.1.7.3 The constitutive equation gap method

The constitutive equation gap method was initially developed as a tool for error quantification in FEM results [62]. The method is based on an energy functional, measuring the difference between a statically admissible stress field, $\boldsymbol{\tau}$, and the stress field corresponding to the kinematically admissible values measured in an experiment ($\boldsymbol{\varepsilon}(\mathbf{u})$). This constitutive gap can be expressed as:

$$\Psi_{CEGM} = \frac{1}{2}\int_{\Omega} \left(\boldsymbol{\tau} - \mathbf{D}^{mat} : \boldsymbol{\varepsilon}(\mathbf{u})\right)^{T} : \mathbf{D}^{mat} : \left(\boldsymbol{\tau} - \mathbf{D}^{mat} : \boldsymbol{\varepsilon}(\mathbf{u})\right) \mathrm{d}\Omega \tag{2.24}$$

where Ω is the region of interest and $\mathbf{D}^{mat}$ is a tensorial operator mapping strains to stresses, which depends on material properties.

The idea is to find a statically admissible stress field that obeys the global equilibrium, as well as a suitable set of material parameters that produce a stress field that minimizes the gap. The method may involve FEM computations, however, what makes it distinct from FEMU is that the statically admissible stress can also be generated for example through Airy functions [63], relieving the need for FE computations.

This method has been found to be particularly suitable in characterising properties of heterogeneous materials. It has been applied mostly to linearly elastic materials [64–66], however it has been also extended to elastoplasticity [63, 67–69] and hyperelasticity [70].

2.1.7.4 The reciprocity gap method

The reciprocity gap method was developed for problems where measurements are known only at the boundary of the body, but not inside. Originally developed to identify anisotropic conductivity properties [71], it was extended to elasticity. The method is based on Maxwell-Betti reciprocal theorem and involves analysing adjoint (virtual) displacement fields. A comprehensive review of reciprocity gap equations can be found in [72]. In particular the method is suitable for crack detection in an elastic medium [73, 74], which can be useful in geological application *e.g.* using measurements taken during earthquakes to understand the structure of Earth [74]. However, this is not a very convenient technique to obtain material parameters and no experimental application can currently be found in the literature.

2.1.7.5 Integrated digital image correlation

An interesting alternative to FEMU-U is the so-called integrated digital image correlation (I-DIC) approach. In this method, the DIC and identification processes

are integrated into a single step, which leads to a very robust processing of the noise [75, 76]. The idea is to use the global approach of DIC, in which the displacement field is defined using a set of nodes and interpolation functions over the entire domain, as opposed to the subset-based DIC. The displacements can be derived from an equivalent FE model of the test but the method is not limited to this approach [77]. The displacements in the DIC are expressed on the same basis as in the FE model so any projection between a FE mesh and the experimental data grid are omitted.

It follows that the correlation problem is coupled to the material parameters used in the FE model, and the minimisation of the correlation function is performed with respect to the sought parameters, rather than the displacement of each individual subset. To solve the correlation problem, sensitivities of displacement fields with respect to the sought mechanical parameters are computed using FEM [76]. This treatment leads to much better handling of the random noise as a result provides much more stable parameter values with respect to subset size and boundary conditions imposed onto the FE model.

2.1.7.6 Conclusions

As outlined in this section, there are many techniques suitable for identification of material parameters from full-field measurements. Techniques such as the equilibrium gap method, or the reciprocity gap method rely on strong assumptions and therefore are suitable only to specific cases. The two most versatile methods are FEMU and the VFM. Their comparison has been summed up in Table 2.2. While both can be applied to a variety of set-ups the VFM has a strong advantage of computational efficiency, with authors reporting the VFM identification being as much as 468 times faster than FEMU [52]. Importantly, both the VFM and FEMU are based on techniques familiar to the engineering community, namely the PVW and FEM and so can be propagated to the end-users easily.

2.2 Digital Image Correlation

2.2.1 Overview

Digital image correlation [2] is a powerful technique for obtaining shapes of objects and full-field deformation fields from experiments. It stems from computer vision techniques, however has been adapted to ensure maximum accuracy given how small measured displacements usually are. The standard method (2D) and stereo (3D) DIC rely on obtaining images of a random speckle pattern covering the surface of specimen during an experiment and correlating it to the reference image. Over the years it became the most popular technique for obtaining full-field measurements. One of the reasons for it is that the random pattern is easy to obtain in practice, in contrast to other methods such as grid method relying on a regular pattern. This section briefly reviews both theoretical and practical sides of DIC. A comprehensive practical guide for DIC can be found in [78].

2.2.2 Principles

DIC is an image matching technique relying on tracking a random pattern of speckles between a reference and deformed images. Typically, the same grey level occurs in an image multiple times, thus it is impossible to correlate a single pixel to another - this problem is known as the correspondence problem. In order to resolve it, DIC relies on analysing a neighbourhood around a pixel, called a subset, and correlating it between the images.

2.2.2.1 Matching

Matching in DIC is obtained by using the concept of optical flow, meaning that the intensity of a given pixel with initial position of (x, y, t) is unchanged as it moves during time increment Δt to $(x + \Delta x, y + \Delta y, t + \Delta t)$. By assuming that the motion across chosen subset is constant, it is possible to formulate a matching criterion, between the reference image F and the deformed image G and minimise it to solve for $\mathbf{d}_{opt} = \{\Delta x, \Delta y\}$. Mathematically, the displacement can be obtained by minimising a sum of squared differences (SSD) between the reference and the deformed images:

$$\mathbf{d}_{opt} = arg\, min \chi_{SSD} \tag{2.25}$$

with the cost function:

$$\chi^2_{SSD} = \sum |G(\boldsymbol{x} + \boldsymbol{d}) - F(\boldsymbol{x})|^2 \tag{2.26}$$

By solving this equation, the average displacement of the subset can be obtained. This procedure is repeated for every subset in the image and the full-field displacement field is reconstructed.

Often, the assumption of optical flow is not obeyed, *e.g.* due to change in lighting. In that case the shape of pattern remains the same, however the intensities of pixels are changed and the SSD criterion fails to identify the correct motion. There are more robust matching criteria to account for an offset (change by a constant value) as well as a scale of lighting (linear transformation of intensities). The former can be addressed by introducing the zero-mean sum of squared differences criterion (ZSSD):

$$\chi^2_{ZSSD} = \sum \left((G_i - \bar{G}) - (F_i - \bar{F}) \right)^2, \tag{2.27}$$

with $\bar{G}, \bar{F}$ being mean grey level across the image. The latter can be accounted for by means of the normalised sum of squared differences criterion (NSSD):

$$\chi^2_{ZSSD} = \sum \left(\frac{\sum F_i G_i}{\sum G_i^2} G_i - F_i \right)^2 \tag{2.28}$$

Finally, when both of the lighting issues are expected, a compound cost function can be constructed, called the zero-mean normalised sum of squared differences criterion (ZNSSD):

$$\chi^2_{ZNSSD} = \sum \left(\left(\frac{\sum \bar{F}_i \bar{G}_i}{\sum \bar{G}_i{}^2} G_i - \bar{G} \frac{\sum \bar{F}_i \bar{G}_i}{\sum \bar{G}_i^2} \right) - (F_i - \bar{F}) \right)^2 \tag{2.29}$$

where:

$$\begin{aligned} \bar{F}_i &= F_i - \bar{F} \\ \bar{G}_i &= G_i - \bar{G} \end{aligned} \tag{2.30}$$

The ZNSSD criterion is the most robust of them all, and does not introduce any significant computational effort [2]. It should be used whenever possible, especially when stereo-DIC is used, as in that case changes in lighting between the two cameras are unavoidable.

2.2.2.2 Shape functions

The analysis presented above relies on a simple assumption that the initially square subset is correlated to a square subset in the deformed image. Often, the material undergoes significant deformation including elongation, compression, rotation, shearing and bending, which significantly distorts the subset. To improve correlation a concept of shape functions was introduced. Shape functions map the the coordinate system of the deformed subset to the reference frame and thus account for the distortion of the subset's shape. Typical types of shape functions include: rigid (translations only), affine (first order deformation), irregular (including cross product of $\Delta x, \Delta y$) and quadratic. The latter lead to the best spatial resolution (at a cost of increased noise) and should be chosen whenever possible.

2.2.2.3 Interpolation functions

In order to evaluate the matching cost function it is often necessary to evaluate grey level values at non-integer positions. This can be achieved by interpolating counts corresponding to the pixel positions with a chosen base of functions. The interpolation leads to a sub-pixel accuracy but inherently introduces a bias to the measurement and so, it is important to chose it appropriately. In commercial software many options are available including: polynomials (bilinear, bicubic), fast Fourier transform-based interpolation (FFT), splines (bicubic) and optimised interpolants (*e.g.* optimised 4-tap filter). The choice of the interpolation functions is often left to the user, however it is worth noting that polynomial interpolators perform poorly (bias of 1/15 pixel when cubic polynomial is used over 3 pixels), thus other functions such as bicubic splines or optimised filters are recommended [2].

2.2.2.4 Stereo calibration

The standard stereo-DIC set-up consists of two cameras imaging the same face of the specimen. Each of the cameras has its own coordinate system in which the images are represented. To correlate the images, a mapping of one camera to another has to be known. In practice this is achieved with a calibration procedure involving imaging a known target plate that has printed fiducial markers on its surface. The target is moved and rotated over the entire field of view to collect as much information about the set-up (including distortions caused by lenses). The location of the markers is identified by both cameras and this information is used to build up a transformation between the coordinate systems. Once it is known, the stereo-vision is capable of measuring movement out-of-plane improving the quality of measurements.

2.2.3 Sources of errors

As a technique for obtaining measurements of kinematic fields, DIC is affected by many sources of errors, both extrinsic (cameras, lighting, movement of specimen in-plane, out-of-plane) as well as intrinsic (matching criterion, subset size, interpolation bias). It is beyond the scope of this review to discuss all factors in-depth, however attention to some of them is necessary.

2.2.3.1 Camera sensor noise

Every camera has an electrical noise associated with its electric sensor, leading to a dynamic change of grey level values even if the image is kept static. The level of noise is not constant the across intensities, but increases as the counts become brighter. Typically, the grey level noise is in the range of 0.5%–1.0% of the dynamic range of camera, and can be obtained by taking multiple static images and evaluating standard deviation of grey level values of each pixel. This serves as a good indicator of the quality of experimental set-up and should always be checked before loading the specimen.

2.2.3.2 Out-of-plane movement

Specimen moving perpendicular towards the camera sensor will become uniformly enlarged introducing artificial biaxial strain to the measurement. The movement of 100 µm with the imaging distance of 500 mm would create an artefact of 200 microstrains, which is comparable to the strains experienced by materials such as metals in the elastic range. This is one of the major error sources for the 2D DIC, and is unavoidable when standard testing machines are used. There are two methods to reduce this effect: using telecentric lenses or stereo-DIC, with the latter used in the majority of cases.

2.2.3.3 Displacement resolution

Displacement resolution is defined as a displacement level that can be attributed to sources of error, most notably camera sensor noise and interpolation bias. It can be identified by correlating two stationary images and investigating standard deviation of the displacement field. A more accurate estimation can be achieved by in-plane translation of the specimen by a known value and investigating the mean and standard deviation of the measured displacements. Typically, a good DIC set-up should yield an accuracy of about 0.02 pixel size. As the subset size increases, the observed displacement noise decreases, however at a cost of spatial resolution. It is therefore a good practice to keep subset size as small as possible (for sake of spatial resolution) as the displacement field can be smoothed out at later stages of analysis.

2.2.3.4 Strain resolution

Similarly, strain resolution can be defined as a strain level that cannot be distinguished from noise. It can be found by investigating standard deviation of strain field corresponding to a static frame. Typically, strain resolution is of order of a couple hundreds of microstrains. The strains can be obtained using either central

finite difference method, or by matching a polynomial to a neighbourhood of the point and computing its spatial derivatives. The larger the chosen neighbourhood is, the lower the strain noise will be. Similarly to the case of displacements, with stronger smoothing spatial resolution is compromised. This is especially important when high strain gradients are expected (*e.g.* in the vicinity of notches) as it may lead to a significant underestimation of strain peaks.

2.3 Novelty statement

2.3.1 Aims and objective

The aim of this project is to develop a new type of virtual fields applicable to the non-linear VFM. The method should be universal and suitable for a vast range of material models, test piece geometries and loading conditions. Ideally, user input should minimal and its impact not affect the identification accuracy. In order to achieve that the following objectives have been outlined.

1. Develop a methodology to generate virtual fields that highlight information in the test based on the sensitivities of stress field to constitutive parameters.

2. Validate the method using a numerical experiment in which the data can be controlled completely. Compare the performance of the method against other known types of virtual fields.

3. Investigate the effect of the user input on the accuracy of identification.

4. Apply the method to identify a large deformation anisotropic plasticity model. Due to the complexity of the problem the robustness of the proposed method can be fully tested and compared against UDVFs.

5. Validate the method experimentally to demonstrate its performance, not only with numerical data, but also with real materials. This objective is a continuation of Objective 4, as the material should follow the same material model and constitute a challenge for the standard virtual fields.

2.3.2 Detailed motivation

From Section 2.1 it is clear that the methods for choosing virtual fields for the non-linear virtual fields method are very limited. Particularly in the case of metal plasticity UDVFs were only used, with the exception of two studies (Table 2.1). UDVFs have been proven to be useful so far, however they have certain limitations that could be improved. In particular, they require a significant input from the user, and their effectiveness is dependent on the user expertise in terms of understanding the VFM theory and mechanics of the test. Although these limitations did not prevent obtaining good results, they might become more serious in the future when more complex heterogeneous tests are developed, and more complex constitutive models are to be identified.

In this work, a new method is proposed to address these concerns and in turns to improve the accuracy and applicability of the non-linear VFM. The method is developed using a general framework that can be applied to any material model,

test geometry and loading without significant input from the VFM user. The development and validation process was gradual and is documented in this thesis.

The sensitivity-based virtual fields were first presented in [12]. In this publication, the general methodology was established and tested using numerically simulated data. In particular, we presented the concept of stress-sensitivity fields to facilitate identification. This concept was used before in the context of material identification [57, 76], but never in the VFM. Here, we propose for the first time that stress-sensitivity fields be used as virtual strains, to highlight areas of the test piece rich in information about each parameter individually, at any time through the test. Then, we presented how those fields could be practically used in the VFM, by means of projecting them onto a base of linear piecewise functions, to reconstruct an associated virtual displacement field. The method was validated using numerically simulated data of a deep-notched test using isotropic plasticity with linear and nonlinear isotropic hardening models. The performance of the method was compared against the two other types of VFs: user-defined and stiffness-based optimised [28] VFs. We found that the SBVFs improved the accuracy of identification and that their effectiveness was largely independent from user input (in terms of mesh size used, material parameters variation and scaling).

The SBVFs were initially developed using the assumption of small deformation. It was realized that this was an important limiting factor of the method applicability, particularly for hyperelastic or ductile materials. Additionally, heterogeneous tests are promising for identification of anisotropic plasticity models commonly used in simulating metal forming processes. These models require multiple mechanical tests to be characterised (*e.g.* eight for Yld2004-18 [79]) and that the number could be potentially reduced by employing more complex mechanical tests. This was addressed in [13], where the SBVFs were extended to the finite deformation framework and applied to characterise anisotropic plasticity models (Hill48, Yld2000-2D). Instead of using the VFM formulation for small deformation, large deformation was used instead, and the SBVFs formulation had to be adjusted accordingly. The equilibrium was expressed in the reference configuration so the virtual mesh used for expressing the VFs was only assembled once. Both Hill48 and Yld2000-2D models were considered, and the identification results were compared against UDVFs as used in [43]. It was found that the SBVFs were effective at extracting material parameters. In particular, it was found that the SBVFs were capable of correctly identifying the Yld2000-2D model from a single test, which was not possible using the UDVFs. Another advantage of the SBVFs is that they are automatically generated and include different stress components in the identification independently from the user, which is important for anisotropic materials.

To prove that the method is effective not only on simulated data, experiments have been carried out using a cold-rolled sheet of DC04 steel. The material is known to be anisotropic and was modelled using Hill48 or Yld2000-2D models, thus the experiments were a continuation of the work previously published. First, the material was characterised using standard techniques including dogbone tests along three directions, and a bulge test. Then deep-notched tests were performed in order to identify the models from a reduced number of tests, using the VFM and SBVFs. Full-field measurements were obtained using DIC and were fed to the developed VFM code to identify models parameters. It was found that the SBVFs were successful at identifying Hill48 model, however the test was not sufficiently

heterogeneous to yield enough information for Yld2000-2D. In general, it was found that the identification with SBVFs yielded more accurate parameters than the one with UDVFs, suggesting that they are a superior replacement for the currently used UDVFs. This has been documented in Chapter 5 and is intended to be submitted to *Experimental Mechanics (Springer)*.

2.3.3 Declaration of authorship

The work presented in [12] was performed in its entirety by the candidate under supervision of Prof. Fabrice Pierron and Dr. Frances Davis.

Next, the work reported in [13] was performed entirely by the candidate. To achieve that, a numerical FEM model of the test, as well as the stress reconstruction routine for Yld2000-2D were supplied by Mr. Marco Rossi, who was added as a co-author of the paper.

Finally, the experimental validation included in Chapter 5 was performed by the candidate, with the exception of the bulge test, which was performed externally, due to lack of the testing machine at the University of Southampton, by Dr. Jin-Hwan Kim, who also kindly wrote Section 3.2.2. of the paper describing the experiment he performed.

Chapter 3

Sensitivity-based virtual fields for the non-linear virtual fields method

Comput Mech (2017) 60:409–431
DOI 10.1007/s00466-017-1411-6

ORIGINAL PAPER

Sensitivity-based virtual fields for the non-linear virtual fields method

Aleksander Marek[1] · **Frances M. Davis**[1] · **Fabrice Pierron**[1]

Received: 19 November 2016 / Accepted: 7 April 2017 / Published online: 28 April 2017

Abstract The virtual fields method is an approach to inversely identify material parameters using full-field deformation data. In this manuscript, a new set of automatically-defined virtual fields for non-linear constitutive models has been proposed. These new sensitivity-based virtual fields reduce the influence of noise on the parameter identification. The sensitivity-based virtual fields were applied to a numerical example involving small strain plasticity; however, the general formulation derived for these virtual fields is applicable to any non-linear constitutive model. To quantify the improvement offered by these new virtual fields, they were compared with stiffness-based and manually defined virtual fields. The proposed sensitivity-based virtual fields were consistently able to identify plastic model parameters and outperform the stiffness-based and manually defined virtual fields when the data was corrupted by noise.

Keywords Virtual fields method · Sensitivity-based virtual fields · Inverse identification · Full field measurement · Elasto-plastic · Digital image correlation

Electronic supplementary material The online version of this article (doi:10.1007/s00466-017-1411-6) contains supplementary material, which is available to authorized users.

✉ Aleksander Marek
A.Marek@soton.ac.uk

Frances M. Davis
Frances.Davis@soton.ac.uk

Fabrice Pierron
F.Pierron@soton.ac.uk

[1] Faculty of Engineering and the Environment, University of Southampton, Highfield SO171BJ, UK

1 Introduction

Owing to the rapid diffusion of full-field deformation measurement techniques like Digital Image Correlation [26], there has been growing effort from the mechanics of materials scientific community to develop new testing methods based on more complex tests to improve the efficiency of constitutive model identification. This is particularly important for models including larger numbers of parameters like anisotropic elasticity and plasticity as well as heterogeneous materials. It is beyond the scope of the present article to review this topic in detail and the reader is referred to the following references for a more complete picture of this topic [2,20,22]. The two main techniques employed in the literature to extract the constitutive parameters from deformation maps are Finite Element Model Updating (FEMU) and the Virtual Fields Method (VFM). FEMU relies on the intuitive idea that parameters can be identified by updating the material parameters in a finite element model until the simulation matches the experiment [2]. An alternative is the Virtual Fields Method [20] which directly calculates the stresses from the measured strains, without a need to conduct forward calculations using FEM. Stress equilibrium is then evaluated in the global sense by means of the principle of virtual work and parameters adjusted until this equilibrium is respected.

The main advantage of the VFM over FEMU is its computational efficiency, particularly for non-linear problems. Recently, authors reported that the VFM was 125 times faster than FEMU for their particular application [30], so there is a definite motivation to choose the VFM over FEMU. However, the choice of the virtual fields (see Sect. 2) plays a crucial role in the VFM. In linear elasticity, manually defined virtual fields were used until the mid-2000s with mixed success [18]. In 2004, a systematic procedure for defining noise minimizing virtual fields was released which enabled the vir-

tual fields to be automatically defined [1]. These automated virtual fields are now routinely used to solve linear elasticity problems, even for heterogeneous materials [11]. This success led them to be implemented on a commercial software platform, MatchID (v. 2.1, www.matchidmbc.be). However, for non-linear constitutive models, no automated approach for defining the virtual fields exists and this constitutes a bottleneck for the establishment of the VFM as the gold standard to inversely identify material properties from full field measurements [22].

In absence of an automated procedure to define virtual fields for non-linear problems, the VFM has been implemented with manually defined virtual fields. Elasto-plasticity was the first type of non-linear constitutive model to be tackled [8]. The non-linear virtual fields method has since been used to study a wide range of materials such as arteries [4], rubbers [10,28,29], composites [7], and metals [12–14,17,25]. As a result, many different non-linear constitutive model types were considered including hyperelasticity, elasto-plasticity, visco-elasticity, and anisotropic plasticity. While manually defining the virtual fields for non-linear problems has been successful, there are several drawbacks. The selection of manual virtual fields relies on the expertise of the investigator. In addition, the fields are generally static and do not evolve with the deformation. The only attempt so far at defining an automated procedure to define the virtual fields adapted the procedure for linear elasticity [1] to elasto-plasticity [19]. The virtual fields obtained were named *stiffness-based* virtual fields since they depend on the elasto-plastic stiffness matrix. However, the problem of systematically defining efficient and robust virtual fields for a general class of non-linear problems hinders the widespread diffusion of the VFM as a standard tool.

In this manuscript, a new type of automated virtual fields for non-linear problems is proposed. In Sect. 2, the virtual fields method is described in detail. Next, the automated virtual fields, the so-called *sensitivity-based* virtual fields, are derived introducing two variants based on total and incremental sensitivity maps. The performances of the proposed sensitivity-based virtual fields are then compared to stiffness based and manually defined virtual fields in Sect. 5 for the simulated experiment described in Sect. 4.

2 Virtual Fields Method

For a solid that is subjected to quasi-static loading the principle of virtual work can be expressed as

$$-\int_V \boldsymbol{\sigma}\left(\mathbf{x},t\right):\boldsymbol{\varepsilon}^*\left(\mathbf{x},t\right)\,dV+\int_{\partial V}\boldsymbol{T}\cdot\boldsymbol{u}^*\left(\mathbf{x},t\right)\,dS=0 \tag{1}$$

where V is the volume of the solid, $\boldsymbol{\sigma}$ is the stress tensor, $\boldsymbol{u}^*$ and $\boldsymbol{\varepsilon}^*$ are the virtual displacement and strain, respectively, and $\boldsymbol{T}$ is the traction vector. Note that the stress tensor, virtual displacement, and virtual strain can vary in space and time. The stress field is calculated directly from the measured displacements (strains) using assumed a certain constitutive relation. The calculations are performed with a numerical implementation of the constitutive model, such as the radial-return algorithm for plasticity. Therefore, no forward problem solving using FEM is required. In Eq. 1, the virtual displacement does not have any physical meaning, and can be any function that is continuous and differentiable over the body. Likewise, the virtual strains do not have any link with the real strains but only serve as a spatial weighting functions (also sometimes called 'test functions'). The virtual strain is calculated from the virtual displacement using the traditional strain-displacement relationship, $\boldsymbol{\varepsilon}^*=1/2\left(\nabla\boldsymbol{u}^*+\nabla\boldsymbol{u}^{*\mathrm{T}}\right)$. The first integral in Eq. 1 is the contribution of *internal virtual work* due to deformation and the second integral is the contribution from *external virtual work* due to externally applied loads.

Since in general, full-field measurements are only performed on the surface of the specimen some assumption on the material behaviour through the thickness must be made. In this manuscript, the assumption of plane stress is used since the samples are loaded in plane and are considered thin. However, alternative assumptions on the behaviour through the thickness are possible. Equation 1 can be re-written for a thin specimen in a state of plane stress:

$$\begin{aligned}&-h\int_S\boldsymbol{\sigma}\left(x,y,t\right)\cdot\boldsymbol{\varepsilon}^*\left(x,y,t\right)dS\\&+h\int_{\partial S}\boldsymbol{T}\cdot\boldsymbol{u}^*\left(x,y,t\right)dL=0\end{aligned} \tag{2}$$

where h is the thickness of the solid, S is the surface of the solid, and ∂S is the boundary of the solid. In Eq. 2, the stress and virtual strain tensors have been written as vectors: $\boldsymbol{\sigma}\left(x,y,t\right)=[\sigma_{11},\sigma_{22},\sigma_{12}]$ and $\boldsymbol{\varepsilon}^*\left(x,y,t\right)=[\varepsilon^*_{11},\varepsilon^*_{22},2\varepsilon^*_{12}]$.

Full-field measurements such as digital image correlation [26] or the grid method [9] determine the displacement at a large number of discrete locations called measurement points. When the number of measurement points is large, the first integral in Eq. 2 can be well-approximated as a discrete sum using the mid-point rule. Often the distribution of the traction is unknown and only the resultant force, $\boldsymbol{F}=\int\boldsymbol{T}dA$, is measured using a load cell. When the resultant force is known, the external virtual work, W^*_{ext}, can be directly calculated provided that the virtual displacements are constant over the area where the unknown traction distribution acts. As a result Eq. 2 can be re-written for any time t as

Comput Mech (2017) 60:409–431 411

$$\left(\sum_{j=1}^{nPts}\left(\boldsymbol{\sigma}^{j}\cdot\boldsymbol{\varepsilon}^{*j}\right)S^{j}\right)-W_{ext}^{*}=0 \tag{3}$$

where $nPts$ is the number of measurement points and S^j is the area of the jth measurement point.

A constitutive relation must be used to calculate the stress from the strain data recorded during an experiment. The constitutive relation relates the measured strains to the stresses, $\boldsymbol{\sigma}=\boldsymbol{\sigma}\left(\boldsymbol{\varepsilon},\boldsymbol{X}\right)$, where $\boldsymbol{X}$ are the unknown constitutive parameters. In the case of linear elastic materials, the constitutive parameters can be identified by solving a set of linear equations. This occurs because the stress is a linear function of the strain. However, for non-linear constitutive relationships, the VFM no longer yields a set of linear equations. As a result, the identification process is based on the minimisation of a cost function with respect to the constitutive parameters. Using a suitable set of virtual displacements, the cost function can be defined as the least squares difference between the internal and external virtual work through time:

$$\Phi(\boldsymbol{X},\boldsymbol{\varepsilon})=\sum_{i=1}^{nVF}\left[\sum_{t=1}^{nTime}\left(\sum_{j=1}^{nPts}\left(\boldsymbol{\sigma}^{j}\left(\boldsymbol{\varepsilon},\boldsymbol{X}\right)\cdot\boldsymbol{\varepsilon}^{*j(i)}\right)S^{j}-W_{ext}^{*}\right)^{2}\right] \tag{4}$$

where nVF and nTime are the numbers of independent virtual fields and time steps, respectively. The difference between the internal and external virtual work will be minimized, indicating that equilibrium has been satisfied, when the parameters have been correctly identified. Therefore, to identify the material parameters for a non-linear constitutive model, the process is iterative.

To identify the constitutive parameters, $\boldsymbol{X}$, a set of virtual displacements and strains must be defined. There is an infinite number of virtual displacement fields that satisfy the principle of virtual work (Eqs. 1–3). In the case of a linear elastic model, when the number of independent virtual fields equals the number of unknowns a linear system is produced that when inverted gives the model parameters. For these linear systems, Avril et al. [1] have proposed a set of optimised virtual fields that minimise the influence of noise on the parameter identification. For non-linear problems, the situation is more complex. The number of virtual fields required for a successful identification is not necessarily equal to the number of parameters. However, the selected virtual fields need to activate the different parameters of the model, and provide a solution which is as robust as possible with respect to measurement noise. Until now, and except the effort reported in [19], the virtual fields were defined intuitively by the user. In this article, a new procedure is devised to automatically generate virtual fields to extract non-linear parameters with a view to increase the robustness from the procedure defined in [19].

3 Theoretical development

As constitutive models become more complex, the number of model parameters tends to increase. The difficulty in identifying these parameters lies in determining where sufficient information on each parameter is coded in space (x, y) and time (t). The idea behind the proposed sensitivity-based virtual fields is that they will focus on regions that carry the most information about the constitutive parameters and follow them through time. By perturbing each model parameter, it is possible to determine the sensitivity of the stress to each parameter in the constitutive model. In a region where the stress change is significant, relevant information is encoded for identifying that parameter. The sensitivity of the stress field is chosen here as this particular field carries information in the VFM. Moreover, the stress field is the only quantity that depends directly on the constitutive parameters in the VFM, so using these stress sensitivity maps seems like a very natural idea to select areas with strong dependence to a given parameter. Since virtual strains can be seen as spatial weight functions, the resulting stress sensitivity map can be used to focus the identification on these critical regions where each model parameter has significant influence. Each model parameter will produce a different stress sensitivity map and therefore requires its own virtual field. Stress sensitivity based virtual fields following the idea outlined above are now derived. It is anticipated that by using these virtual fields to focus on regions where the signal is the most significant for a given parameter, identifiability of all parameters will be improved and the influence of noise on the identification will be reduced.

3.1 Formulation of sensitivity-based virtual fields

To investigate the spatial sensitivity of the stress field to each model parameter, the stress sensitivity defined as

$$\delta\boldsymbol{\sigma}^{(i)}\left(\boldsymbol{\varepsilon},\boldsymbol{X},t\right)=\boldsymbol{\sigma}\left(\boldsymbol{\varepsilon},\boldsymbol{X},t\right)-\boldsymbol{\sigma}\left(\boldsymbol{\varepsilon},\boldsymbol{X}+\delta X_{i},t\right) \tag{5}$$

was calculated. In Eq. 5, $\boldsymbol{X}$ is the vector of the model parameters, i denotes the ith model parameter in vector $\boldsymbol{X}$, and t is the time step. By applying a small variation to a single model parameter, δX_i, it is possible to map in the stress field the most significant spatial changes associated with this model parameter. In regions where $\delta\boldsymbol{\sigma}^{(i)}$ is close to zero, the varied parameter has a minimal effect on the stress, and conversely, large values of $\delta\boldsymbol{\sigma}^{(i)}$ indicate that small changes in X_i produce large changes in the stress.

To minimize the history dependence of the stress sensitivity, the incremental stress sensitivity for each model parameter, $\delta\widetilde{\boldsymbol{\sigma}}^{(i)}$, is calculated as:

$$\delta\widetilde{\boldsymbol{\sigma}}^{(i)}\left(\boldsymbol{\varepsilon}, \boldsymbol{X}, t\right) = \delta\boldsymbol{\sigma}^{(i)}\left(\boldsymbol{\varepsilon}, \boldsymbol{X}, t\right) - \delta\boldsymbol{\sigma}^{(i)}\left(\boldsymbol{\varepsilon}, \boldsymbol{X}, t-1\right) \quad (6)$$

By subtracting the stress sensitivity between two consecutive time steps, only the regions in the stress map that have changed during that particular time increment are highlighted. This is equivalent to a temporal finite difference of the stress sensitivity maps. Note that an incremental stress sensitivity must be calculated for every time step and constitutive parameter.

The idea is to use these incremental stress sensitivity maps as virtual strain maps. However, virtual displacements need to be defined to calculate the virtual work of external forces. Moreover, the virtual displacements are also chosen to eliminate certain unknown contributions of the traction forces at the boundary (this will be referred to as 'virtual boundary conditions' in the rest of the article). The objective is to define a set of virtual displacements such that their associated virtual strain maps 'look like' the incremental sensitivity stress maps. To accomplish this, a least-square projection approach, described next, was implemented.

To define the virtual displacement, $\boldsymbol{u}^*$, from the incremental stress sensitivity defined in Eq. 6, a virtual mesh was implemented as it provides more flexibility to include virtual boundary conditions and ensures numerical stability compared to functions continuously defined over the whole field of view [20]. The domain, S, is broken into several virtual elements, collectively called a virtual mesh. Additional details on the virtual mesh can be found in "Appendix 1".

The virtual strains at each measurement point are related to the virtual displacement at the four nodes of the virtual element that contains the point. A set of three linear equations can be written for each measurement point which relates the local virtual strains to the virtual displacements. When the equations for every element in the mesh are collected the following system of equations is produced:

$$\delta\widetilde{\boldsymbol{\sigma}}^{(i)} = \boldsymbol{B}\,\boldsymbol{u}^{*(i)} \quad (7)$$

where $\boldsymbol{B}$ is the global strain-displacement matrix which maps the virtual displacement at every node into virtual strains. There are $3 \times nPts$ equations with $2 \times nNodes$ unknowns for each model parameter. The virtual boundary conditions place constraints on the virtual displacement, $\boldsymbol{u}^{*(i)}$. When the displacement at a boundary is prescribed, the traction at the surface is generally unknown. To eliminate the contribution of this unknown traction to Eq. 3, the virtual displacement at these boundaries are set to zero. Often, the distribution of the traction is unknown and only the resultant force, $\boldsymbol{F} = \int \boldsymbol{T} dA$, is measured. In this case, a constant virtual displacement is applied on the boundary.

Enforcing the constraints on $\boldsymbol{u}^{*(i)}$, a modified global strain-displacement matrix, $\bar{\boldsymbol{B}}$, is found. The virtual displacements are obtained by multiplying the pseudo-inverse of the modified global strain-displacement matrix with the incremental stress sensitivity, $\boldsymbol{u}^{*(i)} = \text{pinv}\left(\bar{\boldsymbol{B}}\right)\delta\widetilde{\boldsymbol{\sigma}}^{(i)}$. The virtual strains, $\boldsymbol{\varepsilon}^{*(i)}$, also called the sensitivity-based virtual fields, are then calculated using the right hand side of Eq. 7. As a result, the virtual displacements are calculated so that the resulting virtual strains match the incremental stress sensitivity in a least-squares sense. Although $\boldsymbol{u}^{*(i)}$ and $\boldsymbol{\varepsilon}^{*(i)}$ must be calculated several times to perform the parameter identification, $\boldsymbol{B}$ and pinv $\left(\bar{\boldsymbol{B}}\right)$ are only computed once because the virtual mesh and boundary conditions remain unchanged.

3.2 Inverse parameter identification procedure

To identify the model parameters using the sensitivity-based virtual strains and displacements, the following cost function, Φ, is minimized:

$$\Phi\left(\boldsymbol{X}, \boldsymbol{\varepsilon}\right) = \sum_{i=1}^{nParams} \left[\frac{1}{\left(\alpha^{(i)}\right)^2} \times \sum_{t=1}^{nTime} \left(\sum_{j=1}^{nPts} \left(\boldsymbol{\sigma}^j\left(\boldsymbol{\varepsilon}, \boldsymbol{X}, t\right) \cdot \boldsymbol{\varepsilon}^{*j^{(i)}}(t) \right) S^j - W^*_{ext}(t) \right)^2 \right]. \quad (8)$$

In Eq. 8, since the contribution of each parameter can vary greatly in magnitude, it is scaled by $\alpha^{(i)}$. The scale factor, $\alpha^{(i)}$, is calculated for each model parameter from the mean of the n highest internal virtual work (IVW) values where the IVW is defined as:

$$\text{IVW}^{(i)}(t) = \sum_{j=1}^{nPts} \left(\boldsymbol{\sigma}^j\left(\boldsymbol{\varepsilon}, \boldsymbol{X}, t\right) \cdot \boldsymbol{\varepsilon}^{*j^{(i)}}(t) \right) S^j . \quad (9)$$

Scaling is necessary because the constitutive parameters are active over different time scales. As an example when attempting to identify the parameters in a plastic model, the parameters which capture the yielding behaviour will only be active for a short time period while hardening parameters will, in general, be active for much longer times. The suitability of this scaling method is validated in Sect. 5.

3.3 Alternative virtual fields

To quantify the improvement in parameter identification provided by the sensitivity-based virtual fields, their results are compared with that from both uniform and stiffness-based virtual fields. The manually defined uniform virtual field

Comput Mech (2017) 60:409–431 413

applies a linear virtual extension in the x_2-direction and the resulting strain field is uniform. Since the virtual strain is uniform, the stress in the y-direction is integrated and compared directly with the resultant force (Eq. 2). The virtual displacements and strains which define this uniform virtual field are:

$$\begin{cases} u_1^* = 0 \\ u_2^* = x_2 \end{cases} \qquad \begin{cases} \varepsilon_{11}^* = 0 \\ \varepsilon_{22}^* = 1 \\ \varepsilon_{12}^* = 0 \end{cases} \tag{10}$$

The most common approach for the non-linear VFM has been to manually define the virtual fields and therefore it is interesting to evaluate it against the sensitivity-based virtual fields.

Stiffness-based optimised virtual fields [19] were also implemented; these virtual fields are an earlier attempt at developing noise-optimised virtual fields for elasto-plasticity. The stiffness-based virtual fields were derived using the same noise minimization approach developed for virtual fields optimization in linear elasticity [1]. The stiffness-based virtual fields depend on the tangent stiffness matrix, D^{ep}, and scale each element's contribution by its effective von Mises stress. The reason for scaling by the effective von Mises stress is twofold. Firstly, the elements with low stress values generally contribute larger errors to the cost function, due to low signal-to-noise ratio. Secondly, scaling by an element's effective von Mises stress minimises the influence of the early stress–strain history and is therefore a practical way to reduce the importance of areas in the specimen which have not yielded. In the implementation by Pierron et al. [19], the stiffness-based optimised virtual fields were projected onto constant strain triangular elements. In this study the method was extended to quadrilateral elements so that the same type of virtual elements could be implemented for both the sensitivity and stiffness-based virtual fields. A different method must be used to calculate $\boldsymbol{D}^{ep}$ since kinematic hardening is not considered here. The formulation for the elasto-plastic tangent stiffness matrix presented by de Souza et al. [16] was used. In order to integrate the element stiffness matrix, both the elasto-plastic stiffness matrix and the effective von Mises stress were averaged across each virtual element. The mean value for each was assigned to the centroid of the virtual element. The definitions of the modified global stiffness matrix and the tangential elasto-plastic stiffness matrix needed to compute the stiffness-based virtual fields are given in "Appendix 2". This approximation of the element stiffness matrix limits how coarse the virtual mesh can be; the larger an elements is, the more points of measurement it contains as well as the larger area it spans. As a result the value at the centroid is estimated with larger error leading to reduction in effectiveness of noise-optimisation.

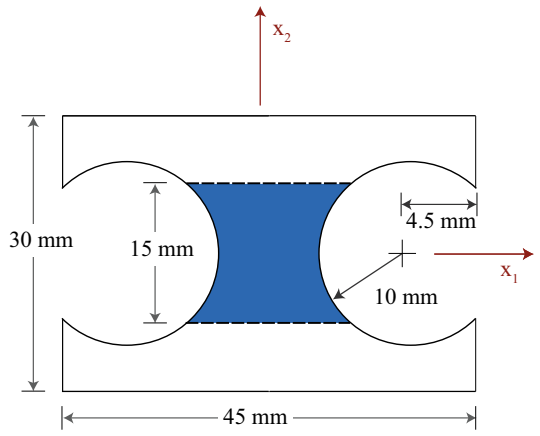

Fig. 1 Geometry for the tensile specimen. The *blue* region in the centre of the specimen is the region of interest (ROI). (Color figure online)

4 Application to simulated test data

To verify the effectiveness of the senstivity-based virtual fields, the method was tested using simulated data from uniaxial tensile test on a double-notched specimen. During the initial portion of the test, the material deforms elastically and no information on the yield or hardening response can be identified. Once the material yields a plastic zone is created. The parameters which define the yield behaviour of the material will be active on the boundary of this growing plastic zone. In the interior of the plastic zone, the parameters which describe the hardening response will be active. Therefore, the proposed sensitivity-based virtual fields for yield and hardening should follow the boundary and interior of the plastic zone, respectively. This can be used as a qualitative check that the sensitivity-based virtual fields have been correctly implemented.

4.1 Double-notched tensile test

The simulated double-notched tensile test data was created to mimic a steel specimen that was subjected to an average longitudinal strain of 1%. The double notched specimen geometry pictured in Fig. 1 was selected because the deep notches produce a heterogeneous strain distribution. Similar geometry has already been used in [19]. The specimen was meshed in ABAQUS (v. 6.13) using 8-node bi-quadratic plane stress quadrilaterals (CPS8) with a total of 12,120 elements. The mesh density was chosen based on a mesh convergence study. The nodes on the bottom edge of the mesh were fixed and a vertical displacement of 0.3 mm was applied to the nodes on the top edge. The loading was imposed in 100 equal steps of 0.003 mm each. As a result, 100 different displacement fields are available for the identification process, simulating the recording of one hundred images during an experiment.

Table 1 Reference parameters for the linear and Voce hardening laws

	σ_0 (MPa)	H (MPa)	R_0 (MPa)	R_{inf} (MPa)	b
Linear	297.5	3170	–	–	–
Voce	179.8	–	3170	117.7	3500

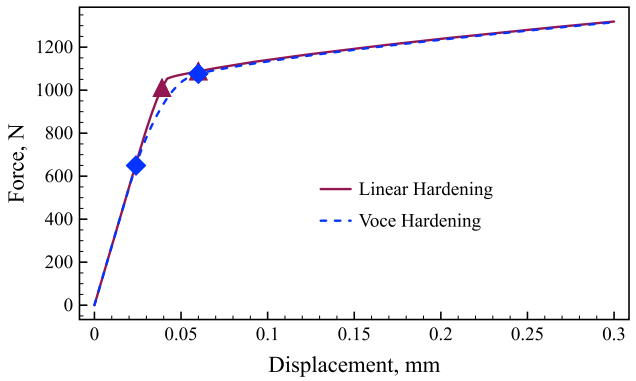

Fig. 2 Force versus displacement curve for the linear and Voce hardening laws. The points highlighted on the *curve* for linear hardening correspond to time steps 13 and 20. The points highlighted on the *curve* for Voce hardening correspond to time steps 8 and 20

Two different constitutive models were considered. For both cases, the material model used linear elasticity ($E = 199$ GPa, $\nu = 0.32$) combined with the von Mises yield criterion. Two different hardening laws were implemented: linear (Eq. 11) and Voce (Eq. 12). For a material that linearly hardens, the updated yield stress, σ_y, is a function of the equivalent plastic strain, $\bar{\varepsilon}^p$, the initial yield stress, σ_0, and the hardening modulus, H.

$$\sigma_y = \sigma_0 + H\bar{\varepsilon}^p \tag{11}$$

A modified form of the Voce hardening law [19] was also implemented to include a non-linear hardening response. In this case, the updated yield stress is a function of the equivalent plastic strain and four model parameters: σ_0, the initial yield stress, R_0, the linear hardening modulus, and R_{inf} and b which describe the non-linear response at yield.

$$\sigma_y = \sigma_0 + R_{inf}\left(1 - \exp(-b\bar{\varepsilon}^p)\right) + R_0\bar{\varepsilon}^p \tag{12}$$

The parameters implemented in the FE model for both hardening laws are presented in Table 1. The values for the Voce law were based on the values cited in [19], whereas the linear hardening model was defined in such a way that it produces the same stress–strain relation as the Voce law as the plastic strain approaches infinity. The force-displacement curve for both hardening models is shown in Fig. 2.

4.2 Simulated experimental data

To simulate the data that would be collected during an actual experiment, the resultant force at the top surface and the strain at the centroid of each element were exported from ABAQUS for each loading step. The strain data was interpolated onto a regular 150×150 mesh, covering the central portion of the specimen (Fig. 1) using the MatLab function *griddata* with a linear interpolant to simulate the format of data obtained from a typical full-field measurement technique such as DIC. Gaussian noise with a standard deviation of $150\,\mu\epsilon$ was artificially added to the simulated strain data to attempt to simulate data collected during an actual experiment. The white (Gaussian) noise was generated in MatLab using the function *randn*. The use of noisy data is necessary to evaluate the ability of the various virtual fields to minimize the effect of experimental noise on the parameter identification. This is thought to be enough to discriminate between the performances of the different virtual fields. Though beyond the scope of the present article, a more robust simulation of experimental data could be undertaken using image deformation [24]. This will be attempted in future work.

5 Results and discussion

5.1 Construction of the sensitivity-based virtual fields

To investigate whether the mathematical formulation presented in Sect. 3.1 highlights the regions where each parameter is active, maps of the equivalent plastic strain, $\bar{\varepsilon}^p$, the stress sensitivity, $\delta\boldsymbol{\sigma}^{(i)}$, and the incremental stress sensitivity, $\delta\widetilde{\boldsymbol{\sigma}}^{(i)}$, were drawn for both the linear and Voce hardening models. The stress sensitivity and incremental stress sensitivity were calculated using Eqs. 5–6 with exact data from their respective finite element models and the reference parameters given in Table 1. The small variation applied to the parameters in Eq. 5 was $\delta X_i = -0.05X_i$. Here, the backwards finite difference was used in order to include slightly more points on the elasto-plastic boundary, compared to the forward finite difference.

5.1.1 Linear hardening

In Figs. 3 and 4, the maps of $\bar{\varepsilon}^p$, $\delta{\sigma_{22}}^{(i)}$, and $\delta\widetilde{\sigma}_{22}{}^{(i)}$ are shown for the linear hardening model at two different load steps. Videos of $\delta{\sigma_{22}}^{(i)}$ and $\delta\widetilde{\sigma}_{22}{}^{(i)}$ for all 100 time steps can be found in the Online Resources 1–2 for the yield stress and hardening modulus, respectively. The two time steps presented in Figs. 3 and 4 show the two main phases in the experiment: initial yielding (time step 13) and hardening of the entire centre region (time step 20). For reference these two time points are also marked in Fig. 2. In the first phase,

Comput Mech (2017) 60:409–431

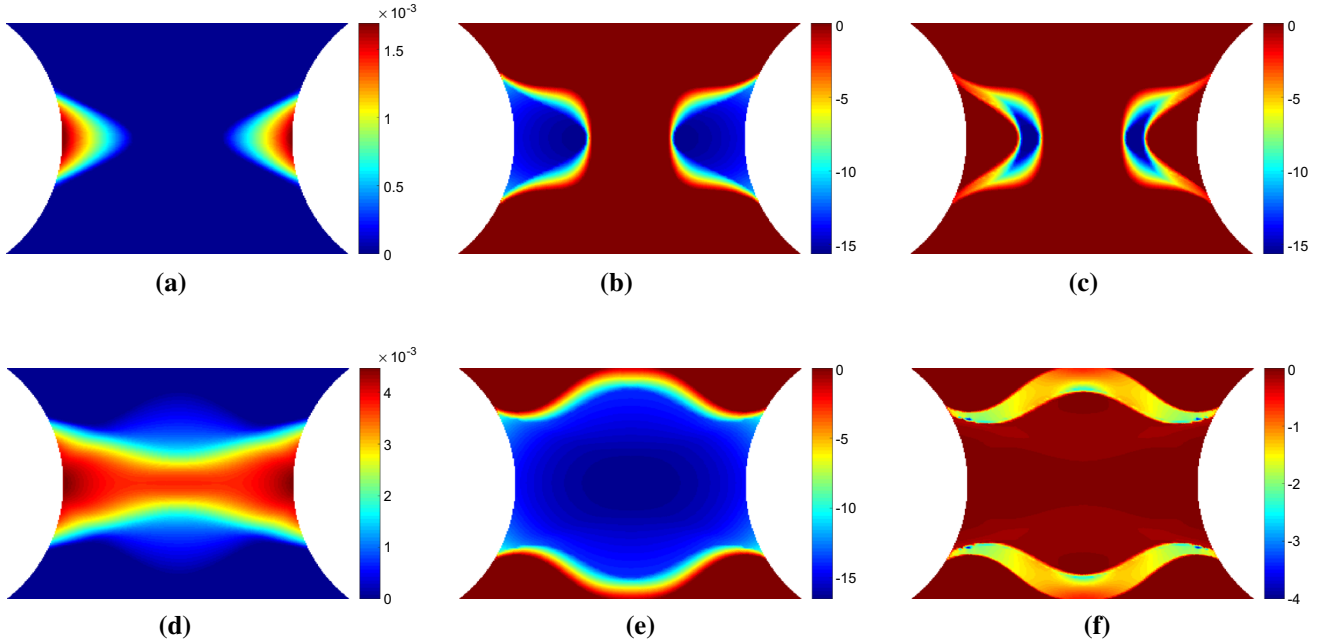

Fig. 3 Maps of **a, d** equivalent plastic strain, **b, e** the vertical component of stress sensitivity to the yield stress, $\delta\sigma_{22}^{(\sigma 0)}$, and **c, f** the incremental stress sensitivity, $\delta\tilde{\sigma}_{22}^{(\sigma 0)}$. The top row of maps **a–c** are for a displacement of 0.039 mm which corresponds to a resultant vertical force of 1011 N. The lower row of maps **d–f** are for a displacement of 0.060 mm which corresponds to a resultant vertical force of 1085 N

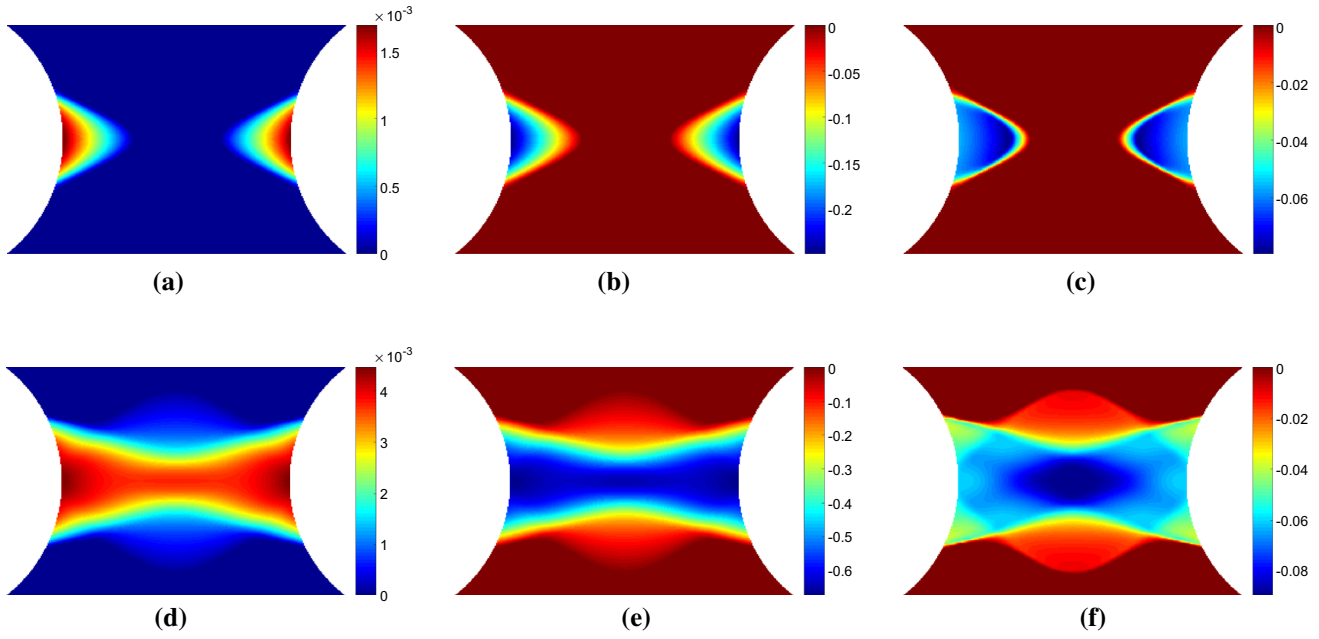

Fig. 4 Maps of **a, d** equivalent plastic strain, **b, e** the vertical component of stress sensitivity to the hardening modulus, $\delta\sigma_{22}^{(H)}$, and **c, f** the incremental stress sensitivity, $\delta\tilde{\sigma}_{22}^{(H)}$. The top row of maps **a–c** are for a displacement of 0.039 mm which corresponds to a resultant vertical force of 1011 N. The lower row of maps **d–f** are for a displacement of 0.060 mm which corresponds to a resultant vertical force of 1085 N

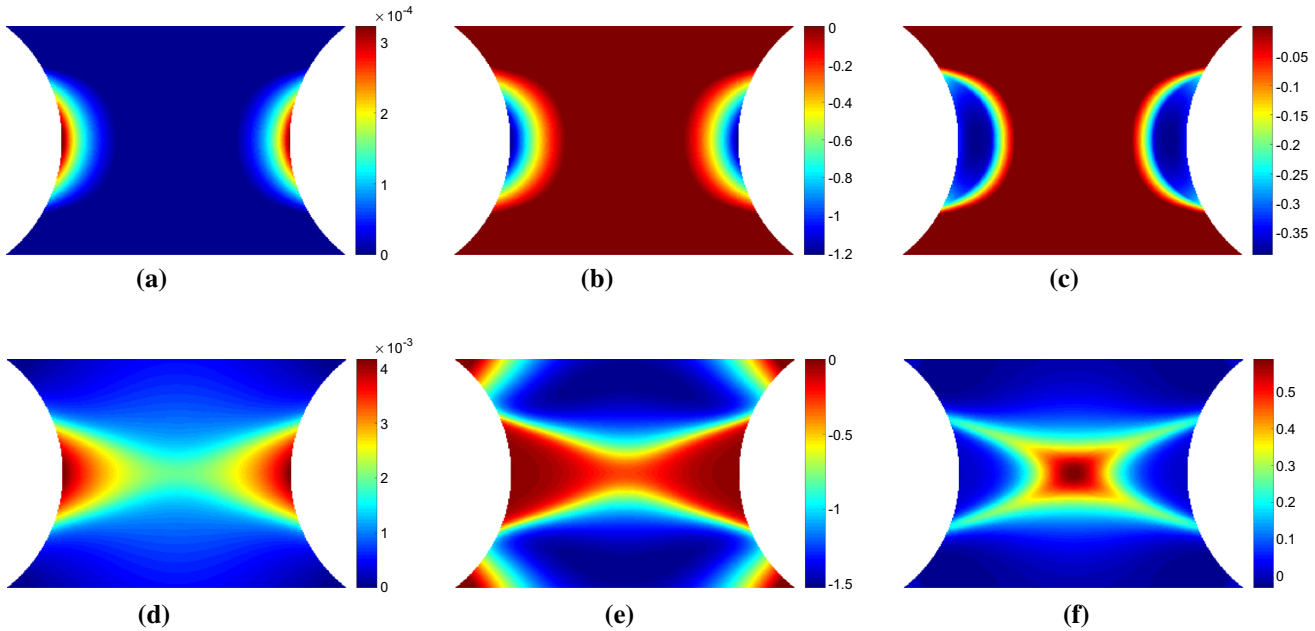

Fig. 5 Maps of **a, d** equivalent plastic strain, **b, e** the vertical component of stress sensitivity to **b**, $\delta\sigma_{22}^{(b)}$, and **c, f** the incremental stress sensitivity, $\delta\tilde{\sigma}_{22}^{(b)}$. The top row of maps **a**–**c** are for a displacement of 0.024 mm which corresponds to a resultant vertical force of 650 N. The lower row of maps **d**–**f** are for a displacement of 0.060 mm which corresponds to a resultant vertical force of 1076 N

the plastic zone propagates from the notches towards the centre of the specimen. In the second phase, the yield zone propagates from the centre towards the top and bottom of the specimen. As shown in Fig. 3b, e the stress sensitivity highlights the plastic zone, very closely resembling the shape of the equivalent plastic strain (Fig. 3a, d). The incremental stress sensitivity for yield stress (Fig. 3c, f) follows the boundary of the equivalent plastic strain, defining the border between the elastic and plastic zones, as expected. The incremental stress sensitivity focuses only on the regions that have yielded between the two increments, removing the history dependent effects shown in the stress sensitivity. However, Fig. 4 indicates that there is not much difference in shape between the stress sensitivity and incremental stress sensitivity for the hardening modulus. The only difference is the locations within the map that are emphasised; the magnitude of the stress sensitivity is the greatest where the equivalent plastic strain is the largest. The incremental stress sensitivity is the highest just behind the border of the plastic zone due to the removal of the history dependence. These results confirm that the incremental stress sensitivity, $\delta\widetilde{\boldsymbol{\sigma}}^{(i)}$, highlights the regions in the specimen where each parameter is active.

5.1.2 Voce hardening

The stress sensitivity and incremental stress sensitivity were also examined for the Voce model. As expected, the Voce parameters, σ_0 and R_0, behave almost exactly as the linear hardening parameters σ_0 and H. The remaining two parameters R_{inf} and b which capture the non-linear yielding response behave quite differently. Videos of the stress sensitivity and incremental sensitivity for all four model parameters are included in the Online Resources 3–6. The maps of both stress sensitivity and incremental sensitivity at two different time steps are presented in Figs. 5 and 6 for R_{inf} and b, respectively. The two time steps correspond again to the propagation of the plastic zone from the notches (a–c) and the merging of the two plastic zones in the centre followed by vertical propagation (d–f). These two time steps are also marked in Fig. 2. At the onset of yielding, the stress sensitivity and incremental stress sensitivity for R_{inf} and b follow the boundary of the plastic zone (Figs. 5, 6a–c). As the plastic zone develops, clear differences between the stress sensitivity and incremental stress sensitivity emerge (Figs. 5, 6e–f). The incremental stress sensitivity for both parameters concentrates in the centre of the specimen, excluding the notched areas where plastic strain is the highest. The large differences in shape between the stress sensitivity and the incremental stress sensitivity are again due to the removal of history dependent effects by the incremental stress sensitivity. As the sample continues to plasticize the incremental stress sensitivities for R_{inf} and b occupy less space. This occurs because the exponential term in Eq. 12, which includes R_{inf} and b, decays to zero for large values of plastic strain. The stress sensitivity clearly highlights areas which are sensitive to a small change

Comput Mech (2017) 60:409–431

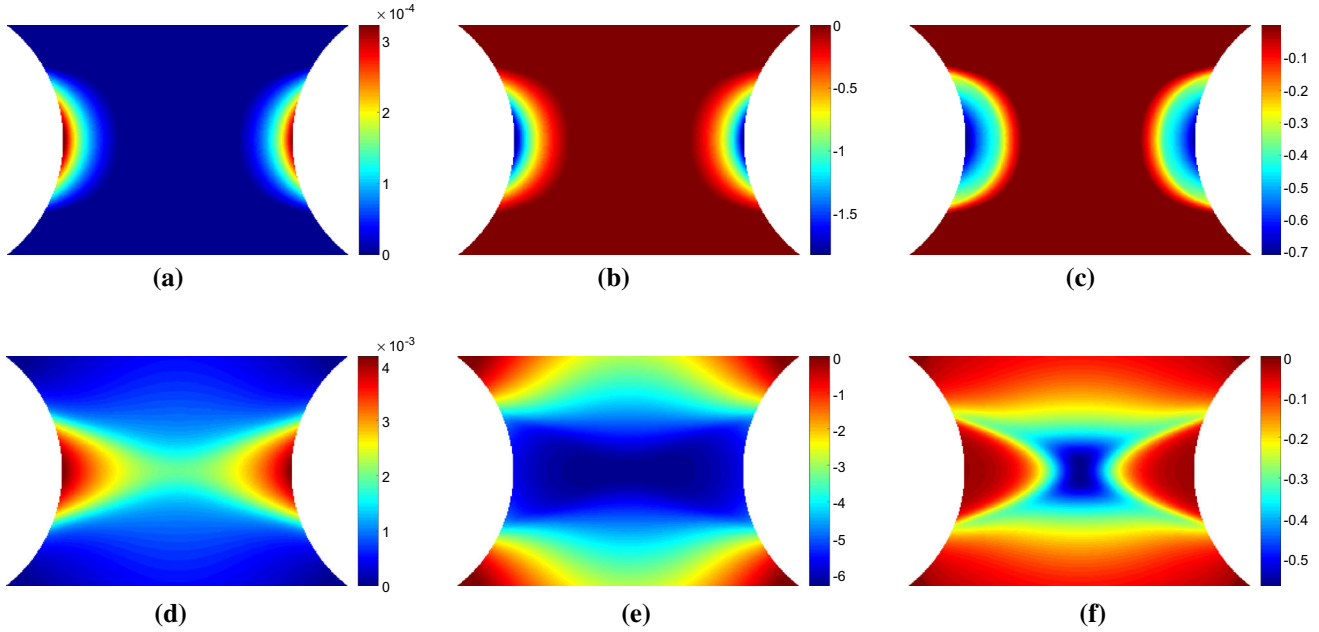

Fig. 6 Maps of **a, d** equivalent plastic strain, **b, e** the vertical component of stress sensitivity to hardening modulus, $\delta\sigma_{22}^{(R_{inf})}$, and **c, f** the incremental stress sensitivity, $\delta\widetilde{\sigma}_{22}^{(R_{inf})}$. The top row of maps **a**–**c** are for a displacement of 0.024 mm which corresponds to a resultant vertical force of 650 N. The lower row of maps **d**–**f** are for a displacement of 0.060 mm which corresponds to a resultant vertical force of 1076 N

in the constitutive parameter but due to the intrinsic history-dependence of plasticity, any region where the parameter was active will still be highlighted. The incremental stress sensitivity effectively filters the history-dependence creating virtual fields that will follow the critical regions through time.

5.1.3 Sensitivity-based virtual fields

Sensitivity-based virtual fields were identified from the incremental stress sensitivity maps, $\delta\widetilde{\boldsymbol{\sigma}}^{(i)}$, using Eq. 7. The virtual fields ε_{22}^{*} that correspond to the incremental stress sensitivities in Figs. 3 and 4c, f are shown in Fig. 7. The piecewise linear functions are capable of reproducing the general spatial features of the stress sensitivity maps. It is worth noting that the virtual fields do not have to follow the sensitivity maps very precisely, but it is sufficient to highlight areas where the signal is present for each parameter at a particular time step. Due to some high gradients in the incremental stress sensitivity maps, the coarse mesh (Fig. 7c, g) struggles to capture these local variations. As the virtual mesh is refined, the features are more accurately reproduced as shown in Fig. 7d–f and h–j. The primary cost of mesh refinement is the computational time required to produce the global strain-displacement matrix, **B**, which is needed to calculate the sensitivity-based virtual fields (Eq. 7). It is worth noting that the exact shape is not required for the method to be successful, as will be shown later; once the general shape is captured (7 × 7 mesh) the virtual mesh has sufficient resolution to identify the model parameters for both the linear and Voce hardening models.

In Figs. 3 and 4, the stress sensitivity and incremental stress sensitivity were plotted in the loading direction. They can also be plotted for the remaining stress components. Figure 8a, d shows the incremental stress sensitivities, $\delta\widetilde{\sigma}_{11}^{(\sigma_0)}$ and $\delta\widetilde{\sigma}_{12}^{(\sigma_0)}$. The incremental stress sensitivity maps correspond to the second time step depicted in Figs. 3 and 4 when the yield zone propagates upwards and downwards from the specimen centre. The sensitivity-based virtual fields ε_{11}^{*} and ε_{12}^{*} are pictured in Fig. 8b, e and c, f for a 7 × 7 and 14 × 14 virtual mesh, respectively. The shapes of ε_{11}^{*} and ε_{12}^{*} are similar to their respective stress sensitivities but, the reconstructions are not as accurate as for ε_{22}^{*}. This mismatch occurs because the three virtual strain components are not independent. Since the incremental stress sensitivity in the loading direction is the largest in magnitude, the least-squares identification of the virtual strains places more weight on matching this component. Employing finer meshes improves the matching of the overall shapes for all three components but the method still struggles to match sharp gradients (e.g. pattern in Fig. 8d). The influence of the virtual mesh density on the parameter identification is further explored for each of the hardening models in Sects. 5.3.4 and 5.4.4.

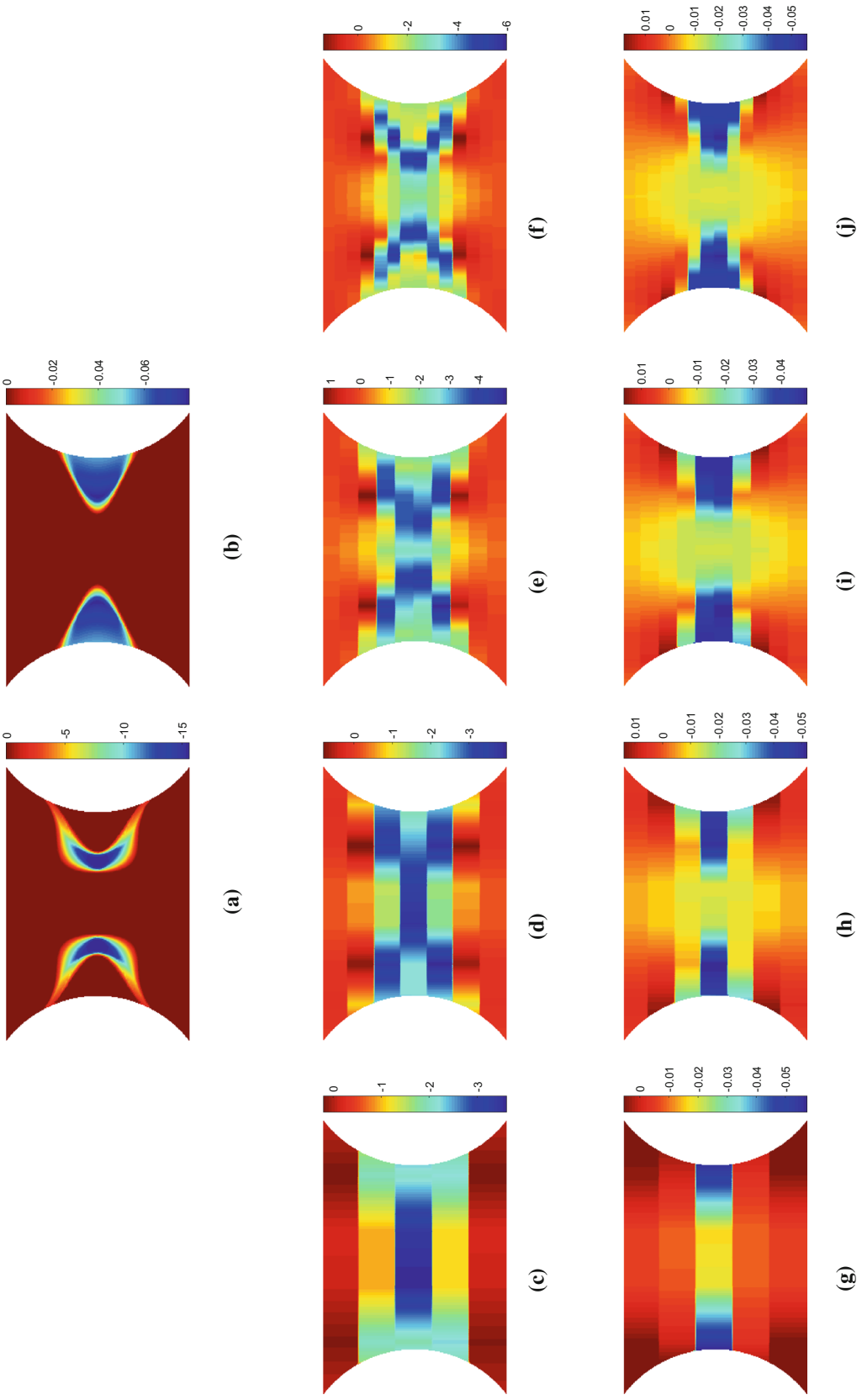

Fig. 7 Maps of the sensitivity based optimised virtual fields (virtual strains) for the linear hardening model for different virtual mesh sizes: **c**, **g** 5×5, **d**, **h** 7×7, **e**, **i** 10×10 and **f**, **j** 14×14. For comparison, **a**–**b** show the incremental stress sensitivities, $\delta\widetilde{\sigma}_{22}^{(\sigma_0)}$ and $\delta\widetilde{\sigma}_{22}^{(H)}$, respectively

Comput Mech (2017) 60:409–431

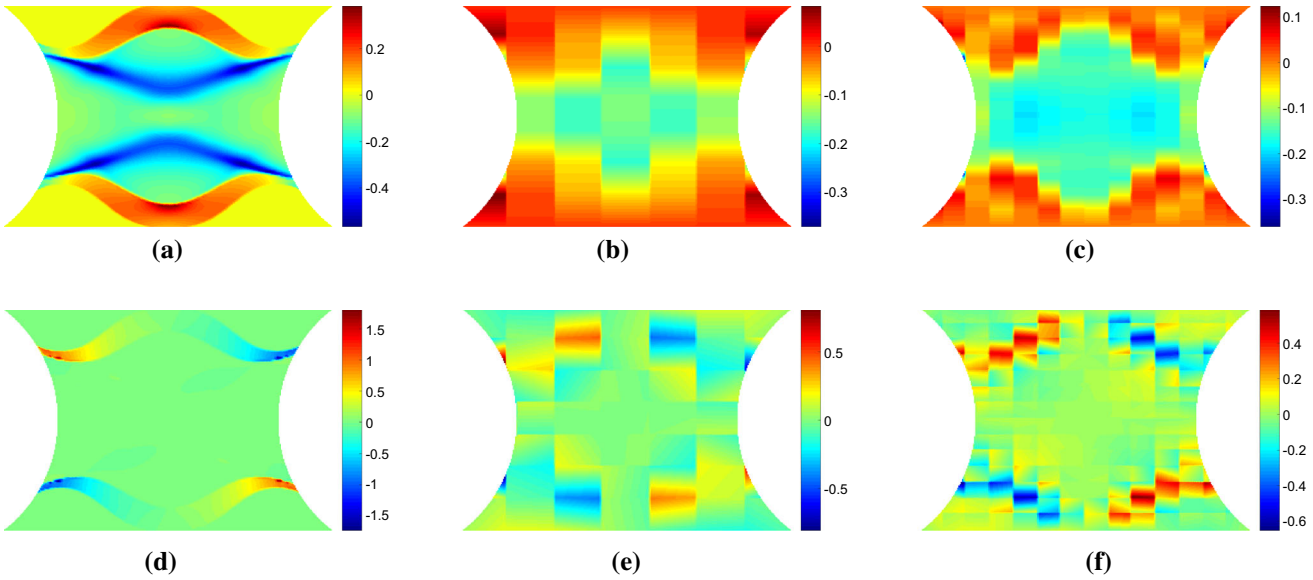

Fig. 8 Maps of **a** $\delta\widetilde{\sigma}_{11}^{(\sigma_0)}$ and **c** $\delta\widetilde{\sigma}_{12}^{(\sigma_0)}$ the incremental stress sensitivity to the yield stress for the linear hardening model. The calculated virtual strains using the sensitivity based virtual fields **b**–**c** ε_{11}^* and **e**–**f** ε_{12}^* for using a (b,e) 7×7 and **c**, **f** 14×14 virtual mesh. The maps correspond to a vertical displacement of 0.060 mm and a resultant force of 1085 N

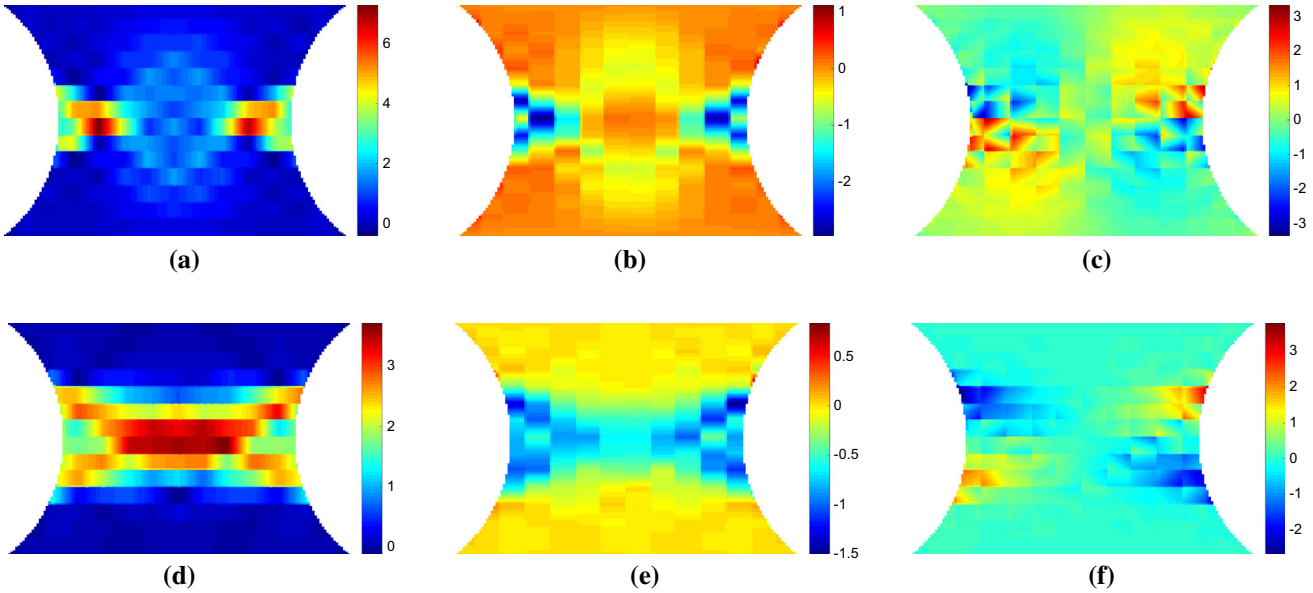

Fig. 9 Virtual fields obtained for the stiffness-based optimised virtual fields (14×14) for the linear hardening model at two different time steps. The *top row* of maps **a**–**c** are for displacement of 0.039 mm which corresponds to a resultant vertical force of 1011 N. The *lower row* of maps **d**–**f** are for a displacement of 0.060 mm which corresponds to a resultant vertical force of 1085 N

5.2 Construction of stiffness-based optimised virtual fields

The stiffness-based optimised virtual fields were found using the method described in "Appendix 2". Only a single set of virtual fields, $\varepsilon^* = [\varepsilon_{11}^*, \varepsilon_{22}^*, 2\varepsilon_{12}^*]$, are calculated at each time step when using the stiffness-based virtual fields. This differs from the sensitivity-based procedure which produces a set of virtual fields for each model parameter. The stiffness-based virtual fields are shown in Fig. 9 for the linear hardening model and a 14×14 virtual mesh. The stiffness-based optimised virtual fields display a chequered pattern which is due to the instability of reduced integration bilinear quadrilateral elements. Employing full integration elements

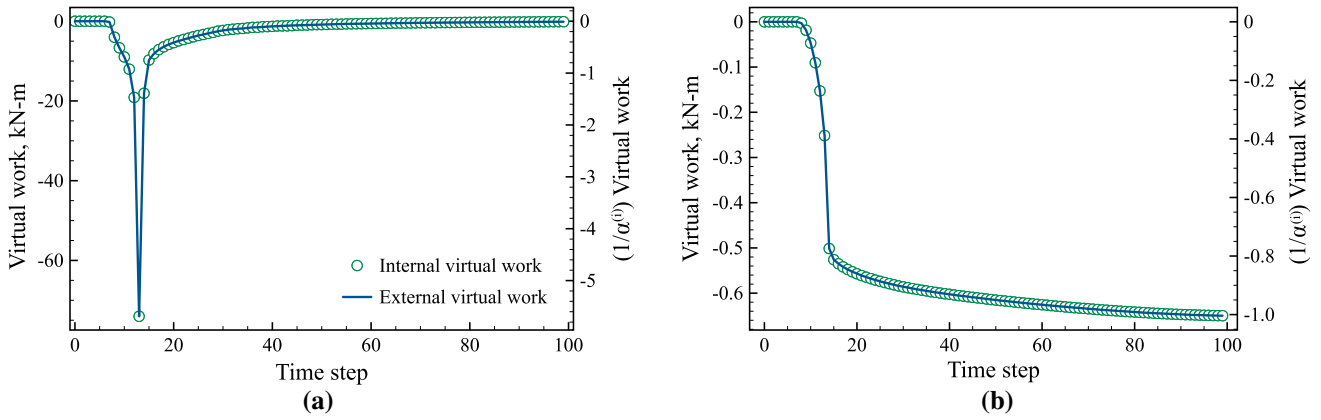

Fig. 10 Evolution of internal (◯) and external (*blue line*) virtual work for the virtual fields for the **a** yield stress and **b** hardening modulus. The *y-axis* on the *left* is unscaled while the *y-axis* on the *right* has been scaled by $\alpha^{(i)}$. (Color figure online)

would remove the chequered pattern at the cost of interpolating the strain at the Gauss points. The full integration approach has been tested and the obtained results were consistent with the ones generated with the reduced integration approach, proving that the pattern does not have a detrimental influence on the identification process here. The shapes of the stiffness-based virtual fields, ε^*_{11}, appear to follow the shapes of the equivalent plastic strain maps (Fig. 3a, d). There does not appear to be any noticeable similarities between the sensitivity-based and stiffness-based virtual fields, indicating the each procedure focuses the identification on different regions.

5.3 Validation on simulated data: linear hardening

The simulated data obtained from the finite element model was used to validate the approach for the linear hardening model. Firstly, the evolution of the internal and external virtual work with respect to time has been investigated to examine the time scale when each parameter is active. Secondly, the sensitivity-based, stiffness-based, and uniform virtual fields were used to identify the linear hardening parameters, σ_0 and H, from the simulated data. Then, noise was added to the strain data to simulate experimental conditions and all three kinds of virtual fields were again used to identify the two model parameters. Finally, the influence of the virtual mesh density on the identified parameters has been evaluated. In this study, the identification of elastic parameters has been ignored as it can be done using only elastic loading with the linear VFM [1], effectively reducing computational effort in minimising the cost function.

5.3.1 Evolution of the internal and external virtual work

To examine the time steps when each parameter is active, the internal virtual work was calculated for each parameter using Eq. 9. Figures 10a, b show the internal and external virtual work for the yield stress and hardening modulus, respectively. The magnitude and shape of the curves for the yield stress and hardening modulus are clearly different. The internal and external virtual work for both the yield stress and hardening modulus remain at zero for the first 9 steps corresponding to elastic loading, hence completely filtering out the elastic part of the test from the cost function. Then at time step 10, which corresponds to the onset of plasticity at the notches, the virtual work starts to increase from zero as expected. The internal virtual work for the yield stress quickly peaks at the 15th time step, which corresponds to the plastic zone spreading across the whole specimen and then decays back to zero. In contrast, the internal virtual work for the hardening modulus continuously increases throughout the test. The magnitude of the internal virtual work for the yield stress and hardening modulus are also markedly different. To properly identify the model parameters using Eq. 8, the virtual work is scaled by $\alpha^{(i)}$ using the 15 highest IVW values to ensure that the contributions of each parameter to the cost function are of the same order. The y-axis on the right hand side of Fig. 10 shows the scaled values for both the internal and external virtual work. Although not backed by any physical argument, the scaling method employed here was proven to be successful as shown in Sect. 5.4.5, where it was found that the number of time steps taken for computing $\alpha^{(i)}$ has minor effect on the identification errors.

5.3.2 Identification without noise

To identify the linear hardening parameters, σ_0 and H, the cost function given in Eq. 8 was minimized using the built in MatLab (v. 6.14b) function *fmincon* and the SQP (Sequential Quadratic Programming) algorithm. The model parameters were constrained to be greater than zero. This restriction was imposed to ensure that the material response was physi-

Comput Mech (2017) 60:409–431 421

Table 2 Identified parameters for the linear hardening model using exact data

	σ_0/σ_0^{ref}	H/H^{ref}
Uniform	1.003	0.994
Stiffness	0.998	0.998
Sensitivity	1.000	1.001

cally reasonable for the steel being studied. The initial guess supplied to the minimization function was generated with a random number generator. To verify that the set of identified material parameters represented a global minimum, 15 different starting points were tried. Since the same set of parameters were consistently obtained independent of the initial guess, the identified parameters were assumed to be the global minimum. The results obtained with the uniform, stiffness-based, and sensitivity-based virtual fields are presented in Table 2. 7×7 and 14×14 virtual meshes were used for the sensitivity-based and stiffness-based virtual fields, respectively; it should be noted that finer meshes are required for the stiffness-based virtual fields as described in Sect. 3.3. All methods accurately identified the model parameters since the principle of virtual work is satisfied exactly on perfect (noise-free) data. This verifies that all three virtual field types were implemented correctly, leading to an identification error smaller than 1% in Table 2. The virtual mesh density for the sensitivity-based virtual fields was varied from 5×5 to 14×14 and no change was observed in the identified model parameters.

5.3.3 Identification with noise

The parameters for the linear hardening model were also identified using noisy data. Gaussian white noise with a standard deviation of 150 $\mu\epsilon$ was added to strain data obtained from the finite element simulation. This level of noise represents what is expected in a well designed and conducted experiment. It should be emphasized that this is only a first approach to noise propagation simulation. Recent studies [24,27] have shown that an image deformation procedure needs to be employed to realistically simulate both systematic and random errors. However, this procedure is more computationally extensive and has so far only been applied to linear elasticity. This approach will be investigated in the future for elasto-plastic identification and a simpler noise study has been employed here. It is thought however that this simplified procedure will be enough to get a first idea about the relative stability of the different virtual fields to noise. As the radial-return algorithm employed here for stress calculation uses strain increments rather than total strain, it is worth comparing the magnitude of the noise to that of the average strain increment. For the strain in the loading direction, ε_{22}, the mean value of strain increment after yielding is 165 $\mu\epsilon$, making the effective signal-to-noise ratio approximately 1.1. Effectively, such high noise can produce spurious elastic unloadings which were shown to heavily influence the cost function and amplify the identification error significantly [15]. In order to increase the signal-to-noise ratio, the number of time steps can be reduced by only using data from every nth time step to increase the strain increment between consecutive frames. This procedure effectively increases the signal-to-noise ratio (due to the rate nature of the plasticity equations). In practice, more images means that temporal smoothing can indeed be used to further increase the signal-to-noise ratio. Moreover, if too few steps are used, then the radial return algorithm will generate stress reconstruction errors so a compromise has to be found. In this paper four different total time steps were tested, 100, 50, 33, and 25, resulting in an effective signal-to-noise ratio of 1.1, 2.1, 3.2, and 4.3, respectively. Although increasing the strain increment can lead to errors in the radial return algorithm, using the simulated data there was found to be a less than 0.1% difference between the stresses predicted using 100 and 25 time steps. Similar to the case without noise, the identification was repeated 15 times and the same parameters were identified independently from the initial guesses. In order to estimate both random and systematic errors, 30 different copies of noise were added to the simulated data. The mean value and the coefficient of variation of the identified parameters for the uniform, stiffness-based, and sensitivity-based virtual fields are given in Table 3 where a virtual mesh size of 7×7 and 14×14 was implemented for the sensitivity-based and stiffness-based virtual fields, respectively.

Table 3 Identified parameters for linear hardening model using noisy data

	Time Steps	Signal-to-noise ratio	σ_0/σ_0^{ref}	H/H^{ref}
Uniform	100	1.1	$1.137 \pm 0.0076\%$	0
	50	2.1	$1.013 \pm 0.031\%$	$1.346 \pm 0.49\%$
	33	3.2	$1.022 \pm 0.024\%$	$0.967 \pm 0.23\%$
	25	4.3	$1.019 \pm 0.024\%$	$0.944 \pm 0.20\%$
Stiffness	100	1.1	$1.140 \pm 0.010\%$	0
	50	2.1	$0.987 \pm 0.041\%$	$1.351 \pm 0.52\%$
	33	3.2	$1.003 \pm 0.013\%$	$1.023 \pm 0.11\%$
	25	4.3	$1.004 \pm 0.015\%$	$1.003 \pm 0.085\%$
Sensitivity	100	1.1	$1.037 \pm 0.26\%$	$1.254 \pm 13\%$
	50	2.1	$1.022 \pm 0.073\%$	$0.999 \pm 1.3\%$
	33	3.2	$1.014 \pm 0.025\%$	$0.994 \pm 0.21\%$
	25	4.3	$1.012 \pm 0.027\%$	$0.978 \pm 0.21\%$

As the signal-to-noise ratio of the strain increment increases with a smaller number of time steps, the accuracy

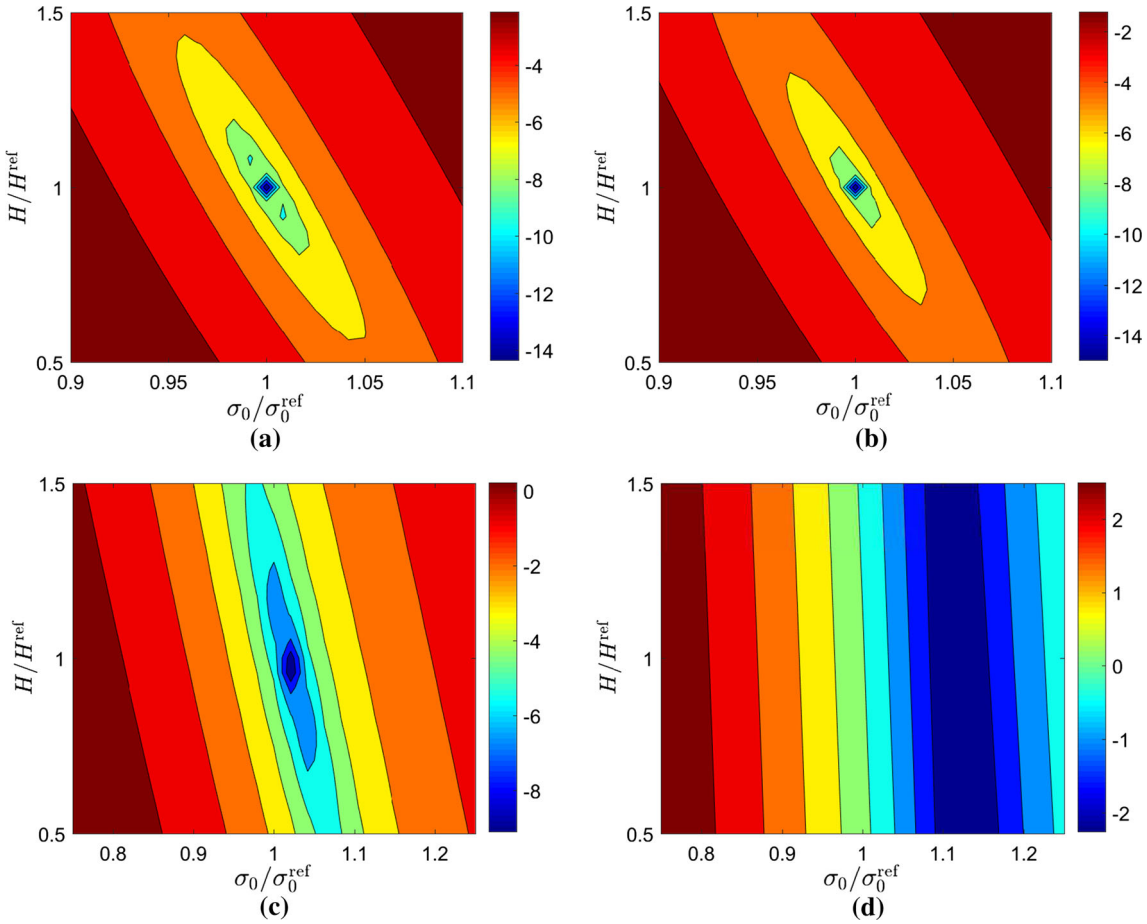

Fig. 11 Plots of the cost functions obtained for the linear hardening model using Eq. 11 and uniform virtual fields (Eq. 10). The *upper row* **a**–**b** corresponds to **a** 33 time steps and **b** 100 time steps for perfect data. The *lower row* **c**–**d** corresponds to **c** 33 time steps and **d** 100 time steps for noisy data. Note that the log of the cost function is plotted to better illustrate the minimum

of the identification increases for all methods. Decreasing from 33 to 25 time steps worsens the accuracy of the identification for the hardening modulus indicating that there is insufficient temporal resolution. Notably, from 50 time steps downwards, the yield stress is accurately identified with all methods. The sensitivity-based virtual fields are able to identify the hardening modulus using 50 steps, which corresponds to a signal-to-noise ratio of 2.1. However the other methods struggle to identify H at signal-to-noise levels below 3.2 (33 time steps). Using all 100 time steps, the lower bound of the optimization algorithm was reached for the uniform and stiffness-based virtual fields resulting in $H = 0$. The zero value for H is compensated for by overestimated σ_0 values. As the signal-to-noise ratio increases, the random error consistently increases as well for every virtual field. The reduction in the number time steps likely causes this increase in random error; the reduction in time steps makes the identification mores susceptible to noise which results in increased random error.

The influence of noise on the cost function can be seen in Figs. 11 and 12 for the uniform virtual field. For exact data (Fig. 11a, b) there is a clear minimum which does not depend on the number of time steps used, supporting the fact that the identified value is the global minimum. When the signal-to-noise ratio is high (low number of time steps) the cost function is not appreciably changed by the addition of noise (Fig. 11a, c). For a smaller signal-to-noise ratio (Fig. 11d), a valley with little sensitivity to hardening modulus was formed. A similar behaviour is observed for the sensitivity-based virtual fields (Fig. 12), though the minimum for H is slightly closer to the expected value.

5.3.4 Sensitivity to the virtual mesh size

As described earlier, the size of the virtual mesh influences how well the virtual strains match the incremental stress sensitivity maps. To determine if the mesh density influences the identification results, three additional mesh densities were tested: 5×5, 10×10, and 14×14. The identification pro-

Comput Mech (2017) 60:409–431

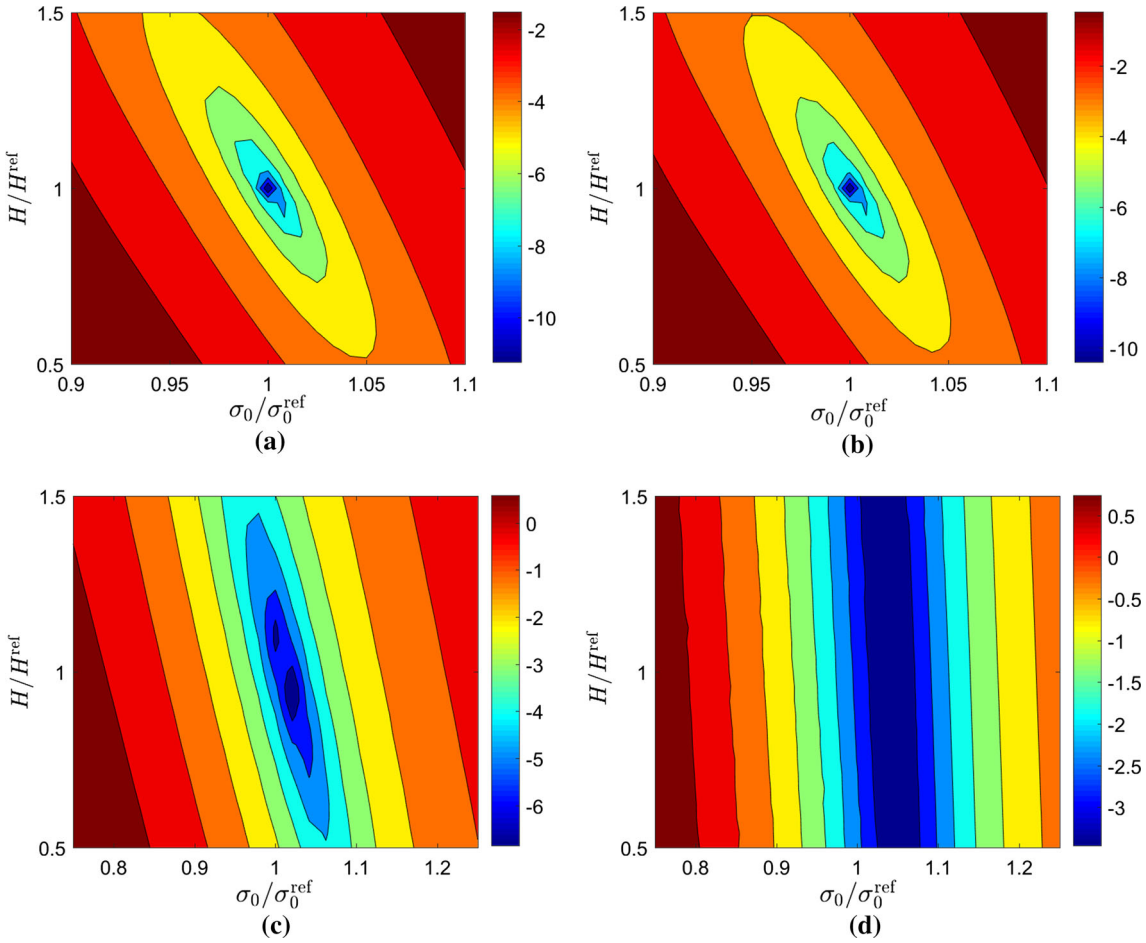

Fig. 12 Plots of the cost functions obtained for the linear hardening model using Eq. 11 and sensitivity-based virtual fields. The *upper row* **a**–**b** corresponds to **a** 33 time steps and **b** 100 time steps for perfect data. The *lower row* **c**–**d** corresponds to **c** 33 time steps and **d** 100 time steps for noisy data. Note that the log of the cost function is plotted to better illustrate the minimum

Table 4 Study of the influence of the mesh size on the identified parameters of the linear hardening law using sensitivity-based virtual fields

Virtual mesh	σ_y/σ_y^{ref}	H/H^{ref}
5×5	$1.014 \pm 0.027\%$	$0.994 \pm 0.23\%$
7×7	$1.014 \pm 0.025\%$	$0.994 \pm 0.21\%$
10×10	$1.013 \pm 0.025\%$	$0.993 \pm 0.21\%$
14×14	$1.013 \pm 0.023\%$	$0.992 \pm 0.19\%$

cedure was run 30 times, each time with a different copy of noise. The mean and coefficient of variation of the parameters are reported in Table 4. The mesh density does not have a significant influence on the mean value of H or σ_0. The coefficient of variation slightly decreases with increasing mesh density. The accurate identification of H and σ_0 also proves that the differences between the incremental stress sensitivity and the derived virtual fields observed in Figs. 8 and 7 do not impact the identification procedure. This is a very positive outcome as a strong virtual mesh sensitivity would have required mesh density optimization.

5.4 Validation on simulated data: Voce hardening

The Voce hardening model was also considered to determine how increasing the complexity of the constitutive relationship would influence the inverse parameter identification. Based on the sensitivity study discussed at the end of this section, a virtual mesh of 14×14 was used and the perturbation and scaling parameters were fixed to $\delta X_i = -0.10 X_i$ and 30% of the highest IVW terms (Eq. 9).

5.4.1 Evolution of the internal and external virtual work

The internal virtual work (Eq. 9) was used to identify when each parameter was active (Fig. 13). The three parameters, σ_0, R_{inf}, and b, that describe the onset of yielding were active

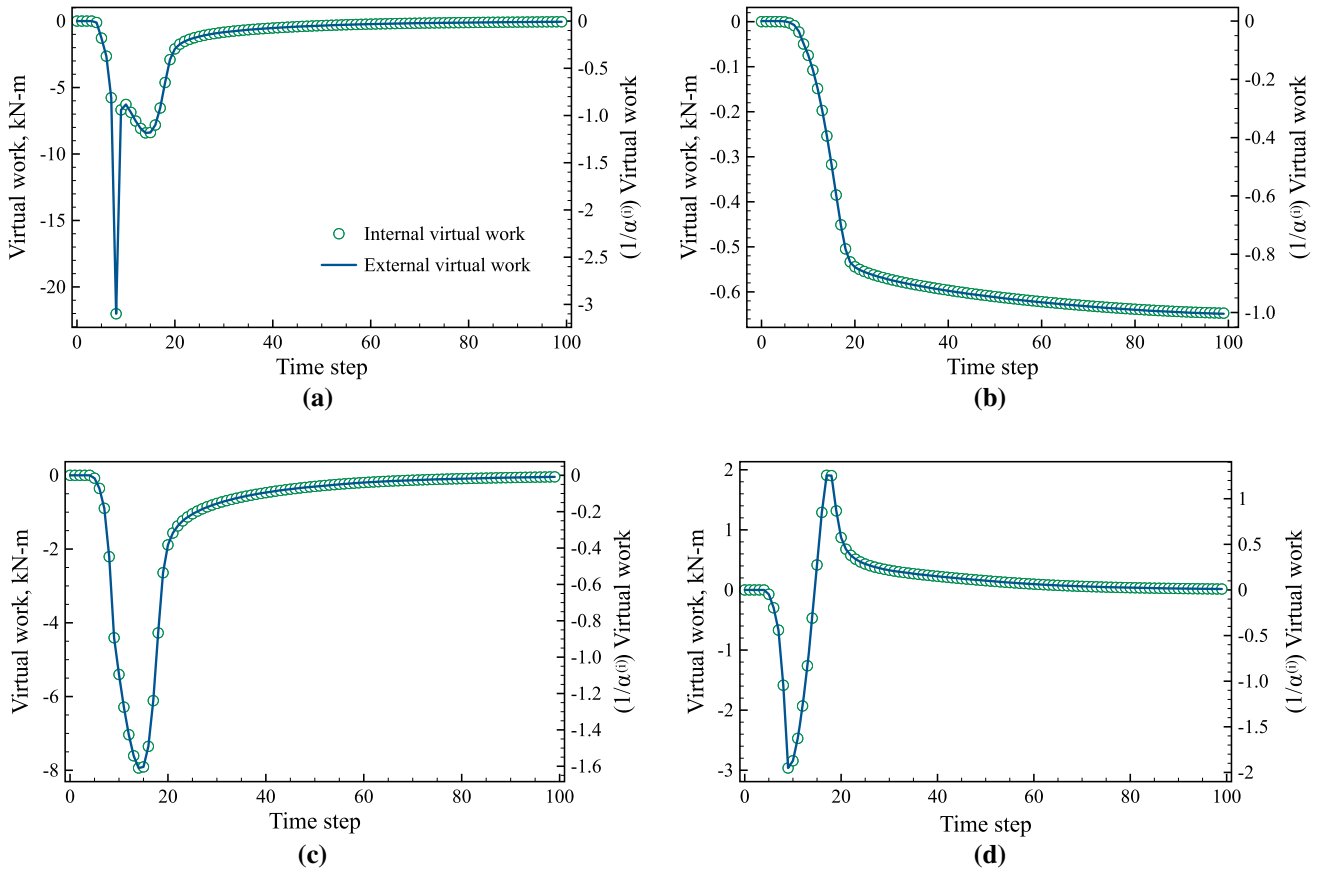

Fig. 13 Evolution of internal (◯) and external (*blue line*) virtual work, respectively for the sensitivity-based virtual fields for **a** σ_0, **b** R_0, **c** R_{inf}, and (d) b. The *y-axis* for each parameter has been scaled by $\alpha^{(i)}$. (Color figure online)

from time steps 7 to 30. The hardening parameter, R_0, also became active at time step 7 but continued to grow until the test ended. The graphs in Fig. 13 have two y-axes, the left-hand axis shows the unscaled values while the right-hand axis has been scaled by $\alpha^{(i)}$ which is the mean of the 30% highest values of the IVW terms.

5.4.2 Identification without noise

The parameters were identified using the same procedure outlined for linear hardening in Sect. 5.3.2. Again all of the model parameters were constrained to be positive. In addition, the hardening parameter, R_0, was constrained such that $R_0 \geq 1000$ MPa in order to narrow the search region. The results obtained for all types of virtual fields, with the same 14×14 virtual mesh for both the sensitivity-based and stiffness-based virtual fields, are shown in Table 5. All of the methods are clearly capable of identifying the model parameters well. It should be noted that parameters σ_0 and R_{inf} are distinguishable only at the onset of plasticity. After some plastic deformation is accumulated, it is the combined value, $Y = \sigma_0 + R_{\text{inf}}$, that influences the cost function. This enables the values of σ_0 and R_{inf} to compensate for one another and as a result, the simulated data mainly contains information about Y and limited data about σ_0 and R_{inf} individually.

Table 5 Identified parameters of the Voce hardening model using exact data

	σ_0/σ_0^{ref}	R_0/R_0^{ref}	$R_{\text{inf}}/R_{\text{inf}}^{ref}$	b/b^{ref}	Y/Y^{ref}
Uniform	1.001	1.000	1.000	1.000	1.000
Stiffness	1.002	1.002	0.997	1.008	1.000
Sensitivity	1.002	1.000	0.998	0.997	1.001

The cost function for the Voce model with exact data is shown in Fig. 14. Since this model has 4 parameters, the cost function is situated in a 4-dimensional space. To visualize the cost function several planes were cut through the cost function. In Fig. 14, six plots showing the interaction between pairs of parameters are reported. In each case, an elongated locus with a unique minimum is observed. The plot of σ_0 vs R_{inf} (Fig. 14b) indicates that there is a strong correlation between the two parameters, represented by the open valley inclined at an angle close to 45°. Both σ_0 and R_{inf} show minimal dependence on b as shown in Fig. 14c, f with open valleys aligned with reference values of the yielding param-

Comput Mech (2017) 60:409–431

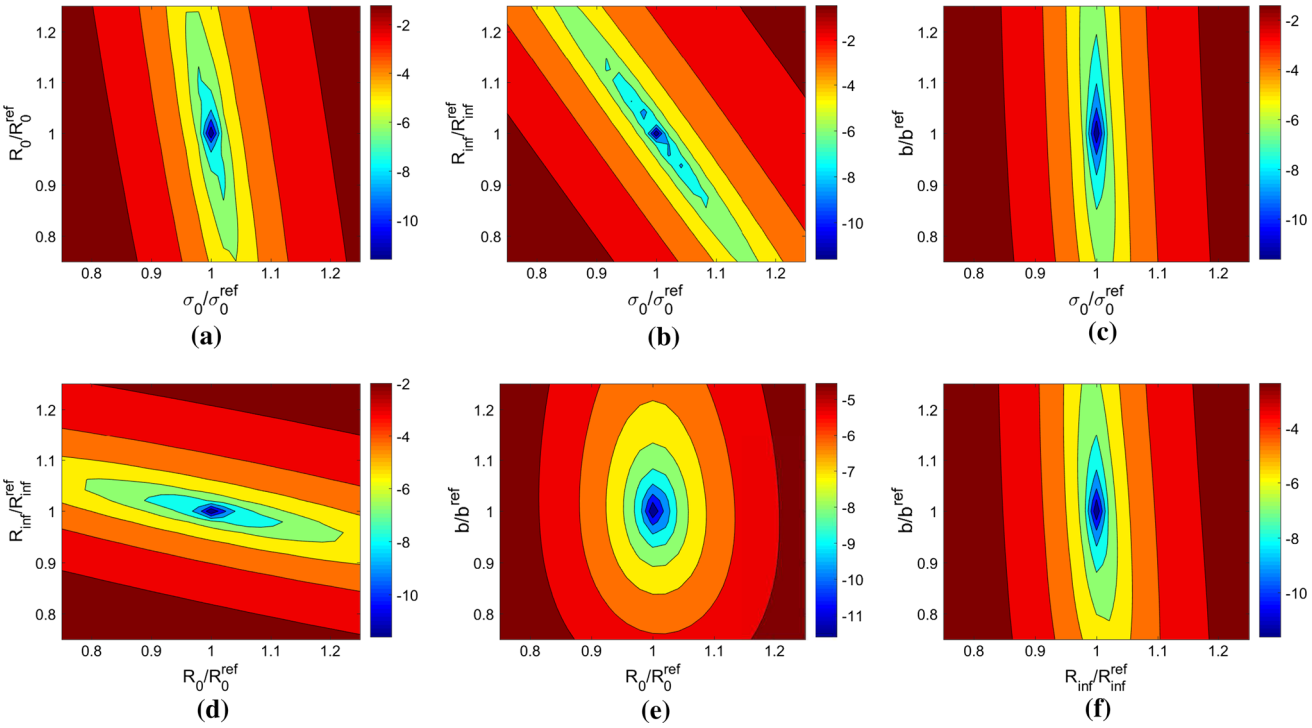

Fig. 14 Cuts through a cost function for Voce model with sensitivity-based virtual fields obtained with exact data and 33 time steps. The *plots* show interaction between pairs of parameters: **a** $\sigma_0 - R_0$, **b** $\sigma_0 - R_{inf}$, **c** $\sigma_0 - b$, **d** $R_0 - R_{inf}$, **e** $R_0 - b$, (f) $R_{inf} - b$. Note that the log of the cost function is *plotted* to better illustrate the minimum

eters. There is however a very well defined minimum on the $R_0 - b$ cut (Fig. 14e), suggesting that the b parameter is found because of this interaction.

5.4.3 Identification with noise

To test the ability of the different virtual fields to minimize the influence of noise, Gaussian noise with a standard deviation of 150 $\mu\epsilon$ was added to the finite element strains. Based on the identification of the linear hardening parameters, only 50, 33, and 25 time steps were used to perform the identification resulting in a signal-to-noise ratio of approximately 2.2, 3.3, and 4.4, respectively. The minimization program was run 15 times varying the initial guess. This time, the different starting points resulted in different sets of identified parameters, so the set of parameters that produced the lowest value of the cost function was taken as the global minimum. This process was repeated 30 times with different copies of noise. Thus far, the incremental stress sensitivity maps have been used to generate the virtual fields, however it is also possible to use Eq. 5 to construct the stress-sensitivity virtual fields. The mean and coefficient of variation of the parameters identified using the noisy data are given in Table 6. It should be noted that for the stress-sensitivity virtual fields only 33 time steps were used.

For the uniform virtual field, the lower bound for R_0 was frequently reached for 50 and 33 time steps ($R_0/R_0^{ref} = 1000/3170 = 0.316$). In fact, the coefficient of variation of R_0 for 33 time steps is zero because the lower bound of the minimization routine was reached with every copy of noise. The sensitivity-based and stiffness-based virtual fields clearly out-perform the uniform virtual fields, most notably for R_0 and b. For the more complex Voce model, the uniform virtual fields struggled to identify the yield stress, σ_0, linear hardening modulus, R_0, and the non-linear yield parameter, b even for high signal-to-noise ratios. The stress-sensitivity virtual fields significantly overestimate σ_0 and b and underestimate of R_{inf}. However the hardening modulus, R_0, is well identified. Since the history dependence has not been removed from the stress-sensitivity virtual fields, the later stages of the test are given a much larger weight and as a result, the stress-sensitivity virtual fields do not identify the yielding parameters well.

To visualize the difference between the parameters in Table 6, the stress–strain curves that would be obtained using the parameters for 33 time steps are shown in Fig. 15. The parameters identified using the sensitivity-based, stress-sensitivity, and stiffness-based virtual fields all produce stress–strain curves that closely follow the reference curve ($R^2 = 0.99$). In Table 6, the uniform and stress-sensitivity virtual fields over-estimate the yield stress and the higher

Table 6 Identified parameters for the Voce hardening model using noisy data

Virtual fields	Time steps	σ_0/σ_0^{ref}	R_0/R_0^{ref}	R_{inf}/R_{inf}^{ref}	b/b^{ref}	Y/Y^{ref}
Uniform	50	$1.218 \pm 0.35\%$	$0.319 \pm 1.8\%$	$1.141 \pm 1.1\%$	$0.332 \pm 0.32\%$	$1.188 \pm 0.27\%$
	33	$1.252 \pm 0.29\%$	0.316 ± 0	$0.988 \pm 0.47\%$	$0.287 \pm 0.23\%$	$1.148 \pm 0.021\%$
	25	$1.234 \pm 0.47\%$	$0.470 \pm 0.78\%$	$0.921 \pm 0.83\%$	$0.328 \pm 0.45\%$	$1.110 \pm 0.12\%$
Stiffness	50	$0.954 \pm 0.76\%$	$1.371 \pm 0.34\%$	$1.035 \pm 1.2\%$	$1.545 \pm 1.4\%$	$0.986 \pm 0.027\%$
	33	$1.072 \pm 0.30\%$	$1.024 \pm 0.10\%$	$0.905 \pm 0.44\%$	$0.971 \pm 0.88\%$	$1.006 \pm 0.020\%$
	25	$1.076 \pm 0.59\%$	$1.007 \pm 0.059\%$	$0.897 \pm 0.86\%$	$0.948 \pm 1.0\%$	$1.005 \pm 0.020\%$
(Incremental) sensitivity	50	$1.102 \pm 2.2\%$	$1.070 \pm 7.3\%$	$0.893 \pm 2.7\%$	$0.949 \pm 8.1\%$	$1.019 \pm 0.54\%$
	33	$1.060 \pm 3.1\%$	$1.012 \pm 2.9\%$	$0.939 \pm 4.0\%$	$0.976 \pm 9.0\%$	$1.013 \pm 0.34\%$
	25	$1.054 \pm 0.77\%$	$1.005 \pm 0.26\%$	$0.941 \pm 1.2\%$	$0.968 \pm 1.4\%$	$1.009 \pm 0.037\%$
Stress sensitivity	33	$1.377 \pm 2.4\%$	$0.921 \pm 9.0\%$	$0.501 \pm 0.33\%$	$1.563 \pm 57\%$	$1.031 \pm 1.4\%$

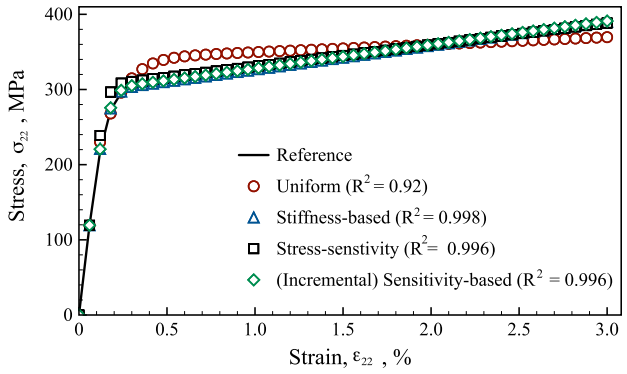

Fig. 15 Stress–strain curve obtained with parameters identified in Table 6 for 33 time steps

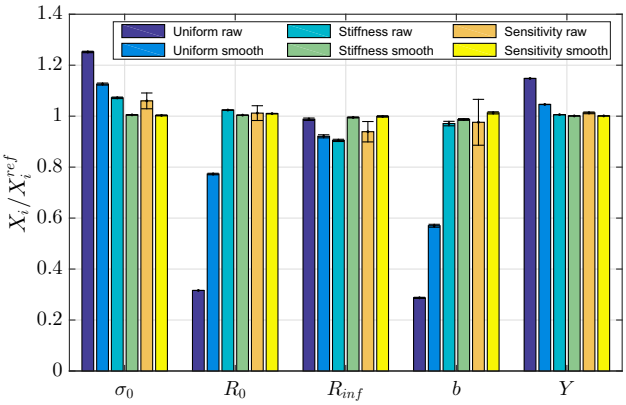

Fig. 16 Comparison of mean values of identified parameters using different VFs over 30 copies of noise. The uncertainty *bars* represents one standard deviation

yield stresses are clearly visible in Fig. 15. While for the uniform virtual field the overestimated yield stress was paired with an underestimated hardening modulus, the stress-sensitivity virtual fields overestimate the yield stress and capture the hardening response. However. this mis-identification of the model parameters for the stress-sensitivity virtual fields does not appear to impair the ability to follow the reference stress–strain curve. In fact, except at the onset of yield; the stress-sensitivity virtual fields generated data, closely follow the incremental stress-sensitivity one.

Typically, to minimize the influence of noise, some form of temporal smoothing would be used on the measured displacement, especially when plasticity occurs since the noise can cause spurious elastic unloading [15]. To determine what effect temporal smoothing would have on the identification, the full data set using all 100 points was smoothed with a simple moving average over a window of five data points. The data was then reduced to 33 points by keeping only every third smoothed data point. Using this temporally smoothed data set, the identification was repeated 30 times to determine the mean and standard deviation of the identified parameters. In Fig. 16, the results for data that has been temporally smoothed is compared with unsmoothed noisy data. The identification using the uniform virtual fields is improved significantly. The parameters for the stiffness-based and sensitivity-based virtual fields are all within 1.5% of the reference values.

5.4.4 Sensitivity to the virtual mesh size

To ensure that the mesh density had a minimal impact on the identification, three additional virtual mesh densities were tested: 5×5, 7×7, and 10×10. Table 7 reports the mean and coefficient of variation obtained for each of the parameters when the identification was run 30 times with different copies of noise. Similar to the results obtained for the linear hardening model, the mesh density did not affect the mean value of the identified parameters but increasing the mesh density tended to cause the random error to slightly decrease.

Comput Mech (2017) 60:409–431

Table 7 Influence of virtual mesh size on identified parameters for Voce model

Mesh	σ_0/σ_0^{ref}	R_0/R_0^{ref}	R_{inf}/R_{inf}^{ref}	b/b^{ref}	Y/Y^{ref}
5×5	$1.094 \pm 4.0\%$	$1.064 \pm 4.7\%$	$0.887 \pm 5.3\%$	$0.920 \pm 13\%$	$1.012 \pm 0.60\%$
7×7	$1.109 \pm 3.8\%$	$1.042 \pm 5.0\%$	$0.864 \pm 5.4\%$	$0.873 \pm 11\%$	$1.012 \pm 0.60\%$
10×10	$1.089 \pm 3.3\%$	$1.042 \pm 3.0\%$	$0.889 \pm 4.4\%$	$0.935 \pm 11\%$	$1.010 \pm 0.40\%$
14×14	$1.090 \pm 2.8\%$	$1.041 \pm 3.6\%$	$0.886 \pm 3.9\%$	$0.926 \pm 7.2\%$	$1.009 \pm 0.40\%$

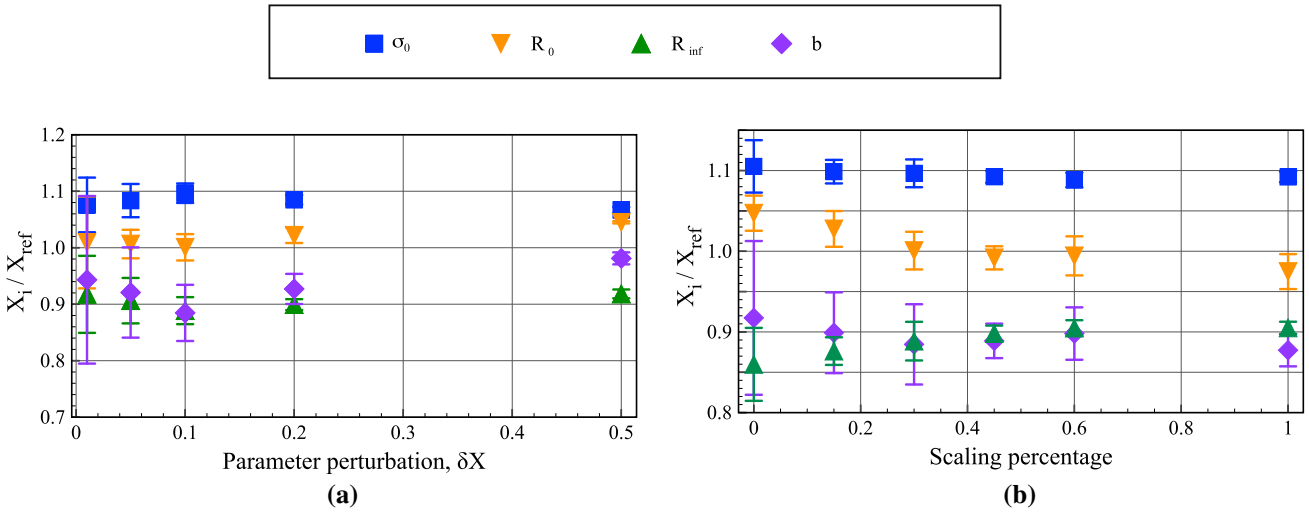

Fig. 17 Relative error on the identification versus the implemented **a** perturbation parameter and **b** scaling percentage. The *error bars* show one standard deviation

5.4.5 Sensitivity to reconstruction parameters

The proposed method includes two parameters that must be selected, the perturbation, δX_i, and the scaling parameter, $\alpha^{(i)}$. The perturbation will influence the stress sensitivity and its reconstruction while the scaling will directly influence the cost function (Eq. 8). For the Voce model results, the perturbation and scaling parameters were fixed to $\delta X_i = -0.10 X_i$ and 30% of the highest IVW terms (Eq. 9), respectively. The effect of both these parameters on the quality of identification was studied on a noisy data set with 33 time steps. The mean and standard deviation for the four model parameters were identified by running the identification 30 times with different copies of noise.

To study the influence of the perturbation, δX_i, a virtual mesh of 14×14 and a scaling parameter of 30% were used. A fine mesh was implemented because smaller virtual elements are needed to capture the fine features and high gradients that would be produced as the perturbation shrinks. Five different values were tested: 0.01, 0.05, 0.1, 0.2 and 0.5. In Fig. 17a the results are presented showing how the identified value of each model parameter varied as a function of the perturbation parameter. The random error on the identification drastically decreases as the perturbation parameter is increased. As the perturbation increases so does the error on the hardening modulus, R_0. The best compromise for the perturbation parameter appears to be 10%, after which the bias on R_0 increases. However, the sensitivity of this parameter is rather small, which is an important feature for the procedure as one would not want the results to be highly affected by the users choice of the perturbation parameter.

The full range of the scaling parameter, $\alpha^{(i)}$, was also investigated using a virtual mesh of 14×14 and a perturbation of 0.10. For the two extreme cases of 0 and 100%, the cost function was scaled by the maximum and mean of the internal virtual work, respectively. In addition, 6 other scaling parameters were also tested, the mean of the highest 10, 15, 20, 30, 45, and 75% of the IVW terms. The results are shown in Fig. 17b. The scaling has a minimal effect on σ_0. The remaining parameters show modest changes of approximately 5% on the mean identified value with the largest variation observed in the hardening modulus, R_0. The optimum scaling parameter appears to be 45% where the random error and bias for all of the parameters is the lowest.

6 Conclusions

In this manuscript, a new set of virtual fields for non-linear constitutive models has been proposed. These virtual fields are formed using incremental stress sensitivity maps to locate the areas and times when each constitutive parameter has the

most impact on the stress. The feasibility of the sensitivity-based virtual fields was tested for small strain plasticity implementing two different hardening laws: linear and Voce. However, the sensitivity-based virtual fields could be broadly implemented for any non-linear constitutive model. The sensitivity-based virtual fields were consistently able to identify the plastic model parameters even for low signal-to-noise ratios (Tables 3 and 6), indicating their ability to smooth out the influence of noise on the parameter identification. While the incremental stress sensitivity virtual fields consistently performed well, the stress-sensitivity based virtual fields failed to accurately identify the parameters. The results obtained with the sensitivity-based virtual fields were also compared with stiffness-based and manually defined uniform virtual fields and the sensitivity-based virtual fields were found to outperform the two alternatives, even though the stiffness-based fields also showed good stability to noise.

The sensitivity-based virtual fields provide a general approach to automatically generate high quality virtual fields for non-linear VFM problems. An open question remains concerning the high random error exhibited by sensitivity-based virtual fields when raw data was used. One possible explanation is that the virtual fields select only 'active' zones in the specimen and filter out the remaining data which makes the identification very sensitive to the noise pattern. This possibility is further supported by observation that the random error drops drastically when the perturbation δX is increased. For the yield-related parameters, the perturbation simply controls the width of the zone around the yield front. Nevertheless, in real experiment, some temporal smoothing would be introduced which reduces the random error to levels exhibited by the other virtual fields as shown in Fig. 16.

The implementation of the sensitivity-based virtual fields also has several limitations which need to be discussed. First, for the identification of the Voce parameters from noisy data, the minimisation routine did not always converge to the global minimum. By running the minimisation 15 times with different starting points, it was possible to identify a global minimum. However, running the optimisation multiple times significantly increased the computational time required to determine the parameters. When applying this technique to other constitutive models, appropriate care is needed to ensure that the global minimum is identified.

In addition, the determination of the sensitivity-based virtual fields requires the user to select an appropriate virtual mesh size and the two reconstruction parameters: the perturbation, δX_i and the scaling parameter, $\alpha^{(i)}$. For both linear and Voce models, increasing the virtual mesh size only marginally improves the quality of the identification (Tables 4 and 7). The factor limiting the maximum size of the virtual mesh is the available computer memory which is needed to calculate the pseudo-inverse of the modified global strain-displacement matrix, $\overline{\mathbf{B}}$, in Eq. 7. On a computer with 4 GB of RAM, the maximum virtual mesh size that could be used was 20×20 for a system that includes 17,000 measurement points. For the Voce model, the choice of the perturbation parameter did not have any significant influence on the mean identified values but had a minor influence on the random error (Fig. 17a). The value of the scaling parameter did influence the mean value particularly for the parameters with limited sensitivity (i.e. b, R_{inf}) as seen in Fig. 17b. To implement these sensitivity-based virtual fields, it will be necessary to perform a sensitivity study using simulated data to identify an optimum set of parameters prior to implementing it on experimental data. It is expected however that in the future, when more experience has been gained on different models and test geometries, guidelines can be produced as to the choice of these parameters to avoid searching for appropriate values.

The primary advantage of the virtual fields method over finite element model updating is its computational efficiency. Using a standard PC with an Intel Core i5 processor (3.20 GHz) and 4 GB of RAM memory, the complete identification procedure for the Voce hardening model takes approximately 25, 30, and 35 min using uniform, stiffness-based, and sensitivity-based virtual fields, respectively. Sensitivity-based virtual fields require approximately 20% more computational time per iteration when compared to the uniform virtual fields. The total time to perform the optimization is heavily dependent on the performance of the radial-return algorithm used to perform the stress reconstruction, keeping in mind that the number of reconstructions increases linearly with the number of model parameters. The times reported here are for a radial-return algorithm in MatLab; however the time spent performing stress reconstructions could be decreased by translating this subroutine into a compiled language. A demo code presenting implementation and general flow of the identification procedure is available in Online Resource 7. It supports all three types of virtual fields used in this work.

Another route to increase computational efficiency is to only selectively update the sensitivity-based virtual fields. For the first several iterations, the virtual fields generated from the initial guess would be used; then, every nth iteration, the sensitivity-based virtual fields would be updated. If the virtual fields are not updated, they can be carried from the previous iteration directly reducing the number of stress reconstructions that are needed. While not critical for the models tested here which included a maximum of 4 parameters, selective updating will likely to be critical to keep the run time down for models with a large number of parameters. This will be investigated in future studies.

In the future, this method will be tested with more complex non-linear constitutive models. Currently, the sensitivity-based virtual field concept is being extended to large deformation and anisotropic plasticity (Hill48, Yld2000-2D). This

Comput Mech (2017) 60:409–431 429

will be applied to tests such as presented in [14,25]. Future work also includes extending the method to dynamic loading [21] where the virtual work due to inertia will be accounted for in Eq. 1. While not addressed in this manuscript, the virtual fields method has already been validated for large strain hyperelasticity [23] and sensitivity-based virtual fields could be used to identify hyperelastic material parameters. It should be noted that for models that do not include history-dependence, it may be appropriate to examine again which of the stress-sensitivity or incremental stress sensitivity performs better for the inverse material parameter identification.

7 Data report

No data are provided with this article as only simulations were used which can easily be reproduced from the information in the article.

Acknowledgements Dr. Frances Davis and Prof. Fabrice Pierron acknowledge support from Engineering and Physical Sciences Research Council (EPSRC) through grant EP/L026910/1. Prof. Fabrice Pierron also expresses gratitude to the Wolfson Foundation for support through a Royal Society Wolfson Research Merit Award. Mr Aleksander Marek acknowledges funding from EPSRC through a Doctoral Training Grant studentship. The authors also acknowledge the use of the IRIDIS High Performance Computing Facility, and associated support services at the University of Southampton, in the completion of this work.

Appendix 1

Virtual mesh: piecewise virtual fields

The use of a virtual mesh, allows the virtual displacement, $\boldsymbol{u}^*$, to be defined in a piecewise manner over the surface of the body. The primary advantage of defining the virtual displacement in a piecewise manner is flexibility; this is particularly useful when defining the sensitivity and stiffness-based virtual fields. The formulation of the piecewise virtual fields is briefly described below; for additional details on implementing piecewise virtual fields see Section 3.6 of [20].

In this work, a virtual mesh consists of isoparametric linear quadrilateral virtual elements defined by four nodes. Each node has two degrees of freedom, the two in-plane virtual displacements. Within an element, virtual displacements are calculated as:

$$\boldsymbol{u}^*(\xi,\eta) = \sum_{i=1}^{4} \boldsymbol{N}^{(i)}(\xi,\eta)\boldsymbol{u}^{*(i)} \tag{13}$$

where ξ and η are the local (natural) coordinates of each element, $\boldsymbol{N}^{(i)}$ is a shape function of node i at point (ξ,η), and $\boldsymbol{u}^{*(i)}$ is a nodal value of displacement at node i. Strain is calculated as a derivative of displacement with respect to the global coordinate system:

$$\begin{aligned}\boldsymbol{\varepsilon}^*(x,y) &= \sum_{i=1}^{4} \boldsymbol{B}^{(i)}(x,y)\boldsymbol{u}^{*(i)} \\ &= \sum_{i=1}^{4} \boldsymbol{J}^{-1}\boldsymbol{B}^{(i)}(\xi,\eta)\boldsymbol{u}^{*(i)},\end{aligned} \tag{14}$$

where x and y are the global coordinates, $J_{ij} = \frac{\partial x_i}{\partial \xi_j}$ is the Jacobian matrix of local-to-global coordinate transformation, and $\boldsymbol{B}^{(i)}$ is a strain transformation matrix for node i. The shape functions then define the virtual displacement over the element and the virtual strains. Boundary conditions are also easily enforced directly at the constrained nodes.

Appendix 2

Derivation of stiffness-based virtual fields for quadrilateral elements

Stiffness-based virtual fields were derived by estimating the effect that noise has on the data and developing a special class of virtual fields that minimise the influence of the noise [19]. The stiffness-based virtual fields can be obtained by inverting the following system:

$$\begin{bmatrix} \boldsymbol{H} & \boldsymbol{\Gamma}^T \\ \boldsymbol{\Gamma} & \boldsymbol{0} \end{bmatrix} \begin{bmatrix} \boldsymbol{u}^* \\ \boldsymbol{\lambda} \end{bmatrix} = \begin{bmatrix} \boldsymbol{0} \\ \boldsymbol{u}_{BC} \end{bmatrix} \tag{15}$$

where $\boldsymbol{H}$ is the matrix derived from the tangent stiffness matrix, $\boldsymbol{\lambda}$ is a vector containing Lagrangian multipliers, $\boldsymbol{u}_{BC}$ is a vector containing values of the prescribed displacements and $\boldsymbol{\Gamma}$ is a matrix containing prescribed virtual boundary conditions. For the specific case presented in Sect. 4.1, the vertical displacements at the top boundary are equal to L, the length of specimen, and the displacement at the bottom boundary is equal to 0. Matrix $\boldsymbol{H}$ is obtained from:

$$\boldsymbol{H} = \boldsymbol{K}^*\boldsymbol{K}^* \tag{16}$$

where $\boldsymbol{K}^*$ is the modified global stiffness matrix, as defined in Eq. 17. It depends on n, the number of virtual elements, t, the thickness of specimen, σ^{eq}, the effective von Mises stress,

$\boldsymbol{B}$, the strain-displacement matrix, and $\boldsymbol{D}^{ep}$, the tangential elasto-plastic stiffness matrix.

$$\boldsymbol{K}^{*} = \sum_{elem=1}^{n} \int_{A} t\,\sigma^{eq} \left(\boldsymbol{B}^{T}\boldsymbol{D}^{ep}\boldsymbol{B}\right) dA \tag{17}$$

There are a few differences between the original formulation given in Pierron et al. [19] and the implementation used in this manuscript. Originally, the experimental data were interpolated onto a grid consisting of triangular elements and, as a result, the virtual elements were constant strain triangular elements. To be consistent with the quadrilateral mesh used for the sensitivity-based virtual fields, the method for the stiffness-based virtual fields was reformulated for a quadrilateral mesh. For a linear quadrilateral element, the integration of the stiffness matrix is not a trivial task unless the strains are known at the Gauss (integration) points. However, this is not generally the case. To avoid interpolating the strains at the Gauss points and performing additional stress reconstructions at the Gauss points, another approach was taken. The tangential elasto-plastic stiffness matrix, $\boldsymbol{D}^{ep}$, was computed as an average value across each element taking into account all measurements points within an element. For the radial-return algorithm used in this work, the consistent elasto-plastic tangential stiffness matrix for von Mises plasticity with isotropic hardening is [16]:

$$\begin{aligned}
\boldsymbol{D}^{ep} &= \boldsymbol{E} - \alpha(\boldsymbol{E}\boldsymbol{P}\boldsymbol{\sigma}_{n+1}) \otimes (\boldsymbol{E}\boldsymbol{P}\boldsymbol{\sigma}_{n+1}) \\
\boldsymbol{E} &= \left[\boldsymbol{C} + \Delta\gamma\,\boldsymbol{P}\right]^{-1} \\
\alpha &= \frac{1}{\boldsymbol{\sigma}_{n+1}^{T}\boldsymbol{P}\boldsymbol{E}\boldsymbol{P}\boldsymbol{\sigma}_{n+1} - \frac{2\sigma^{eq} d\sigma_y/d\bar{\varepsilon}^{p}}{3-2d\sigma_y/d\bar{\varepsilon}^{p}\Delta\gamma}}
\end{aligned} \tag{18}$$

where $\boldsymbol{C}$ is the plane stress compliance matrix, $\boldsymbol{P}$ is a matrix mapping a stress vector to the equivalent stress (Eq. 19). $\Delta\gamma$ is the plastic multiplier obtained in a implicit Newton-Raphson radial return scheme, σ^{eq} is the equivalent stress, σ_y is hardening law and $\otimes$ is a dyadic product of two vectors.

$$\left(\sigma^{eq}\right)^{2} = \frac{3}{2}\boldsymbol{\sigma}^{T}\boldsymbol{P}\boldsymbol{\sigma}, \quad \boldsymbol{P} = \frac{1}{3}\begin{bmatrix} 2 & -1 & 0 \\ -1 & 2 & 0 \\ 0 & 0 & 6 \end{bmatrix} \tag{19}$$

This averaged tangential elasto-plastic stiffness matrix was assumed to be valid at the centroid of the element and the element stiffness matrix was integrated using the standard reduced integration scheme for a 4-noded quadrilateral. The effective von Mises stress was also calculated by taking the average value across the element. Note that this simplification is not physical, but since the virtual fields are just mathematical test functions, it is a reasonable simplification. This approach of taking the average value across each virtual element limits the coarseness of the stiffness-based virtual fields. If the virtual elements become too large the assumption of using the average value at the centroid will lead to inappropriate virtual fields.

References

1. Avril S, Grédiac M, Pierron F (2004) Sensitivity of the virtual fields method to noisy data. Comput Mech 34(6):439–452. doi:10.1007/s00466-004-0589-6
2. Avril S, Bonnet M, Bretelle A-S, Grédiac M, Hild F, Ienny P, Latourte F, Lemosse D, Pagano S, Pagnacco E, Pierron F (2008) Overview of identification methods of mechanical parameters based on full-field measurements. Exp Mech 48(4):381–402. doi:10.1007/s11340-008-9148-y
3. Avril S, Pierron F, Pannier Y, Rotinat R (2008) Stress reconstruction and constitutive parameter identification in plane-stress elasto-plastic problems using surface measurements of deformation fields. Exp Mech 48(4):381–402. doi:10.1007/s11340-007-9084-2
4. Avril S, Badel P, Duprey A (2010) Anisotropic and hyperelastic identification of in vitro human arteries from full-field optical measurements. J Biomech 43(15):2978–2985. doi:10.1016/j.jbiomech.2010.07.004
5. Belytschko T, Liu WK, Moran B (2000) 8—Element technology. In: Nonlinear finite elements for continua and structures, chap 8, Wiley, Chichester, pp 455–456
6. Grama SN, Subramanian SJ, Pierron F (2015) On the identifiability of Anand visco-plastic model parameters using the Virtual Fields Method. Acta Mater 86:118–136. doi:10.1016/j.actamat.2014.11.052
7. Grédiac M, Auslender F, Pierron F (2001) Applying the virtual fields method to determine the through-thickness moduli of thick composites with a nonlinear shear response. Compos A Appl Sci Manuf 32(12):1713–1725. doi:10.1016/S1359-835X(01)00029-X
8. Grédiac M, Pierron F (2006) Applying the Virtual Fields Method to the identification of elasto-plastic constitutive parameters. Int J Plast. doi:10.1016/j.ijplas.2005.04.007
9. Grédiac M, Sur F, Blaysat B (2016) The grid method for in-plane displacement and strain measurement. Rev Anal Strain 52(3):205–243. doi:10.1111/str.12182
10. Guelon T, Toussaint E, Le Cam JB, Promma N, Grédiac M (2009) A new characterisation method for rubber. Polym Testing 28(7):715–723. doi:10.1016/j.polymertesting.2009.06.001
11. Kim J-H, Pierron F, Wisnom MR, Syed-Muhamad K (2007) Identification of the local stiffness reduction of a damaged composite plate using the virtual fields method. Compos A Appl Sci Manuf 38(9):2065–2075. doi:10.1016/j.compositesa.2007.04.006
12. Kim J-H, Kim D, Han HN, Barlat F, Lee M-G (2013) Strain rate dependent tensile behavior of advanced high strength steels: experiment and constitutive modeling. Mater Sci Eng A 559:222–231. doi:10.1016/j.msea.2012.08.087
13. Kim JH, Serpantié A, Barlat F, Pierron F, Lee MG (2013) Characterization of the post-necking strain hardening behavior using the virtual fields method. Int J Solids Struct 50(24):3829–3842. doi:10.1016/j.ijsolstr.2013.07.018
14. Kim J-H, Barlat F, Pierron F, Lee M-G (2014) Determination of anisotropic plastic constitutive parameters using the virtual fields method. Exp Mech 54(7):1189–1204. doi:10.1007/s11340-014-9879-x
15. Le Louëdec G, Pierron F, Sutton M, Reynolds AP (2013) Identification of the local elasto-plastic behavior of FSW welds using the Virtual Fields Method. Exp Mech. doi:10.1007/s11340-012-9679-0

16. de Souza Neto E, Perić D, Owen D (2008) Finite elements in small-strain plasticity problems. In: Computational Methods for Plasticity, Chap 7, Wiley, pp 232–235. doi:10.1002/9780470694626
17. Pannier Y, Avril S, Rotinat R, Pierron F (2006) Identification of elasto-plastic constitutive parameters from statically undetermined tests using the virtual fields method. Exp Mech 46(6):735–755. doi:10.1007/s11340-006-9822-x
18. Pierron F, Grédiac M (2000) Identification of the through-thickness moduli of thick composites from whole-field measurements using the Iosipescu fixture: theory and simulations. Compos A Appl Sci Manuf 31(4):309–318. doi:10.1016/S1359-835X(99)00080-9
19. Pierron F, Avril S, The Tran V (2010) Extension of the virtual fields method to elasto-plastic material identification with cyclic loads and kinematic hardening. Int J Solids Struct. doi:10.1016/j.ijsolstr.2010.06.022
20. Pierron F, Grédiac M (2012) The Virtual Fields Method. Springer, Berlin. doi:10.1007/978-1-4614-1824-5
21. Pierron F, Zhu H, Siviour CR (2014) Beyond Hopkinson's bar. Philos Trans R Soc A 20130:195. doi:10.1098/rsta.2013.0195 372 (September 2015)
22. Prates PA, Pereira AFG, Sakharova NA, Oliveira MC, Fernandes JV (2016) Inverse strategies for identifying the parameters of constitutive laws of metal sheets. Adv Mater Sci Eng. doi:10.1155/2016/4152963
23. Promma N, Raka B, Grédiac M, Toussaint E, Le Cam JB, Balandraud X, Hild F (2009) Application of the virtual fields method to mechanical characterization of elastomeric materials. Int J Solids Struct 46(3–4):698–715. doi:10.1016/j.ijsolstr.2008.09.025
24. Rossi M, Lava P, Pierron F, Debruyne D, Sasso M (2015) Effect of DIC spatial resolution, noise and interpolation error on identification results with the VFM. Strain 51(3):206–222. doi:10.1111/str.12134
25. Rossi M, Pierron F, Štamborská M (2016) Application of the virtual fields method to large strain anisotropic plasticity. Int J Solids Struct. doi:10.1016/j.ijsolstr.2016.07.015
26. Sutton MA, Orteu JJ, Schreier HW (2009) Image correlation for shape, motion and deformation measurements: basic concepts, theory and applications. pp 1–321. doi:10.1007/978-0-387-78747-3
27. Wang P, Pierron F, Rossi M, Lava P, Thomsen OT (2016) Optimised experimental characterisation of polymeric foam material using DIC and the Virtual Fields Method. Strain 52(1):59–79. doi:10.1111/str.12170
28. Yoon S-H, Giannakopoulos I, Siviour CR (2015) Application of the Virtual Fields Method to the uniaxial behavior of rubbers at medium strain rates. Int J Solids Struct 69–70:553–568. doi:10.1016/j.ijsolstr.2015.04.017
29. Yoon S-H, Winters M, Siviour CR (2016) High strain-rate tensile characterization of EPDM rubber using non-equilibrium loading and the Virtual Fields Method. Exp Mech 56(1):25–35. doi:10.1007/s11340-015-0068-3
30. Zhang L, Thakku SG, Beotra MR, Baskaran M, Aung T, Goh JCH, Strouthidis NG, Girard M (2016) Verification of a virtual fields method to extract the mechanical properties of human optic nerve head tissues in vivo. Biomec Model Mechanobiol. doi:10.1007/s10237-016-0858-2

3.1 Addendum

The definition of t after Eq. 5 should read: t 'is the time index'.

The paragraph after Eq. 7 should read:
where $\boldsymbol{B}$ is the global strain-displacement matrix which maps the virtual displacement at every node into virtual strains.There are $3 \times nPts$ equations with $2 \times nNodes$ unknowns for each model parameter, where $nPts$ is the number of data points, factor of three comes from the number of stress tensor components, $nNodes$ is the total number of virtual nodes and the factor of two comes from two degrees of freedom of each node. Importantly, the unit of $\boldsymbol{B}$ is 1/length which comes from the spatial differentiation of shape functions (scalar). Eq. 7 leads to virtual displacements that have a unit of the stress sensitivities unit multiplied by length. Again, it needs to be reminded that the virtual displacements have no physical significance and the unit is irrelevant. When multiple virtual fields are combined in one cost function, virtual displacements need to be normalised so that they have compatible units (unitless), as outlined later.

The virtual boundary conditions place constraints on the virtual displacement, $\boldsymbol{u}^{*(i)}$. When the displacement at a boundary is prescribed, the traction at the surface is generally unknown. To eliminate the contribution of this unknown traction to Eq. 7, the virtual displacement at these boundaries are set to zero. Often, the distribution of the traction is unknown and only the resultant force, $\boldsymbol{F} = \int \boldsymbol{T} dA$, is measured. In this case, a constant virtual displacement is applied on the boundary.'

The end of the paragraph before the beginning of Section 4 should be corrected to:
'This approximation of the element stiffness matrix limits how coarse the virtual mesh can be; the larger an element~~s~~ is, the more points of measurement it contains as well as the larger area it spans. As a result the value at the centroid is estimated with larger error leading to reduction in effectiveness of noise-optimisation.'

Caption of Fig. 8 should read:
'Maps of (a) $\delta\widetilde{\sigma}_{11}^{(\sigma_0)}$ and ~~(c)~~ (d) $\delta\widetilde{\sigma}_{12}^{(\sigma_0)}$ the incremental stress sensitivity to the yield stress for the linear hardening model. The calculated virtual strains using the sensitivity based virtual fields (b-c) ε_{11}^* and (e-f) ε_{12}^* for using a (b,e) 7 x 7 and (c,f) 14 x 14 virtual mesh. The maps correspond to a vertical displacement of 0.060 mm and a resultant force of 1085 N.'

Section 5.3.1 should read:
'To examine the time steps when each parameter is active, the internal virtual work was calculated for each parameter using Eq. 9. Figures 10 a-b show the internal and external virtual work for the yield stress and hardening modulus, respectively. The magnitude and shape of the curves for the yield stress and hardening modulus are clearly different. The internal and external virtual work for both the yield stress and hardening modulus remain at zero for the first 9 steps corresponding to elastic loading, hence completely filtering out the elastic part of the test from the cost function. Then at time step 10, which corresponds to the onset of plasticity at the notches, the magnitude of virtual work starts to increase from zero as expected. The internal virtual work for the yield stress quickly peaks at the 15^{th} time step, which corresponds to the plastic zone spreading across the whole specimen and then decays back to zero. In contrast, the magnitude of internal virtual work for the hardening modulus continuously increases throughout the test. The magnitude of the internal

virtual work for the yield stress and hardening modulus are also markedly different. To properly identify the model parameters using Eq. 8, the virtual work is scaled by $\alpha^{(i)}$ using the 15 highest IVW values to ensure that the contributions of each parameter to the cost function are of the same order. The y-axis on the right hand side of Fig.10 shows the scaled values for both the internal and external virtual work. Although not backed by any physical argument, the scaling method employed here was proven to be successful as shown in Sect. 5.4.5, where it was found that the number of time steps taken for computing $\alpha^{(i)}$ has minor effect on the identification errors.'

The last sentence on page 422 (first column) should read:
'The reduction in the number time steps likely causes this increase in random error; the reduction in time steps makes the identification mores susceptible to noise which results in increased random error.'

Chapter 4

Extension of the sensitivity-based virtual fields to large deformation anisotropic plasticity

International Journal of Material Forming
https://doi.org/10.1007/s12289-018-1428-1

ORIGINAL RESEARCH

Extension of the sensitivity-based virtual fields to large deformation anisotropic plasticity

Aleksander Marek[1] · **Frances M. Davis**[1] · **Marco Rossi**[2] · **Fabrice Pierron**[1]

Received: 23 May 2018 / Accepted: 5 July 2018

Abstract

The virtual fields method is an approach to inversely identify material parameters using full-field deformation data. In this work, we extend the sensitivity-based virtual fields to large deformation anisotropic plasticity. The method is firstly generalized to the finite deformation framework and then tested on numerical data obtained from a finite element model of a deep-notched specimen subjected to a tensile loading. We demonstrated the feasibility of the method for two anisotropic plasticity models: Hill48 and Yld2000-2D, and showed that all the parameters could be characterise from such a test. The sensitivity-based virtual fields performed better than the currently accepted standard approach of user-defined ones in terms of accuracy and robustness. The main advantage of the sensitivity-based virtual fields comes from the automation of virtual fields generation. The process can be applied to any geometry and any constitutive law.

Keywords The virtual fields method · Anisotropic plasticity · Sensitivity-based virtual fields · Material testing · Full-field measurements

Introduction

Accurate modelling of metal forming processes is of key interest to industries such as automotive. One of the main issues in simulating processes such as deep drawing of metal sheets is ensuring that the chosen constitutive model represents the material accurately. Many of the metallic materials used in this industry exhibit anisotropic properties due to texture induced during cold rolling which highly affect deformation of it during forming processes (e.g. earrings formation during deep drawing [20]).

One of the most popular anisotropic plasticity yield criteria is Hill48 [19], which in case of plane stress conditions requires four parameters, generally identified from three uniaxial tests performed in three directions: rolling (RD), transverse (TD) and 45° to RD. In many cases, experimental results suggest that Hill48 is not capable of predicting biaxial yield behaviour accurately, and thus has limited applicability for forming predictions. Numerous models were proposed to capture the biaxial behaviour of sheet metals more accurately, such as: Yld89 [9], Stoughton's model of 2002 and further refinement of 2009 [43, 44], BBC2000 [6], BBC2005 [5], Yld2000-2D [8] and Yld2004-18 [7]. Often, the usefulness of these complex models is limited by the significant effort required to accurately identify their parameters experimentally. In particular, many of these models require performing an additional biaxial test, such as bulge or equibiaxial tension on cruciform specimens, increasing the cost of the procedure. Therefore, there is a drive to improve testing techniques and a promising way to achieve this goal is to collect experimental data using more advanced methods, such as full-field measurements e.g. digital image correlation (DIC).

New tests can be designed in order to collect more data within a single run, compared to the standard methods. The use of full-field measurements makes it possible to choose complex geometries for the test specimens, introducing heterogeneous strain fields, thereby enabling the yield envelope to be probed at thousands of different stress states at once. One of the main challenges in such approach is to extract the material parameters from the collected data. Two of the most used inverse techniques capable of doing this are finite element model updating (FEMU) and the virtual fields

✉ Aleksander Marek
A.Marek@soton.ac.uk

1 Faculty of Engineering and the Environment, University of Southampton, Highfield, SO171BJ, UK

2 Faculty of Engineering, Università Politecnica delle Marche, Monte Dago, via Brecce Bianche, 60131, Ancona, Italy

Published online: 24 July 2018

method (VFM). It was demonstrated that these approaches can reduce the number of tests needed to fully characterize anisotropic models, in particular Hill48, or Yld2000-2D [11, 13, 18, 21, 35, 38, 39].

The virtual fields method is a very efficient technique for extraction of material parameters from full-field measurements. One of the main advantages of the VFM over the FEMU is that it is significantly faster in terms of the computational time. In fact, some authors reported that for their particular application the VFM was 125 times faster than FEMU [47]. This is especially important as the complexity of material models and the number of data points available from the measurements grow. Another advantage of the VFM is that it acts directly on collected data and no numerical simulations are required. As a result, the method can be integrated directly into a DIC platform making it more accessible to practising engineers. The method has already been applied to a range of materials and constitutive laws such as arteries [2], rubbers [17, 45, 46], composites [15], and metals [22, 24, 25, 33, 39].

One of the main challenges in the VFM is the choice of virtual fields. These are test functions that act upon the reconstructed stress fields to check for stress equilibrium. Their choice strongly affects the accuracy of the identification. Until recently, no structured method was available to generate high quality virtual fields for non-linear problems. Currently, the standard approach is to rely on user-defined virtual fields (UDVFs), using standard expansion bases such as polynomials or harmonic functions. The effectiveness of these user-defined virtual fields strongly depends on their choice, and requires the user to understand the method in depth to be able to select these fields in an informed way. Recently, a new approach for generating high quality virtual fields has been developed, leading to the so-called sensitivity-based virtual fields (SBVFs) [28]. They outperformed UDVFs in case of isotropic plasticity, and are generic enough to be applied to any constitutive model.

In this work, we have extended the SBVFs to the case of large deformation anisotropic plasticity, and demonstrated their feasibility to calibrate Hill48 and Yld2000-2D yield functions from a deep notched specimen subject to tensile loading.

Theory

Brief recall of the finite deformation framework

Let us consider a body $\mathscr{B}$, where the position of particles in the reference configuration is given by $\mathbf{X}$ and in the deformed one by $\mathbf{x}$. The motion of each material point can be described by a function $\mathbf{x} = \phi(\mathbf{X}, t)$, which maps the position of every particle in the reference configuration to the current deformed configuration. The displacement field is defined as the difference between the current and the reference positions:

$$\mathbf{u}(\mathbf{X}, t) = \mathbf{x} - \mathbf{X} \tag{1}$$

The deformation gradient is defined as:

$$\mathbf{F} = \frac{\partial \mathbf{x}}{\partial \mathbf{X}} = \frac{\partial \mathbf{u}}{\partial \mathbf{X}} + \mathbf{I}, \tag{2}$$

where $\mathbf{I}$ is the second order identity tensor. Using polar decomposition, the deformation gradient can be written as the product of two second order tensors:

$$\mathbf{F} = \mathbf{V}\mathbf{R} \tag{3}$$

where $\mathbf{V}$ is the left stretch tensor and $\mathbf{R}$ is the rotation tensor. The left stretch tensor can be conveniently calculated as:

$$\mathbf{V} = \sqrt{\mathbf{F}\mathbf{F}^T} \tag{4}$$

where the root operator refers to the root of a matrix. A consequence of such mathematical description is that for every point, a local coordinate system rotates during deformation, as outlined in Fig. 1. This is an important feature to consider when the body includes a texture, as its orientation will follow any local rotations.

A convenient measure of strain, called Hencky strain, can be constructed from the left stretch tensor:

$$\boldsymbol{\varepsilon}_L = \ln \mathbf{V} \tag{5}$$

This strain measure can be used to formulate constitutive laws within the finite deformation framework. For further details on continuum mechanics the reader is referred to [12].

The virtual fields method

Quasi-static equilibrium can be expressed in so-called 'weak form' in which it is enforced as a weighted average over the entire domain, expressed here in the current configuration $\mathscr{B}_t$, in absence of volume forces:

$$-\int_{\mathscr{B}_t} \boldsymbol{\sigma} : \frac{\partial \mathbf{u}^*}{\partial \mathbf{x}} d\mathscr{B}_t + \int_{\partial \mathscr{B}_t} (\boldsymbol{\sigma}\mathbf{n}) \cdot \mathbf{u}^* d\partial\mathscr{B}_t = 0 \tag{6}$$

where $\partial\mathscr{B}_t$ is the boundary of $\mathscr{B}_t$, $\mathbf{n}$ is the outwards vector of $\partial\mathscr{B}_t$ and $\boldsymbol{\sigma}$ is the Cauchy stress tensor.

Equation 6, called the principle of virtual work (PVW), is satisfied for any continuous function $\mathbf{u}^*$ (called virtual displacements) that is piecewise-differentiable. Both stress and test function (virtual displacements) are expressed in the current configuration in the case of Eq. 6.

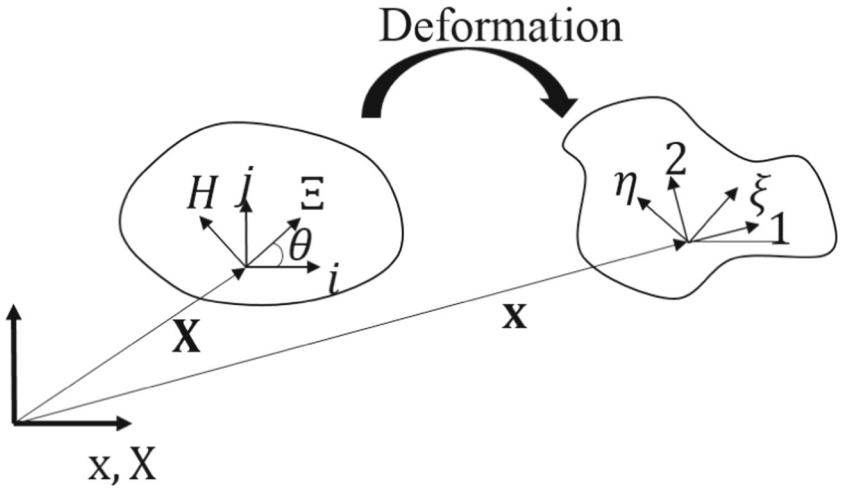

Fig. 1 Definition of coordinate systems, **X** is the initial position of a material point and **x**, its current position, (i, j) is the initial orientation of local coordinate system, $(1, 2)$ is the corotational system, (Ξ, H) is the material coordinate system in the reference configuration and (ξ, η) is the material coordinate system in the current configuration

The PVW can be alternatively formulated in the reference configuration. In that case, another stress tensor is defined, called the first Piola-Kirchhoff stress tensor **P**:

$$\mathbf{P} = \det(\mathbf{F})\boldsymbol{\sigma}\mathbf{F}^{-T} \tag{7}$$

Notably, the first Piola-Kirchhoff stress tensor is asymmetric due to the asymmetry of the deformation gradient.

As a result, in the reference configuration, the PVW can be expressed as:

$$-\int_{\mathscr{B}_0} \mathbf{P} : \frac{\partial \mathbf{U}^*}{\partial \mathbf{X}} d\mathscr{B}_0 + \int_{\partial\mathscr{B}_0} (\mathbf{PN}) \cdot \mathbf{U}^* d\partial\mathscr{B}_0 = 0 \tag{8}$$

where $\mathscr{B}_0$ is the considered body in the reference configuration and $\partial\mathscr{B}_0$ its boundary. This form is much more suitable for practical implementation in case of the proposed method, as the virtual fields $\mathbf{U}^*$, defined in the reference configuration $\mathscr{B}_0$, do not need updated virtual boundary conditions, as will become apparent later in the article. This approach has been used by most of the VFM community [36, 38, 39, 41]. Noticeably, it was demonstrated that the current configuration formulation could be successfully applied to the case of hyperelasticity as well [2, 23, 32].

The VFM uses the PVW to identify material parameters from kinematic data and loading. Generally, kinematic fields are measured by means of full-field techniques such as DIC over the entire domain. This data is then used to reconstruct the stress field using a set of material parameters, denoted here as $\boldsymbol{\chi}$. The calculated stresses must be in equilibrium with the measured loading, which is enforced through either Eq. 6 or 8. As the correct values of the constitutive parameters are unknown at the start of the process, the stress field is first estimated with a guessed set of parameters and the equilibrium can be checked by means of Eq. 8:

$$\Phi(\boldsymbol{\chi}) = \left[-\int_{\mathscr{B}_0} \mathbf{P}(\boldsymbol{\chi}) : \frac{\partial \mathbf{U}^*}{\partial \mathbf{X}} d\mathscr{B}_0 + \int_{\partial\mathscr{B}_0} (\mathbf{P}(\boldsymbol{\chi})\mathbf{N}) \cdot \mathbf{U}^* d\partial\mathscr{B}_0 \right]^2 \tag{9}$$

The material parameters are found through an iterative minimisation of the cost function, i.e. the correct material parameters produce a stress field that minimises the gap in the PVW. Since the full-field measurements provide spatially dense data, the integral of the stresses can be approximated by a discrete sum. Additionally, multiple load levels (time steps) have to be included to involve all the parameters of the constitutive model. Multiple independent virtual fields can be used to involve data in the cost function in various ways, which generally leads to better conditioning of the cost function, resulting in more robust minimisation and more accurate identification. Finally, a general form of the cost function can be expressed as:

$$\Phi(\boldsymbol{\chi}) = \sum_{i=1}^{\mathrm{nVF}} \left\{ \sum_{t=1}^{\mathrm{nTime}} \left[\overbrace{\sum_{j=1}^{\mathrm{nPts}} \left(\mathbf{P}^j(\boldsymbol{\varepsilon}_L, \boldsymbol{\chi}) : \frac{\partial \mathbf{U}^{*j^{(i)}}}{\partial \mathbf{X}} S^j h \right)}^{W_{int}} - \underbrace{\int_{\partial\mathscr{B}_0} (\mathbf{P}(\boldsymbol{\varepsilon}_L, \boldsymbol{\chi})\mathbf{N}) \cdot \mathbf{U}^{*(i)} \mathrm{d}\partial\mathscr{B}_0}_{W_{ext}} \right]^2 \right\}. \tag{10}$$

where W_{int} is the virtual work of internal forces and W_{ext} is the virtual work of external forces, S^j is the surface area of j-th point and h is the thickness of specimen.

Since in most of cases the measurements are only performed at the surface of specimen, some assumption

about the through-thickness distribution of the mechanical fields must be made. Often, plane stress is assumed, provided the thickness of specimen is small in comparison to the other two dimensions and the loading is in plane. The measurements provide in-plane kinematic quantities and the out-of-plane stresses are considered negligible ($\sigma_{13} = \sigma_{23} = \sigma_{33} = 0$). However, when the PVW is formulated in the reference configuration (8), the 2D Cauchy stress must be pulled-back from $\mathscr{B}_t$ to $\mathscr{B}_0$, as shown in Eq. 7. In reality, the gradient of deformation is fully 3D and so some additional assumptions must be made. Assuming that for a thin specimen the out-of-plane shearing is negligible ($F_{13} = F_{23} = F_{31} = F_{32} = 0$), the Jacobian ($\det(\mathbf{F})$) can be now expressed as:

$$\det(\mathbf{F}) = \mathrm{F}_{33}(\mathrm{F}_{11}\mathrm{F}_{22} - \mathrm{F}_{12}\mathrm{F}_{21}). \tag{11}$$

The in-plane values are measured, however, the out-of-plane term is still unknown. It can be approximated by calculating the out-of-plane strain during stress reconstruction using the elasto-plastic constitutive law:

$$\Delta\varepsilon_{33} = -\frac{\nu}{1-\nu}\left(\Delta\varepsilon^e_{11} + \Delta\varepsilon^e_{22}\right) - \left(\Delta\varepsilon^p_{11} + \Delta\varepsilon^p_{22}\right) \tag{12}$$

Here, the Hooke's law was assumed for the elastic part and the isochoric flow for the plastic part of the strain increments. This strain can be then used to calculate the missing component:

$$F_{33}(t) = 1 + \frac{\partial u_3}{\partial x_3} = 1 + \varepsilon_{33}(t) = 1 + \int_{t_0}^{t} \Delta\varepsilon_{33} dt. \tag{13}$$

It should be noted that if the isochoric flow assumption becomes questionable, back-to-back camera systems can be used to determine an average value of ε_{33}, as shown in [14]. Finally, with known Jacobian it is possible to pull-back the Cauchy stress to the reference configuration.

Sensitivity-based virtual fields

The test functions (virtual fields) in Eq. 10 are arbitrary and must be selected before the identification is conducted. The selection of virtual fields has a significant impact on the accuracy of the identification. These functions influence the amount of error introduced to the cost function by selecting which data points, and with what weight, are introduced to the cost function. The main difference between virtual fields arises in the way they propagate experimental noise.

In linear elasticity, an automated procedure has been published in 2004, relying on the minimization of the impact of noise on the identified parameters, i.e., finding the virtual fields leading to the maximum likelihood solution for a given basis of functions to expand the virtual fields [3]. This is now routinely used by the VFM community and also implemented on the commercial DIC/VFM platform MatchID [29]. An attempt at extending this to non-linear laws, namely, isotropic elasto-plasticity, was published in 2010 [34]. The idea there was to use a piecewise linear definition of the virtual fields based on the tangent stiffness matrix. The method did improve results but was found to lack flexibility as it required an expression for the tangent matrix. Also, for non-linear models where strains are generally larger, sensitivity to noise is not necessarily the most relevant criterion to select virtual field.

Recently, a new type of virtual field for the non-linear laws was proposed [28]. They are automatically generated during the identification procedure with very limited user input. These fields, called sensitivity-based virtual fields, are based on the reconstructed stress field and so, easily and automatically adapt to any geometry and material model. They were shown to outperform the user-defined virtual fields for isotropic small-strain plasticity and seemed very promising for more complex problems. They were also shown to outperform the tangent-matrix fields from [34], though only marginally for this particular case.

The main idea behind the sensitivity-based virtual fields is to find areas during the test, both in space and time, where the information about each parameter is contained. A separate virtual field is constructed automatically for each constitutive parameter which allows the cost function to represent each parameter with maximised sensitivity. In order to locate areas where the information is encoded for the *i-th* parameter, an incremental stress sensitivity is calculated. By perturbing the value of the *i-th* parameter during the stress reconstruction for a given set of current parameters, a change in stress field is noted, highlighting areas where the parameter is active in influencing the stress. This information is encoded in a map called stress sensitivity:

$$\delta\mathbf{P}^{(i)}(\boldsymbol{\chi}, t) = \mathbf{P}(\boldsymbol{\chi} + \delta\chi_i, t) - \mathbf{P}(\boldsymbol{\chi}, t) \tag{14}$$

where $\delta\chi_i$ is a perturbation of the i-*th* parameter, typically $-0.2\chi_i \leq \delta\chi_i \leq -0.1\chi_i$. The negative sign is taken to expand the VFs over points currently not active, as opposed to penalizing points that just became active (e.g. in the case of yield stresses). Furthermore, incremental stress sensitivity maps are found as:

$$\delta\widetilde{\mathbf{P}}^{(i)}(\boldsymbol{\chi}, t) = \frac{\delta\mathbf{P}^{(i)}(\boldsymbol{\chi}, t) - \delta\mathbf{P}^{(i)}(\boldsymbol{\chi}, t-1)}{\Delta t}. \tag{15}$$

These sensitivity maps, either incremental (15) or total (14) can be used as virtual strains to provide relevant weight to the stresses in the PVW equation. This incremental approach was proposed in order to effectively decouple the influence of yielding-related parameters from hardening parameters which act at different time scales.

The incremental sensitivity maps cannot however be directly used in the PVW as the corresponding virtual displacements, needed in the PVW, are unknown. However,

it is possible to construct virtual displacements such that the resulting virtual strain fields 'look like' the incremental sensitivity maps. This can be achieved by performing a least-square match, under some constraints, between virtual strain fields and incremental stress sensitivity.

An effective way to solve the matching problem is to construct a virtual mesh, which consists of virtual nodes connected through virtual elements. The virtual mesh defines the virtual displacements at the nodes and interpolate them within an element using classical FE shape functions. The nodes are connected with 4-node quadrilateral elements and the interpolation is done using standard bi-linear shape functions (N). The virtual fields can be calculated using the values of virtual displacements at each of the node and the spatial derivatives of the shape functions. For every point of measurement, the virtual strain fields can be found as a function of virtual displacements of the neighbouring nodes. This function is linear with respect to the displacements and can be expressed using the strain-displacement matrix $\mathbf{B}_{el}$, which relates virtual displacements at the nodes to the virtual strains at the considered data point:

$$\frac{\partial \mathbf{U}^*}{\partial \mathbf{X}} = \mathbf{B}_{el}\mathbf{U}^* \tag{16}$$

where $\mathbf{U}^*$ is a vector containing the virtual displacements of the element nodes and $\dfrac{\partial \mathbf{U}^*}{\partial \mathbf{X}}$ is a vector containing values of virtual strains[1] at the data point. It is chosen here to express the virtual fields in the reference configuration, as a results $\mathbf{B}_{el}$ does not change with deformation. It can be expressed as:

$$\mathbf{B}_{el} = \begin{bmatrix} \frac{\partial N_1}{\partial X_1} & 0 & \frac{\partial N_2}{\partial X_1} & 0 & \frac{\partial N_3}{\partial X_1} & 0 & \frac{\partial N_4}{\partial X_1} & 0 \\ 0 & \frac{\partial N_1}{\partial X_2} & 0 & \frac{\partial N_2}{\partial X_2} & 0 & \frac{\partial N_3}{\partial X_2} & 0 & \frac{\partial N_4}{\partial X_2} \\ \frac{\partial N_1}{\partial X_2} & 0 & \frac{\partial N_2}{\partial X_2} & 0 & \frac{\partial N_3}{\partial X_2} & 0 & \frac{\partial N_4}{\partial X_2} & 0 \\ 0 & \frac{\partial N_1}{\partial X_1} & 0 & \frac{\partial N_2}{\partial X_1} & 0 & \frac{\partial N_3}{\partial X_1} & 0 & \frac{\partial N_4}{\partial X_1} \end{bmatrix}. \tag{17}$$

For every point, matrix $\mathbf{B}_{el}$ can be generated and then assembled into a global strain-displacement matrix ($\mathbf{B}_{glob}$) which relates virtual displacements from all virtual nodes to the virtual strains at all data points. The global strain-displacement matrix has then to be modified to account for virtual boundary conditions. Often, it is necessary to constrain the virtual displacement in the direction of applied loading to be constant across the loading edge, so that only the resultant load appears in the PVW equation and not its (unknown) distribution. This simplifies the traction contribution to the PVW (6, 8) to become:

$$\int_{\partial\mathscr{B}_0} (\mathbf{PN})\cdot\mathbf{U}^* d\partial\mathscr{B}_0 = \mathbf{U}^* \cdot \int_{\partial\mathscr{B}_0} \mathbf{PN} d\partial\mathscr{B}_0 = \mathbf{U}^*\cdot\mathbf{F}^{load}, \tag{18}$$

where $\mathbf{F}^{load}$ is the total force applied. Imposing these constraints into $\mathbf{B}_{glob}$, a modified global strain-displacement matrix is found, $\bar{\mathbf{B}}_{glob}$. In order to solve the least-square problem, a pseudo-inverse of this matrix is found which can be used to generate the corresponding virtual displacements:

$$\mathbf{U}^{*(i)}(t) = \mathrm{pinv}(\bar{\mathbf{B}}_{glob})\delta\widetilde{\mathbf{P}}^{(i)}(\boldsymbol{\chi}, t). \tag{19}$$

These virtual displacements now produce virtual strain fields that 'look like' the incremental stress sensitivity maps and obey the necessary virtual boundary conditions. The virtual strain fields are finally found with the following formula:

$$\frac{\partial \mathbf{U}^{*(i)}}{\partial \mathbf{X}} = \mathbf{B}_{glob}\mathbf{U}^{*(i)}. \tag{20}$$

Note that the construction of the sensitivity-based virtual fields must be performed at every time step. However, as mentioned before, if the reference configuration is chosen for the PVW, the matrix $\mathbf{B}_{glob}$ is assembled only once for the entire identification.

Computing stress sensitivities significantly increases the identification time, as it virtually doubles the number of necessary stress reconstructions. To improve the computational efficiency, a selective updating scheme can be employed. Recall that any continuous virtual displacement fields constitute a valid choice, including the sensitivity-based virtual fields based on incorrect (e.g. initial) parameters. Effectively, these can be used to put the minimisation algorithm in the neighbourhood of the solution without updating them, but carrying across the iterations. As the algorithm converges, the virtual fields can be updated with parameters much closer to the correct values, saving many stress reconstructions and significantly improving computational efficiency.

Finally, in order to balance the contributions from each virtual field, a scaling is introduced. The virtual displacements are scaled by a factor dependent on the current internal virtual work contributions (W_{int}). For each iteration, W_{int} is calculated (10), and then sorted according to the absolute values over all time steps. The scaling parameter is calculated as a mean out of the top x^{th}

[1] 'virtual strain' is used here inaptly, to relate to the application of the PVW in small deformation framework. In fact, here, we should say 'virtual displacement derivatives' or 'virtual displacement gradients' but 'virtual strain' is more compact and convenient.

percentile of the sorted values. This ensures that virtual fields contributions associated with each parameter are of similar orders of magnitude.

Numerical simulations

The standard way to test anisotropic materials is to conduct tensile tests on dog-bone specimens cut at different angles to the rolling direction of the sheet (typically 0°/45°/90°). If the material model under inspection includes a parameter related to biaxial yield stress, an additional test is required, either a bulge test or equibiaxial tension on a cruciform specimen. The major limitation of this approach is that a single test provides only one data point on the yield locus and many tests are needed to match the yield surface.

An alternative is to run a test with enough stress heterogeneity to identify all necessary parameters at once. Some of the heterogeneity in the tensile test can be obtained by means of material orientation, geometric features, and loading. Rossi et al. [39] proposed a test on a deep-notched specimen under tensile loading capable of identifying the Hill48 model using a single specimen. The test is replicated here and combined with the sensitivity-based virtual fields to test their applicability to large strain anisotropic plasticity. This does not mean that this test is optimal in any way, but it can serve as a clear comparison on how VFs selection impacts the identification. Many different geometries have been proposed in the literature to produce heterogeneous states of stress and strain, it is beyond the scope of the present paper to investigate this. However, future work will look at specimen optimization, in the same spirit as for composites testing in elasticity [16].

FE model

The test proposed by Rossi et al. involved tensile loading applied to a flat coupon with two circular notches, which introduce heterogeneous deformation [39]. It was simulated in Abaqus (v. 6.13) to generate synthetic data which were then used to test the identification algorithm. The geometry of the specimen is presented in Fig. 2. The mesh density was chosen according to a convergence study. The thickness of the plane stress elements was chosen as 0.74 mm, similar to that used in [38] and typical of thin anisotropic metal sheets for the automotive industry. The bottom edge was fixed, while a constant vertical displacement of 6.75 mm was applied across the top edge, which was additionally fixed in the lateral direction to simulate the effect of the grip of a test machine. The initial material orientation was defined by specifying the angle (θ) between the rolling direction and the horizontal axis of the model, indicating the principal material axes (Ξ, H) needed to describe the anisotropic

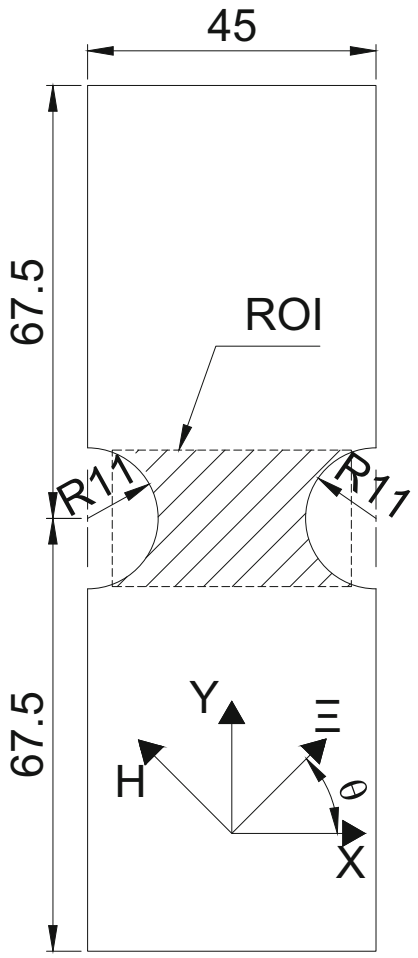

Fig. 2 Geometry of the specimen used in the simulated test. Dimensions in mm

properties (see Fig. 2). Overall, total vertical strains of about 40% were obtained with the model.

Constitutive models

In the VFM, the stress field is reconstructed explicitly from the kinematic measurements through an assumed constitutive law. In this work, two different large strain plasticity models were considered: Hill48 and Yld2000-2D.

The elastic response was modelled with Hooke's law extended to finite deformation:

$$\Delta\boldsymbol{\sigma} = \mathbf{D}\Delta\boldsymbol{\varepsilon}^{e}_{L}, \tag{21}$$

where $\Delta\boldsymbol{\sigma}$ is the rate of change of the Cauchy stress, $\mathbf{D}$ is the elastic operator for plane stress and $\Delta\boldsymbol{\varepsilon}^{e}_{L}$ is an increment of the elastic part of the Hencky strain. Here, we assume that both Young's modulus E, and Poisson's ratio ν needed to construct $\mathbf{D}$ are known. They can be identified from full-field data using the noise-optimised virtual fields in elasticity [4], considering only the initial elastic steps.

In order to ensure the objectivity of the model, a corotational frame was adopted. The reference frame at each material point rotates with the material. Fig. 1 presents the corotational and material frames in both reference and current configurations. Initially, the corotational frame (i, j) is co-linear with the global frame. The angle between the material coordinate system (Ξ, H) and the global reference frame is known. This angle can be used to construct a tensor $(\mathbf{R}_{\text{mat}})$ rotating the local coordinate system to the material one. Due to deformation, the corotational frame rotates with $\mathbf{R}$ and in the current configuration is denoted $(1, 2)$. The angle between the current material coordinate system (ξ, η) and the corotational frame is fixed and related to $\mathbf{R}_{\text{mat}}$. The strain increment in the current material frame (ξ, η) can be expressed in terms of the strain increment in the global frame (i, j):

$$\Delta\boldsymbol{\varepsilon}_L{}^{(\xi,\eta)} = \mathbf{R}^T \mathbf{R}_{mat}^T \Delta\boldsymbol{\varepsilon}_L^{(i,j)} \mathbf{R}_{mat} \mathbf{R}. \tag{22}$$

More complex strategies could be employed to account for the evolution of material texture such as that presented in [31]. They would have to be implemented in the constitutive routine used to reconstruct stress (Fig. 4). Consequently, an inverse rotation could be performed in order to represent the reconstructed stress tensor in the global coordinate system, in which the PVW is expressed.

The strain increments in the global coordinate system are simply calculated as the difference between two consecutive total strains:

$$\Delta\boldsymbol{\varepsilon}_L^{(i,j)}(t) = \boldsymbol{\varepsilon}_L^{(i,j)}(t) - \boldsymbol{\varepsilon}_L^{(i,j)}(t-1) \tag{23}$$

For each of the two plastic models investigated, Hill48 and Yld2000-2D, an associated flow rule was assumed, as well as an additive decomposition of strain increments:

$$\Delta\boldsymbol{\varepsilon}_L = \Delta\boldsymbol{\varepsilon}_L^e + \Delta\boldsymbol{\varepsilon}_L^p, \tag{24}$$

where $\Delta\boldsymbol{\varepsilon}_L^e$ is the elastic strain increment and $\Delta\boldsymbol{\varepsilon}_L^p$ is the plastic strain increment.

A yield criterion, in general, can be written as:

$$f = \sigma_{eq} - \sigma_y \leq 0. \tag{25}$$

where σ_{eq} is an equivalent stress formulated differently for each plasticity model and σ_y is a yield stress evolving according to a hardening law. A shared feature of both models is that they are formulated in terms of Cauchy stress expressed in the current material frame (ξ, η in Fig. 1).

Hill48 is a popular model for anisotropic plasticity [19]. When plane stress is assumed the equivalent stress can be expressed as:

$$\sigma_{\text{eq}}^{\text{Hill}} = \sqrt{G\sigma_{11}^2 + F\sigma_{22}^2 + H(\sigma_{11} - \sigma_{22})^2 + 2N\sigma_{12}^2}. \tag{26}$$

This model depends on 4 independent parameters defining the anisotropy. A suitable way to express the governing parameters is to relate them to mechanical quantities measured in an experiment. In this paper the plastic potentials (R_{ij}) are used to define the criterion:

$$\begin{cases} F = \frac{1}{2}\left[\frac{1}{R_{22}^2} + \frac{1}{R_{33}^2} - \frac{1}{R_{11}^2}\right] \\ G = \frac{1}{2}\left[\frac{1}{R_{11}^2} + \frac{1}{R_{33}^2} - \frac{1}{R_{22}^2}\right] \\ H = \frac{1}{2}\left[\frac{1}{R_{11}^2} + \frac{1}{R_{22}^2} - \frac{1}{R_{33}^2}\right] \\ N = \frac{1}{2}\frac{1}{R_{12}^2} \end{cases} \tag{27}$$

where $R_{ij} = \dfrac{\sigma_{ij}^y}{\sigma_0}$. Note that σ_{11}^y and σ_{22}^y are the yield stresses identified in planar uniaxial tests conducted at 0° and 90° respectively and σ_{33}^y is the through-thickness yield stress. Finally, σ_{12}^y is the yield stress identified under pure shear. Furthermore, it was assumed that the yield stress in the hardening law is equal to σ_{11}^y, i.e. $\sigma_0 = \sigma_{11}^y$, as this reduces the number of variables to be identified by one, and does not affect the formulation of model.

Although the model is popular in literature, it suffers from poor performance when used in context of sheet materials subject to biaxial loading [30, 39, 44]. This is mostly due to the quadratic nature of the law which does not represent real materials accurately. It was found that non-quadratic models such as Yld2000-2D or Stoughton2009 predict the behaviour of sheet metals such as steel or aluminium more accurately [44].

Yld2000-2D [8] was developed strictly for plane stress conditions for which the equivalent stress can be calculated as:

$$\sigma_{\text{eq}}^{\text{Yld}} = \left[\frac{1}{2}\left(|X_1' - X_2'|^a + |2X_2'' + X_1''|^a + |2X_1'' + X_2''|^a\right)\right]^{1/a} \tag{28}$$

where a is an exponent based on the metal micro-structure ($a = 8$ for FCC and $a = 6$ for BCC) and X_1', X_2' and X_1'', X_2'' are principal values of two stress tensors $\boldsymbol{X}'$, $\boldsymbol{X}''$ which are defined as linear combinations of the Cauchy stress:

$$\begin{cases} \boldsymbol{X}' = \mathbf{L}'\boldsymbol{\sigma} \\ \boldsymbol{X}'' = \mathbf{L}''\boldsymbol{\sigma} \end{cases} \tag{29}$$

Matrices $\mathbf{L}'$ and $\mathbf{L}''$ are given by:

$$\mathbf{L}' = \begin{bmatrix} \frac{2\alpha_1}{3} & -\frac{2\alpha_1}{3} & 0 \\ -\frac{2\alpha_2}{3} & \frac{2\alpha_2}{3} & 0 \\ 0 & 0 & \alpha_7 \end{bmatrix} \tag{30}$$

Table 1 Reference parameters defining the plastic anisotropy of the material

Hill48				Yld2000-2D							
R_{11}	R_{22}	R_{33}	R_{12}	α_1	α_2	α_3	α_4	α_5	α_6	α_7	α_8
1.000	1.054	1.276	0.738	1.11	1.35	1.21	1.11	1.07	0.96	1.21	1.15

The parameters were adapted from [39]

$$\mathbf{L}'' = \begin{bmatrix} \frac{8\alpha_5 - 2\alpha_3 - 2\alpha_6 + 2\alpha_4}{9} & -\frac{4\alpha_6 - 4\alpha_4 - 4\alpha_5 + \alpha_3}{9} & 0 \\ -\frac{4\alpha_3 - 4\alpha_5 - 4\alpha_4 + \alpha_6}{9} & \frac{8\alpha_4 - 2\alpha_6 - 2\alpha_3 + 2\alpha_5}{9} & 0 \\ 0 & 0 & \alpha_8 \end{bmatrix} \tag{31}$$

The model involves 8 independent parameters, α_1–α_8, and can accurately represent the behaviour both in simple tension as well as biaxial loading.

Two different hardening laws were adopted here: linear (32) and the power law hardening (33):

$$\sigma_y = \sigma_0 + H\bar{\varepsilon}^p \tag{32}$$

$$\sigma_y = \sigma_0 + H\left(\bar{\varepsilon}^p\right)^n \tag{33}$$

Linear hardening is defined with two parameters: initial yield stress σ_0 and hardening modulus H. The non-linear power law includes 3 parameters: initial yield stress σ_0, hardening modulus H, and an exponent n. The equivalent plastic strain $\bar{\varepsilon}^p$ is integrated over the history of deformation by means of summing the equivalent plastic strain increments obtained at each increment:

$$\Delta\bar{\varepsilon}^p = \frac{\boldsymbol{\sigma} : \Delta\boldsymbol{\varepsilon}^p}{\sigma_y}. \tag{34}$$

The reference parameters used to generate the models are presented in Tables 1 and 2.

For each of the constitutive models a routine was produced integrating the constitutive equations using an implicit scheme with a radial-return algorithm, returning the state of stress and out-of-plane strain at each time step, with both being rotated back to the global coordinate system.

For Hill48, 6 data sets were generated in total, considering both hardening models at the three different material orientations (30°, 45°, 60°). Due to its computational intensity, only one model was considered for Yld2000-2D, simulating linear hardening with a material orientation of 45°.

Table 2 Reference parameters for the hardening laws based on properties of BH340 steel alloy

Linear		Power law		
σ_0	H	σ_0	K	n
256	855	203	439	0.3195

While in this work the constitutive modelling was kept simple, the proposed methodology is valid for any chosen material model. In practice, the investigator supplies a constitutive law to be identified (see Fig. 4). The model can be arbitrarily complex, as long as it is capable of reconstructing the stress field based on the measured kinematic data (e.g. deformation gradient) and internal state variables that can be carried over between different load levels. By choosing more complex models that account for e.g. multiplicative decomposition of deformation gradient [27], hyperelasticity [42], anisotropic hardening [10] or even complete anisotropic elastoplasticity [40] more complex material description could be reached, but this has not been considered in this work.

Data processing

Following the FE simulations, raw displacements and positions of data points were extracted from Abaqus and exported into Matlab (2016a). The cloud of points was then interpolated onto a rectangular grid of 409 × 349 data points, corresponding to the data density typical of a DIC measurement. The region of interest was then trimmed to a grid of 362 × 202 points spanning the region of interest (ROI) (Fig. 2), which produced 57,392 data points. In the case of Yld2000-2D model, to reduce the computational time, a coarser data grid was used: 214 × 119 producing 20,024 points in total.

The displacements were then corrupted with a Gaussian white noise, with standard deviation of 0.3 μm, representative of a real experiment. For each data point, displacements were smoothed using spatial and temporal filters, as typically done for experimental data. Temporal smoothing was performed using the Savitzky-Golay method with a polynomial order m_{temp} and a window size of w_{temp}. This was complemented with a spatial smoothing using a Gaussian filter of standard deviation σ_{spat}, with the window size adjusted to be the maximum odd number smaller than $3 \times \sigma_{\text{spat}} \times 2$. While temporal smoothing was performed on all 400 time steps obtained from Abaqus, only some of the temporal data points were passed to the identification procedure. The main reason for that was to decrease the computational effort, but also this increased the size of the strain increments mitigating the impact of strain noise on

the error in the stress reconstruction. The time steps used for the identification are graphically presented on the global force-displacement curves in Fig. 3.

For each model, a different number of time steps was taken. In the case of Hill48 with linear hardening, the calculations were relatively fast, thus having many temporal points was not a problem. Ultimately, 83 frames were considered. In the case of the power law hardening, during deformation a plastic instability occurred and the strains began to localize in a very small band, causing a geometrical softening. This data was discarded, as shown in the figure. Overall, only 60 frames were used, with a maximum plastic strain of about 30%. Finally, for Yld2000-2D only 27 time steps were used, as the constitutive law itself is much more computationally demanding, and having more points would just lead to inconvenient computational times, unnecessary at this first validation stage.

After smoothing and down-sampling were performed, the deformation gradient $\mathbf{F}$ was calculated using central finite difference, which was then used to calculate $\mathbf{V}$ with Eq. 4, $\mathbf{R}$ with Eq. 3 and $\boldsymbol{\varepsilon}_L$ with Eq. 5. The set of the three quantities ($\mathbf{F}$, $\mathbf{R}$, $\boldsymbol{\varepsilon}_L$) for all data points constitutes the kinematic data used to identify the material parameters.

The kinematic data was then used as an input to an in-house Matlab code implementation of the VFM. The stresses were calculated using the deformation data and an initial guess for the material parameters. The SBVFs were calculated during the stress reconstruction process which allowed the values of the cost function to be calculated with Eq. 10. The material parameters were refined iteratively by means of the Matlab function `fmincon` minimising (10) with a sequential quadratic programming algorithm (`SQP`). Starting points were selected randomly from the interval between 50% and 200% of the reference values using a random number generator. Two starting points were used for each data set in order to ensure that the identified parameters corresponded the the global minimum. The identification algorithm is summarized in Fig. 4 in the form of a flowchart. Finally, the identified parameters were compared against the reference values to quantify the accuracy of procedure.

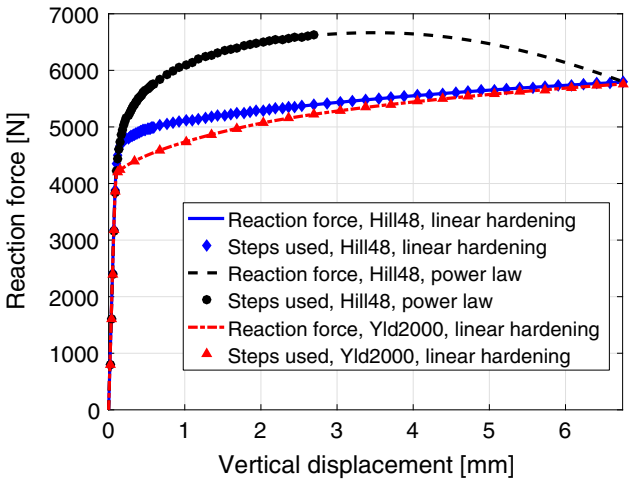

Fig. 3 Reaction force vs imposed vertical displacement obtained in Abaqus. Markers indicate time steps taken for identification

The SBVFs were updated when the first-order optimality [1] fell below certain threshold (1×10^{-4}), indicating convergence of the procedure. The virtual fields were recomputed and stored in memory, and the threshold was scaled down by a factor of 2.3 to allow further refinement. Sometimes, after selective updating was performed, the value of cost function would increase, creating an apparent local minimum terminating the minimisation. To prevent this, the value of cost function was offset below previous iteration when the update was performed. This scheme leads to an increasing rate of updates as the solution converges, providing valid values of virtual fields at the optimum. In total, about 10–15 virtual fields were computed throughout the identification consisting of more than 100 iterations, with the number controlled indirectly by the two parameters (first-order optimality threshold and threshold refinement parameter).

User-defined virtual fields

This works aims at extending the SBVFs to large deformation anisotropic plasticity. As mentioned earlier, the specimen design was previously proposed by Rossi et al. [39] who employed UDVFs to identify Hill48 parameters using a single test, as well as Yld2000-2D parameters using a combination of three tests. In this work, their user-defined virtual fields were used as a benchmark to test the suitability of the SBVFs. They showed that suitable VFs for the test consisted of a combination of three virtual fields, defined with the following virtual displacements:

$$\begin{cases} u_x^{*(1)} = 0 \\ u_y^{*(1)} = \frac{y}{H} \end{cases} \tag{35}$$

$$\begin{cases} u_x^{*(2)} = \frac{x}{W} \frac{(|y| - H)}{H} \\ u_y^{*(2)} = 0 \end{cases} \tag{36}$$

$$\begin{cases} u_x^{*(3)} = \frac{1}{\pi} \sin\left(\pi \frac{x}{W}\right) \cos\left(\pi \frac{y}{2H}\right) \\ u_y^{*(3)} = \frac{1}{\pi} \sin\left(\pi \frac{x}{W}\right) \cos\left(\pi \frac{y}{2H}\right) \end{cases} . \tag{37}$$

The virtual displacements are defined in the coordinate system presented in Fig. 5. The virtual fields are constructed in a way to include all stress components in the cost function.

It is worth noticing, that only the first virtual field (35) includes the virtual work of external forces. This impacts the balance of contributions from each virtual field to the cost function. Traditionally, the residual is scaled by the virtual work of external forces to provide a dimensionless value

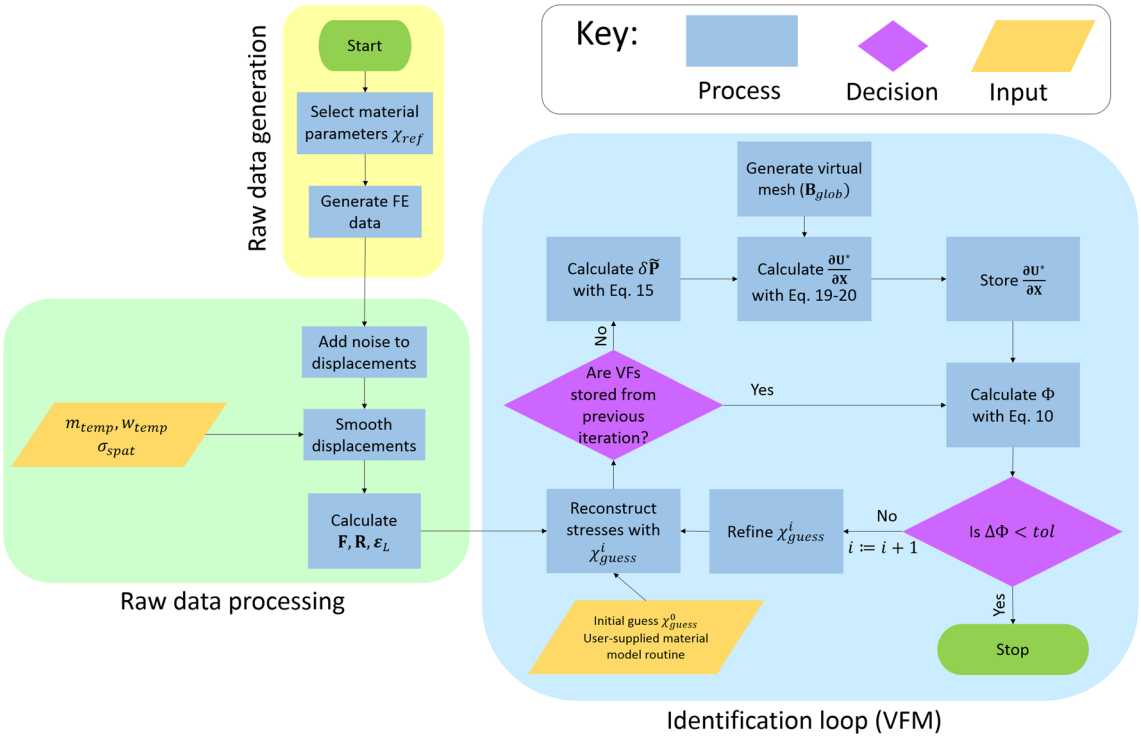

Fig. 4 Flowchart representing the algorithm for material identification. There are three major parts: generation of raw data, processing of raw data and material identification with the VFM

[33]. This was not possible here, as two of the virtual fields do not include the contribution of the external forces. To overcome this problem, scaling by the maximum value of the internal virtual work was introduced, which normalises the peaks of the internal virtual work to 1. To balance all three fields even further, the residual coming from the first virtual field was scaled by a factor 500, which was found to produce the best results. This workaround scaling shows that the manually defined virtual fields lack generality, and must be individually tailored for each application, which is a significant disadvantage.

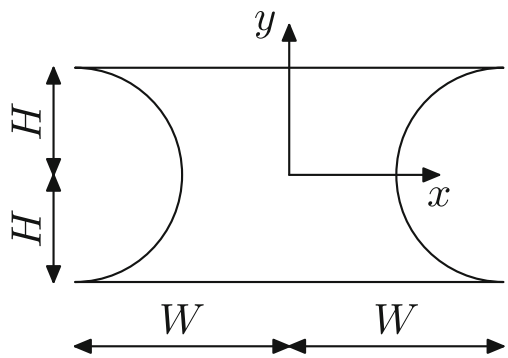

Fig. 5 The coordinate system used to define virtual fields manually within the region of interest

Error quantification

As the number of material parameters in the constitutive models increases, quantifying the accuracy of identification becomes a challenging task. Often, these models are defined with parameters that lack physical meaning, and on its own have limited impact on the model outcome, which is driven by the compound action of all of the parameters, as for Yld2000-2D. It is therefore important to establish tools to compare different sets of identified parameters in order to quantify the accuracy of the identification meaningfully.

Because of the rather large number of parameters and their individual lack of physical meaning, a direct comparison between reference and identified parameters on a one to one basis is not always relevant to draw meaningful conclusions. The apparent uniaxial yield stress $\hat{\sigma}$ as a function of material orientation was found to provide a convenient and physical-based way of evaluating identification errors. Assuming a yield criterion of the form of Eq. 25 and a uniaxial state of stress at angle θ with respect to the material coordinate system, the stress state in the material coordinate system can be expressed as:

$$\boldsymbol{\sigma} = \begin{bmatrix} \cos^2(\theta)\hat{\sigma} \\ \sin^2(\theta)\hat{\sigma} \\ \cos(\theta)\sin(\theta)\hat{\sigma} \end{bmatrix}. \tag{38}$$

This stress can be introduced into the expression of σ_{eq} and the criterion can now be algebraically transformed into:

$$\hat{\sigma} = \hat{\sigma}(\theta, \bar{\varepsilon}^p, \boldsymbol{\xi}) \tag{39}$$

Using Eq. 39, it is possible to reconstruct the variation of the yield stress with angle θ and equivalent plastic strain $\bar{\varepsilon}^p$. Such map can be calculated for both the reference and identified parameters, so that they can be meaningfully compared. The error can be quantified by looking at the map of relative error:

$$r(\theta, \bar{\varepsilon}^p) = \left| \frac{\hat{\sigma}_{ref} - \hat{\sigma}_{ident}}{\hat{\sigma}_{ref}} \right| . \tag{40}$$

The map can be used to investigate whether the error is associated with the variation of yield stress with material orientation and/or hardening. Alternatively, the mean of the error map, $\bar{r}$, gives a single numerical value for the accuracy of the identification, later referred to as the global error:

$$\bar{r} = \frac{1}{\pi/2 \times \bar{\varepsilon}^p_{max}} \int_0^{\frac{\pi}{2}} \int_0^{\bar{\varepsilon}^p_{max}} r(\theta, \bar{\varepsilon}^p) \mathrm{d}\theta \mathrm{d}\bar{\varepsilon}^p . \tag{41}$$

This approach enables the reference and identified sets of parameters to be compared in a more meaningful way as opposed to parameter by parameter and furthermore, it also allows for meaningful comparisons across different material models.

Results

Validation of the method

As a first validation of the methodology, the six raw FE data sets generated for the Hill48 model were used. Since the data did not contain any noise, no smoothing was used. The following parameters were selected for generation of the sensitivity-based virtual fields: $\delta\chi_i = -0.15\chi_i$, virtual mesh of 14×14 elements, and the scaling parameters based on the mean of top 30$^{\text{th}}$ percentile of the internal virtual work terms. As shown before, the choice of the parameters has a limited impact on the identification and mostly affects the random portion of the error [28]. The results of the identifications are presented in Table 3.

Clearly, for linear hardening, all tests were successful at identifying the material parameters. Although marginal here, it is worth noting that the mean error for sensitivity-based VFs is already consistently smaller compared to the user-defined ones. The single tests performed at either 30° or 60° were only performed usig exact data and the linear hardening. As they are unlikely to be practical when experimental and modelling errors are introduced, they were disregarded for the more complex cases. For the power law hardening, the identified values were also very close to the reference. With the exception of the combined 30°+60° tests using the user-defined VFs, the mean error was consistently below 2%, showing that the methodology adopted here has a potential of identifying Hill48 parameters using a single test. The combined test was adopted in order to obtain more data over uniaxial states of stress, in comparison to the 45° test. The latter, probes the yield envelope under combined shear and normal loading, with very little data points containing information about pure σ_{11} or σ_{22} behaviour. By including both 30° and 60° tests, more information is available about these regions, as well about shearing behaviour enabling identification all of the parameters.

Scaling of UDVFs is of crucial importance. Without introducing the scaling discussed in Section "User-defined virtual fields", the UDVFs lead to large identification errors. In particular, the yield stress is correctly identified only near the material orientation angle, while the remaining

Table 3 Identified parameters and mean error as defined in Eq. 41 for the Hill48 model using exact data for both linear and power law hardening

Orientation	Hardening	VFs	σ^0_{11}	σ^0_{22}	σ^0_{33}	σ^0_{12}	H	n	Mean error [%]
45°	Linear	UD	1.007	1.003	1.001	0.990	1.037	[-]	0.6
45°		SB	1.002	1.000	1.001	0.997	0.996	[-]	0.2
30°		UD	1.020	1.029	0.997	0.985	1.025	[-]	1.2
30°		SB	1.003	1.000	1.001	0.997	0.994	[-]	0.3
60°		UD	1.012	1.053	1.019	0.999	1.021	[-]	1.6
60°		SB	1.000	1.009	1.003	1.002	0.995	[-]	0.3
30° + 60°		UD	1.030	1.030	1.002	0.984	1.049	[-]	1.5
30° + 60°		SB	1.001	1.001	1.000	0.996	0.993	[-]	0.4
45°	Power	UD	1.000	1.018	0.989	0.955	1.020	0.973	1.7
45°		SB	1.020	1.015	1.014	1.005	1.039	1.036	1.1
30° + 60°		UD	1.104	1.102	1.086	1.057	1.136	1.206	3.3
30° + 60°		SB	1.003	1.003	1.003	0.999	1.005	1.008	0.1

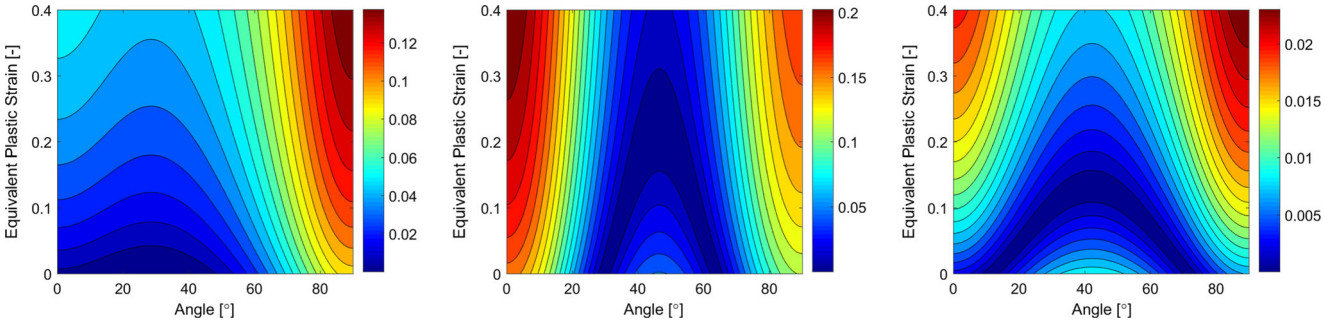

(a) 30° test without scaling (b) 45° test without scaling (c) 45° test with scaling

Fig. 6 Error maps as defined in Eq. 40 demonstrating the effect of scaling between the three UDVFs (35–37) for 30° and 45° tests with linear hardening. Without introducing scaling anisotropy is poorly identified (Fig. 6a and b). The scaling significantly improves the identification: see the difference between Fig. 6b and c

orientations are characterised incorrectly, as shown in Fig. 6a and b. The reason for this is most likely due to the first set of UDVFs (35) being overrepresented in the cost function. As a result, the vertical component of the stress field represented in the global frame is the major source of information, leading to insensitivity of the cost function to the other two stress components. The identification can be improved by introducing the scaling which restores the balance between the three virtual fields. In that case the anisotropy is recognized much better, as shown in the difference between Fig. 6b and c.

Effect of noise in the data

Having validated the methodology, the effect of noise on the identified parameters was studied. Since in practice, spatial and temporal smoothing are always implemented, we also implemented this here to simulate the experimental process more realistically. Without any smoothing, the difference between UDVFs and SBVFs was even larger, but this was thought to be a somewhat unfair comparison. First, a sensitivity study was conducted to determine the optimal smoothing parameters. The study was performed using fixed settings, i.e. sensitivity-based virtual fields, linear hardening and the same level of noise in each run. In total, 30 copies of noise were processed. The spatial smoothing parameters were chosen under fixed temporal smoothing, likewise the temporal parameters were chosen under fixed spatial smoothing. As presented in Table 4, the smoothing has a limited effect on the magnitude of both systematic and random errors (global error value and its spread respectively), which suggests that the choice of parameters is not critical for the identification here. Generally, the stronger the smoothing, the smaller the random portion of error, at a cost of increased systematic error. However, it was found previously that significant noise can cause spurious elastic unloadings, which strongly affect both errors [26]. As a result, some smoothing settings can improve both errors at the same time. In order to balance systematic and random errors, spatial smoothing with a window of 9 was selected, combined with 11 points temporal smoothing using 3rd order polynomial.

The selected smoothing parameters were used to study the effect of the virtual fields on the systematic and random errors. The identification was run on 30 copies of noise, as this gives enough statistical representation to establish the random part of the error. The results are presented in Tables 5 and 6 for the linear and the power law respectively.

Table 4 Identified parameters and mean errors as defined by Eq. 41 for Hill48 model with linear hardening using different smoothing combinations

σ_{spat}/ window	w_{temp}/ m_{temp}	σ_{11}^0	σ_{22}^0	σ_{33}^0	σ_{12}^0	H	Mean error [%]
1.0/5	11/3	0.974 ± 0.27	0.961 ± 0.26	0.998 ± 0.07	1.108 ± 0.15	0.858 ± 0.43	4.08 ± 0.09
1.3/7	11/3	0.967 ± 0.26	0.965 ± 0.242	0.988 ± 0.06	1.031 ± 0.15	0.941 ± 0.43	1.99 ± 0.11
1.5/9	11/3	0.966 ± 0.29	0.968 ± 0.25	0.984 ± 0.06	1.008 ± 0.16	0.963 ± 0.46	1.45 ± 0.13
1.85/11	11/3	0.963 ± 0.31	0.967 ± 0.25	0.980 ± 0.07	0.991 ± 0.17	0.975 ± 0.51	1.70 ± 0.15
1.5/9	11/3	0.966 ± 0.29	0.968 ± 0.25	0.984 ± 0.06	1.008 ± 0.16	0.963 ± 0.46	1.45 ± 0.13
1.5/9	15/3	0.977 ± 0.24	0.971 ± 0.21	0.985 ± 0.06	1.026 ± 0.13	0.975 ± 0.36	1.50 ± 0.08
1.5/9	21/3	1.035 ± 0.33	1.013 ± 0.35	0.999 ± 0.10	1.011 ± 0.54	1.055 ± 0.66	2.33 ± 0.08

The parameters are expressed relative to the reference values and the uncertainty represents a coefficient of variation expressed in %

Table 5 Identified parameters for Hill48 model with linear hardening

Orientation	VFs	σ_{11}^0	σ_{22}^0	σ_{33}^0	σ_{12}^0	H	Mean error [%]
45°	UD	0.954 ± 0.15	1.021 ± 0.20	0.994 ± 0.03	1.034 ± 0.11	0.903 ± 0.35	2.13 ± 0.04
45°	SBs	0.9656 ± 0.29	0.968 ± 0.25	0.984 ± 0.06	1.008 ± 0.16	0.963 ± 0.46	1.45 ± 0.13
30° + 60°	UD	1.041 ± 0.33	1.042 ± 0.03	1.010 ± 0.01	1.009 ± 0.03	1.048 ± 0.05	2.56 ± 0.01
30° + 60°	SB	0.993 ± 0.08	0.992 ± 0.08	0.994 ± 0.02	1.036 ± 0.09	0.962 ± 0.16	1.29 ± 0.04

The parameters are expressed relative to the reference values and the uncertainty represents a coefficient of variation expressed in %

Hill48 identification

Linear hardening

In the case of linear hardening, the sensitivity-based virtual fields provide more accurate identification, however with about three times larger random error compared to the UDVFs. Although individual parameters exhibit errors as large as 5%, the global error is significantly smaller, indicating compensation between parameters. Remarkably, the overall error is very small, for the level of white noise added to the displacements. It must be noted that when no smoothing was used on the data, the accuracy was poor and the global error was about 20%. By replacing a single test (45°) with two combined tests (30° + 60°), the random part of the error is reduced by a factor of 4. This was expected as more information is used, which averages out noise more effectively. The effect on the systematic error is not as notable; for the sensitivity-based VFs the mean error is slightly reduced, while for the user-defined VFs it increased a bit, as shown in Fig. 7a.

Power law hardening

The results are markedly different for the power law hardening. Firstly, the effect of noise is significantly larger compared to the linear hardening case, as shown in Fig. 7 (note the difference in scaled between Fig. 7a and b). The mean errors for the 45° tests are between 4 and 5%, compared to about 2% for the simpler hardening law (Fig. 7). While level of error is still satisfactory, it must be noted that it represents a lower bound as the simulation of experimental uncertainties remains very basic. Unlike the linear hardening case, the random error was the smallest when the SBVFs were used and the smallest systematic error was obtained with the UDVFs. Significant improvement was found when the single test was replaced by the combined tests, both in terms of systematic and random errors. This indicates that the additional test contributes significant data to the cost function. Since the smoothing parameters were chosen for the linear hardening model, it is possible that a different combination of parameters would provide smaller errors, and differentiate between the two virtual fields types in a different way.

While the single mean error term makes it straightforward to compare the overall accuracy of the identification the influence of errors on the yielding and hardening parameters can be more readily understood by examining the error maps, proposed in Section "Error quantification". In Fig. 8 the SBVFs provided the larger errors at 45°, even though the single test at 45° contains direct information about yielding at this orientation. For the UDVFs the error was the lowest for angles close to the specimen orientation, for the single test at 45° and for the combined tests at both ends of the angle spectrum, as expected from a mechanical perspective. A possible explanation is the overconstraining of the sensitivity-based virtual fields. As four independent stress sensitivity components are mapped onto only two virtual displacements maps, the resulting virtual fields are not reproduced perfectly. This appears to be especially true for the shearing components as they are cross-derivatives of the calculated virtual displacements. This might enhance the error on the shearing yield stress, observed as a slightly larger error at 45°. Further study needs to be done to confirm

Table 6 Identified parameters for Hill48 model and the power law hardening

Orientation	VFs	σ_{11}^0	σ_{22}^0	σ_{33}^0	σ_{12}^0	H	n	Mean error [%]
45°	UD	0.842 ± 1.11	0.891 ± 1.55	0.925 ± 0.68	0.995 ± 0.47	0.849 ± 1.12	0.900 ± 1.18	4.67 ± 0.34
45°	SB	0.929 ± 0.43	0.929 ± 0.44	0.962 ± 0.38	1.031 ± 0.33	1.045 ± 0.55	1.028 ± 0.75	4.35 ± 0.10
30° + 60°	UD	1.020 ± 0.26	1.021 ± 0.26	1.032 ± 0.28	1.053 ± 0.30	1.042 ± 0.24	1.074 ± 0.59	2.60 ± 0.08
30° + 60°	SB	0.967 ± 0.18	0.968 ± 0.18	0.996 ± 0.17	1.045 ± 0.17	1.026 ± 0.27	1.043 ± 0.40	3.15 ± 0.06

The parameters are expressed relative to the reference values and the uncertainty represents a coefficient of variation expressed in %

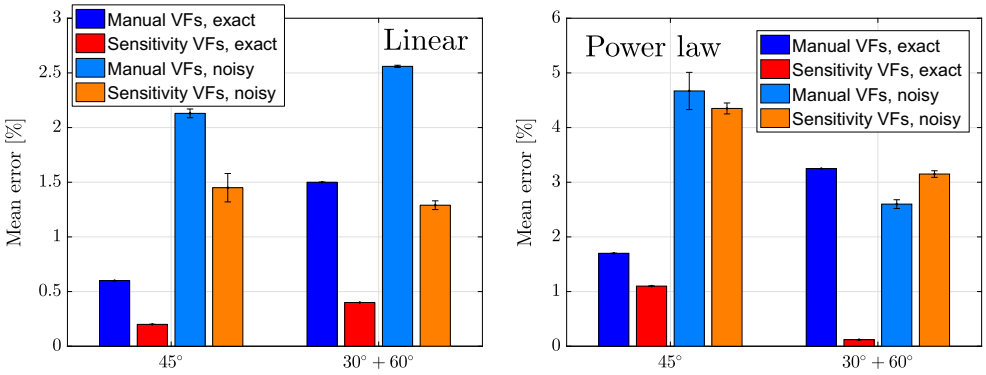

(a) linear hardening (b) power law hardening

Fig. 7 Bar plot representing systematic and random errors for the two tests with different virtual fields. The height of the bar indicates the systematic error, while the error bar represents ± the standard deviation

this hypothesis. While the Hill48 model is acceptably identified using either UDVFs or SBVFs it must be noted that the UDVFs presented in Eqs. 35–37 were the result of a long process of trial and error by the lead author of [39], which was time-consuming. The SBVFs provide nearly equivalent results using a systematic procedure without any trial and error, resulting in a much faster and more rigorous process.

The quality of the virtual fields can be indirectly quantified by means of the curvature of the cost function at the minimum. Theoretically, the more curved the cost function, the more stable the identification. Additionally,

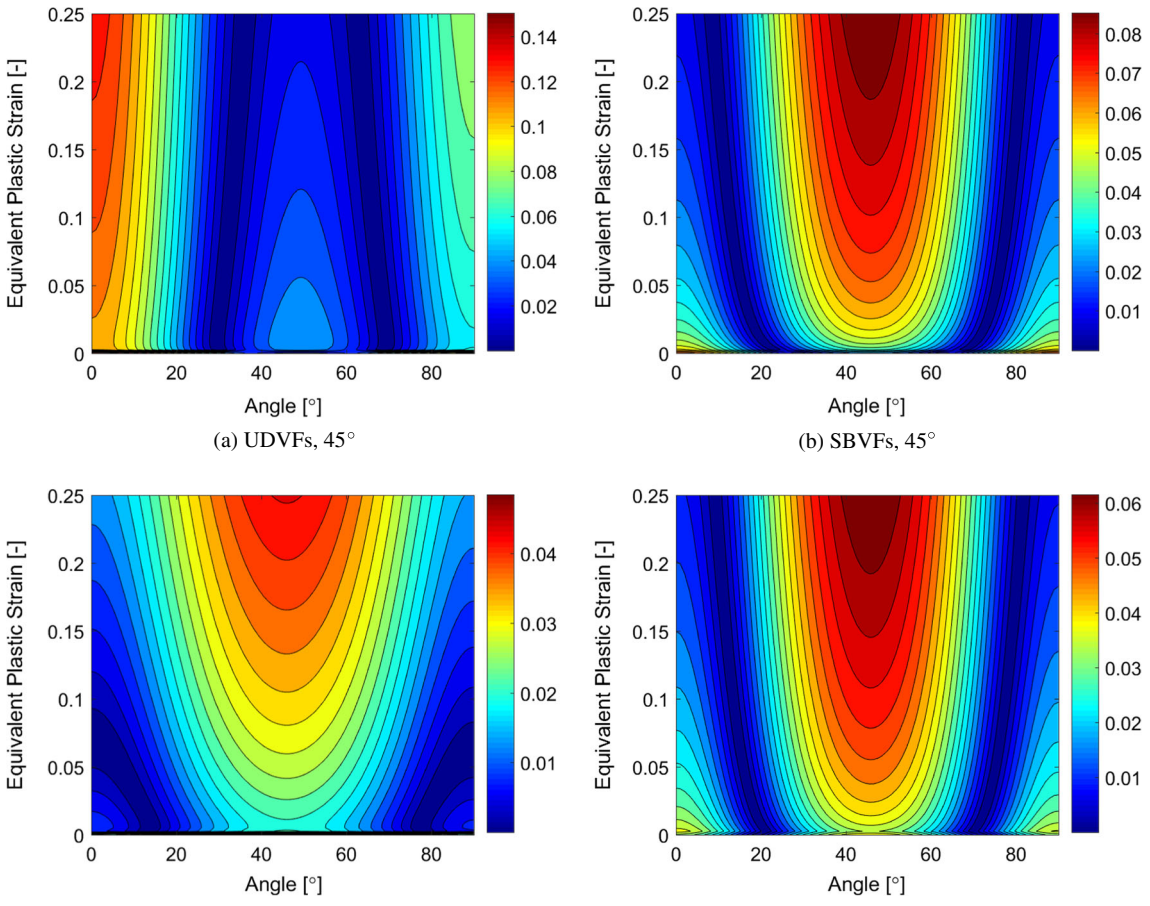

(a) UDVFs, 45° (b) SBVFs, 45°

(c) UDVFs, 30° + 60° (d) SBVFs, 30° + 60°

Fig. 8 Error maps obtained with the mean parameters identified from the tests using manually-defined and sensitivity-based virtual fields

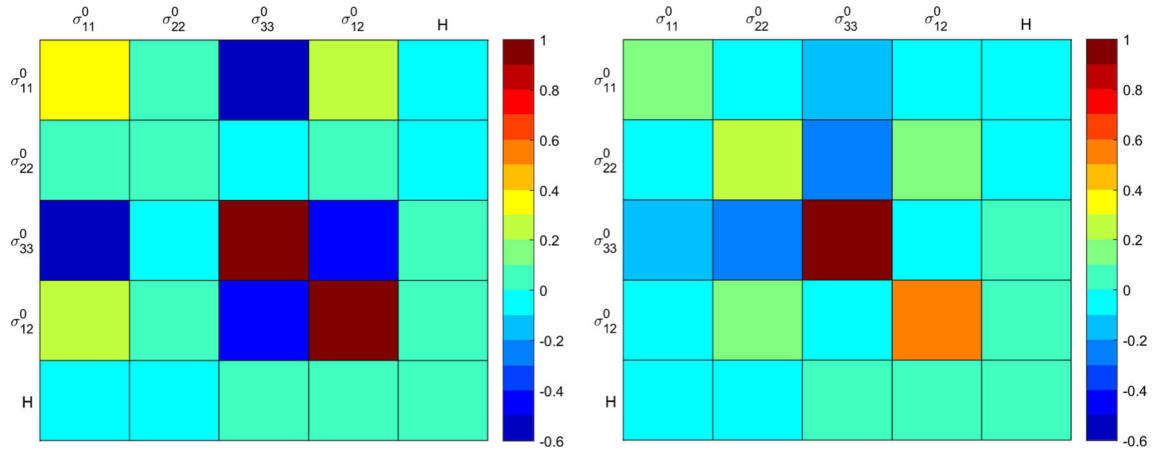

(a) $\frac{H_{UDVFs}}{6.86 \times 10^{-2}}$ (b) $\frac{H_{SBVFs}}{2.00 \times 10^{0}}$

Fig. 9 Graphical representation of Hessians computed for Hill48 model with the exact data

a much desired feature is to have balanced values on the diagonal of the Hessian matrix, as this means balanced sensitivity of the cost function to all of the parameters. The Hessian can be mathematically expressed as:

$$H_{VF} = \frac{1}{\Phi_{ident}} \frac{\partial^2 \Phi_{VF}}{\partial \chi_i \partial \chi_j} \tag{42}$$

where H_{VF} is the Hessian matrix for a given virtual field, Φ_{ident} is the value of cost function at minimum, and $\frac{\partial^2 \Phi_{VF}}{\partial \chi_i \partial \chi_j}$ is the second derivative of the cost function with respect to the material parameters. The balance of the terms is mostly dominated by the mechanics of the test, however it can be improved by a good choice of virtual fields. In order to investigate how the balance is affected by this choice, it is convenient to look at the Hessian scaled by the largest term. The curvatures of the cost function for the linear hardening case are presented in the figure below:

By comparing the two Hessians (Fig. 9) it is apparent that the SBVFs do slightly better job at balancing σ^y_{11} and σ^y_{22} (UDVFs have virtually zero sensitivity to σ^y_{22}), at a cost of decreased sensitivity to σ^y_{12}. This is consistent with the observations made regarding Fig. 8, where SBVFs noted larger error at about 45° compared to the UDVFs.

Yld2000-2D identification

In the case of the Yld2000-2D model, the main goal was to explore the comparative robustness of the UD and SB VFs when the model is richer in parameters to be identified. Only exact data from the 45° test were used, as it is already a good example of the UDVFs underperforming. The identified parameters are presented in Table 7. It is worth noting, that in the case of Yld2000-2D, the anisotropic parameters do not have any obvious physical meaning, thus comparing them on a parameter to parameter basis is not so relevant to draw conclusions as discussed in Section "Error quantification". The distribution of initial and final yield stresses are presented in Fig. 10 and the identified yield loci are shown in Fig. 11. The superiority of the SBVFs is spectacular. The distribution of anisotropy is very well identified and the main source of error comes from the hardening modulus, which is consistent with the trend observed for Hill48. In the case of the UDVFs, the identification was highly inaccurate. The parameters found were significantly different from the reference, and four out of eight reached identification constraints (set to 50% and 200% of the reference). Most likely, this is due to the generic nature of the fields. Yld2000-2D is a more complex model

Table 7 Identified values of parameters for the Yld2000-2D from a 45° test using exact data

VFs	α_1	α_2	α_3	α_4	α_5	α_6	α_7	α_8	σ_0	H	Global error [%]
Reference	1.11	1.35	1.21	1.11	1.07	0.96	1.21	1.15	256.00	855.00	[-]
UDVFs	2.22	0.68	1.68	1.49	0.54	0.48	1.04	0.77	241.39	783.14	14.6
SBVFs	1.17	1.41	1.24	1.15	1.11	1.04	1.26	1.20	264.74	934.26	1.6

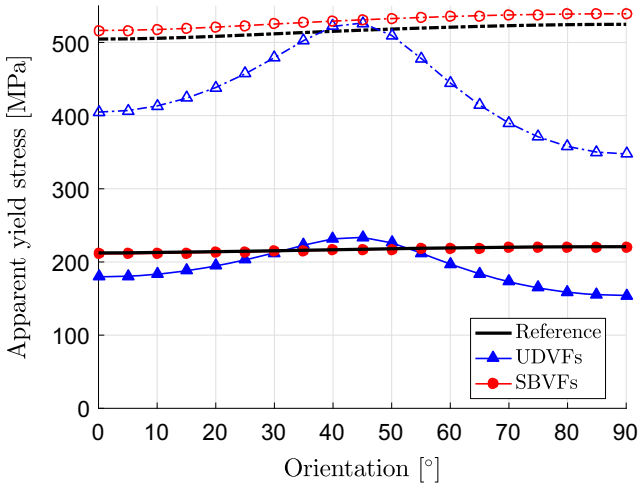

Fig. 10 Variation of the yield stress with the θ angle for the Yld2000-2D model. The identified curves were generated using parameters identified in a 45° test using noiseless data

in which each parameter has a small effect on the overall yield surface, thus extracting data correctly challenges the virtual fields much more, compared to the case of Hill48, for which the used UDVFs were specifically developed. This can be observed by looking into Hessians, computed with Eq. 42 and presented graphically in Fig. 12.

In both cases, there is a strong sensitivity to the shearing components (α_7, α_8) and a moderate one for α_4. When the UDVFs were used, there was very little sensitivity to the remaining parameters, except for the cross-correlation between α_7 and three other parameters: α_3, α_5 and α_8. In contrast, for the SBVFs, many more parameters were active. There was a cross-correlations between α_7 and all other parameters, as well as small to moderate sensitivities for all

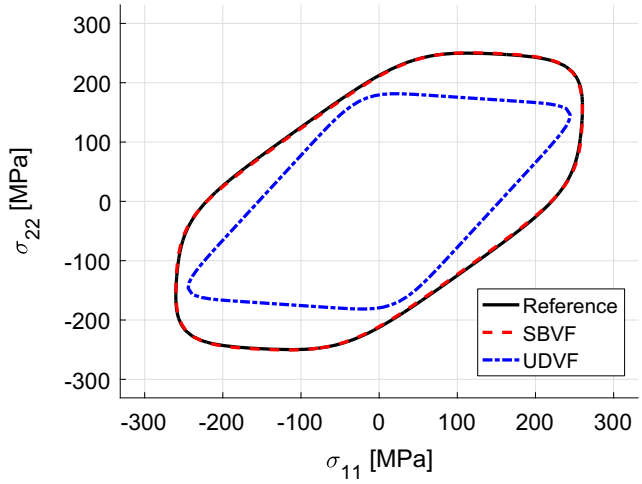

Fig. 11 Initial shape of the yield stress surface for the Yld2000-2D model. The identified curves were generated using parameters identified in noiseless 45° test data. The outline is drawn at 0 shear stress

α parameters, showing that most of the material parameters were active during the test and the SBVFs were capable of balancing their contribution.

Computational efficiency

One of the important practical aspects of the type of methodology presented here concerns computational efficiency. Information on computing times are often left out in publications on this topic and therefore, it is difficult to compare computational efficiency with competing techniques motivating our decision to report this information.

The identification was run on a standard PC with an Intel Core i5 processor (3.20GHz) and 24 GB of RAM memory. The stress reconstruction routines were coded in Matlab, however they were automatically translated to C language and called as `mex` file using Matlab coder tool. This procedure improved the efficiency of the stress reconstruction routine, which is the most computationally demanding process. The approximate running times of identification for Hill48 model can be found in Fig. 13. In case of Yld2000-2D the time needed to obtain the results were 122 and 278 hours respectively for the UDVFs and SBVFs.

In the case of Hill48 model, the identification took approximately six hours for linear hardening and between eight and ten hours in the case of power law hardening, due to the additional unknown parameter. The SBVFs are not significantly slower compared to the UDVFs, and the difference is mostly due to the additional stress reconstructions needed to calculate the incremental stress sensitivities. The number of these reconstructions can be controlled by the number of times the SBVFs are updated, and so the difference could be brought down even more. It should also be emphasized that these computing times would be significantly reduced using a compiled programming language instead of Matlab.

In the case of the Yld2000-2D model the identification times were much longer, mostly due to very slow stress reconstruction procedure, which on average took ten minutes for the chosen data density. Additionally, as 10 unknown parameters were sought, the calculations of the gradients in the minimisation problem call for many stress reconstructions, further increasing the disparity between Hill48 and Yld2000-2D. As a comparison, the FEM model used to generate the data, took 4 hours to complete.

Although the running times were very high, there are many ways in which they could be improved. First, and as stated before, efficient implementation in a fast language would lead to a significant improvement. Second, replacing the implicit stress reconstruction algorithm with a direct method such as the one used in [39] would make the stress reconstruction faster, especially in the case of Yld2000-2D

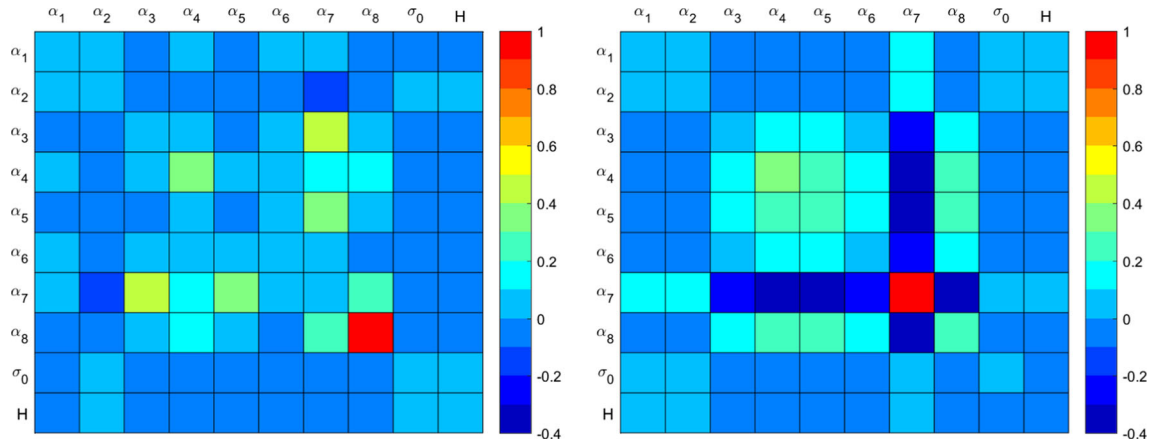

(a) $\frac{H_{UDVFs}}{2.21 \times 10^2}$ (b) $\frac{H_{SBVFs}}{3.28 \times 10^5}$

Fig. 12 Graphical representation of Hessians computed for Yld2000-2D model with the exact data

for which computing derivatives for the implicit scheme is a very computationally intensive process. The direct method is valid only for large deformation data (with plastic flow well established), however it could be coupled with the implicit algorithm for elasto-plastic transition. It was found that when the SQP algorithm was replaced with the Levenberg-Marquardt algorithm, the computations were up to 10 times faster, indicating that choosing a proper tool for minimising the cost function is crucial. For instance, the identification of the Yld2000-2D model using the SBVFs was reduced from 278 hours with SQP to merely 26 with Levenberg-Marquardt. The major advantage of the Levenberg-Marquardt algorithm is that it requires significantly fewer iteration to find a minimum, compared to the SQP algorithm. In the case of Hill48 identifications the former converged in approximately 8 iterations, compared to 130 of the latter. However, the efficiency of the Levenberg-Marquardt algorithm heavily relies on the initial guess which must be close to the solution to obtain fast convergence. This is not required by SQP which can find the solution from any starting point.

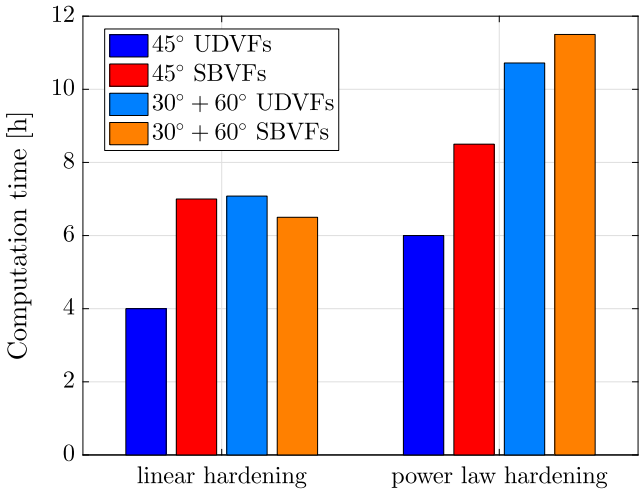

Fig. 13 Average computational time for the exact data presented in the paper (Hill48 model)

Choosing an optimal data density remains an open problem. In this work, about 60,000 spatial data points were used for the identification problem. However, this could potentially be reduced. For DIC measurements, the number of data points could be effectively controlled by means of the stepsize. Additionally, the number of load steps taken into consideration could be varied. It is worth noting that if temporal smoothing is performed on the entire collected data, even the time steps not used explicitly in the identification affect the outcome, as the information is passed through the temporal filter. The limiting factor for the temporal resolution is related to the stress reconstruction algorithm, i.e. in the case of implicit algorithms the larger the strain increments, the larger the reconstruction error. More studies are needed on the optimal number of data points for accurate reconstruction of material parameters. To define optimal spatial and temporal sampling leading to acceptable systematic and random errors, the impact of DIC parameters, and smoothing would need to be assessed with a synthetic image deformation procedure as in [37].

Conclusions and future work

In this work we extended the sensitivity-based virtual fields, originally proposed in [28] to large deformation anisotropic plasticity, which is the main novelty of this contribution. We tested the performance of the fields using a deep-notched tensile test, already used in that context by Rossi et al. [39], and found that the proposed virtual fields can be successfully applied to the problem.

It was found that for the Hill48 model both UDVFs and SBVFs were capable of correctly identifying the parameters from a single test. It must be noted that the UDVFs were developed using a trial-and-error approach by the lead author of [39]. In that context, the systematic procedure of SBVFs seems to be especially appealing as it removes the need of an informed input by the user to arrive at correct parameters. This is especially important with even more complex models such as Yld2000-2D where deriving appropriate UDVFs is a challenging task.

The main advantage of the new fields comes from the automatic generation procedure, with limited input from the investigator, involved only in setting virtual mesh density and scaling parameters. It was found before that these parameters have very limited effect on the overall identification and can be chosen *a priori* without a significant impact on the parameter values [28]. As a result, high quality virtual fields are generated for any material model, regardless of the test configuration. This opens up possible implementation in a user-friendly VFM software for non-linear model identification, like the MatchID DIC/VFM platform [29]. We demonstrated the effectiveness of the method on both Hill48 and Yld2000-2D, with the latter especially successful in comparison to the standard approach.

The identifiability of Hill48 model from a single test has been already established before [13, 39]. Interestingly, the results suggest that a single test performed at 45° may contain enough information to characterise the Yld2000-2D criterion as well. In fact, if confirmed experimentally, it would give an exciting alternative to the standard test protocol involving three uniaxial tests and one biaxial, significantly reducing the experimental effort to characterise a material. This would be possible due to the ability of the SBVFs to identify in space and time when each parameter is active and focus exclusively on those regions when identifying the parameters.

The method is currently being validated experimentally on an automotive DC04 steel alloy. The results from both UDVFs and SBVFs will be compared to the parameters identified with the standard multi-test protocol to confirm whether the Yld2000 criterion can indeed be identified from a single heterogeneous test, which would be a significant step forward to reduce identification costs and time scales.

Although a relatively simple material model was employed in this work, the presented method is general and can be used with any constitutive model. There are no limitations on the complexity of material model used within the VFM framework, given that it reconstructs stress field from measured kinematic fields (deformation gradient) and some internal state variables (that can be resolved by considering history of deformation). It must be stressed that usually the more complex the model, the more material parameters must be identified experimentally. The method proposed here allows for complete identification of material parameters given the experiment contains sufficient information. To the authors' best knowledge there is no systematic way of assessing the level of information that a test contains given a constitutive model. Investigating this in future would be certainly of importance for designing better experiments.

The new route to virtual field selection demonstrated here has potential in many applications, in particular for non-linear models with large numbers of parameters. An obvious extension would be hyper-visco-elastic models. The VFM has been applied to such materials in the past, see [17] for instance, but always with UDVFs, limiting the complexity of the considered models. Another area of interest concerns transient dynamic tests to identify the high strain rate elasto-plastic response of materials. Finally, now that a systematic route has been clearly identified to generated virtual fields automatically for non-linear laws, the problem of test optimization can be addressed. This has been studied for linear elasticity in the past, thanks to the availability of the noise-optimized virtual fields from [3], and can now be addressed for non-linear models using a procedure similar to that in [16].

Acknowledgements Dr. Frances Davis and Prof. Fabrice Pierron acknowledge support from Engineering and Physical Sciences Research Council (EPSRC) through grant EP/L026910/1. Prof. Fabrice Pierron also expresses gratitude to the Wolfson Foundation for support through a Royal Society Wolfson Research Merit Award. Mr Aleksander Marek acknowledges funding from EPSRC through a Doctoral Training Grant studentship. The authors also acknowledge the use of the IRIDIS High Performance Computing Facility, and associated support services at the University of Southampton, in the completion of this work. Dr. Davis also acknowledges support from the Leverhulme Early Career Fellowship.

Compliance with Ethical Standards

Conflict of interests Prof. Pierron is a co-founder of the MatchID company

References

1. Matlab documentation: First-order optimality measure. https://uk.mathworks.com/help/optim/ug/first-order-optimality-measure.html, last accessed 26/02/2018
2. Avril S, Badel P, Duprey A (2010) Anisotropic and hyperelastic identification of in vitro human arteries from full-field optical measurements. J Biomech 43(15):2978–2985. https://doi.org/10.1016/j.jbiomech.2010.07.004
3. Avril S, Grédiac M, Pierron F (2004) Sensitivity of the virtual fields method to noisy data. Comput Mech 34(6):439–452. https://doi.org/10.1007/s00466-004-0589-6
4. Avril S, Pierron F (2007) General framework for the identification of constitutive parameters from full-field measurements in linear elasticity. Int J Solids Struct 44(14-15):4978–5002. https://doi.org/10.1016/j.ijsolstr.2006.12.018
5. Banabic D, Aretz H, Comsa DS, Paraianu L (2005) An improved analytical description of orthotropy in metallic sheets. Int J Plast 21(3):493–512. https://doi.org/10.1016/j.ijplas.2004.04.003
6. Banabic D, Comsa SD, Balan T (2000) A new yield criterion for anisotropic sheet metals under plane stress conditions. In: Proceedings of the Cold Metal Forming 2000 Conference, pp 217–224. Cluj Napoca
7. Barlat F, Aretz H, Yoon J, Karabin M, Brem J, Dick R (2005) Linear transfomation-based anisotropic yield functions. Int J Plast 21(5):1009–1039. https://doi.org/10.1016/j.ijplas.2004.06.004
8. Barlat F, Brem J, Yoon J, Chung K, Dick R, Lege D, Pourboghrat F, Choi SH, Chu E (2003) Plane stress yield function for aluminum alloy sheets—-part 1: theory. Int J Plast 19(9):1297–1319. https://doi.org/10.1016/s0749-6419(02)00019-0
9. Barlat F, Lian K (1989) Plastic behavior and stretchability of sheet metals. part i: a yield function for orthotropic sheets under plane stress conditions. Int J Plast 5(1):51–66. https://doi.org/10.1016/0749-6419(89)90019-3
10. Barlat F, Vincze G, Grácio J, Lee MG, Rauch E, Tomé C (2014) Enhancements of homogenous anisotropic hardening model and application to mild and dual-phase steels. Int J Plast 58:201–218. https://doi.org/10.1016/j.ijplas.2013.11.002
11. Belhabib S, Haddadi H, Gaspérini M, Vacher P (2008) Heterogeneous tensile test on elastoplastic metallic sheets: Comparison between FEM simulations and full-field strain measurements. Int J Mech Sci 50(1):14–21. https://doi.org/10.1016/j.ijmecsci.2007.05.009
12. Belytschko T, Liu WK, Moran B (2006) Nonlinear finite elements for continua and structures. Wiley, Chichester
13. Bertin M, Hild F, Roux S (2017) On the identifiability of hill-1948 plasticity model with a single biaxial test on very thin sheet. Strain 53(5):e12,233. https://doi.org/10.1111/str.12233
14. Davis F, L'Hommel J, Le Cam JB, Pierron F (2017) Quantification of the compressibility of elastomers using DIC. In: Conference Proceedings of the Society for Experimental Mechanics Series, pp 199–201. Springer International Publishing. https://doi.org/10.1007/978-3-319-51439-0_47
15. Grédiac M, Auslender F, Pierron F (2001) Applying the virtual fields method to determine the through-thickness moduli of thick composites with a nonlinear shear response. Compos A: Appl Sci Manuf 32(12):1713–1725. https://doi.org/10.1016/s1359-835x(01)00029-x
16. Gu X, Pierron F (2016) Towards the design of a new standard for composite stiffness identification. Compos A: Appl Sci Manuf 91:448–460. https://doi.org/10.1016/j.compositesa.2016.03.026
17. Guélon T, Toussaint E, Cam JBL, Promma N, Grédiac M (2009) A new characterisation method for rubber. Polym Test 28(7):715–723. https://doi.org/10.1016/j.polymertesting.2009.06.001
18. Güner A, Soyarslan C, Brosius A, Tekkaya A (2012) Characterization of anisotropy of sheet metals employing inhomogeneous strain fields for Yld2000-2D yield function. Int J Solids Struct 49(25):3517–3527. 10.1016/j.ijsolstr.2012.05.001
19. Hill R (1948) A theory of the yielding and plastic flow of anisotropic metals. Proceedings of the Royal Society A: Mathematical. Phys Eng Sci 193(1033):281–297. https://doi.org/10.1098/rspa.1948.0045
20. Jansen Y, Logé RE, Manach PY, Carbuccia G, Milesi M (2016) On the benefits of a stress criterion for the simulation of cup drawing process. Int J Mater Form 10(5):707–716. https://doi.org/10.1007/s12289-016-1313-8
21. Khalfallah A, Bel Hadj Salah H, Dogui A (2002) Anisotropic parameter identification using inhomogeneous tensile test. European Journal of Mechanics - A/Solids 21(6):927–942. https://doi.org/10.1016/s0997-7538(02)01246-9
22. Kim JH, Serpantié A, Barlat F, Pierron F, Lee MG (2013) Characterization of the post-necking strain hardening behavior using the virtual fields method. Int J Solids Struct 50(24):3829–3842. https://doi.org/10.1016/j.ijsolstr.2013.07.018
23. Kim JH, Avril S, Duprey A, Favre JP (2011) Experimental characterization of rupture in human aortic aneurysms using a full-field measurement technique. Biomech Model Mechanobiol 11(6):841–853. https://doi.org/10.1007/s10237-011-0356-5
24. Kim JH, Barlat F, Pierron F, Lee MG (2014) Determination of anisotropic plastic constitutive parameters using the virtual fields method. Exp Mech 54(7):1189–1204. https://doi.org/10.1007/s11340-014-9879-x
25. Kim JH, Kim K, Han HN, Barlat F, Lee MG (2013) Strain rate dependent tensile behavior of advanced high strength steels: Experiment and constitutive modeling. Mater Sci Eng: A 559:222–231. https://doi.org/10.1016/j.msea.2012.08.087
26. Le Louëdec G, Pierron F, Sutton M, Reynolds AP (2012) Identification of the local elasto-plastic behavior of FSW welds using the virtual fields method. Exp Mech 53(5):849–859. https://doi.org/10.1007/s11340-012-9679-0
27. Lee EH (1969) Elastic-plastic deformation at finite strains. J Appl Mech 36(1):1. https://doi.org/10.1115/1.3564580
28. Marek A, Davis FM, Pierron F (2017) Sensitivity-based virtual fields for the non-linear virtual fields method. Comput Mech 60(3):409–431. https://doi.org/10.1007/s00466-017-1411-6
29. MatchID: www.matchid.eu, last accessed 29/06/2018
30. Min J, Carsley JE, Lin J, Wen Y, Kuhlenkötter B (2016) A non-quadratic constitutive model under non-associated flow rule of sheet metals with anisotropic hardening: Modeling and experimental validation. Int J Mech Sci 119:343–359. https://doi.org/10.1016/j.ijmecsci.2016.10.027
31. Montáns FJ, Benítez JM, Caminero MA (2012) A large strain anisotropic elastoplastic continuum theory for nonlinear kinematic hardening and texture evolution. Mech Res Commun 43:50–56. https://doi.org/10.1016/j.mechrescom.2012.03.001
32. Palmieri G, Sasso M, Chiappini G, Amodio D (2010) Virtual fields method on planar tension tests for hyperelasticity materials characterisation. Strain 47:196–209. https://doi.org/10.1111/j.1475-1305.2010.00759.x
33. Pannier Y, Avril S, Rotinat R, Pierron F (2006) Identification of elasto-plastic constitutive parameters from statically undetermined tests using the virtual fields method. Exp Mech 46(6):735–755. https://doi.org/10.1007/s11340-006-9822-x

34. Pierron F, Avril S, Tran VT (2010) Extension of the virtual fields method to elasto-plastic material identification with cyclic loads and kinematic hardening. Int J Solids Struct 47(22-23):2993–3010. https://doi.org/10.1016/j.ijsolstr.2010.06.022
35. Pottier T, Toussaint F, Vacher P (2011) Contribution of heterogeneous strain field measurements and boundary conditions modelling in inverse identification of material parameters. European Journal of Mechanics - A/Solids 30(3):373–382. https://doi.org/10.1016/j.euromechsol.2010.10.001
36. Promma N, Raka B, Grédiac M, Toussaint E, Cam JBL, Balandraud X, Hild F (2009) Application of the virtual fields method to mechanical characterization of elastomeric materials. Int J Solids Struct 46(3-4):698–715. https://doi.org/10.1016/j.ijsolstr.2008.09.025
37. Rossi M, Lava P, Pierron F, Debruyne D, Sasso M (2015) Effect of DIC spatial resolution, noise and interpolation error on identification results with the VFM. Strain 51(3):206–222. https://doi.org/10.1111/str.12134
38. Rossi M, Pierron F (2011) Identification of plastic constitutive parameters at large deformations from three dimensional displacement fields. Comput Mech 49(1):53–71. https://doi.org/10.1007/s00466-011-0627-0
39. Rossi M, Pierron F, Štamborská M (2016) Application of the virtual fields method to large strain anisotropic plasticity. Int J Solids Struct 97-98:322–335. https://doi.org/10.1016/j.ijsolstr.2016.07.015
40. Sanz MÁ, Montáns FJ, Latorre M (2017) Computational anisotropic hardening multiplicative elastoplasticity based on the corrector elastic logarithmic strain rate. Comput Methods Appl Mech Eng 320:82–121. https://doi.org/10.1016/j.cma.2017.02.027
41. Sasso M, Chiappini G, Rossi M, Cortese L, Mancini E (2013) Visco-hyper-pseudo-elastic characterization of a fluoro-silicone rubber. Exp Mech 54(3):315–328. https://doi.org/10.1007/s11340-013-9807-5
42. Simo JC, Ortiz M (1985) A unified approach to finite deformation elastoplastic analysis based on the use of hyperelastic constitutive equations. Comput Methods Appl Mech Eng 49:221–245. https://doi.org/10.1016/0045-7825(85)90061-1
43. Stoughton TB (2002) A non-associated flow rule for sheet metal forming. Int J Plast 18(5-6):687–714. https://doi.org/10.1016/s0749-6419(01)00053-5
44. Stoughton TB, Yoon JW (2009) Anisotropic hardening and non-associated flow in proportional loading of sheet metals. Int J Plast 25(9):1777–1817. https://doi.org/10.1016/j.ijplas.2009.02.003
45. Yoon SH, Giannakopoulos I, Siviour CR (2015) Application of the virtual fields method to the uniaxial behavior of rubbers at medium strain rates. Int J Solids Struct 69-70:553–568. https://doi.org/10.1016/j.ijsolstr.2015.04.017
46. Yoon SH, Winters M, Siviour CR (2015) High strain-rate tensile characterization of EPDM rubber using non-equilibrium loading and the virtual fields method. Exp Mech 56(1):25–35. https://doi.org/10.1007/s11340-015-0068-3
47. Zhang L, Thakku SG, Beotra MR, Baskaran M, Aung T, Goh JCH, Strouthidis NG, Girard MJA (2017) Verification of a virtual fields method to extract the mechanical properties of human optic nerve head tissues in vivo. Biomech Model Mechanobiol 16(3):871–887. https://doi.org/10.1007/s10237-016-0858-2

The first paragraph in the virtual fields method section should read:
'Quasi-static equilibrium can be expressed in so-called 'weak form' in which it is enforced as a weighted average over the entire domain, expressed here in the current (deformed) configuration $\mathscr{B}_t$, in absence of volume forces:'

The paragraph underneath Eq. 8 should read:
'where $\mathscr{B}_0$ is the considered body in the reference configuration and $\partial\mathscr{B}_0$ its boundary. This form is much more suitable for practical implementation in case of the proposed method, as the virtual fields $\mathbf{U}^*$, defined in the reference (unloaded) configuration $\mathscr{B}_0$, do not need updated virtual boundary conditions, as will become apparent later in the article. This approach has been used by most of the VFM community [36, 38, 39, 41]. Noticeably, it was demonstrated that the current configuration formulation could be successfully applied to the case of hyperelasticity as well [2, 23, 32].'

The paragraph underneath Eq. 27 should read:
'where $R_{ij} = \dfrac{\sigma^y_{ij}}{\sigma_0}$. Note that σ^y_{11} and σ^y_{22} are the yield stresses identified in planar uniaxial tests conducted at 0° and 90° respectively and σ^y_{33} is the through-thickness yield stress. Finally, σ^y_{12} is the yield stress identified under pure shear. Although the model is defined for plane stress and $\sigma_{33} = 0$, the information about σ^y_{33} can be obtained from the combination of associated flow rule assumption and Lankford coefficients. Furthermore, it was assumed that the yield stress in the hardening law is equal to σ^y_{11}, *i.e.* $\sigma_0 = \sigma^y_{11}$, as this reduces the number of variables to be identified by one, and does not affect the formulation of model.'

The units in Table 2 should be defined as follows:
$\sigma 0$: MPa; H: MPa; σ_0: MPa; K: MPa; n: [−].

Parameters in Table 3 should be changed to the following:
σ^0_{11}: $\frac{\sigma^0_{11}}{\sigma^{0(ref)}_{11}}[-]$; σ^0_{22}: $\frac{\sigma^0_{22}}{\sigma^{0(ref)}_{22}}[-]$; σ^0_{33}: $\frac{\sigma^0_{33}}{\sigma^{0(ref)}_{33}}[-]$; σ^0_{12}: $\frac{\sigma^0_{12}}{\sigma^{0(ref)}_{12}}[-]$; H: $\frac{H}{H^{(ref)}}[-]$; n: $\frac{n}{n^{(ref)}}[-]$.

Parameters in Table 4 should be changed to the following:
σ^0_{11}: $\frac{\sigma^0_{11}}{\sigma^{0(ref)}_{11}}[-]$; σ^0_{22}: $\frac{\sigma^0_{22}}{\sigma^{0(ref)}_{22}}[-]$; σ^0_{33}: $\frac{\sigma^0_{33}}{\sigma^{0(ref)}_{33}}[-]$; σ^0_{12}: $\frac{\sigma^0_{12}}{\sigma^{0(ref)}_{12}}[-]$; H: $\frac{H}{H^{(ref)}}[-]$.

Parameters in Table 5 should be changed to the following:
σ^0_{11}: $\frac{\sigma^0_{11}}{\sigma^{0(ref)}_{11}}[-]$; σ^0_{22}: $\frac{\sigma^0_{22}}{\sigma^{0(ref)}_{22}}[-]$; σ^0_{33}: $\frac{\sigma^0_{33}}{\sigma^{0(ref)}_{33}}[-]$; σ^0_{12}: $\frac{\sigma^0_{12}}{\sigma^{0(ref)}_{12}}[-]$; H: $\frac{H}{H^{(ref)}}[-]$.

Parameters in Table 6 should be changed to the following:
σ^0_{11}: $\frac{\sigma^0_{11}}{\sigma^{0(ref)}_{11}}[-]$; σ^0_{22}: $\frac{\sigma^0_{22}}{\sigma^{0(ref)}_{22}}[-]$; σ^0_{33}: $\frac{\sigma^0_{33}}{\sigma^{0(ref)}_{33}}[-]$; σ^0_{12}: $\frac{\sigma^0_{12}}{\sigma^{0(ref)}_{12}}[-]$; H: $\frac{H}{H^{(ref)}}[-]$; n: $\frac{n}{n^{(ref)}}[-]$.

Units in Table 7 should be as follows:
α_1–α_8: [-]; σ_0: MPa; H: MPa.

Chapter 5

Experimental validation of the sensitivity-based virtual fields for identification of anisotropic plasticity models.

Experimental Mechanics manuscript No.
(will be inserted by the editor)

Experimental validation of the sensitivity-based virtual fields for identification of anisotropic plasticity models.

Aleksander Marek · Frances M. Davis · Jin-Hwan Kim · Fabrice Pierron

Received: date / Accepted: date

Abstract In this work, the sensitivity-based virtual fields have been applied to identify two anisotropic plasticity models (Hill48, Yld2000-2D) using a deep-notched tensile test performed on flat samples of cold-rolled sheet of DC04 steel. The material was characterised using the standard protocol to obtain the reference sets of parameters. Deformation data was obtained during deep-notched tests using stereo digital image correlation and the virtual fields method was employed to identify material parameters. It was found that the sensitivity-based virtual fields outperform the standard user-defined virtual fields in terms of accuracy.

Keywords the virtual fields method · anisotropic plasticity · sensitivity-based virtual fields · digital image correlation · inverse identification

1 Introduction

To describe material behaviour accurately, models become increasingly complex and involve more and more material parameters that need to be identified from mechanical tests. Typically, parameters are measured with a number of simple homogeneous tests, where each test provides limited information about the inferred model. As a result, many tests are generally needed to fully characterise such material models. On the other hand, developments in full-field measurements offer the ability to collect large amounts of data with the potential to improve identification of material properties. This can be used to design a new class of tests, where deformation is heterogeneous, leading to a range of multi-axial stress states within a single specimen. Probing material behaviour under such loading provides an opportunity for a reduction of the number of tests needed for characterisation, and the development of better models.

The problem of increasing amount of experimental effort needed to characterise a material is an important one for the sheet metal forming community, where accurate characterisation of plastic anisotropy is essential. For instance, the simplest anisotropic model, Hill48 [1], requires three uniaxial tests performed at three distinct orientations ($0^\circ/45^\circ/90^\circ$) to be fully characterised for plane stress applications. The model however is well known to be performing poorly, especially under biaxial loading where it cannot accurately represent the behaviour of most commonly used alloys. Many improvements have been proposed, often involving biaxial data in the formulation, significantly increasing the experimental effort involved in identifying the models. Popular models that can accurately capture the response of sheet metals, such as: Yld89 [2], Stoughton's model of 2002 [3], BBC2000 [4], BBC2005 [5] and Yld2000-2D [6] require four tests in total: three uniaxial and one equibiaxial tests. Furthermore, there are even more complex material models such as CB2001 [7, 8] involving five uniaxial and one biaxial tests and Stoughton's model of 2009 [9] or Yld2004-18p [10] that require seven uniaxial (performed in increments of 15°) and one biaxial tests. Although these models improve the accuracy of numerical simulations, they often imply an extensive experimental effort involved in the characterisation of materials.

A possible strategy to reduce the number of experiments to identify a given model is to use full-field measurements and design heterogeneous tests from which more data could be collected, compared to homogeneous counterparts. Standard tests produce uniform/simple stress field that can be an-

A. Marek (✉) · F. M. Davis · F. Pierron
Faculty of Engineering and the Environment, University of Southampton, Highfield, SO171BJ, UK
E-mail: A.Marek@soton.ac.uk

J.-H. Kim
GIFT, Pohang University of Science and Technology, San 31 Hyoja-dong, Nam-gu, Pohang, Gyeongbuk 790-784, Republic of Korea

alytically linked to the applied load, these are generally referred to as 'statically determinate'. This approach produces a single data point on the yield surface per test. Heterogeneous, statically non-determinate tests on the other hand produce a cloud of points in the stress space, each exhibiting a unique combination of stress/strain states, to which the model can be matched. In this approach, test design and material parameters extraction from the collected data represent specific challenges, as the stress field is not known *a priori*. To identify material parameters from full-field data, inverse techniques need to be employed.

Two of the most popular inverse techniques for extracting constitutive parameters from full-field measurements are finite element model updating (FEMU) and the virtual fields method (VFM). In the former, a model of the experiment is built up using finite element method (FEM) and the experimental data are matched to their simulated counterparts. The matching can be done over the loading force, displacements, strains, or even the identified biaxial stress [11]. In the VFM, the stress equilibrium is enforced over the entire region of interest (ROI). It depends on the stress field reconstructed from the measured deformation through the assumed constitutive law and the material parameters are found such that they minimise the gap in the stress equilibrium. The method has successfully been applied to metal plasticity [12–16], composites [17], concrete [18], elastomers [19–22] and biological tissues [23, 24] to cite but a few.

One of challenges in performing a successful statistically indeterminate test is to ensure that it contains enough heterogeneity, *i.e.* a sufficiently large number of unique stress states that describe the entire constitutive model. In practice, the test is usually performed on a standard test machine and the heterogeneity is achieved by means of the geometry of the specimen. Notched samples were proven to be particularly popular for testing ductile materials. With sufficiently deep notches it is possible to activate all stress components, which is important when dealing with anisotropic materials [11, 16, 25]. An alternative is to machine a special specimen such as Σ-shaped sample in [15]. A methodical approach to design adequate heterogeneous tests is still an open problem. Recently, there were a few attempts at using optimisation techniques that iterate through a number of design variables to improve a measure for strain heterogeneity [26, 27]. For other constitutive models, test design optimization has been studied in more depth, initially using strain heterogeneity metrics as well [28], then using balanced identification uncertainty over the whole set of parameters [29, 30]. However, all failed to take into account the systematic error arising from the finite spatial resolution of the camera. The next generation of test optimization procedures relies on synthetic image deformation and minimizes the maximum identification error including the systematic error [31, 32]. Extending this strategy to elastoplasticity models is the next step.

In terms of anisotropic plasticity, a number of different test configurations were used to identify popular models, with most of the effort dedicated to Hill48, due to its popularity and simplicity. The problem was tackled as early as in 1998 by a pioneering work of Meuwissen *et al.* [33] who used a specimen with asymmetrically placed notches. They measured displacements using a discrete number of trackers, and compared them with a numerical model to fit the parameters. Since then, many approaches have been adopted to characterise Hill48 [15, 16, 25, 34–41], the Ferron model [42], Yld96 [34], Bron and Besson model [38,39] and Yld2000-2D [11, 16]. They included a mixture of tensile tests performed on specimens including geometric features such as holes or notches and non-standard biaxial tests leading to a heterogeneous state of stress. However, Hill48 has proved inadequate to accurately describe the behaviour of many anisotropic elastoplastic materials [9, 16, 38]. One of the challenges of fully characterising more advanced constitutive models such as Yld2000-2D is the activation and identification of all material parameters involved (eight or more).

In the VFM the effectiveness of parameters extraction relies on using robust virtual fields. These are spatial weight functions allowing to probe parts of the specimens for information. Traditionally, they are defined manually by the investigator using analytical functions such as polynomials, sinusoids, exponential functions etc. and are called user-defined virtual fields (UDVFs). This approach was successfully applied in the case of anisotropic plasticity by [15, 16, 43], however it was noted that the choice of virtual fields was essential for good accuracy. The choice is dependent on the expertise of the user, and might be time consuming as it involves a trial-and-error procedure. Moreover, this intuition-led choice has no reason to be optimal for the extraction of all parameters. This is particularly important for less influential parameters which may only affect the deformation fields over certain time steps and specific areas of the specimen. Recently, a new type of virtual fields has been proposed to address the limitations described above, namely the sensitivity-based virtual fields [44, 45]. These fields are automatically generated for any constitutive model, and any test geometry based on the sensitivity of reconstructed stress field to each material parameter. This framework provides enhanced flexibility and allows to tackle complex constitutive models more effectively.

In this work, we present an experimental validation of the sensitivity-based virtual fields for anisotropic plasticity. We have tested a cold-rolled sheet of DC04 steel and performed standard characterisation to obtain material parameters for Hill48 and Yld2000-2D models. Then, heterogeneous tests (deep-notched specimens) were performed along different orientations and the VFM with the SBVFs were

used to characterise the models leading to reduction of the number of tests. We have shown that the SBVFs were able to identify Hill48 model with a single test performed at 45°, and the Yld2000-2D model could be identified with three tests if the optimisation problem was constrained with the data from bulge test.

2 Theory

2.1 Brief recall of the finite deformation framework

Let us consider a body $\mathscr{B}$, where the position of particles in the reference configuration is given by $\mathbf{X}$ and in the deformed one by $\mathbf{x}$. The motion of each material point can be described by a function $\mathbf{x} = \phi(\mathbf{X}, t)$, which maps the position of every particle in the reference configuration to the current deformed configuration. The displacement field is defined as the difference between the current and the reference positions:

$$\mathbf{u}(\mathbf{X}, t) = \mathbf{x} - \mathbf{X} \tag{1}$$

The deformation gradient is defined as:

$$\mathbf{F} = \frac{\partial \mathbf{x}}{\partial \mathbf{X}} = \frac{\partial \mathbf{u}}{\partial \mathbf{X}} + \mathbf{I}, \tag{2}$$

where $\mathbf{I}$ is the second order identity tensor. Using polar decomposition, the deformation gradient can be written as the product of two second order tensors:

$$\mathbf{F} = \mathbf{V}\mathbf{R} \tag{3}$$

where $\mathbf{V}$ is the left stretch tensor and $\mathbf{R}$ is the rotation tensor. The left stretch tensor can be conveniently calculated as:

$$\mathbf{V} = \sqrt{\mathbf{F}\mathbf{F}^T} \tag{4}$$

where the root operator refers to the root of a matrix. A consequence of such mathematical description is that for every point, a local coordinate system rotates during deformation, as outlined in Fig. 1. This is an important feature to consider when the body includes a texture, as its orientation will follow any local rotations.

A convenient measure of strain, called Hencky strain, can be constructed from the left stretch tensor:

$$\boldsymbol{\varepsilon}_L = \ln \mathbf{V} \tag{5}$$

This strain measure can be used to formulate constitutive laws within the finite deformation framework. For further details on continuum mechanics the reader is referred to [46].

2.2 Constitutive models

In this study we considered two different yield models suitable for cold-rolled sheets: Hill48 and Yld2000-2D [1, 6]. The former is relatively simple extension of the von Mises criterion to account for anisotropy and the equivalent stress can be expressed as:

$$\sigma_{\text{eq}}^{\text{Hill}} = \sqrt{G\sigma_{11}^2 + F\sigma_{22}^2 + H(\sigma_{11} - \sigma_{22})^2 + 2N\sigma_{12}^2}. \tag{6}$$

The plastic potentials (R_{ij}) were used to obtain the governing parameters from an experiment:

$$\begin{cases} F = \frac{1}{2}\left[\frac{1}{R_{22}^2} + \frac{1}{R_{33}^2} - \frac{1}{R_{11}^2}\right] \\ G = \frac{1}{2}\left[\frac{1}{R_{11}^2} + \frac{1}{R_{33}^2} - \frac{1}{R_{22}^2}\right] \\ H = \frac{1}{2}\left[\frac{1}{R_{11}^2} + \frac{1}{R_{22}^2} - \frac{1}{R_{33}^2}\right] \\ N = \frac{1}{2}\frac{1}{R_{12}^2} \end{cases} \tag{7}$$

where $R_{ij} = \dfrac{\sigma_{ij}^y}{\sigma_0}$. Note that σ_{11}^y and σ_{22}^y are the yield stresses identified in planar uniaxial tests conducted at 0° and 90° respectively and σ_{33}^y is the through-thickness yield stress. Finally, σ_{12}^y is the yield stress identified under pure shear. Although the model is defined for plane stress and $\sigma_{33} = 0$, the information about σ_{33}^y can be obtained from the combination of associated flow rule assumption and Lankford coefficients. The reference yield stress was assumed to coincide with σ_{11}^y, *i.e.* $\sigma_0 = \sigma_{11}^y$, as this reduces the number of variables to be identified by one, and does not affect the formulation of model. Additionally, plane stress was assumed, as the tested samples were thin relative to their in-plane dimensions, and associated flow rule was used.

Yld2000-2D was developed strictly for plane stress condition for which the equivalent stress can be calculated as:

$$\sigma_{\text{eq}}^{\text{Yld}} = \left[\frac{1}{2}\left(|X_1' - X_2'|^a + |2X_2'' + X_1''|^a + |2X_1'' + X_2''|^a\right)\right]^{1/a} \tag{8}$$

where a is an exponent based on the metal micro-structure ($a = 8$ for FCC and $a = 6$ for BCC) and X_1', X_2' and X_1'', X_2'' are the principal values of two stress tensors $\boldsymbol{X}'$, $\boldsymbol{X}''$ which are defined as linear combinations of the Cauchy stress:

$$\begin{cases} \boldsymbol{X}' = \mathbf{L}'\boldsymbol{\sigma} \\ \boldsymbol{X}'' = \mathbf{L}''\boldsymbol{\sigma} \end{cases} \tag{9}$$

Matrices $\mathbf{L}'$ and $\mathbf{L}''$ are given by:

$$\mathbf{L}' = \begin{bmatrix} \frac{2\alpha_1}{3} & -\frac{2\alpha_1}{3} & 0 \\ -\frac{2\alpha_2}{3} & \frac{2\alpha_2}{3} & 0 \\ 0 & 0 & \alpha_7 \end{bmatrix} \tag{10}$$

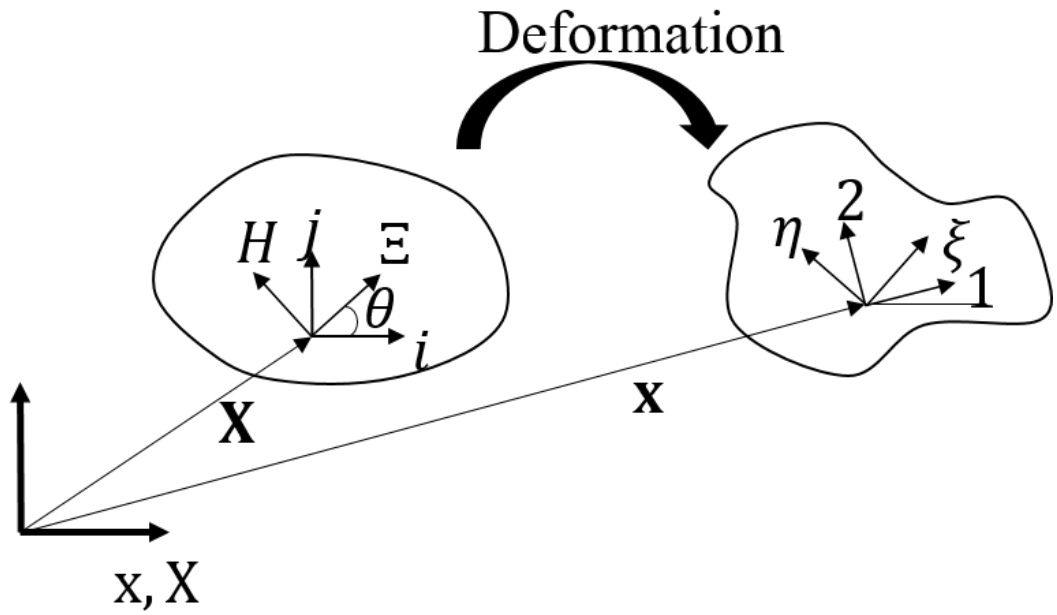

Fig. 1 Definition of coordinate systems, **X** is the initial position of a material point and **x**, its current position, (i,j) is the initial orientation of the local coordinate system, $(1,2)$ is the corotational system, (Ξ,H) is the material coordinate system in the reference configuration and (ξ,η) is the material coordinate system in the current configuration

$$\mathbf{L}'' = \begin{bmatrix} \frac{8\alpha_5-2\alpha_3-2\alpha_6+2\alpha_4}{9} & -\frac{4\alpha_6-4\alpha_4-4\alpha_5+\alpha_3}{9} & 0 \\ -\frac{4\alpha_3-4\alpha_5-4\alpha_4+\alpha_6}{9} & \frac{8\alpha_4-2\alpha_6-2\alpha_3+2\alpha_5}{9} & 0 \\ 0 & 0 & \alpha_8 \end{bmatrix} \tag{11}$$

The model involves 8 independent parameters, α_1–α_8, which are generally obtained using 3 tensile tests performed at 0°, 45°, 90°, a biaxial test (bulge test), as well as a test for measuring $r_b = \frac{\dot{\varepsilon}_{xx}}{\dot{\varepsilon}_{yy}}$ at balanced equibiaxial loading. Again, associated flow rule was assumed here as well.

A non-linear isotropic hardening power law (Ludwik) was chosen with the following form:

$$\bar{\sigma} = \sigma_0 + K(\bar{\varepsilon}^p)^n \tag{12}$$

where σ_0, K, n are material parameters and $\bar{\varepsilon}^p$ is the equivalent plastic strain integrated throughout the history of deformation.

The constitutive computations are performed in a material coordinate system (ξ,η) which is aligned with manufacturing directions: rolling (RD) and transverse (TD) directions. Since the kinematic fields are computed in the global frame (i,j), for each data point strain and stress tensors need to be rotated to the material frame:

$$\Delta\boldsymbol{\varepsilon}_L^{(\xi,\eta)} = \mathbf{R}^T\mathbf{R}_{mat}^T\Delta\boldsymbol{\varepsilon}_L^{(i,j)}\mathbf{R}_{mat}\mathbf{R}. \tag{13}$$

where $\mathbf{R}_{mat}$ is a rotation tensor projecting the global frame onto the material frame in the unloaded configuration (Fig. 1). Once the stress tensor is reconstructed it is rotated back to the global frame in which the VFM equations are formulated.

2.3 Virtual Fields Method

The Virtual Fields Method is an inverse technique to identify material parameters from full-field measurements. It relies on the force equilibrium through the principle of virtual work (PVW). In the case of static loading under absence of body forces, it can be expressed in the reference body configuration as [47]:

$$-\int_{\mathscr{B}_0}\mathbf{P}:\frac{\partial\mathbf{U}^*}{\partial\mathbf{X}}d\mathscr{B}_0 + \int_{\partial\mathscr{B}_0}(\mathbf{PN})\cdot\mathbf{U}^*d\partial\mathscr{B}_0 = 0 \tag{14}$$

where $\mathscr{B}_0$ is the considered body in the reference configuration, $\partial\mathscr{B}_0$ its boundary, **N** is the outwards vector of $\partial\mathscr{B}_0$, **P** is the 1st Piola-Kirchhoff stress tensor and $\mathbf{U}^*$ is a vectorial test function called virtual displacement. Virtual displacement fields need to be continuous and piecewise differentiable.

The stress tensor (**P**) is directly reconstructed from measured kinematic fields by means of an assumed constitutive law and a guessed set of material parameters ($\boldsymbol{\chi}$). The validity of the guess is assessed by the residual value evaluated with Eq. 14.

As the full-field measurements provide spatially rich data, the first integral in Eq. 14 can be replaced with a discrete sum of all points in the region of interest (ROI). By selecting

virtual displacements as constant across $\partial\mathscr{B}_0$, the second integral in Eq. 14 can be replaced by a product of $\mathbf{U}^* \cdot \mathbf{F}^{load}$, where $\mathbf{F}^{load}$ is the total load measured with the test machine load cell. This procedure replaces generally unknown distribution of tractions over the loading edges with a quantity easy to measure.

Since the PVW has to be evaluated over the entire volume, but the measurements are taken only at the surface of the specimen, it is necessary to make some assumption regarding the variation of kinematic fields through the thickness. If the specimen is thin, plane stress assumption is reasonable and the PVW can be expressed in terms of a cost function as:

$$\Phi(\boldsymbol{\chi}) = \sum_{i=1}^{\text{nVF}} \left\{ \sum_{t=1}^{\text{nTime}} \left[\overbrace{\sum_{j=1}^{\text{nPts}} \left(\mathbf{P}^j(\boldsymbol{\varepsilon}_L, \boldsymbol{\chi}) : \frac{\partial \mathbf{U}^{*j^{(i)}}}{\partial \mathbf{X}} S^j h \right)}^{W^*_{int}} - \underbrace{\mathbf{U}^{*(i)} \cdot \mathbf{F}^{load}}_{W^*_{ext}} \right]^2 \right\}. \quad (15)$$

where S^j is the surface area of each measurement point and h is the thickness of specimen. This cost function can include a number of independent virtual fields and load levels (time steps). The identification is carried out by minimising Eq. 15 with respect to the sought material parameters.

It is worth noting that Eq. 14 is formulated in terms of the 1st Piola-Kirchhoff stress tensor, while most constitutive laws relate kinematic fields to the Cauchy stress tensor. The former can be obtained from the latter with:

$$\mathbf{P} = \det(\mathbf{F})\boldsymbol{\sigma}\mathbf{F}^{-T} \quad (16)$$

where $\mathbf{F}$ is the deformation gradient tensor. Since in reality the deformation is fully 3D, so is the deformation gradient and this has to be reflected in the computation of its determinant. By assuming negligible out-of-plane shearing, the determinant can be computed as:

$$\det(\mathbf{F}) = \mathrm{F}_{33}(\mathrm{F}_{11}\mathrm{F}_{22} - \mathrm{F}_{12}\mathrm{F}_{21}). \quad (17)$$

Since the in-plane values are directly measured the only unknown is the out-of-plane component. It can be estimated with a constitutive law (*e.g.* assuming plane stress elasticity and isochoric plastic flow), or can be directly measured by means of back-to-back camera systems as shown in [48].

The virtual displacement (and its spatial derivatives, later simply referred to as virtual fields (VFs)) spatially probe the reconstructed stress field for information. As a result, the choice of VFs is crucial and has strong influence on identification quality. Ideally, VFs should be focused on areas rich in information and minimize the influence of the measurement noise. In the case of non-linear material models, selecting VFs usually relies on the manual definition by means of simple mathematical functions, such as polynomials or sinusoids [15,16]. The effectiveness of these VFs called user-defined VFs (UDVFs) heavily depends on the expertise of the investigator. It is worth noting that usually UDVFs are kept constant across the history of deformation, whereas the information evolves as the loading changes. As a result, a VF that is relevant *e.g.* for identification of yield-related parameters might not be as effective for identification of the hardening law. Recently, a new automated method for generating high-quality virtual fields has been proposed [44,45]. These fields called sensitivity-based virtual fields (SBVFs), are designed to highlight areas rich in information for each parameter separately, resulting in better identification, without significant input from the investigator.

2.4 Sensitivity-based virtual fields

The sensitivity-based virtual fields [44,45] are automatically generated for every material parameter. These SBVFs are good at finding information about each parameter separately and coupling them together in one cost function to identify all material parameters. Each virtual field is constructed based on the sensitivity of the reconstructed stress field to a given material parameter. The procedure for generating virtual fields is discussed in details in [44] with the extension to large-deformation in [45]. Here, we shortly summarize the necessary steps to generate SBVFs.

For each material parameter a map of stress sensitivity is calculated through:

$$\delta\mathbf{P}^{(i)}(\boldsymbol{\chi}, t) = \mathbf{P}(\boldsymbol{\chi} + \delta\chi_i, t) - \mathbf{P}(\boldsymbol{\chi}, t) \quad (18)$$

where $\delta\chi_i$ is a small variation of parameter χ_i, typically $\delta\chi_i = -0.20 - -0.10\chi_i$. The fields are calculated at all considered load levels, generating a temporal map of stress sensitivities.

In plasticity, the response is history dependent with yield-related parameters being active from the onset of plasticity throughout the whole history, while hardening parameters are active only during accumulation of plastic deformation. In order to decouple the influence of yield stress from that of hardening, a new stress sensitivity field is derived, called the incremental stress sensitivity field:

$$\delta\widetilde{\mathbf{P}}^{(i)}(\boldsymbol{\chi}, t) = \frac{\delta\mathbf{P}^{(i)}(\boldsymbol{\chi}, t) - \delta\mathbf{P}^{(i)}(\boldsymbol{\chi}, t-1)}{\Delta t}. \quad (19)$$

These fields highlight the information about a given parameter in the test and are an excellent candidate for virtual fields. In order to apply them in the VFM, virtual fields are generated such that the spatial derivative of virtual displacement fields matches the incremental stress sensitivity fields in a least-square sense. Additionally, the VFs need to be constructed in a way that the corresponding virtual displacement

field is known. To achieve that, a virtual mesh is employed to express virtual fields using piecewise linear functions. It consists of linear quadrilateral elements enclosing the ROI, which are used to express both virtual displacement and virtual strains fields based on the nodal values through interpolation functions.

To construct SBVFs, a global strain-displacement map is constructed: for each data point, the spatial derivatives of the virtual displacement are written as functions of the nodal virtual displacements through the element shape functions. All such equations are concatenated in one matrix ($\mathbf{B}_{glob}$). The matrix is then modified to account for the wanted virtual boundary conditions (e.g. $\mathbf{U}^* = \text{const}$ over $\partial\mathscr{B}_0$), yielding the modified virtual strain-displacement matrix: $\bar{\mathbf{B}}_{glob}$. Then, the incremental stress sensitivity map is projected in a least-square sense onto the virtual mesh, using a pseudo-inverse of $\bar{\mathbf{B}}_{glob}$:

$$\mathbf{U}^{*(i)}(t) = \text{pinv}(\bar{\mathbf{B}}_{glob})\delta\widetilde{\mathbf{P}}^{(i)}(\boldsymbol{\chi},t). \tag{20}$$

Finally, the identified virtual displacements are used to calculate virtual fields at all data points:

$$\frac{\partial \mathbf{U}^{*(i)}}{\partial \mathbf{X}} = \mathbf{B}_{glob}\mathbf{U}^{*(i)}. \tag{21}$$

The procedure yields a separate virtual field for every material parameter, at every data point and every time step which is then used to evaluate Eq. 15.

3 Experimental procedure

3.1 Specimen preparation

Specimens were water-jet cut out of a cold-rolled sheet of DC04 low-carbon alloy steel with a nominal thickness of 1.5 mm. Three geometries were tested: a standard dogbone (DB) specimen, a rectangular specimen for bulge test and a deep-notched (DN) specimen for heterogeneous test (Fig. 2). The specimens surfaces were first cleaned with sandpaper to remove oxides and then coated with a rubber-based white paint (Rust-oleum Peel coat, white matt finish) to provide good contrast for black speckles. An optimised speckle pattern [49] was printed on the specimen using a flat-bed printer (Canon Océ Arizona 1260 XT) which provided good consistency and reproducibility. An average speckle size of approximately 65 µm was achieved (Fig. 3).

3.2 Experimental set-up

3.2.1 Tensile testing

Both DB and DN samples were tested using a servo-hydraulic test machine with a 100 kN load cell and hydraulic grips.

Table 1 Summary of the tests performed.

Name of specimen	Angle (α) to the RD	Number of samples
DB-0	0	3
DB-90	90	3
DB-45	45	3
DN-30	30	3
DN-45	45	4
DN-60	60	3

Deformation was measured using a stereo- digital image correlation (DIC) set-up, with two digital Manta G-504b cameras (5 Mpx), instrumented with 105 mm lenses and polarisers. A LED light panel equipped with a polariser was used to illuminate the samples. By setting cross-polarization specular reflection was minimised which resulted in a grey-level histogram spread across most of the dynamic range of the cameras. The reference images for correlation were taken while maintaining zero load; the specimen was loaded in displacement control divided into three phases: slow rate (elastic range), medium rate (transition to high rate) and high rate where majority of plastic deformation happened, as indicated in Fig. 5. The images were taken every 1 s and synchronised with the force measured from the load cell. The set-up is illustrated in Fig. 4. The summary of tested samples is presented in Table 1.

3.2.2 Bulge tests

Since the yield stress and r-value information in balanced biaxial state is required for determination of the anisotropic constitutive parameters, the hydraulic bulge test was carried out using an Erichsen bulge/FLC tester model 161.

A steel sheet specimen is mounted on the bulge test apparatus as in Fig. 6. Then the specimen is clamped between the lower blank holder and the upper die. To prevent slipping of the specimen during the test, plastic flow is restricted with a drawbead and high blank holding force. The diameter of the area of interest in the test device is 200 mm. The hydraulic pressure is applied on the bottom side of the specimen to produce bulging and plastic deformation.

A stereo digital image correlation technique was used for measurement of curvature and strain fields as shown in Fig. 7. Two 2448 $\times$ 2048 pixels 14 bit CCD cameras were used for the measurement. The important correlation variables chosen in the DIC analysis were: subset: 41, step: 7, image pixel size: 0.117 mm.

In the bulge test, the biaxial stress-strain curve is derived from the membrane stress and the thickness strain near the pole of the bulged specimen [50].

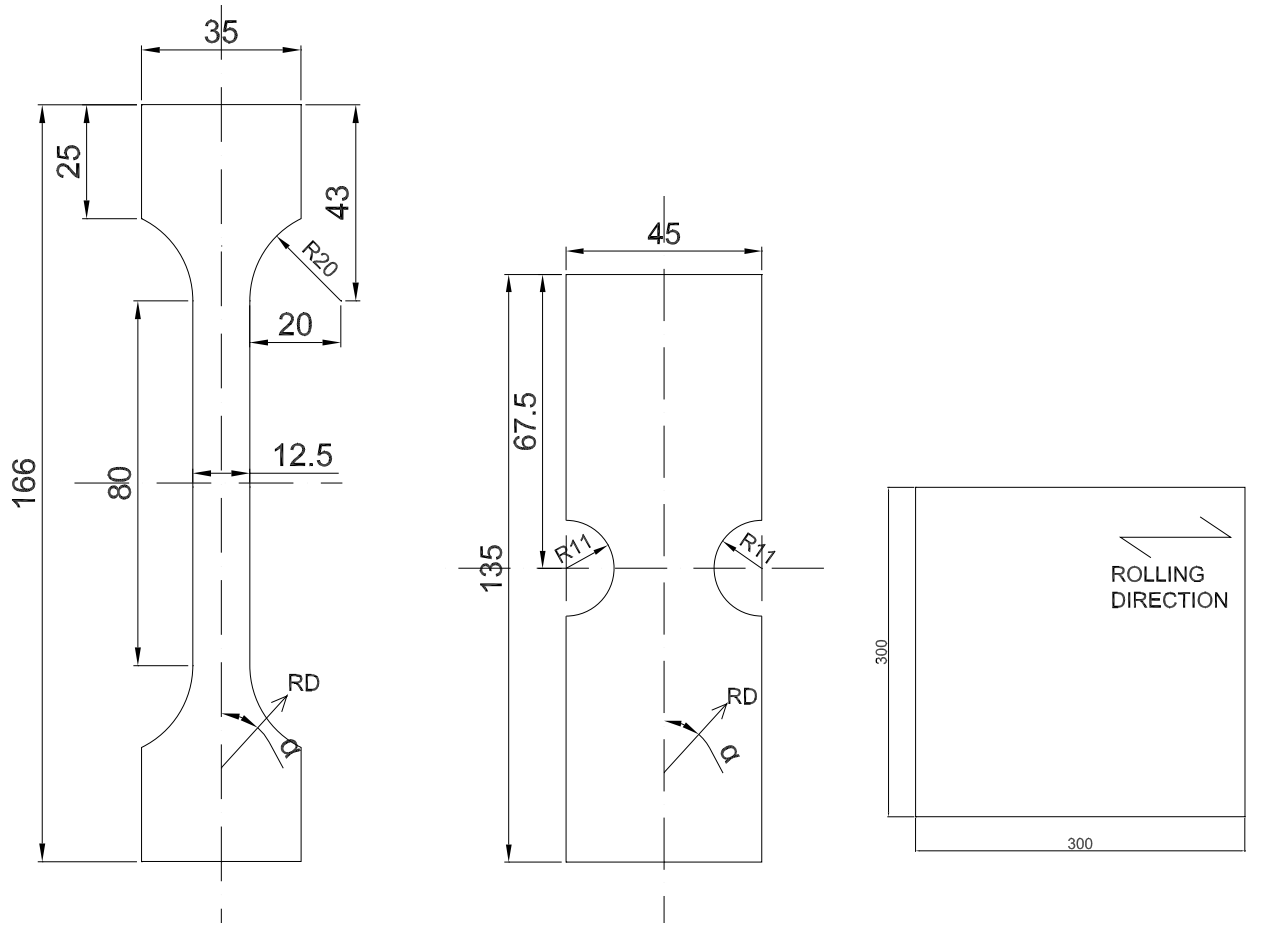

(a) Dogbone (DB) specimen (b) Deep-notched (DN) specimen (c) Bulge specimen (not to scale with (a) and (b))

Fig. 2 Geometry of the specimens used in the test. Dimensions in mm.

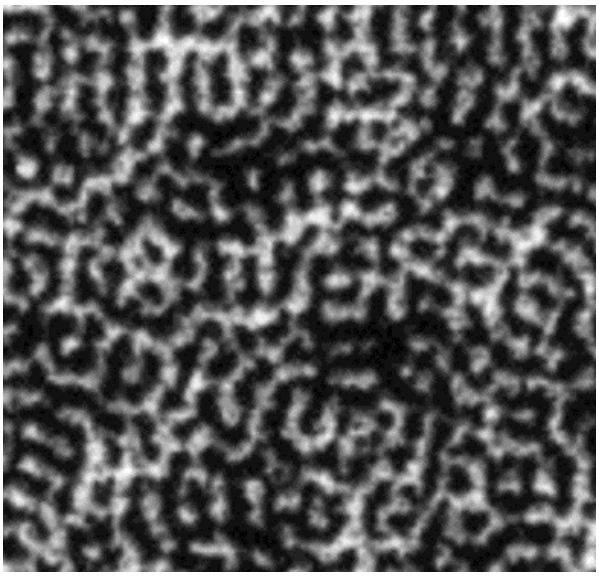

Fig. 3 Quality of the printed speckle pattern. Speckles are approximately 65 µm across.

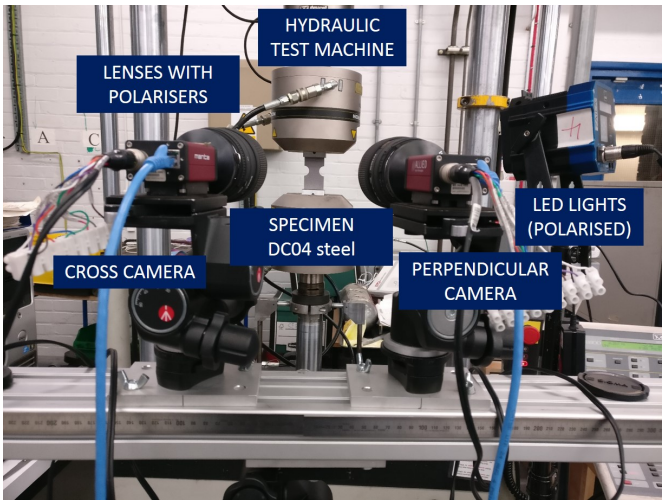

Fig. 4 Experimental set-up.

In membrane theory of a thin-walled pressure vessel, stress is calculated as:

$$\sigma = \frac{pR}{2t} \tag{22}$$

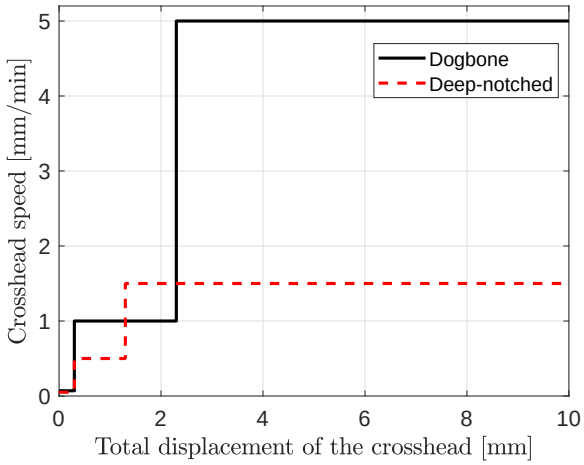

Fig. 5 Loading rate used in the tensile tests.

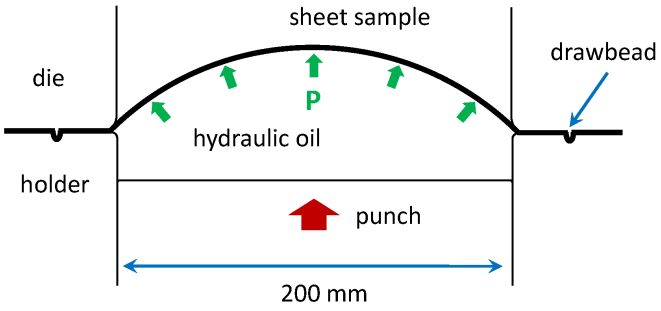

Fig. 6 Schematic diagram of the bulge test.

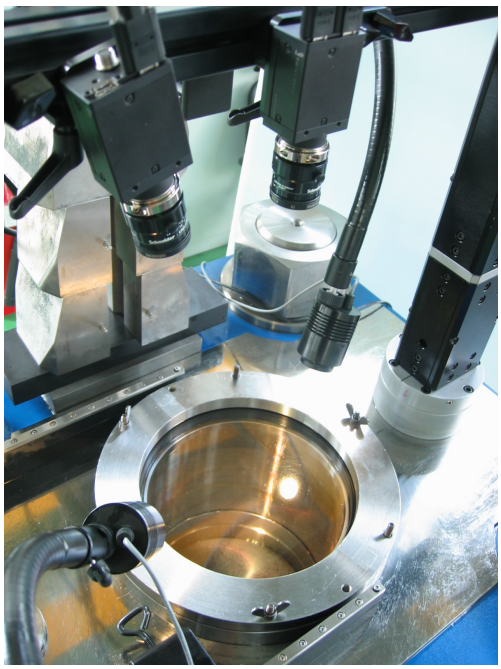

Fig. 7 View of the bulge test experimental set-up.

where p is the pressure obtained from a pressure sensor, R the current radius of curvature and t the current thickness. The current thickness is calculated from:

$$t = t_0 \exp \varepsilon_t \tag{23}$$

where t_0 is the initial thickness and ε_t the thickness strain ($\varepsilon_t \approx -\varepsilon_1 - \varepsilon_2$, where ε_1 and ε_2 are major and minor strains). The current radius of curvature R is obtained from:

$$R = \frac{1}{\kappa} \tag{24}$$

where κ is the curvature.

Two specimens were tested and it was found that the deviation was very small between the two membrane stress-thickness strain curves.

3.3 Data processing

3.3.1 Dogbone specimens

Raw grey-level images were exported to a DIC package (MatchID 2018.2.2) and processed using stereo-DIC. Due to significant plastic deformation of the specimen upstream of the gauge section the small ROI that remained in the camera field of view for the whole test was selected. The camera parameters and DIC settings are summarized in Table 2. The measured fields were used to reconstruct the stress-strain curve and identify yield stress and hardening law for each of orientation ($0^\circ/45^\circ/90^\circ$), using the uniform and uni-axial stress assumptions. Von Mises plasticity was used as in a homogeneous test anisotropy cannot be inferred. The average longitudinal plastic strain was plotted against the average transverse plastic strain, and a straight line was fitted to the data in order to obtain Lankford coefficient [51]. The line passed through the origin and was fitted to the data corresponding to 8–12% range of plastic deformation.

3.4 Deep-notched specimen

Again, raw grey-level images were exported to MatchID and displacements in the gauge section were obtained using stereo-DIC, with the parameters presented in Table 3. The data was exported to Matlab, where displacements were temporarily and spatially smoothed and then down-sampled to a number of load levels (time steps). Gaussian filter (defined with σ_{smooth} parameter) with edge correction was used for spatial smoothing and Savitzky-Golay filter was used for temporal smoothing, characterised with two parameters: polynomial order m_{TS} and the window size w_{TS}. The down-sampling purpose was to improve signal-to-noise ratio of strain increments and reduce the computational effort. The frames were selected such that the maximal measured strain was about

Table 2 DIC settings for a dogbone specimen.

Technique used	Stereo Digital Image Correlation
Sensor (px) and digitization	2452 × 2056, 8-bit
Camera noise (% of range)	1.0
Lens, polariser and imaging distance	105 mm (F-mount), linear, 1 m
Frame rate (Hz)	1
Pixel to mm conversion	1 px = 20 µm
ROI (mm)	12.5 × 38.0
DIC software	MatchID 2018.2.2
Subset size, step size	27, 7
Interpolation, shape functions, correlation criterion, stereo transformation	Bicubic spline, affine, ZNSSD, affine
Reference image	Updated (incremental correlation)
Pre-smoothing	Gaussian, 5 px
Displacement resolution	0.02 px, 0.4 µm
Edge data	Extrapolated from shape functions
Strain computation	Central finite difference
Strain resolution (raw)	1000 $\mu\varepsilon$

Table 3 DIC settings for a deep-notched specimen.

Technique used	Stereo Digital Image Correlation
Sensor (px) and digitization	2452 × 2056, 8-bit
Camera noise (% of range)	0.8
Lens, polariser and imaging distance	105 mm (F-mount), linear, 1 m
Frame rate (Hz)	1
Pixel to mm conversion	1 px = 16 µm
ROI (mm)	30.0 × 18.0
DIC software	MatchID 2018.2.2
Subset size, step size	21, 7
Interpolation, shape functions, correlation criterion, stereo transformation	Bicubic spline, quadratic, ZNSSD, affine
Reference image	Fixed
Pre-smoothing	Gaussian, 5 px
Displacement resolution	0.01 px, 0.25 µm
Edge data	Extrapolated from shape functions
Strain computation	Central finite difference
Strain resolution (raw)	600 $\mu\varepsilon$
Displacement spatial smoothing: filter, magnitude	Gaussian (with edge corrections), 2
Displacement temporal smoothing: filter, order, window	Savitzky-Golay, 3, 11

10% as that was the maximal strain level used in the standard characterisation. Central finite difference was used to compute kinematic data (deformation gradient, rotation tensor, Hencky logarithmic strains), which were then passed to an in-house VFM code to identify the material parameters.

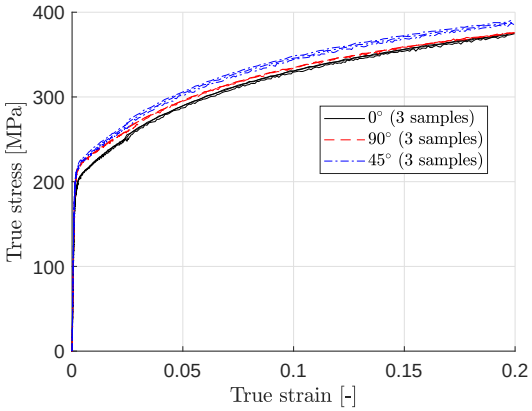

Fig. 8 Stress-strain curves measured with the dogbone tests.

4 Results and discussion

4.1 Dogbone testing

For each of the orientations (0°/45°/90°), three specimens were tested. The measured true stress-strain curves are presented in Fig. 8. A visible bump around the strain value of 3% is believed to be caused by the step change in the crosshead velocity as indicated in Fig. 5 and is consistently seen in all collected data (including DN samples). The curves were used to identify the hardening parameters (Eq. 12) and coefficients for Hill48 (Eq. 6) and Yld2000-2D (Eq. 8). The hardening law was identified using strain of up to 10%, as at the higher deformation the assumed hardening model does not capture the material behaviour accurately. This could be improved upon in the future, however the main objective of this contribution is to demonstrate the effectiveness of the SBVFs, as opposed to improving constitutive description of a material. Apart from the yield stress defining the hardening law (σ_0), a 0.2% offset yield stress ($\sigma^y_{0.002}$) was identified to quantify the anisotropy between orientations.

Longitudinal plastic strain was plotted against transverse plastic strain as shown in Fig. 9. The Lankford coefficients were identified in the range of 8%–12%. Across all samples the trend has shown good linear relationship with a little variation between different samples. All of the identified parameters are presented in Table 4.

The ratios of flow stress in each direction to the flow stress in RD have been investigated under different values of plastic work. This is now a standard practice in evaluating anisotropy of metal sheets, as the ratios are difficult to identify reliably at low levels of plastic deformation, especially when the bulge test is employed [10]. The obtained curves are presented in Fig. 10.

Clearly, the anisotropy in yield stress changes rapidly at low deformation levels. This has to be taken into consideration when selecting the reference parameters for comparison

Table 4 Parameters identified using dogbone specimens. The uncertainty is presented as a single standard deviation.

Specimen	$\sigma^y_{0.002}$ [MPa]	σ_0	K [MPa]	n [-]	$r_{0.08-0.12}$ [-]
DB-0	203 ± 1	164 ± 2	459 ± 4	0.43 ± 0.01	1.90 ± 0.08
DB-45	218 ± 3	185 ± 3	475 ± 5	0.46 ± 0.01	1.35 ± 0.09
DB-90	217 ± 2	185 ± 1	445 ± 5	0.47 ± 0.01	2.05 ± 0.13

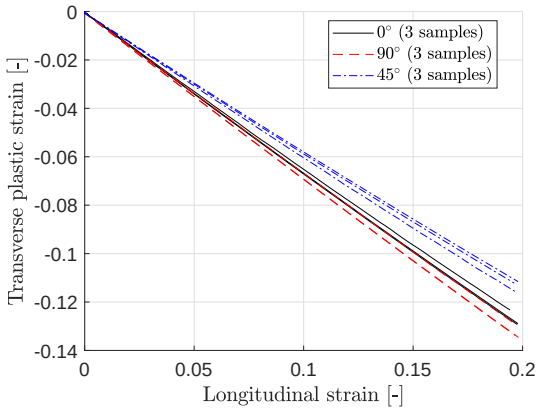

Fig. 9 Longitudinal versus transverse plastic strains measured using dogbone samples. The data was used to calculate Lankford coefficients in the range of 8%–12%.

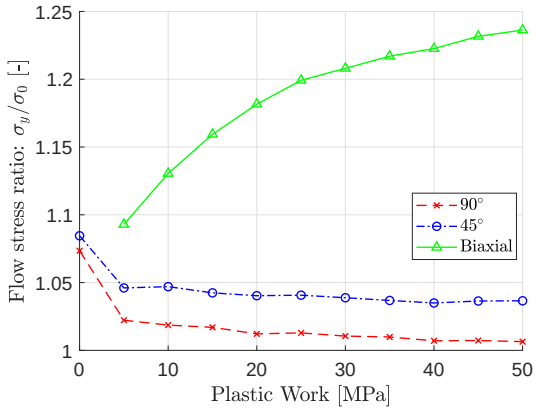

Fig. 10 Variation of flow stress ratios with plastic work.

with the DN results. It is reasonable to consider the average ratios based on plastic work above 10 MPa and more: 1.014 for 90° and 1.040 for 45°. The ratios were then used to calculate the yield stresses at 90° and 45° degrees from the hardening at 0°:

$$\bar{\sigma} = \bar{\sigma}^y_{11} = 164 + 459(\bar{\varepsilon}^p)^{0.43} \tag{25}$$

resulting in: $\sigma_{45} = 1.040 \times \sigma_0 = 170.56$ MPa and $\sigma_{90} = 1.014 \times \sigma_0 = 166.30$ MPa.

The collected data was used to obtain Hill48 parameters in two ways: using all Lankford coefficients and σ_0 for DB-0, or using σ_0 from all tests and the Lankford coefficient for DB-90 [52]. The variation of the initial yield stress and Lankford coefficient with orientation of material is presented in Fig. 11. The corresponding parameters are presented in Table 5. Importantly, the two sets differ only by the magnitude of σ^y_{12} which drives the values at 45°.

The biaxial flow stress (σ_b) and the strain ratio at balanced biaxial loading ($r_b = 0.77$) were measured in the bulge test. The ratio of σ_b to the RD flow stress as a function of work hardening is presented in Fig. 10. The equibiaxial yield stress varies significantly at low level of deformation due to differential hardening [53]. This ultimately leads to a set of different Yld2000-2D surfaces identified from the standard tests, two of the surfaces identified (with ratios taken at 10 and 25MPa) are presented in Fig. 12. As seen from the plot, the biaxial yield stress is over-predicted when Hill48 is used, due to lack of flexibility of the model.

Naturally, Yld2000-2D offers much better fit to the experimental data as demonstrated in Fig. 11, where the variation in both yield stress and Lankford parameters is captured correctly with a single set of parameters.

The identified parameters for Yld2000-2D models are presented in Table 6 for two different levels of work hardening (10 MPa and 25 MPa).

4.2 Deep-notched test

Three directions were tested: (30°/45°/60°), so that different test configurations could be combined together in a single test function. For instance, by combining two tests performed at 30° and 60°, richer data is available to identify the model, which should improve accuracy of identification. As indicated in Tables 2–3, DN tests exhibited smaller strain error on unsmoothed data. This is believed to be caused by slightly smaller pixel size, as well as better lightning set-up during DN experiments.

Figure 13(a) shows an image of a typical specimen in the unloaded configuration. Only the region bounded by the solid box was correlated with the DIC and the data corresponding to the dashed box was then passed on to the identification routine. The strain fields obtained at 10.5 kN (45° specimen) are presented in Figs. 13(b)–13(d). The base of white paint did not fail during the experiment, however it debonded from the specimen when the neck started to develop, see Fig. 14. If observation of the strain localization was of interest, the base layer could be removed, and white speckles could be used instead of black ones. In that case,

Table 5 Reference parameters for Hill48 identified from dogbone testing.

Model fitted to	σ^y_{11} [MPa]	σ^y_{22} [MPa]	σ^y_{33} [MPa]	σ^y_{12} [MPa]
Yield stresses	164.0	166.3	201.2	94.1
Lankford coefficients	164.0	166.1	201.2	104.6

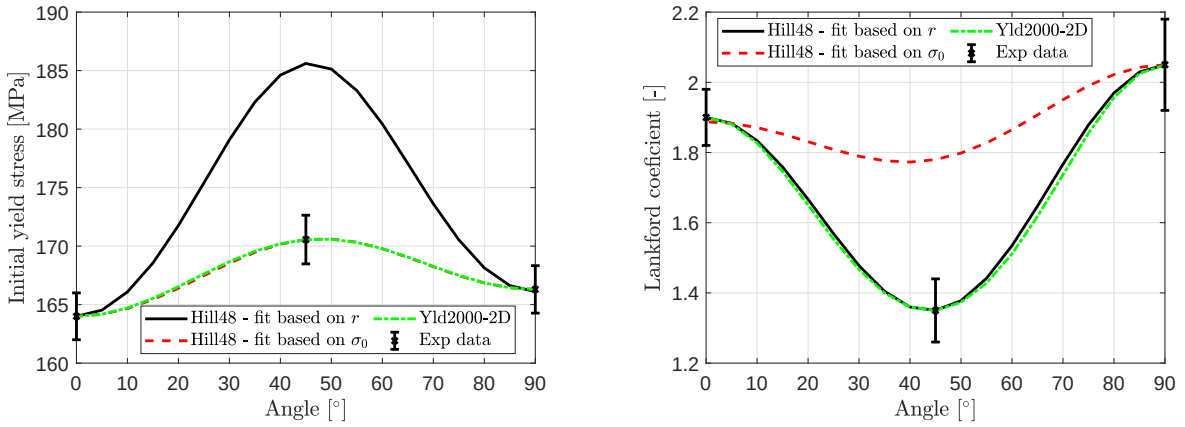

(a) Variation of the initial yield stress.

(b) Variation of Lankford coefficient.

Fig. 11 Variation of yield stress and r parameter with orientation of the material obtained using Hill48 and Yld2000-2D models.

Table 6 Reference parameters for Yld2000-2D identified from dogbone testing and the bulge test.

Plastic work [MPa]	Corresponding strain at 0° [%]	α_1 [-]	α_2 [-]	α_3 [-]	α_4 [-]	α_5 [-]	α_6 [-]	α_7 [-]	α_8 [-]
10	4.4	1.071	1.000	0.774	0.899	0.923	0.880	0.975	1.010
25	9.7	1.061	0.994	0.663	0.879	0.899	0.740	0.964	1.092

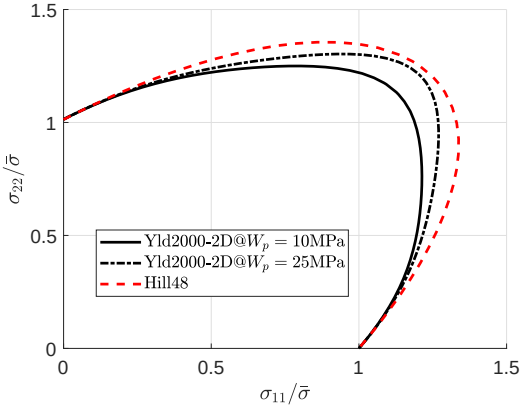

Fig. 12 Identified yield surfaces using the standard testing protocol using two models: Hill48 and Yld2000-2D.

the contrast could be achieved by means of the material surface, combined with cross-polarization of light to remove the specular reflection.

Displacements obtained in MatchID were exported to Matlab, temporarily smoothed with $m_{TS} = 3$ and window $w_{TS} = 11$, then the data was down-sampled to the desired number of load levels and spatially smoothed with a Gaussian of kernel ($\sigma_{smooth} = 2$). The kinematic data was fed to the in-house VFM program to identify the parameters of Hill48 and Yld2000-2D. For the identification, a virtual mesh of 10 $\times$ 10 elements, a material variation of 15% ($\delta\chi_i = -0.15\chi_i$) and a scaling parameter [45] of 0.3 were used. Additionally, the elastic properties were set *a priori* to the typical values for steel, *i.e.* E =200 GPa and $\nu = 0.3$.

Minimisation of the cost function (Eq. 15) was carried out in Matlab, starting from four points selected with a random number generator. Initially, Levenberg-Marquardt algorithm was used (`lsqnonlin`) but it was found that the algorithm could not converge to a unique global minimum. The method was then switched to `fmincon` with the sequential quadratic programming algorithm (SQP) which was capable of converging to the same solution regardless of the starting point.

To quantify the identification accuracy a metric based on reconstructed apparent yield stress was used [45]. In this approach, instead of comparing parameters on a one-by-one basis, a model is used to reconstruct the apparent yield stress that would cause yielding at a given orientation in a 1D loading scenario (see Fig. 11(a)). Additionally, the effect of hardening can be accounted for which results in a map of the apparent yield stress as a function of orientation and level of plastic strain. The global mean error is constructed as a mean

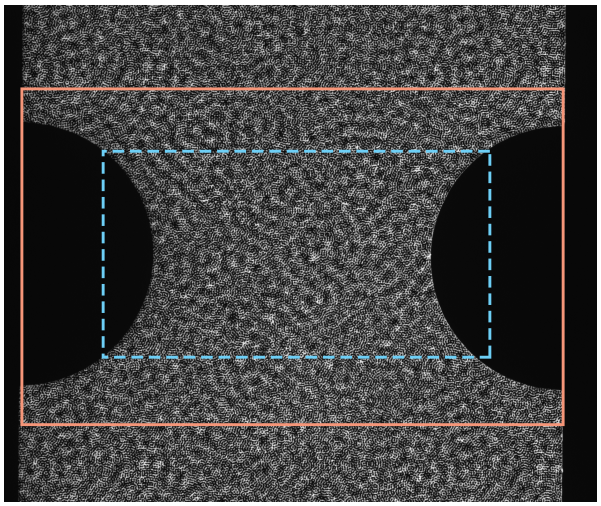

(a) Raw image of a DN specimen. The solid box represents the correlation region, the dashed box represents the region used in identification.

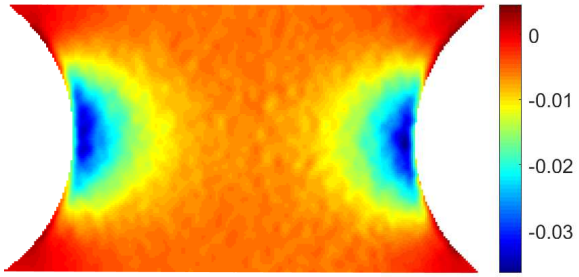

(b) Horizontal strain at 10.5 kN.

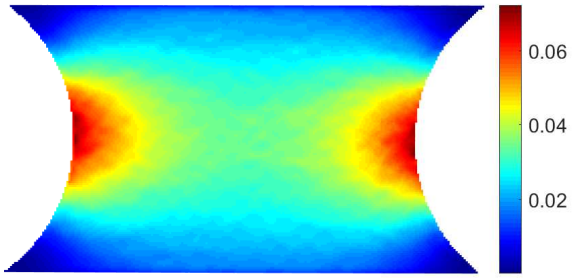

(c) Vertical strain at 10.5 kN.

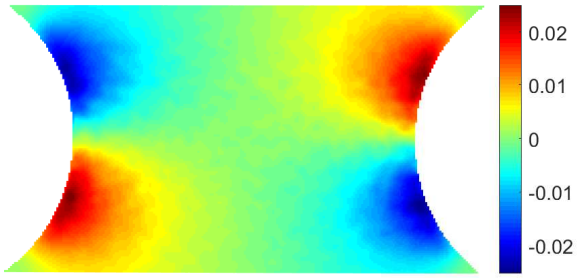

(d) Shear strain at 10.5 kN.

Fig. 13 Image of a tested DN specimen. (a) is a grey level map with marked correlation region (solid box) and region used in identifications (dashed). (b)–(d) represents strain maps obtained from the DIC using spatial smoothing of $\sigma_{smooth} = 2$ and temporal smoothing of $m_{TS} = 3$, $w_{TS} = 11$.

difference between the map corresponding to the reference parameters (from uniaxial dogbone tests) and the map corresponding to the identified parameters. This procedure helps quantify the identification error in a more meaningful way in comparison to standard one-by-one parameter comparison.

4.2.1 Identification of Hill48 with SBVFs

The first set of parameters was identified using specimens cut at 45° to RD. In total, four different samples were tested and processed and the details regarding time steps included in the identifications are presented in Table A.1. The identified parameters were used to compute the mean error based on the apparent yield stress metric. A typical map corresponding to DN-45-3 is shown in Fig. 15. The dashed cut (Fig. 15(b)) shows how well the yield stress was reconstructed at equivalent plastic strain of 0.002, and the solid cut shows the hardening behaviour along the orientation of 45°. Note that although the maximal strain used in the identification was 10%, the corresponding value in the middle of the ROI did not exceed 6%, explaining poorer identification of the hardening law at larger strains. The identified parameters and the corresponding mean error values for all samples are shown in Table 7, and graphically in terms of the apparent yield stress and predicted Lankford coefficients in Fig. 16.

Figure 16 offers an interesting insight into the relevance of Hill48 model for the tested material. From the four specimens tested, two produced a shallow variation of yield stress with orientation, corresponding to matching model to yield stresses, and the other two produced pronounced curves corresponding to the matching based on Lankford coefficients. This indicates that the model is struggling to describe the

Table 7 Identified parameters using DN test for Hill48 model.

Specimen	σ_{11} [MPa]	σ_{22} [MPa]	σ_{33} [MPa]	σ_{12} [MPa]	K [MPa]	n [-]	r_0	r_{90}	r_{45}	Mean error [%]
DN-45-1	137.8	147.0	163.3	96.2	272.4	0.316	1.40	1.98	0.94	8.6
DN-45-2	141.5	147.5	160.5	95.3	357.1	0.366	1.33	1.64	0.92	4.9
DN-45-3	152.2	148.8	158.9	88.4	342.7	0.305	1.30	1.17	1.12	3.0
DN-45-4	147.1	143.3	151.4	84.0	345.5	0.278	1.25	1.11	1.12	2.7
Reference	147.0	149.1	180.6	84.4	298	0.260	1.90	2.05	1.35	0.0

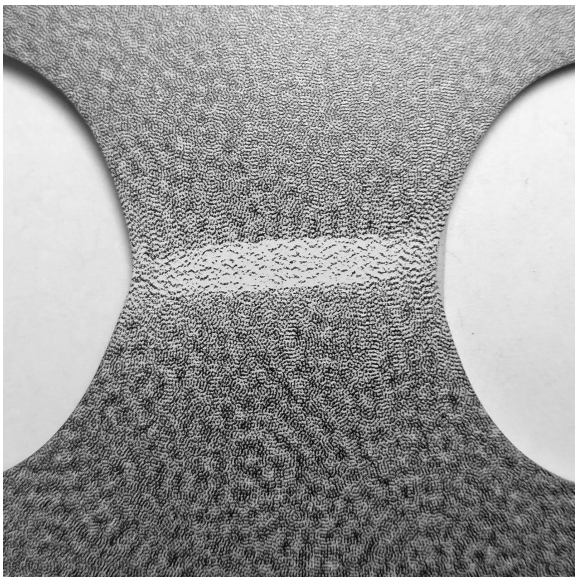

Fig. 14 A deformed DN specimen. The white base paint has debonded over the area of strain localization.

data and indeed there is no unique solution to the matching problem because of over-constraining of the model. In all cases it is seen that the Lankford coefficients are significantly underestimated. The vertical position of the reconstructed Lankford curves is driven by σ_{33}^{y} which also controls how far the biaxial part of the yield surface extends. As in the DN tests much richer information is available in comparison the the homogeneous counterparts, the limitations of the model become much clearer. Because of the interactions between the yield surface, the flow potential and the biaxial yield stress, it is impossible to match all the data at the same time with Hill48. This signifies that more advanced constitutive models are required to accurately describe the material under investigation.

4.2.2 Identification of Hill48 with UDVFs

An alternative to the SBVFs are the user-defined VFs. A set of viable virtual fields for Hill48 and the geometry used in this test has been presented in [16] based on a trial-and-error method and expertise of the lead author. These fields are:

$$\begin{cases} u_x^{*(1)} = 0 \\ u_y^{*(1)} = \dfrac{y}{H} \end{cases} \tag{26}$$

$$\begin{cases} u_x^{*(2)} = \dfrac{x}{W}\dfrac{(|y|-H)}{H} \\ u_y^{*(2)} = 0 \end{cases} \tag{27}$$

$$\begin{cases} u_x^{*(3)} = \dfrac{1}{\pi}\sin\left(\pi\dfrac{x}{W}\right)\cos\left(\pi\dfrac{y}{2H}\right) \\ u_y^{*(3)} = \dfrac{1}{\pi}\sin\left(\pi\dfrac{x}{W}\right)\cos\left(\pi\dfrac{y}{2H}\right) \end{cases} . \tag{28}$$

The virtual displacements were defined in the coordinate system presented in Fig. 18 and were constructed in a way to include all stress components in the cost function.

The same data as used in Sect. 4.2.1 was fed to the VFM algorithm, however now the UDVFs were used instead. The identified parameters were used to reconstruct variation of the yield stress and Lankford coefficient with orientation as shown in Fig. 19.

It is apparent from the figure that the UDVFs were not as successful at characterising Hill48 model as SBVFs were. The yield stress was accurately predicted at about 45° which corresponds to the orientation of the test specimen, however large errors were noted elsewhere. By using the same metric as before, the global error was calculated and was found to be approximately 20% for all specimens apart from the specimen 1. Judging based on the Lankford coefficients it is clear that the reconstructed parameters are not physical as they lead to a non-continuous distribution.

The first virtual field (Eq. 26) represents a uniform extension, which leads to a direct comparison between the measured force and the force reconstructed from the stress field. In the case of anisotropic properties this integral quantity is not sufficient to describe the model, as Fig. 19(c) demonstrates; regardless of a very good matching between the forces, the behaviour of the material is correctly identified only around the orientation of 45°.

Although other virtual fields have been included in the cost function, they were formulated in a way not to include the work of external forces. As a result, the residuals corresponding to those fields are much smaller than the one of the first field and they are not very effective at including the other two stress components in the cost function. These results highlight the problem of manually defining virtual

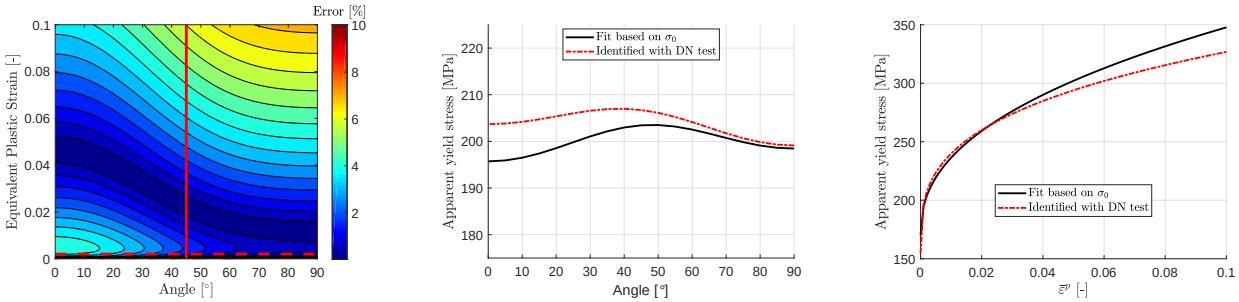

(a) The error map obtained with the reference parameters and the parameters identified from a single DN test at 45°.

(b) Cut through the dashed line in (a).

(c) Cut through the solid line in (a).

Fig. 15 Difference between parameters identified in a single DN test compared to the reference data from 3 DB tests. (a) the error map, (b) variation of yield stress with orientation at 0 plastic strain, (c) variation of yield stress at 45° with plastic strain.

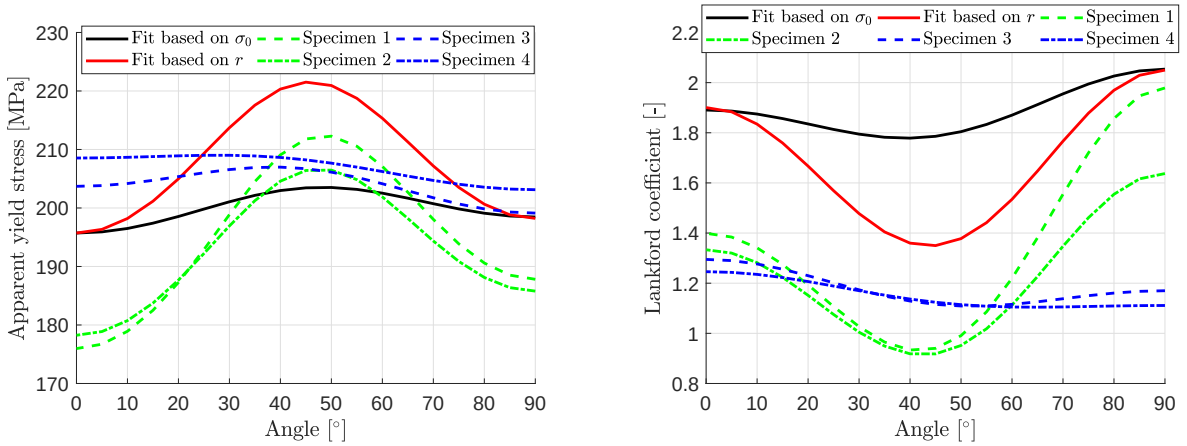

(a) Apparent yield stress reconstructed using identified data with DN tests at 45° ($\bar{\varepsilon}^p = 0.002$).

(b) Lankford coefficient reconstructed using identified data with DN tests at 45°.

Fig. 16 Reconstructed apparent yield stresses and Lankford coefficients using Hill48 and parameters identified with the DN tests performed at 45°.

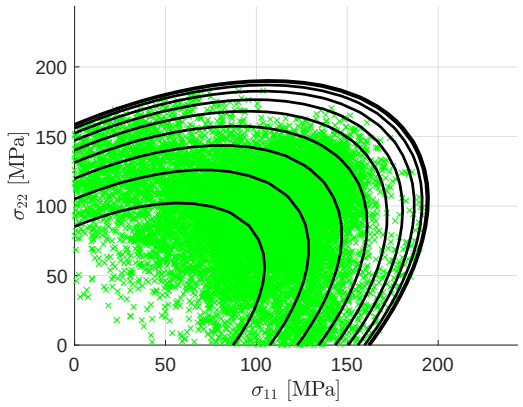

Fig. 17 Identified Hill48 yield surface for specimen DN-45-3 marked with all stress states for which yielding occurred ($0 < \bar{\varepsilon}^p < 1 \times 10^{-5}$). The yield surface was drawn at $\bar{\varepsilon}^p = 1 \times 10^{-5}$ and the contours represent increase of shear stress by $0.1\sigma_{12}^y$.

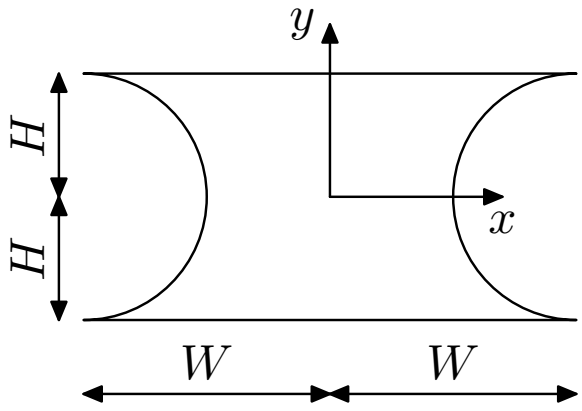

Fig. 18 The coordinate system used to define virtual fields manually within the region of interest.

fields, as they need to be hand tailored to every application with a great care and expertise in order to be functional.

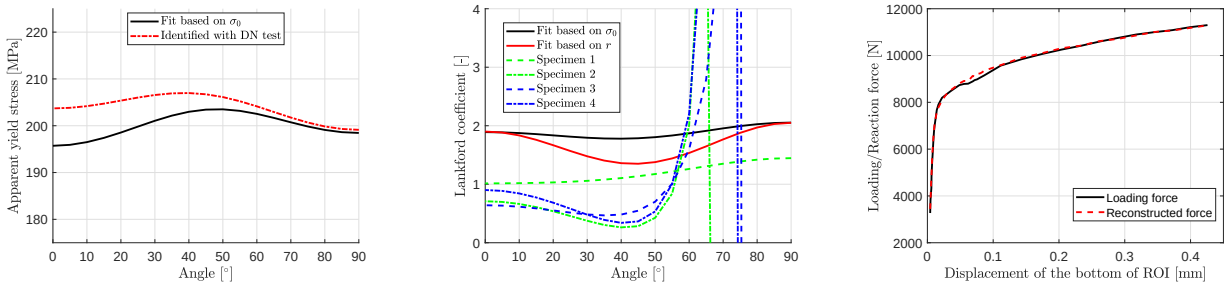

(a) Apparent yield stress reconstructed using identified data with DN tests at 45° and UDVFs($\bar{\varepsilon}^p = 0.002$)

(b) Lankford coefficient reconstructed using identified data with DN tests at 45° and UDVFs

(c) Real and reconstructed forces for Specimen 3 using UDVFs

Fig. 19 Identification of Hill48 model using a single DN test at 45° and UDVFs. (a) reconstructed yield stress variation with orientation; (b) reconstructed variation of Lankford coefficient with orientation; (c) reconstructed loading force from stresses for specimen 3.

4.2.3 The influence of data amounts on Hill48 parameters

In order to investigate whether the results depend on how much data is supplied to the identification, a study was performed where increasingly more time steps were fed to the cost function. As a baseline specimen DN-45-4 was chosen, which in the original study contained the maximal strain of 10.5%.

Here, for each consecutive identification, additional two time steps were added equal to approximately addition of 1.4% strain, up to the total of 20.3% strain in the horizontal direction, as indicated in Fig. 20. In principle, as the larger deformation is supplied to the identification, more emphasis should be put on the model to match Lankford coefficients more accurately. However, the incremental stress sensitivities related to yielding tend to filter out time steps at which majority of deformation happens. To address that, two studies were run: one in which incremental stress sensitivities were used as a base for generating SBVFs, and another one where total stress sensitivities (Eq. 18) were used instead. The findings of this study are presented in Figs. 21 and 22 for incremental and total stress sensitivities respectively and the mean error as a function of maximal strain supplied is presented in Fig. 23.

Surprisingly, the results obtained using the total (as opposed to incremental) stress sensitivities are much more consistent and stable with respect to the total number of time steps used. Additionally, the mean error is lower than the one corresponding to the incremental stress sensitivities. Although the identification was improved when the SBVFs were calculated with total stress sensitivities, no improvement in reconstruction of Lankford coefficients was found, despite supplying total strain as large as 20%.

A possible explanation for the under-performance of the SBVFs based on incremental stress sensitivities is due to filtering out large amounts of data from the cost function by the fields. As mentioned in Sect. 2.4, the incremental

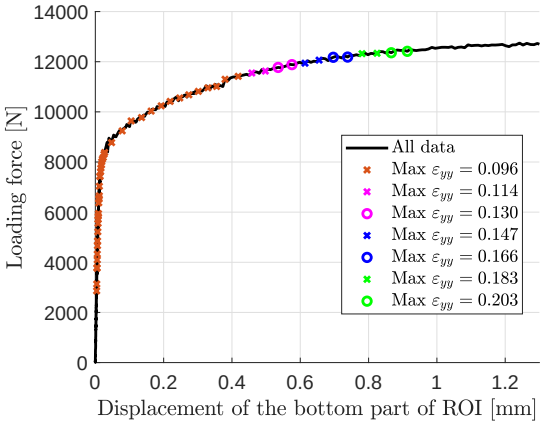

Fig. 20 Force versus the displacement of the bottom of the ROI for DN-45-3. Markers indicate data points included in the identification.

form of stress sensitivities was introduced to filter out history dependence of plasticity models and highlight transition zones between elasticity and plasticity. As a result, as soon as majority of the ROI undergoes yielding a very little region remains highlighted and not much data is contributed to the cost function. This might have a detrimental effect in anisotropic plasticity, particularly when associated-flow models are used, as the information about the anisotropy can be queried at different levels of plastic work, not only during initial yielding, but also during accumulation of deformation.

4.2.4 Identification of Yld2000-2D with SBVFs

Yld2000-2D model was identified using data from 3 experiments (DN-30-2, DN-45-3, DN-60-2) at the same time to maximise the range of stress states represented in the cost function. To simplify the problem, the reference flow curve (Eq. 25) was used, instead of identifying it together with the anisotropic coefficients. The total stress sensitivity fields

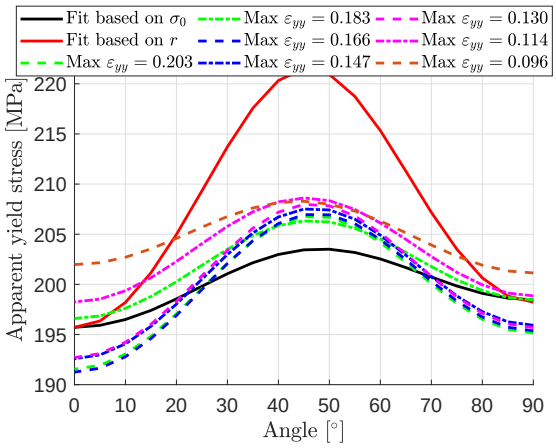

(a) Apparent yield stress reconstructed using identified data with DN tests along 45° using incremental stress sensitivities and various levels of maximal strain ($\bar{\varepsilon}^p = 0.002$).

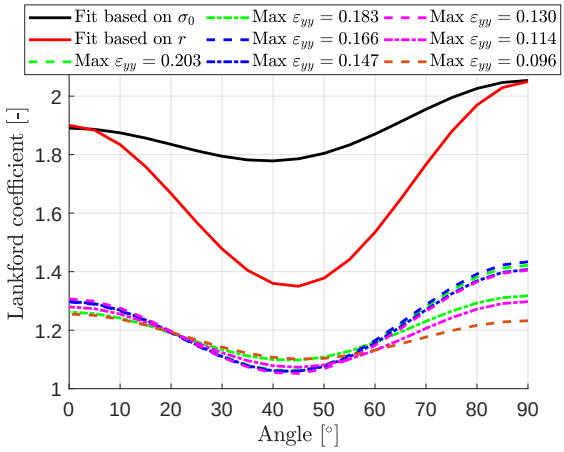

(b) Lankford coefficient reconstructed using identified data with DN tests along 45° using incremental stress sensitivities and various levels of maximal strain.

Fig. 21 Reconstructed apparent yield stresses and Lankford coefficients using Hill48 and parameters identified with the DN tests performed along 45° using incremental stress sensitivities to generate SBVFs.

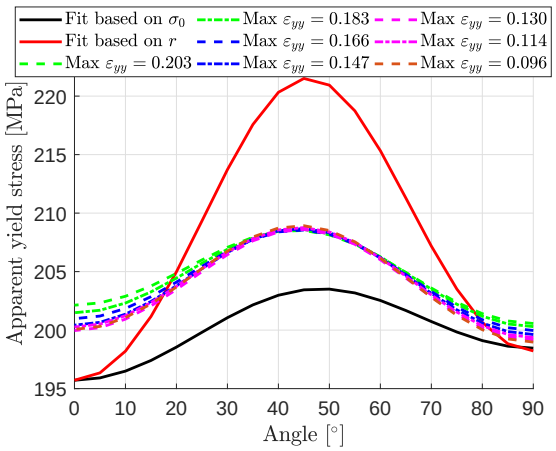

(a) Apparent yield stress reconstructed using identified data with DN tests along 45° using total stress sensitivities and various levels of maximal strain ($\bar{\varepsilon}^p = 0.002$).

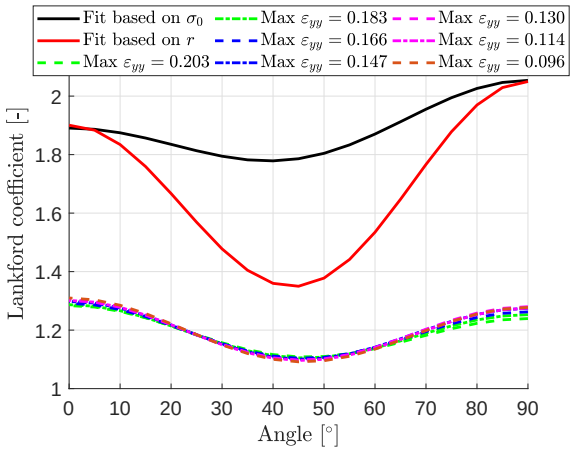

(b) Lankford coefficient reconstructed using identified data with DN tests along 45° using total stress sensitivities and various levels of maximal strain.

Fig. 22 Reconstructed apparent yield stresses and Lankford coefficients using Hill48 and parameters identified with the DN tests performed along 45° using stress sensitivities to generate SBVFs.

were used to generate SBVFs as there was no need to decouple yield and hardening related parameters. The cost function was minimised using the `fmincon` function in Matlab with the SQP algorithm. An additional constraint was added to the minimisation problem to ensure that the flow curve represents the behaviour of the material along RD [11]:

$$\left|\frac{2\alpha_1+\alpha_2}{3}\right|^6+\left|\frac{2\alpha_3-2\alpha_4}{3}\right|^6+\left|\frac{4\alpha_5-\alpha_6}{3}\right|^6=2 \tag{29}$$

Three starting points were selected using a random number generator and two of them converged to the same solution, shown in Table 8, and in terms of the yield surface in Fig. 24.

The identified yield surface shows a good agreement with the reference one in the regions where data were present, however deviates significantly near the biaxial stress state. In the region covered with data points, the difference between the two surfaces is less than 5% in terms of the shear stress. The poor description around the biaxial stress state indicates that the tests are not sufficiently heterogeneous for how flexible the Yld2000-2D function is, *i.e.* the data used in the identification is not diverse enough to constrain the shape of the yield surface over the all possible loading states. A similar observation was recently reported in [54], where authors demonstrated that their model was matched very well in the domain represented in the tests, however it did

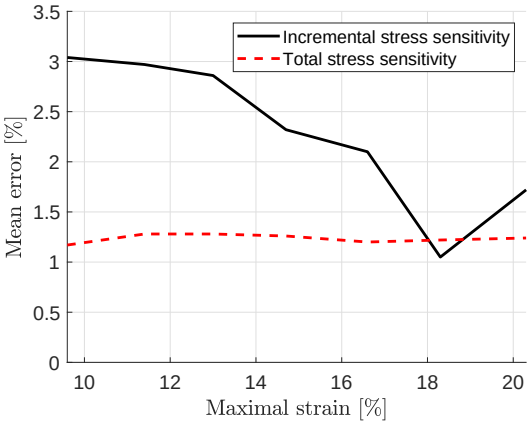

Fig. 23 Variation of mean error for Hill48 model identified using DN-45-4 specimen and SBVFs.

Table 8 Anisotropic parameters for Yld2000-2D identified with DN tests.

Test	α_1 [-]	α_2 [-]	α_3 [-]	α_4 [-]	α_5 [-]	α_6 [-]	α_7 [-]	α_8 [-]
DN-30-2+ DN-45-3+ DN-60-2	1.193	0.882	0.694	0.872	0.940	1.266	1.012	0.846
DN-30-2+ DN-45-3+ DN-60-2 + Bulge	1.097	0.967	0.781	0.894	0.918	0.893	0.978	0.967
Reference	1.061	0.994	0.663	0.879	0.899	0.740	0.964	1.092

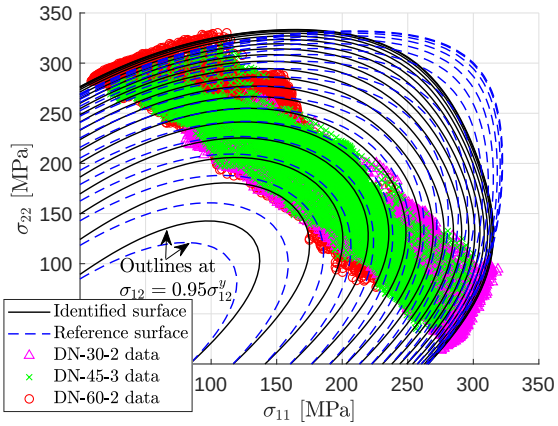

Fig. 24 Comparison of the identified Yld2000-2D yield surface and the references one (corresponding to 10 MPa of plastic work). The yield surface and the experimental data points were plotted for equivalent plastic strain of 3% to represent only the load-paths achieving significant plastic strains. The outlines are drawn for change in the shear stress corresponding to 5% of the yield stress under pure shear.

not provide good predictions outside of it. They suggested that adding an additional information to the cost function (in their case a test at different load rate) could significantly improve predictions over wider domain and relieve the issue of non-uniqueness of the material parameters.

To confirm this hypothesis another identification has been carried out, using exactly the same test configuration as above, however adding additional constraints to the optimisation problem. The optimisation function was constrained such that the identified yield surface passed through σ_b and r_b measured in the bulge test. Again three starting points were used, two of which converged to the same solution. The identified yield surface, apparent yield stress and Lankford coefficients are presented in Fig. 25. The identified model matches the reference well in terms of the yield surface and the Lankford coefficients, confirming that the three deep-notched tests did not represent enough data to identify Yld2000-2D. Once the additional constraints were added to the optimisation the SBVFs did a good job at identifying the correct parameters.

To have further insight into the completeness of the test, the number of DN tests has been gradually reduced, first to two tests ($30° + 60°$) and then to a single test ($45°$), both of which included information from the bulge test. The parameters were identified with these reduced tests using the same methodology as described before. To quantify the accuracy of identifications 3D yield surfaces were compared; each surface was reconstructed in the spherical coordinate system consisting of three variables: the azimuth angle, β, in σ_{11}-σ_{22} plane, the elevation angle, ψ, above the plane, and the radius length d. For every combination of the two

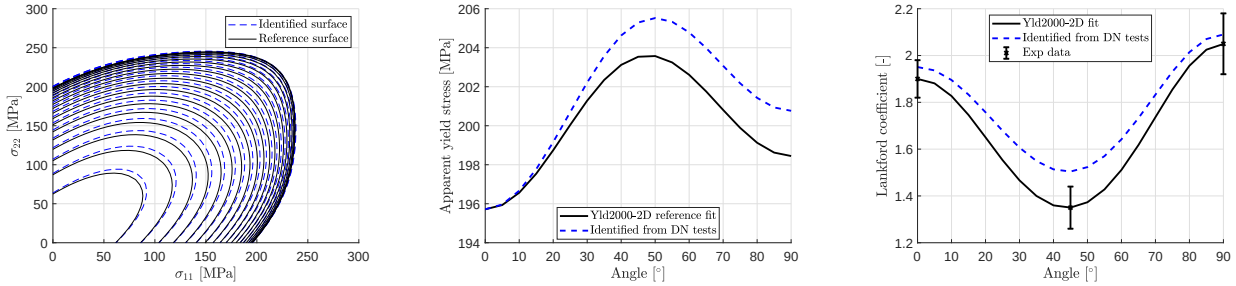

(a) Identified yield surface from three deep-notched tests under constraints of biaxial behaviour

(b) Reconstructed apparent yield stress for Yld2000-2D (at $\bar{\varepsilon}^p = 0.002$)

(c) Reconstructed Lankford coefficients for Yld2000-2D

Fig. 25 Comparison of the identified Yld2000-2D yield surface and the references one (corresponding to 10 MPa of plastic work). The yield surface was identified using three deep-notched tests and the data from the bulge test.

angles, the distance from the origin to the yield surface was calculated and compared between the reference and identified sets of parameters. The error has been defined as a relative difference between the two distances:

$$r_{err}(\beta,\psi,\boldsymbol{\chi}^{id}) = \left| \frac{d^{ref}(\beta,\psi,\boldsymbol{\chi}^{ref}) - d^{id}(\beta,\psi,\boldsymbol{\chi}^{id})}{d^{ref}(\beta,\psi,\boldsymbol{\chi}^{ref})} \right| \quad (30)$$

The error is convenient for comparing 3D yield surfaces as it offers one-to-one correspondence between the models. The error maps associated with the three test combinations are presented in Fig. 26. From the figure, it is clear that the more tests were included in the identification, the smaller the difference between the reference and identified models. Particularly, the errors were pronounced in regions not represented in tests, *e.g.* between the uniaxial test along 45° and the equibiaxial region. When two or three tests were used, some error was also found close to the uniaxial tension at 90°. This however, could be explained by the fact that the reference set of parameters was generated with the average flow stress ratios; in reality, the reference yield surface represents material behaviour approximately over a large range of plastic work, whereas DN tests contain information corresponding mostly to the low plastic work at which the ratios vary considerably (Fig. 10). In the case of the single test, the error in this region is much larger, suggesting that the test is not sufficient to characterise all possible orientation angles of the material.

The results suggest that the DN tests alone are not rich enough to fully identify Yld2000-2D model. A possible solution to that problem is development of another test, that inspects the yield surface under a completely different combination of stress states and combining them together to enrich the cost function. A good candidate would be a modified biaxial tension test, such as the one presented in [55]. In this test, most of the load-paths are located near the bi-axial tip of the yield surface complementing the distribution obtained in the DN tests.

Full-field measurements give an insight into a large range of load paths to which the model is calibrated to. These identified parameters represent a more complete response of the material, compared to the parameters derived from three uniaxial tests and a biaxial one. Further work needs to be done to establish which of the two sets of parameters is better. The validation procedure could be performed by modelling an independent test using the two models, and comparing the predictions with measurements. This is an exciting opportunity for future studies.

5 Conclusions

In this work we have tested a sheet of DC04 steel alloy using the standard testing protocol and experiments on deep-notched specimens to identify two constitutive models: Hill48 and Yld2000-2D. The virtual fields method, combined with the sensitivity-based virtual fields, has been employed to extract constitutive parameters from full-field measurements. The main outcomes of this study can be summarized as follows:

- The results presented in this contribution suggest that the sensitivity-based virtual fields are effective at extracting information about material parameters regardless of the complexity of the model.
- When the heterogeneous tests were used to identify Hill48, the material parameters converged either to a solution based on Lankford coefficients, or the one based on the yield stresses, but the absolute value of the Lankford coefficients was always underestimated. We suggest that the underlying mechanism lies in the over-constraining of the model, and that the biaxial behaviour influences the identified Lankford coefficients. Overall, the three standard tests were successfully replaced with one deep-notched test performed at 45°
- User-defined virtual fields, selected based on the recommendations of [16], were used as an alternative to the

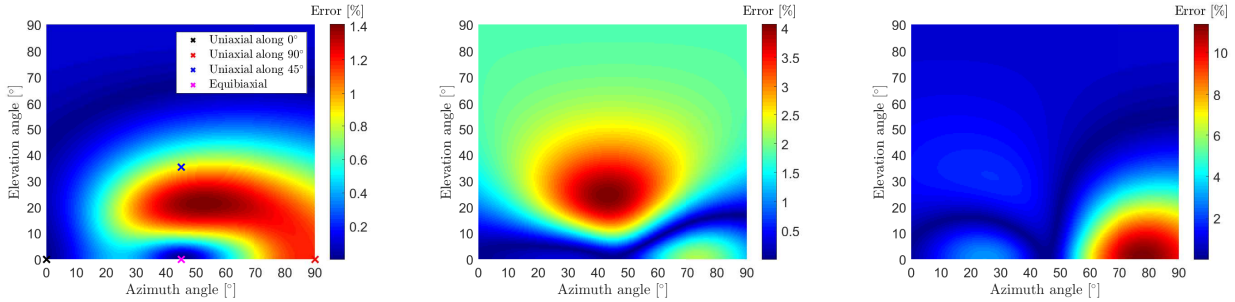

(a) $45° + 30° + 60°$+bulge (b) $30° + 60°$+bulge (c) $45°$+bulge

Fig. 26 Error maps for combinations of DN tests used to identify Yld2000-2D. The increasing number of tests included in identification decreases the overall error.

SBVFs. It was found that the identified parameters were less accurate compared to ones obtained with the SBVFs. The behaviour of the material was only matched along the orientation of the test used for characterisation (45°) and overall, much larger global errors were noted.

– For Hill48 using total, as opposed to the incremental, stress sensitivity fields to generate SBVFS, improved consistency of the identification. This is most likely due to incremental stress sensitivity fields filtering out the majority of the supplied data, especially once the entire ROI has yielded. On the contrary, when the total stress sensitivity fields are used, time steps with larger plastic deformation have more impact on the cost function and identification.
– The number of load levels included in the identification did not significantly influence the values of identified material parameters for Hill48
– Deep-notched tests were not rich enough to identify Yld2000-2D over all possible loading states. It was found that the identified and the reference yield surfaces matched well, but only in the regions represented in the test. When data from the bulge test was used to constrain the cost function, the identified model matched the reference very well over the entire stress space.
– It was found that commonly used Levenberg-Marquardt algorithm was not capable of finding the global minimum of the cost function. The sequential quadratic programming algorithm was used instead as it was robust enough to converge to the global minimum from a number of independent starting points.

The authors believe that the sensitivity-based virtual fields provide a significant step forward to calibrate non-linear models with the VFM, but there are still some problems worth investigating. In particular, there are no guidelines on the selection of how much data should be used in identification (e.g. maximum strain, magnitude of strain increments). This should be studied rigorously, particularly employing the procedure of image deformation to account for the DIC parameters involved in the data processing [56]. Finally, the selection of the sample geometry still remains an open problem, and the results could certainly be improved further if the test was richer in terms of load paths.

6 Acknowledgements

Dr. Frances Davis and Prof. Fabrice Pierron acknowledge support from Engineering and Physical Sciences Research Council (EPSRC) through grant EP/L026910/1. Prof. Fabrice Pierron also expresses gratitude to the Wolfson Foundation for support through a Royal Society Wolfson Research Merit Award. Mr Aleksander Marek acknowledges funding from EPSRC through a Doctoral Training Grant studentship. Dr. Davis also acknowledges support from the Leverhulme Early Career Fellowship.

7 Data statement

Data supporting this study are openly available from the University of Southampton repository at http://dx.doi.org/10.5258/SOTON/ The repository contains raw images of deep-notch tests and the VFM program (implemented in Matlab) used for identification of material properties.

References

1. R. Hill. A theory of the yielding and plastic flow of anisotropic metals. Proceedings of the Royal Society A: Mathematical, Physical and Engineering Sciences, 193(1033):281–297, 1948.
2. F. Barlat and K. Lian. Plastic behavior and stretchability of sheet metals. part i: A yield function for orthotropic sheets under plane stress conditions. International Journal of Plasticity, 5(1):51–66, jan 1989.
3. T. B. Stoughton. A non-associated flow rule for sheet metal forming. International Journal of Plasticity, 18(5-6):687–714, oct 2002.
4. D. Banabic, S. D. Comsa, and T. Balan. A new yield criterion for anisotropic sheet metals under plane stress conditions. In Proceedings of the Cold Metal Forming 2000 Conference, pages 217–224, Cluj Napoca, 2000.
5. D. Banabic, H. Aretz, D. S. Comsa, and L. Paraianu. An improved analytical description of orthotropy in metallic sheets. International Journal of Plasticity, 21(3):493–512, mar 2005.
6. F. Barlat, J.C. Brem, J.W. Yoon, K. Chung, R.E. Dick, D.J. Lege, F. Pourboghrat, S.-H. Choi, and E. Chu. Plane stress yield function for aluminum alloy sheets—part 1: theory. International Journal of Plasticity, 19(9):1297–1319, 2003.
7. O. Cazacu and F. Barlat. Generalization of drucker's yield criterion to orthotropy. Mathematics and Mechanics of Solids, 6(6):613–630, dec 2001.
8. O. Cazacu and F. Barlat. Application of the theory of representation to describe yielding of anisotropic aluminum alloys. International Journal of Engineering Science, 41(12):1367–1385, jul 2003.
9. T. B. Stoughton and J. W. Yoon. Anisotropic hardening and non-associated flow in proportional loading of sheet metals. International Journal of Plasticity, 25(9):1777–1817, sep 2009.
10. F. Barlat, H. Aretz, J.W. Yoon, M.E. Karabin, J.C. Brem, and R.E. Dick. Linear transfomation-based anisotropic yield functions. International Journal of Plasticity, 21(5):1009–1039, 2005.
11. A. Güner, C. Soyarslan, A. Brosius, and A.E. Tekkaya. Characterization of anisotropy of sheet metals employing inhomogeneous strain fields for Yld2000-2D yield function. International Journal of Solids and Structures, 49(25):3517–3527, 2012.
12. Y. Pannier, S. Avril, R. Rotinat, and F. Pierron. Identification of elasto-plastic constitutive parameters from statically undetermined tests using the virtual fields method. Experimental Mechanics, 46(6):735–755, 2006.
13. J.-H. Kim, K. Kim, H. N. Han, F. Barlat, and M.-G. Lee. Strain rate dependent tensile behavior of advanced high strength steels: Experiment and constitutive modeling. Materials Science and Engineering: A, 559:222–231, jan 2013.
14. J.-H. Kim, A. Serpantié, F. Barlat, F. Pierron, and M.-G. Lee. Characterization of the post-necking strain hardening behavior using the virtual fields method. International Journal of Solids and Structures, 50(24):3829–3842, 2013.
15. J.-H. Kim, F. Barlat, F. Pierron, and M.-G. Lee. Determination of anisotropic plastic constitutive parameters using the virtual fields method. Experimental Mechanics, 54(7):1189–1204, 2014.
16. M. Rossi, F. Pierron, and M. Štamborská. Application of the virtual fields method to large strain anisotropic plasticity. International Journal of Solids and Structures, 97-98:322–335, 2016.
17. M. Grédiac, F. Auslender, and F. Pierron. Applying the virtual fields method to determine the through-thickness moduli of thick composites with a nonlinear shear response. Composites Part A: Applied Science and Manufacturing, 32(12):1713–1725, dec 2001.
18. F. Pierron and P. Forquin. Ultra high speed full-field deformation measurements on concrete spalling specimens and stiffness identification with the virtual fields method. Strain, 48(5):388–405, 2012.
19. T. Guélon, E. Toussaint, J.-B. Le Cam, N. Promma, and M. Grédiac. A new characterisation method for rubber. Polymer Testing, 28(7):715–723, 2009.
20. M. Sasso, G. Chiappini, M. Rossi, L. Cortese, and E. Mancini. Visco-hyper-pseudo-elastic characterization of a fluoro-silicone rubber. Experimental Mechanics, 54(3):315–328, 2013.
21. S-H Yoon, I. Giannakopoulos, and C. R. Siviour. Application of the virtual fields method to the uniaxial behavior of rubbers at medium strain rates. International Journal of Solids and Structures, 69-70:553–568, 2015.
22. S.-H. Yoon, M. Winters, and C. R. Siviour. High strain-rate tensile characterization of EPDM rubber using non-equilibrium loading and the virtual fields method. Experimental Mechanics, 56(1):25–35, 2015.
23. S. Avril, P. Badel, and A. Duprey. Anisotropic and hyperelastic identification of in vitro human arteries from full-field optical measurements. Journal of Biomechanics, 43(15):2978–2985, 2010.
24. L. Zhang, S. G. Thakku, M. R. Beotra, M. Baskaran, T. Aung, J. C. H. Goh, N. G. Strouthidis, and M. J. A. Girard. Verification of a virtual fields method to extract the mechanical properties of human optic nerve head tissues in vivo. Biomechanics and Modeling in Mechanobiology, 16(3):871–887, 2017.
25. S. Belhabib, H. Haddadi, M. Gaspérini, and P. Vacher. Heterogeneous tensile test on elastoplastic metallic sheets: Comparison between FEM simulations and full-field strain measurements. International Journal of Mechanical Sciences, 50(1):14–21, 2008.
26. N. Souto, S. Thuillier, and A. Andrade-Campos. Design of an indicator to characterize and classify mechanical tests for sheet metals. International Journal of Mechanical Sciences, 101-102:252–271, 2015.
27. N. Souto, A. Andrade-Campos, and S. Thuillier. Mechanical design of a heterogeneous test for material parameters identification. International Journal of Material Forming, 10(3):353–367, 2016.
28. M. Grédiac and F. Pierron. A t-shaped specimen for the direct characterization of orthotropic materials. International Journal for Numerical Methods in Engineering, 41(2):293–309, 1998.
29. F. Pierron, G. Vert, R. Burguete, S. Avril, R. Rotinat, and M. R. Wisnom. Identification of the orthotropic elastic stiffnesses of composites with the virtual fields method: Sensitivity study and experimental validation. Strain, 43(3):250–259, aug 2007.
30. K. Syed-Muhammad, E. Toussaint, and M. Grédiac. Optimization of a mechanical test on composite plates with the virtual fields method. Structural and Multidisciplinary Optimization, 38(1):71–82, may 2008.
31. P. Wang, F. Pierron, M. Rossi, P. Lava, and O. T. Thomsen. Optimised experimental characterisation of polymeric foam material using DIC and the virtual fields method. Strain, 52(1):59–79, 2015.
32. X. Gu and F. Pierron. Towards the design of a new standard for composite stiffness identification. Composites Part A: Applied Science and Manufacturing, 91:448–460, 2016.
33. M.H.H. Meuwissen, C.W.J. Oomens, F.P.T. Baaijens, R. Petterson, and J.D. Janssen. Determination of the elasto-plastic properties of aluminium using a mixed numerical–experimental method. Journal of Materials Processing Technology, 75(1-3):204–211, 1998.
34. A. Khalfallah, H. Bel Hadj Salah, and A. Dogui. Anisotropic parameter identification using inhomogeneous tensile test. European Journal of Mechanics - A/Solids, 21(6):927–942, 2002.
35. T. Pottier, F. Toussaint, and P. Vacher. Contribution of heterogeneous strain field measurements and boundary conditions modelling in inverse identification of material parameters. European Journal of Mechanics - A/Solids, 30(3):373–382, 2011.
36. T. Pottier, P. Vacher, F. Toussaint, H. Louche, and T. Coudert. Out-of-plane testing procedure for inverse identification purpose:

Application in sheet metal plasticity. Experimental Mechanics, 52(7):951–963, oct 2011.
37. S. Schmaltz and K. Willner. Comparison of different biaxial tests for the inverse identification of sheet steel material parameters. Strain, 50(5):389–403, jan 2014.
38. W. Liu, D. Guines, L. Leotoing, and E. Ragneau. Identification of sheet metal hardening for large strains with an in-plane biaxial tensile test and a dedicated cross specimen. International Journal of Mechanical Sciences, 101-102:387–398, oct 2015.
39. S. Zhang, L. Léotoing, D. Guines, and S. Thuillier. Potential of the cross biaxial test for anisotropy characterization based on heterogeneous strain field. Experimental Mechanics, 55(5):817–835, 2015.
40. M. Bertin, F. Hild, and S. Roux. On the identifiability of hill-1948 plasticity model with a single biaxial test on very thin sheet. Strain, 53(5):e12233, jun 2017.
41. M. Bertin, F. Hild, and S. Roux. On the identifiability of the hill-1948 model with one uniaxial tensile test. Comptes Rendus Mécanique, 345(6):363–369, jun 2017.
42. M. Teaca, I. Charpentier, M. Martiny, and G. Ferron. Identification of sheet metal plastic anisotropy using heterogeneous biaxial tensile tests. International Journal of Mechanical Sciences, 52(4):572–580, apr 2010.
43. M. Rossi and F. Pierron. Identification of plastic constitutive parameters at large deformations from three dimensional displacement fields. Computational Mechanics, 49(1):53–71, 2011.
44. A. Marek, F. M. Davis, and F. Pierron. Sensitivity-based virtual fields for the non-linear virtual fields method. Computational Mechanics, 60(3):409–431, 2017.
45. A. Marek, F. M. Davis, M. Rossi, and F. Pierron. Extension of the sensitivity-based virtual fields to large deformation anisotropic plasticity. International Journal of Material Forming, Available online 2018.
46. T. Belytschko, W. K. Liu, and B. Moran. Nonlinear Finite Elements for Continua and Structures. Wiley, 2006.
47. F. Pierron and M. Grédiac. The Virtual Fields Method. Springer, 2012.
48. F. Davis, J. L'Hommel, J.-B. Le Cam, and F. Pierron. Quantification of the compressibility of elastomers using DIC. In Conference Proceedings of the Society for Experimental Mechanics Series, pages 199–201. Springer International Publishing, 2017.
49. S. Bossuyt. Optimized patterns for digital image correlation. In Conference Proceedings of the Society for Experimental Mechanics Series, pages 239–248. Springer New York, sep 2012.
50. ISO 16808. Metallic materials - Sheet and strip - Determination of biaxial stress-strain curve by means of bulge test with optical measuring systems. Technical report, International Organisation of Standardization, 2014.
51. BS EN ISO 10113:2014. Metallic materials - Sheet and strip - Determination of plastic strain ration (ISO 10113:2006). Standard, British Standards Institution, 2014.
52. P. Dasappa, K. Inal, and R. Mishra. The effects of anisotropic yield functions and their material parameters on prediction of forming limit diagrams. International Journal of Solids and Structures, 49(25):3528–3550, 2012.
53. T. Kuwabara, A. Van Bael, and E. Iizuka. Measurement and analysis of yield locus and work hardening characteristics of steel sheets with different r-values. Acta Materialia, 50(14):3717–3729, aug 2002.
54. E.M.C. Jones, J.D. Carroll, K.N. Karlson, S.L.B. Kramer, R.B. Lehoucq, P.L. Reu, and D.Z. Turner. Parameter covariance and non-uniqueness in material model calibration using the virtual fields method. Computational Materials Science, 152:268–290, 2018.
55. S. Coppieters, T. Hakoyama, D. Debruyne, S. Takahashi, and T. Kuwabara. Inverse yield locus identification using a biaxial tension apparatus with link mechanism and displacement fields. Journal of Physics: Conference Series, 1063:012039, 2018.
56. M. Rossi, P. Lava, F. Pierron, D. Debruyne, and M. Sasso. Effect of DIC spatial resolution, noise and interpolation error on identification results with the VFM. Strain, 51(3):206–222, 2015.

A Appendix

This appendix contains detailed information about the data used in this report. Table A.1 shows which images (available from the online repository) were used in the identifications carried out. Image offset is the number of the first image correlated in the DIC software; load steps taken indicate numbers of *correlated* images included in the identifications (notation used here is consistent with the Matlab notation).

Table A.1 Detailed information about images used to define data sets for each individual test.

Specimen	Image offset	Load steps taken	Max strain [%]	Image capture rate [Hz]
DN-45-1	20	[30:5:100, 110:10:340]	10.2	1
DN-45-2	20	[30:5:240]	10.0	0.5
DN-45-3	21	[90:10:200, 220:20:360, 370:10:530]	10.3	1
DN-45-4	15	[100:10:490, 495:5:505]	10.5	1
DN-30-1	20	[40:10:160, 190:30:370, 380:10:480, 485]	9.9	1
DN-30-2	17	[80:10:180, 200:30:400, 390:10:500]	10.6	1
DN-30-3	11	[80:10:180, 200:20:360, 365:5:450, 455:10:495]	10.3	1
DN-60-1	21	[60:10:160, 190:30:460, 470:10:570]	10.8	1
DN-60-2	12	[80:10:180, 200:30:400, 390:10:500]	10.1	1
DN-60-3	11	[80:10:180, 200:20:360, 365:5:450, 455:10:505]	10.5	1

Chapter 6

Conclusions and future work

6.1 Conclusions

In this work, a new type of virtual fields, called sensitivity-based virtual fields, was proposed. They were formulated upon the idea of constructing a separate virtual field for each material parameter sought. That way, each field could be specialized in extracting information about the corresponding parameter, leading to a more robust identification overall. The fields are constructed based on the sensitivity of the reconstructed stress field to each of the constitutive parameters. The method is set within a general framework, allowing for any geometry, loading and material model, making it applicable to many experimental set-ups. Importantly, it overcomes some of the limitations of currently popular user-defined virtual fields, which lack generality and require significant input from the user (see Section 2.3).

The first part of the project was to establish a complete methodology for generation and use of the SBVFs. In [12] we demonstrated the basic principles behind SBVFs and tested their performance in the case of small-deformation isotropic plasticity. We studied the impact of the user inputs (virtual mesh size, value of material parameters variation and scaling) on the accuracy, and compared the fields against other two types that were previously used for the non-linear VFM, namely UDVFs and stiffness-based virtual fields. We found that the SBVFs were reliable and identified material properties with very good accuracy. In particular, when non-linear hardening was considered, they outperformed uniform UDVFs, and were far superior when high levels of noise were considered.

The method was later extended to the large-deformation framework and applied in the context of anisotropic plasticity [13]. This application was motivated by the fact that most commonly used anisotropic models require many tests for complete characterisation (*e.g.* seven uniaxial and a biaxial one for Yld2004-18 [79]), which could significantly be reduced by means of heterogeneous tests. The SBVFs were extended to account for both anisotropy and large deformation, and were tested using numerically simulated data with Hill48 and Yld2000-2D models. It was found that one test was sufficient to replace the standard protocol involving three uniaxial tests in the case of Hill48. Additionally, it was demonstrated that when noiseless data was used, Yld2000-2D could be characterised with a single test when SBVFs were used. This was not possible to achieve with UDVFs, illustrating the power the new method.

Finally, the method was validated experimentally on a cold-rolled sheet of DC04

steel alloy (Chapter 5). First, the material was tested using the standard characterisation protocol to obtain reference parameters, then deep-notched tests were performed along various orientations using digital image correlation. It was demonstrated that the SBVFs performed well in the identification of material anisotropy both in the case of Hill48 and Yld2000-2D. As expected, a significant model error was evidenced when Hill48 was employed, confirming the need for advanced constitutive models. These models on the other hand are often impractical as they require many material tests for characterisation. Full-field experiments can significantly improve this process in the future, by providing tests rich in data capable of characterising materials with less experimental effort. In particular, we showed that a single deep-notched test is sufficient to identify Hill48 model. It was also found that Yld2000-2D was matched well in the regions were data were available, however it was not enough to match it across the entire stress space due to the flexibility of the model. When biaxial data from the bulge test were added as constraints to the optimisation problem, the reference yield surface was recovered from the full-field measurements.

Although the SBVFs were developed and tested using metal plasticity, they are general and can be applied to any material model, test geometry and loading, making them extremely flexible. This has been demonstrated by using them with the direct inertial impact test, to identify rate-dependent properties of steel and aluminium alloys [80]. In this test, acceleration fields, measured with a ultra-high speed camera, take up the role of a load cell. It was demonstrated that the SBVFs performed very well, with the parameters identified from the dynamic test matching the quasi-static reference parameters for the rate-independent aluminium. On the other hand, a significant increase in yield stress and hardening modulus was found for the rate dependent 316L steel.

The potential of the SBVFs has already been recognised as they have been implemented in the commercial DIC/VFM platform MatchID ([25], *version* 2018.1.1). They were validated against UDVFs using independently generated data by means of the image deformation procedure. They were shown to outperform UDVFs in the case of isotropic plasticity and hyperelasticity [81].

6.2 Future work

The proposed method is very general and provides significant opportunities for future applications. This section attempts at highlighting a few of the major ones.

6.2.1 Effects of the amounts of data on the identification

Full-field measurements offer significant volumes of experimental data. During an experiment, cameras can be triggered with chosen frequency, often leading to thousands of images, which cannot all be included in the identification due to limited computational capacities of computers. At the moment, there are no guidelines on how many load/image steps should be included in the identification, and how average strain increment affects the results (in the case of metal plasticity). Often, authors do not even report how many images were used in the identification and thus it is difficult to objectively select the number of images for identification in a rational way. It would be interesting to investigate how strain increment magnitude, and

maximum strain fed to the identification algorithm affect the overall outcome. One of the objectives would be to investigate the impact of these variables on yield and hardening-related parameters separately. This could be achieved by means of the image deformation technique. However, simply relying on perfect data (numerically generated) might not be sufficient as real materials also suffer from model errors, thus it is recommended to include some experimental data as well. The information propagates between images through temporal smoothing, thus the effects of spatial and temporal filters should also be included in the study.

6.2.2 Design of a better heterogeneous test for anisotropic plasticity

One of the most promising routes for future research concerns the design of a better test for the identification of the Yld2000-2D model. In particular, it is believed that one of the issues right now is the lack of data points near the biaxial stress state. This is especially true when the effects of distortional hardening are to be included, as the shape of the yield surface changes considerably during biaxial hardening. Currently, systematic methods for designing heterogeneous tests are scarce [82–84]. The standard practice is to modify a tensile/biaxial test by means of introducing notches or holes that will produce heterogeneity. One of the possible ways of tackling the problem is to use optimisation algorithms to produce a test that maximizes certain heterogeneity criterion. The geometry could be defined by a number of holes, notches or curves and improved systematically to produces the desired data, relevant to the model. Apart from relying simply on maximisation of a heterogeneity criterion, an additional criterion could be added, based on the systematic and random errors associated with the identified parameters from the test.

Conversely, another approach could be tried, where the desired stress heterogeneity/distribution is assumed *a priori* and then the geometry and loading of the mechanical test is reconstructed backwards from that by means of machine learning algorithms such as neural networks. This approach, if possible, would enable to design completely new tests, with information far superior compared to modified homogeneous tests, that usually suffer from *e.g.* monotonic strain paths. Additionally, this approach is most likely to transcend traditional expertise of mechanical engineers and would promote collaboration with computer scientists.

It would be interesting to investigate whether the SBVFs could be directly used to estimate the suitability of a test for a given constitutive model. This could be achieved by looking at the magnitude of the generated virtual fields (or simply stress sensitivities) for each material parameter. Theoretically, if the model contains information about a parameter, the stress sensitivity field should highlight this information. By establishing some guidelines on the absolute values of stress sensitivities it should be possible to rank the 'completeness' of a test, providing good feedback about its applicability.

One of the main challenges in developing new tests is ensuring that the idealised test could be practically reproduced using laboratory equipment. In particular, full-field measurements are limited by spatial resolution of the cameras and as such the measured stress/strain heterogeneity is dependent on the DIC set-up. The effect of cameras and DIC procedure on measured errors could be quantified with the image deformation technique. Additionally, materials are usually tested using a standard

test machines and therefore the loading can be imposed only with a limited number of actuators (one in the case of uniaxial, and two in the case of biaxial machines). At this stage, the most plausible approach is to develop an idealised experiment numerically and adapt it to practicalities using engineering judgement. However, it is possible that in the future the numerical procedures will be advanced enough to account for those limitations during the design procedure, *e.g.* by means of developing additional test fixtures in order to achieve a complex loading.

6.2.3 Application to other constitutive models

The proposed method is very general and can be applied to any constitutive model. One of the main challenges of identifying advanced constitutive models is to ensure that the tests contain enough information to identify all of the sought parameters. The aim of this section is to provide some prospects and challenges in some of the most popular classes of models.

6.2.3.1 Anisotropic plasticity

The SBVFs were proven to be useful for anisotropic plasticity. They enabled to characterise Hill48 criterion with just a single test instead of three standard tests and matched Yld2000-2D model well in the parts of yield surface where data was available. There are however many outstanding issues. First, it would be interesting to look into kinematic hardening using the SBVFs, as this is an important model frequently used for simulating real structures. Secondly, it was pointed out that sheet metals exhibit anisotropy during hardening, *i.e.* the shape of the yield surface changes as the material hardens under different stress states. It would be interesting to look if a distortional hardening model could be characterised using a full-field experiment by means of the VFM and SBVFs.

To follow directly upon the findings of the third paper presented in this thesis, Hill48 with a non-associative flow rule could be implemented to see if it reduces the modelling error [85]. However, there are physical arguments against non-associative flow rule so this should be handled with care [86]. Yld2000-2D identification could be improved by replacing the deep-notched test with a more complete one, such as biaxial tension test on a modified specimen [87]. The model then could be replaced with Yld2004-18, which as an extension of Yld2000-2D to 3D state of stress. This model has the advantage of predicting the variable number of ears in a deep-drawing test on circular blanks [79]. Since it is unlikely to identify out-of-plane shear properties from a plane stress test, it would be possible to supplement the cost function with numerically predicted values based on crystal plasticity models [88, 89].

6.2.3.2 Strain-rate dependent plasticity

Image-based inertial impact (IBII) tests [90] can be used to investigate the properties of materials at very high strain rates. The SBVFs have already been applied in that context [80], however the research was only preliminary and further work is needed. One of the main ideas that could be explored is the parametrization of the strain-rate dependence, *i.e.* implementation of a hardening law dependent on strain-rate variables, such as the Johnson-Cook model. This is particularly interesting as in the IBII the strain-rate is not uniform during the test so it is difficult to associate

the specimen response with any particular strain rate. By identifying a strain-rate dependent law, the relationship would be explicit and the characterisation of the strain-rate effects would be more accurate. The SBVFs are particularly suitable for this task, as they are capable of generating virtual fields that are sensitive to strain-rate related parameters, in contrast to static rigid-body virtual fields commonly used with the IBII tests [91].

6.2.3.3 Hyperelasticty

Hyperelasticity defines a broad range of constitutive models and would be very interesting to look at with the VFM. Currently, few elastomer-related models have been identified with the VFM [31–33, 92], all using relatively simple virtual fields (UDVFs, randomly generated (piecewise heuristic [92])). The information in the test evolves with loading thus the intuition-based UDVFs that do not evolve during experiment may impose serious limitations on the effectiveness of the identification procedure. The SBVFs offer a natural succession to the UDVFs as they are independent from the user inputs. It can be expected that hyperelasticity will pose different challenges to the SBVFs compared to metal plasticity, however the concept should still be sound.

Bibliography

[1] F. Hild and S. Roux. Digital image correlation: from displacement measurements to identification of elastic properties - a review. *Strain*, 42(2):69–80, 2006, doi:10.1111/j.1475-1305.2006.00258.x.

[2] H. Schreier, J.-J. Orteu, and M. A. Sutton. *Image Correlation for Shape, Motion and Deformation Measurements*. Springer, 2009.

[3] M. Grédiac, F. Sur, and B. Blaysat. The grid method for in-plane displacement and strain measurement: A review and analysis. *Strain*, 52(3):205–243, 2016, doi:10.1111/str.12182.

[4] E.M.C. Jones, J.D. Carroll, K.N. Karlson, S.L.B. Kramer, R.B. Lehoucq, P.L. Reu, and D.Z. Turner. Parameter covariance and non-uniqueness in material model calibration using the virtual fields method. *Computational Materials Science*, 152:268–290, 2018, doi:10.1016/j.commatsci.2018.05.037.

[5] S. Avril, M. Bonnet, A.-S. Bretelle, M. Grédiac, F. Hild, P. Ienny, F. Latourte, D. Lemosse, S. Pagano, E. Pagnacco, and F. Pierron. Overview of identification methods of mechanical parameters based on full-field measurements. *Experimental Mechanics*, 48(4):381–402, 2008, doi:10.1007/s11340-008-9148-y.

[6] M.H.H. Meuwissen, C.W.J. Oomens, F.P.T. Baaijens, R. Petterson, and J.D. Janssen. Determination of the elasto-plastic properties of aluminium using a mixed numerical–experimental method. *Journal of Materials Processing Technology*, 75(1-3):204–211, 1998, doi:10.1016/S0924-0136(97)00366-X.

[7] J.-H. Kim, F. Pierron, M. R. Wisnom, and S. Avril. Local stiffness reduction in impacted composite plates from full-field measurements. *Composites Part A: Applied Science and Manufacturing*, 40(12):1961–1974, 2009, doi:10.1016/j.compositesa.2009.09.024.

[8] F. Pierron and P. Forquin. Ultra high speed full-field deformation measurements on concrete spalling specimens and stiffness identification with the virtual fields method. *Strain*, 48(5):388–405, 2012, doi:10.1111/j.1475-1305.2012.00835.x.

[9] G. Palmieri, M. Sasso, G. Chiappini, and D. Amodio. Virtual fields method on planar tension tests for hyperelasticity materials characterisation. *Strain*, 47:196–209, 2010, doi:10.1111/j.1475-1305.2010.00759.x.

[10] S. Avril, P. Badel, and A. Duprey. Anisotropic and hyperelastic identification of in vitro human arteries from full-field optical measurements. *Journal of Biomechanics*, 43(15):2978–2985, 2010, doi:10.1016/j.jbiomech.2010.07.004.

[11] F. Pierron and M. Grédiac. *The Virtual Fields Method*. Springer, 2012.

[12] A. Marek, F. M. Davis, and F. Pierron. Sensitivity-based virtual fields for the non-linear virtual fields method. *Computational Mechanics*, 60(3):409–431, 2017, doi:10.1007/s00466-017-1411-6.

[13] A. Marek, F. M. Davis, M. Rossi, and F. Pierron. Extension of the sensitivity-based virtual fields to large deformation anisotropic plasticity. *International Journal of Material Forming*, Available online 2018, doi:10.1007/s12289-018-1428-1.

[14] E. Turco. Tools for the numerical solution of inverse problems in structural mechanics: review and research prospectives. *European Journal of Environmental and Civil Engineering*, 21(5):1–46, 2016, doi:10.1080/19648189.2015.1134673.

[15] M. Grédiac and A. Vautrin. A new method for determination of bending rigidities of thin anisotropic plates. *Journal of Applied Mechanics*, 57(4):964, 1990, doi:10.1115/1.2897668.

[16] M. Grédiac. On the direct determination of invariant parameters governing anisotropic plate bending problems. *International Journal of Solids and Structures*, 33(27):3969–3982, 1996, doi:10.1016/0020-7683(95)00220-0.

[17] S. Avril, J. M. Huntley, F. Pierron, and D. D. Steele. 3D Heterogeneous Stiffness Reconstruction Using MRI and the Virtual Fields Method. *Experimental Mechanics*, 48(4):479–494, 2008, doi:10.1007/s11340-008-9128-2.

[18] M. Rossi, L. Cortese, K. Genovese, A. Lattanzi, F. Nalli, and F. Pierron. Evaluation of volume deformation from surface DIC measurement. *Experimental Mechanics*, 58(7):1181–1194, 2018, doi:10.1007/s11340-018-0409-0.

[19] A. Ravindran, K. M. Ragsdell, and G. V. Reklaitis. *Engineering Optimization: Method and Applications*. Wiley, 2006.

[20] M. Grédiac, E. Toussaint, and F. Pierron. Special virtual fields for the direct determination of material parameters with the virtual fields method. 1– principle and definition. *International Journal of Solids and Structures*, 39(10):2691–2705, 2002, doi:10.1016/S0020-7683(02)00127-0.

[21] M. Grédiac, E. Toussaint, and F. Pierron. Special virtual fields for the direct determination of material parameters with the virtual fields method. 2– application to in-plane properties. *International Journal of Solids and Structures*, 39(10):2707–2730, 2002, doi:10.1016/S0020-7683(02)00128-2.

[22] E. Toussaint, M. Grédiac, and F. Pierron. The virtual fields method with piecewise virtual fields. *International Journal of Mechanical Sciences*, 48(3):256–264, 2006, doi:10.1016/j.ijmecsci.2005.10.002.

[23] R. de Borst, M. A. Crisfield, et al. Non-linear finite element analysis. In *Non-linear Finite Element Analysis of Solids and Structures*, chapter 2, pages 33–37. Wiley, 2012.

[24] S. Avril and F. Pierron. General framework for the identification of constitutive parameters from full-field measurements in linear elasticity. *International Journal of Solids and Structures*, 44(14-15):4978–5002, 2007, doi:10.1016/j.ijsolstr.2006.12.018.

[25] MatchID. https://www.matchid.eu/, last accessed 11/11/2018,.

[26] N. Nigamaa and S.J. Subramanian. Identification of orthotropic elastic constants using the eigenfunction virtual fields method. *International Journal of Solids and Structures*, 51(2):295–304, 2014, doi:10.1016/j.ijsolstr.2013.09.021.

[27] S. J. Subramanian and N. Nigamaa. On a boundary condition used in virtual fields methods. *Mechanics Research Communications*, 63:41–47, 2015, doi:10.1016/j.mechrescom.2014.11.008.

[28] F. Pierron, S. Avril, and V. The Tran. Extension of the virtual fields method to elasto-plastic material identification with cyclic loads and kinematic hardening. *International Journal of Solids and Structures*, 47(22-23):2993–3010, 2010, doi:10.1016/j.ijsolstr.2010.06.022.

[29] S. Coppieters, S. Cooreman, H. Sol, P. Van Houtte, and D. Debruyne. Identification of the post-necking hardening behaviour of sheet metal by comparison of the internal and external work in the necking zone. *Journal of Materials Processing Technology*, 211(3):545–552, 2011, doi:10.1016/j.jmatprotec.2010.11.015.

[30] N. Promma, B. Raka, M. Grédiac, E. Toussaint, J.-B. Le Cam, X. Balandraud, and F. Hild. Application of the virtual fields method to mechanical characterization of elastomeric materials. *International Journal of Solids and Structures*, 46(3-4):698–715, 2009, doi:10.1016/j.ijsolstr.2008.09.025.

[31] M. Sasso, G. Chiappini, M. Rossi, L. Cortese, and E. Mancini. Visco-hyper-pseudo-elastic characterization of a fluoro-silicone rubber. *Experimental Mechanics*, 54(3):315–328, 2013, doi:10.1007/s11340-013-9807-5.

[32] S-H Yoon, I. Giannakopoulos, and C. R. Siviour. Application of the virtual fields method to the uniaxial behavior of rubbers at medium strain rates. *International Journal of Solids and Structures*, 69-70:553–568, 2015, doi:10.1016/j.ijsolstr.2015.04.017.

[33] S.-H. Yoon, M. Winters, and C. R. Siviour. High strain-rate tensile characterization of EPDM rubber using non-equilibrium loading and the virtual fields method. *Experimental Mechanics*, 56(1):25–35, 2015, doi:10.1007/s11340-015-0068-3.

[34] J.-H. Kim, S. Avril, A. Duprey, and J.-P. Favre. Experimental characterization of rupture in human aortic aneurysms using a full-field measurement technique. *Biomechanics and Modeling in Mechanobiology*, 11(6):841–853, 2011, doi:10.1007/s10237-011-0356-5.

[35] L. Zhang, S. G. Thakku, M. R. Beotra, M. Baskaran, T. Aung, J. C. H. Goh, N. G. Strouthidis, and M. J. A. Girard. Verification of a virtual fields method to extract the mechanical properties of human optic nerve head tissues in vivo. *Biomechanics and Modeling in Mechanobiology*, 16(3):871–887, 2017, doi:10.1007/s10237-016-0858-2.

[36] M. Grédiac and F. Pierron. Applying the virtual fields method to the identification of elasto-plastic constitutive parameters. *International Journal of Plasticity*, 22(4):602–627, 2006, doi:10.1016/j.ijplas.2005.04.007.

[37] Y. Pannier, S. Avril, R. Rotinat, and F. Pierron. Identification of elasto-plastic constitutive parameters from statically undetermined tests using the virtual fields method. *Experimental Mechanics*, 46(6):735–755, 2006, doi:10.1007/s11340-006-9822-x.

[38] S. Avril, F. Pierron, Y. Pannier, and R. Rotinat. Stress reconstruction and constitutive parameter identification in plane-stress elasto-plastic problems using surface measurements of deformation fields. *Experimental Mechanics*, 48(4):403–419, 2007, doi:10.1007/s11340-007-9084-2.

[39] S. Avril, F. Pierron, M.A. Sutton, and J. Yan. Identification of elasto-visco-plastic parameters and characterization of Lüders behavior using digital image correlation and the virtual fields method. *Mechanics of Materials*, 40(9):729–742, 2008, doi:10.1016/j.mechmat.2008.03.007.

[40] J.-H. Kim, A. Serpantié, F. Barlat, F. Pierron, and M.-G. Lee. Characterization of the post-necking strain hardening behavior using the virtual fields method. *International Journal of Solids and Structures*, 50(24):3829–3842, 2013, doi:10.1016/j.ijsolstr.2013.07.018.

[41] M. Rossi and F. Pierron. Identification of plastic constitutive parameters at large deformations from three dimensional displacement fields. *Computational Mechanics*, 49(1):53–71, 2011, doi:10.1007/s00466-011-0627-0.

[42] J.-H. Kim, F. Barlat, F. Pierron, and M.-G. Lee. Determination of anisotropic plastic constitutive parameters using the virtual fields method. *Experimental Mechanics*, 54(7):1189–1204, 2014, doi:10.1007/s11340-014-9879-x.

[43] M. Rossi, F. Pierron, and M. Štamborská. Application of the virtual fields method to large strain anisotropic plasticity. *International Journal of Solids and Structures*, 97-98:322–335, 2016, doi:10.1016/j.ijsolstr.2016.07.015.

[44] D. Notta-Cuvier, B. Langrand, E. Markiewicz, F. Lauro, and G. Portemont. Identification of Johnson-Cook's viscoplastic model parameters using the virtual fields method: Application to titanium alloy Ti6Al4V. *Strain*, 49(1):22–45, 2012, doi:10.1111/str.12010.

[45] S.N. Grama, S.J. Subramanian, and F. Pierron. On the identifiability of Anand visco-plastic model parameters using the virtual fields method. *Acta Materialia*, 86:118–136, 2015, doi:10.1016/j.actamat.2014.11.052.

[46] D. Notta-Cuvier, B. Langrand, F. Lauro, and E. Markiewicz. An innovative procedure for characterising a coupled elastoplastic damage model of behaviour using the virtual fields method. *International Journal of Solids and Structures*, 69-70:415–427, 2015, doi:10.1016/j.ijsolstr.2015.05.009.

[47] G. Valeri, B. Koohbor, A. Kidane, and M. A. Sutton. Determining the tensile response of materials at high temperature using DIC and the virtual fields method. *Optics and Lasers in Engineering*, 91:53–61, 2017, doi:10.1016/j.optlaseng.2016.11.004.

[48] G. Le Louëdec, F. Pierron, M. Sutton, and A. P. Reynolds. Identification of the local elasto-plastic behavior of FSW welds using the virtual fields method. *Experimental Mechanics*, 53(5):849–859, 2012, doi:10.1007/s11340-012-9679-0.

[49] G. Le Louëdec, F. Pierron, M. A. Sutton, C. Siviour, and A. P. Reynolds. Identification of the dynamic properties of Al 5456 FSW welds using the virtual fields method. *Journal of Dynamic Behavior of Materials*, 1(2):176–190, 2015, doi:10.1007/s40870-015-0014-6.

[50] K.M. Saranath and M. Ramji. Local zone wise elastic and plastic properties of electron beam welded Ti-6Al-4V alloy using digital image correlation technique: A comparative study between uniform stress and virtual fields method. *Optics and Lasers in Engineering*, 68:222–234, 2015, doi:10.1016/j.optlaseng.2015.01.005.

[51] J. Fu, F. Barlat, J.-H. Kim, and F. Pierron. Identification of nonlinear kinematic hardening constitutive model parameters using the virtual fields method for advanced high strength steels. *International Journal of Solids and Structures*, 102-103:30–43, 2016, doi:10.1016/j.ijsolstr.2016.10.020.

[52] J.M.P. Martins, A. Andrade-Campos, and S. Thuillier. Comparison of inverse identification strategies for constitutive mechanical models using full-field measurements. *International Journal of Mechanical Sciences*, 145:330–345, 2018, doi:10.1016/j.ijmecsci.2018.07.013.

[53] E. Pagnacco, D. Lemosse, I.N.S.A de Rouen, F. Hild, and F. Amiot. Inverse strategy from displacement field measurement and distributed forces using FEA. In *2005 SEM Annual Conference & Exposition on Experimental and Applied Mechanics*, 2005.

[54] J.-P. Ponthot and J.-P. Kleinermann. A cascade optimization methodology for automatic parameter identification and shape/process optimization in metal forming simulation. *Computer Methods in Applied Mechanics and Engineering*, 195(41-43):5472–5508, 2006, doi:10.1016/j.cma.2005.11.012.

[55] T. Pottier, F. Toussaint, and P. Vacher. Contribution of heterogeneous strain field measurements and boundary conditions modelling in inverse identification of material parameters. *European Journal of Mechanics - A/Solids*, 30(3):373–382, 2011, doi:10.1016/j.euromechsol.2010.10.001.

[56] D. Lecompte, A. Smits, H. Sol, J. Vantomme, and D. Van Hemelrijck. Mixed numerical–experimental technique for orthotropic parameter identification using biaxial tensile tests on cruciform specimens. *International Journal of Solids and Structures*, 44(5):1643–1656, 2007, doi:10.1016/j.ijsolstr.2006.06.050.

[57] S. Cooreman, D. Lecompte, H. Sol, J. Vantomme, and D. Debruyne. Elastoplastic material parameter identification by inverse methods: Calculation of the sensitivity matrix. *International Journal of Solids and Structures*, 44(13):4329–4341, 2007, doi:10.1016/j.ijsolstr.2006.11.024.

[58] S. Zhang, L. Léotoing, D. Guines, and S. Thuillier. Potential of the cross biaxial test for anisotropy characterization based on heterogeneous strain field. *Experimental Mechanics*, 55(5):817–835, 2015, doi:10.1007/s11340-014-9983-y.

[59] A. Güner, C. Soyarslan, A. Brosius, and A.E. Tekkaya. Characterization of anisotropy of sheet metals employing inhomogeneous strain fields for Yld2000-2D yield function. *International Journal of Solids and Structures*, 49(25):3517–3527, 2012, doi:10.1016/j.ijsolstr.2012.05.001.

[60] D. Claire, F. Hild, and S. Roux. A finite element formulation to identify damage fields: the equilibrium gap method. *International Journal for Numerical Methods in Engineering*, 61(2):189–208, 2004, doi:10.1002/nme.1057.

[61] D. Claire, F. Hild, and S. Roux. Identification of a damage law by using full-field displacement measurements. *International Journal of Damage Mechanics*, 16(2):179–197, 2007, doi:10.1177/1056789506064940.

[62] P. Ladevèze, Ph. Rougeot, P. Blanchard, and J.P. Moreau. Local error estimators for finite element linear analysis. *Computer Methods in Applied Mechanics and Engineering*, 176(1-4):231–246, 1999, doi:10.1016/s0045-7825(98)00339-9.

[63] F. Latourte, A. Chrysochoos, S. Pagano, and B. Wattrisse. Elastoplastic behavior identification for heterogeneous loadings and materials. *Experimental Mechanics*, 48(4):435–449, 2007, doi:10.1007/s11340-007-9088-y.

[64] G. Geymonat and S. Pagano. Identification of mechanical properties by displacement field measurement: A variational approach. *Meccanica*, 38(5):535–545, 2003, doi:10.1023/a:1024766911435.

[65] T. Merzouki, H. Nouri, and F. Roger. Direct identification of nonlinear damage behavior of composite materials using the constitutive equation gap method. *International Journal of Mechanical Sciences*, 89:487–499, 2014, doi:10.1016/j.ijmecsci.2014.10.002.

[66] M. B. Azzouna, P. Feissel, and P. Villon. Robust identification of elastic properties using the modified constitutive relation error. *Computer Methods in Applied Mechanics and Engineering*, 295:196–218, 2015, doi:10.1016/j.cma.2015.04.004.

[67] B. Blaysat, E. Florentin, G. Lubineau, and A. Moussawi. A dissipation gap method for full-field measurement-based identification of elasto-plastic material parameters. *International Journal for Numerical Methods in Engineering*, 91(7):685–704, 2012, doi:10.1002/nme.4287.

[68] T. Madani, Y. Monerie, S. Pagano, C. Pelissou, and B. Wattrisse. Enhanced features of a constitutive equation gap identification method for heterogeneous elastoplastic behaviours. *Advanced Modeling and Simulation in Engineering Sciences*, 4(1), dec 2017, doi:10.1186/s40323-017-0092-1.

[69] T. Madani, Y. Monerie, S. Pagano, C. Pelissou, and B. Wattrisse. Identification of heterogeneous elastoplastic behaviors using the constitutive equation gap method. *Experimental Mechanics*, 58(6):919–939, 2018, doi:10.1007/s11340-018-0389-0.

[70] Sh. Guchhait and B. Banerjee. Constitutive error based material parameter estimation procedure for hyperelastic material. *Computer Methods in Applied Mechanics and Engineering*, 297:455–475, 2015, doi:10.1016/j.cma.2015.09.012.

[71] A. P. Calderón. On an inverse boundary problem. *Computational & Applied Mathematics*, 25(2-3):133–138, 2006.

[72] M. Bonnet and A. Constantinescu. Inverse problems in elasticity. *Inverse Problems*, 21(2):R1–R50, 2005, doi:10.1088/0266-5611/21/2/r01.

[73] S. Andrieux, A. B. Abda, and H. D. Bui. Reciprocity principle and crack identification. *Inverse Problems*, 15(1):55–65, 1999.

[74] H. D. Bui, A. Constantinescu, and H. Maigre. Numerical identification of linear cracks in 2D elastodynamics using the instantaneous reciprocity gap. *Inverse Problems*, 20(4):993–1001, 2004, doi:10.1088/0266-5611/20/4/001.

[75] J. Réthoré. A fully integrated noise robust strategy for the identification of constitutive laws from digital images. *International Journal for Numerical Methods in Engineering*, 84(6):631–660, 2010, doi:10.1002/nme.2908.

[76] F. Mathieu, H. Leclerc, F. Hild, and S. Roux. Estimation of elastoplastic parameters via weighted FEMU and integrated-DIC. *Experimental Mechanics*, 55(1):105–119, 2014, doi:10.1007/s11340-014-9888-9.

[77] G. Besnard, F. Hild, and S. Roux. "finite-element" displacement fields analysis from digital images: Application to portevin–le châtelier bands. *Experimental Mechanics*, 46(6):789–803, 2006, doi:10.1007/s11340-006-9824-8.

[78] E.M.C. Jones and M.A. Iadicola. A good practices guide for digital image correlation. Technical report, International Digital Image Correlation Society, 2018.

[79] F. Barlat, H. Aretz, J.W. Yoon, M.E. Karabin, J.C. Brem, and R.E. Dick. Linear transfomation-based anisotropic yield functions. *International Journal of Plasticity*, 21(5):1009–1039, 2005, doi:10.1016/j.ijplas.2004.06.004.

[80] A. Marek, F. M. Davis, and F. Pierron. Determination of high strain rate properties of metals using the virtual fields method. In *BSSM conference 2018*, 2018.

[81] P. Lava, J. Furmanski, A. Marek, F. M. Davis, and F. Pierron. Evaluation of sensitivity-based virtual fields for non-linear parameter identification including DIC filtering effects. In *BSSM conference 2018*, 2018.

[82] N. Souto, S. Thuillier, and A. Andrade-Campos. Design of an indicator to characterize and classify mechanical tests for sheet metals. *International Journal of Mechanical Sciences*, 101-102:252–271, 2015, doi:10.1016/j.ijmecsci.2015.07.026.

[83] N. Souto, A. Andrade-Campos, and S. Thuillier. Mechanical design of a heterogeneous test for material parameters identification. *International Journal of Material Forming*, 10(3):353–367, 2016, doi:10.1007/s12289-016-1284-9.

[84] X. Gu and F. Pierron. Towards the design of a new standard for composite stiffness identification. *Composites Part A: Applied Science and Manufacturing*, 91:448–460, 2016, doi:10.1016/j.compositesa.2016.03.026.

[85] J. Lian, F. Shen, X. Jia, D.-C. Ahn, D.-C. Chae, S. Münstermann, and W. Bleck. An evolving non-associated Hill48 plasticity model accounting for anisotropic hardening and r-value evolution and its application to forming limit prediction. *International Journal of Solids and Structures*, 151:20–44, 2018, doi:10.1016/j.ijsolstr.2017.04.007.

[86] J.F.W. Bishop and R. Hill. CXXVIII. A theoretical derivation of the plastic properties of a polycrystalline face-centred metal. *The London, Edinburgh, and Dublin Philosophical Magazine and Journal of Science*, 42(334):1298–1307, 1951, doi:10.1080/14786444108561385.

[87] S. Coppieters, T. Hakoyama, D. Debruyne, S. Takahashi, and T. Kuwabara. Inverse yield locus identification using a biaxial tension apparatus with link mechanism and displacement fields. *Journal of Physics: Conference Series*, 1063:012039, 2018, doi:10.1088/1742-6596/1063/1/012039.

[88] K. Zhang, B. Holmedal, O.S. Hopperstad, S. Dumoulin, J. Gawad, A. Van Bael, and P. Van Houtte. Multi-level modelling of mechanical anisotropy of commercial pure aluminium plate: Crystal plasticity models, advanced yield functions and parameter identification. *International Journal of Plasticity*, 66:3–30, 2015, doi:10.1016/j.ijplas.2014.02.003.

[89] R. Esmaeilpour, H. Kim, T. Park, F. Pourboghrat, Z. Xu, B. Mohammed, and F. Abu-Farha. Calibration of barlat Yld2004-18P yield function using CPFEM and 3D RVE for the simulation of single point incremental forming (SPIF) of 7075-O aluminum sheet. *International Journal of Mechanical Sciences*, 145:24–41, 2018, doi:10.1016/j.ijmecsci.2018.05.015.

[90] L. Fletcher and F. Pierron. An image-based inertial impact (IBII) test for tungsten carbide cermets. *Journal of Dynamic Behavior of Materials*, 2018, doi:10.1007/s40870-018-0172-4.

[91] S. Dreuilhe, F. Davis, C. Sivour, and F. Pierron. Latest results for elasto-plastic identification at high rates using inertial impact. In *Dynamic Behavior of Materials, Volume 1*, pages 93–95. Springer International Publishing, 2017.

[92] T. Guélon, E. Toussaint, J.-B. Le Cam, N. Promma, and M. Grédiac. A new characterisation method for rubber. *Polymer Testing*, 28(7):715–723, 2009, doi:10.1016/j.polymertesting.2009.06.001.